Electron-Based Dissociation Techniques in Mass Spectrometry for the Structural Characterisation of Small Molecules and Synthetic and Natural Peptides

ANDREW THOMAS BALL

University of Durham

Department of Chemistry

Electron-Based Dissociation Techniques in Mass Spectrometry for the Structural Characterisation of Small Molecules and Synthetic and Natural Peptides

A thesis submitted in partial fulfilment of the requirements for the degree of

Doctor of Philosophy

Andrew Thomas Ball

2019

Abstract

The work detailed herein describes the development of electron-based tandem mass spectrometric techniques for the structural elucidation of small pharmaceutical molecules and peptides. Electron-induced dissociation (EID), electron-capture dissociation (ECD) and, for the first time, electron-transfer dissociation (ETD) have been shown to generate complementary information to collision-induced dissociation (CID), for the analysis of small pharmaceutical molecules and peptides.

For EID of phosphorylated small molecules, selecting precursor ions with varying numbers of sodium atoms associated with the ion allowed for targeted bond dissociation. When no sodium atoms were associated with the precursor ion, EID induced bond dissociation at the non-phosphorylated end of the precursor ion. When precursor ions with one or two sodium atoms were selected for EID, the product ions formed were the result of bond dissociation closer to, and on, the phosphate moiety.

For the first time, ETD has been successfully performed on small organic molecules. Either proton-transfer or electron-transfer occurred following interaction of a multiply protonated precursor molecule and an ETD reagent radical anion. When electron-transfer occurred, product ions were formed unique to ETD, providing complementary information to CID. Following proton-transfer, limited bond dissociation was observed. By the

use of supercharging reagents (SCRs), small molecules added to the ESI solution to aid in ionisation, the abundance of doubly protonated small organic molecules was increased with respect to singly protonated small organic molecules. The increased abundance of doubly protonated molecules allowed for the use of ETD, where the ratio of multiply protonated precursor molecules to ETD reagent radical anions is a key factor in generating efficient ETD. The efficiency of ETD for analytes over an ultra-high-performance liquid chromatography (UHPLC) gradient was significantly improved by dynamically controlling the ion abundance of multiply protonated precursor molecules, as the molecules eluted from UHPLC column. The controlled precursor ion abundance enabled the ratio of analyte to ETD reagent to remain relatively constant, resulting in more efficient ETD across the entire UHPLC peak.

Contents

Abbreviations

AAS	Atomic absorption spectroscopy
AC	Alternating current
AIMS	Aspiration ion mobility spectrometry
APCI	Atmospheric pressure chemical ionisation
ASAP	Atmospheric solids analysis probe
CCS	Collisional cross-section
CD	Circular dichroism
CEM	Chain ejection model
CI	Chemical ionisation
CID	Collision-induced dissociation
com	Centre-of-mass
CRM	Charge residue model
CSD	Charge state distribution
DC	Direct current
DFT	Density functional theory
DMS	Differential-mobility separation
DRE	Dynamic range enhancement
DTIMS	Drift-time ion mobility spectrometry
ECD	Electron-capture dissociation
EDD	Electron detachment dissociation
EED	Electron excitation dissociation
EI	Electron ionisation
EICC	Extracted ion current chromatogram

EID	Electron-induced dissociation
EIEIO	Electron impact excitation of ions from organics
ESI	Electrospray ionisation
ETcaD	Electron-transfer collision activated dissociation
ETD	Electron-transfer dissociation
FAIMS	Field-asymmetric waveform ion mobility separation
FTICR	Fourier transform ion cyclotron resonance
FTMS	Fourier transform mass spectrometry
GC	Gas chromatography
hECD	Hot electron capture dissociation
HPLC	High performance liquid chromatography
IEM	Ion evaporation model
IMS	Ion mobility separation
IR	Infrared spectroscopy
IRMPD	Infrared multi-photon dissociation
LC	Liquid chromatography
LIT	Linear ion trap
LoD	Limit of detection
LoQ	Limit of quantification
MALDI	Matrix-assisted laser desorption/ionisation
MS	Mass spectrometry
MSMS	Tandem mass spectrometry
nESI	Nano electrospray ionisation
NMR	Nuclear magnetic resonance spectroscopy

oaToF	Orthogonal acceleration time-of-flight
PK	Pharmacokinetics
PTM	Post-translational modification
PTR	Proton-transfer reaction
QET	quasi-equilibrium theory
QIT	Quadrupole ion trap
QqQ	Triple quadrupole
qToF	Quadrupole time-of-flight
RF	Radio frequency
RT	Retention time
RRKM	Rice–Ramsperger–Kassel–Marcus Theory
SC	Supercharging
SCM	Superconducting magnet
SCR	Supercharging reagent
SID	Surface-induced dissociation
SORI	Sustained off-resonance irradiation
TIMS	Trapped ion mobility spectrometry
ToF	Time-of-flight
ToF-ToF	Tandem time-of-flight
TWIMS	Traveling wave ion mobility spectroscopy
UHPLC	Ultra-high-performance liquid chromatography
UV-Vis	Ultraviolet-visible spectroscopy
WREnS	Waters research enabled software

Declaration

The work presented herein was undertaken in the Department of Chemistry at Durham University between April 2013 and October 2016. In July 2014 work was undertaken at Waters, Winslow over five days. Unless otherwise state all work is my own and has not been submitted previously for a qualification at this or any other university.

Statement of copyright

Acknowledgements

There are many people I would like to thank, who have been integral in supporting me while undertaking my doctoral study.

Firstly, I would like to thank each of my supervisors, at Durham University Dr Jackie Mosely, at AstraZeneca Dr Anthony Bristow and Martin Simms and at Waters, Dr Mike Morris. Additionally, I would like to thank everyone in Durham University's mass spectrometry group, including but not limited to Peter Stokes, Dr David Parker, Dr Aruna Prakash, Dr Vian Sdiq and Chris Whitmore. Each and every one of them have been amazingly supportive throughout the entire process and were able to give me advice and guidance whenever it was needed.

Secondly, I would like to acknowledge Jonathan Williams, Jeff Brown and Emmy Hoyes at Waters, who were an indispensable help for all of the work with the WREnS LC-ETD work. Also at Waters, I would like to thank Giovanni Gallo and Amy Bartlett for giving me time to finish writing my thesis while working for Waters.

Finally, I would like to thank my family and friends, especially Chris and Julie Ball, and my wife Kitty Ball, for their constant and unwavering support throughout this long process. Without them, this would not have been possible.

1. Introduction

Mass spectrometry (MS) is an analytical technique utilised for its detection and characterisation applications within many industries including food, chemical and pharmaceutical. The basis of MS is the ionisation of a molecule of interest, followed by the observation of how the subsequent ions separate based on their individual mass-to-charge (*m/z*) ratio within a mass analyser prior to detection. There have been many developments in recent years of both instrumentation and applications, notably the advent of new tandem mass spectrometric techniques. Tandem mass spectrometry (MSMS) is a widely used technique that enables the activation and subsequent dissociation of precursor ions to give information about the structure of an ion. An integral part of this technique is the many different fragmentation processes that exist, each designed for a slightly different purpose and many giving unique and complementary information. The main fragmentation techniques in use today are collision-induced dissociation (CID) [1], electron-capture dissociation (ECD), [2],[3] electron-induced dissociation (EID) [4] and electron-transfer dissociation (ETD) [5].

1.1. Mass spectrometry in the pharmaceutical industry

The basis of the pharmaceutical industry is to conceive, develop, produce and market medicinal drugs for use by the populous. There are many analytical challenges during drug development and production that need to be taken into account. Chief among them is the high sensitivity required to analyse very small amounts of analyte, as a high cost can be associated with the production of even a milligram of product. There are many different methods by which new drugs can be discovered, from identifying the active ingredients within natural products, to full synthesis of new molecules specifically designed to target an exact biological entity such as a receptor. Regardless of the origin of a chemical compound, analytical techniques are required to identify constituents of raw materials, to characterise new molecules of interest, or to identify the purity of synthetic target molecules, all with limited samples available. Many different spectroscopic techniques such as infrared spectroscopy (IR), Raman spectroscopy and nuclear magnetic resonance (NMR) spectroscopy are employed, which work well for molecule identification, can provide information about bond energies and the chemical environment that various atoms within the molecule are situated in. Mass spectrometry (MS) is a key tool adopted by the pharmaceutical industry that has many benefits, in particular its high sensitivity. The ability to detect ritonavir at 200 pg/mL by liquid chromatography coupled mass spectrometry (LC-MS) exemplifies this. [6]

Low limits of detection and quantification (LLoD/LLoQ) are also important analytical criteria that need to be considered when choosing an analysis method for limited quantities of analytes. During both initial synthesis and large-scale production, it is necessary to analyse the product to determine the presence of, and identify and quantify contaminants, all of which are likely to be at extremely low concentrations. These can be anything from analogous by-products, traces of solvent, unreacted chemical precursor, environmental contaminants and even dimers and isomers of the final product. In general, it is greatly dependant on the type of contaminant as to the type of analysis that needs to be undertaken. MS is ideally suited to this application due to its high sensitivity, for example, organic contaminants are assayed using LC-MS and are routinely at the attomole level (10^{-18} moles). This is highlighted by Reddy *et al.* who were able to detect and characterise unknown contaminants in simvastatin using HPLC-MSMS within a 0.1 mg/mL solution. [7]

The matrix an analyte is contained within also needs to be considered, making the selectivity of a method important. One aspect of studying new drugs that require high selectivity and separation is to determine how the body will affect the drug post-administration. This can be affected by many factors, such as how that drug is administered and the chosen dose. These studies are known as pharmacokinetic (PK) studies. During these studies, the characterisation of metabolites over time needs to be undertaken to track how the molecule interacts within the body until excreted. Many detection methods have been used for this purpose, including ultraviolet-

visible spectroscopy (UV-Vis), fluorescence spectroscopy, various electrochemical methods and colourimetric techniques. Different types of NMR spectroscopy, including ^{1}H, ^{13}C and ^{19}F have also been used for this purpose and been shown to give significant structural information for metabolites. [8] Although these methods can give good results, they lack the sensitivity for dealing with ever decreasing doses, and therefore concentrations of drugs that are now being more commonly administered. MS is ideal for this purpose, as it possesses the high sensitivity needed to analyse very low concentrations over long periods of time. When coupled to liquid or gas chromatography (LC-MSMS or GC-MSMS), MS has the ability to deal with the complex biological matrices normally encountered in this kind of study and shows high selectivity between analogous molecules. Some studies have also used a mix of many techniques, such as HPLC-NMR-MS, which offers an all-encompassing technique that provides separation, data on chemical environments and mass information. Hyphenated techniques like HPLC-NMR-MS bring high precision and repeatability to measurements due to increased selectivity, in this case based on chemical separation, chemical environments and mass.[9] All of the analytical criteria need to be met for an analysis to be fit for purpose; for example, MS would not be suitable for semi-quantitation of a mixture of compounds without the separation offered by techniques such as HPLC.

GC and LC coupled MS allows compounds separated by differences such as polarity, size and stability to be analysed by MS. Most techniques are

limited in the compounds they can analyse such as atomic absorption spectroscopy (AAS) with metals. MS has somewhat overcome this problem by using different ionisation procedures in order to create ions within the gas phase to be separated and detected. Although there are various techniques, electron ionisation (EI) and electrospray ionisation (ESI) are the most frequently used, with techniques such as matrix-assisted laser desorption/ionisation (MALDI), atmospheric pressure solids analysis probe (ASAP), atmospheric pressure chemical ionisation (APCI) and chemical ionisation (CI) being implemented to a lesser degree. EI produces radical cations by colliding electrons, produced from a cathode, with gaseous analyte molecules and is normally used for small, volatile, non-polar organic molecules, although derivatised polar molecules can also be ionised. [10] As EI is a 'hard' technique, high dissociation is usually observed meaning that complicated spectra can be displayed which may not always be desirable. [11] ESI is a much 'softer' technique *i.e.* ESI generally causes much less dissociation, giving rise to more simple spectra. ESI works by spraying an analyte dissolved in a polar solvent through a cone with a high voltage gradient that forms ions in solution, then by way of a hot sheath gas, solvent evaporation occurs leaving behind analyte ions. This technique works well for polar or ionic compounds, for example many drugs, and can be easily coupled to LC. [12]

1.2. Instrumentation

Although all mass spectrometers follow the same analytical path, *i.e.* analyte ionisation, separation based on ions' mass-to-charge ratio (*m/z*) and detection, the way in which different instruments accomplish this may vary. Due to the high number of techniques available, this section will focus only on the instrumentation used for this work as shown in Table 1.1.

Instrument	Ion Source	Mass Analyser
Synapt G2-S (Waters Corp.)	Electrospray	TriWave cell, orthogonal time-of-flight
LTQ-FT (ThermoFinnigan Corp.)	Electrospray	Linear ion trap, Fourier transform ion cyclotron resonance cell

Table 1.1. List of instruments used to show ionisation source and mass analysers.

1.2.1 Ionisation sources

In order for an analyte molecule to be analysed by mass spectrometry, it must first be ionised since neutral molecules are not affected by electric or magnetic fields. Many techniques for molecule ionisation have been conceived for use with mass spectrometry, with each method producing ions with varying stabilities and types, *e.g.* odd-electron radical ions or even-electron ions. Figure 1.1 compares some of the relevant and common ionisation techniques. Techniques at the 'softer' end of the scale generally

do not cause bond dissociation, whereas techniques at the 'harder' end of the scale often induce dissociation.

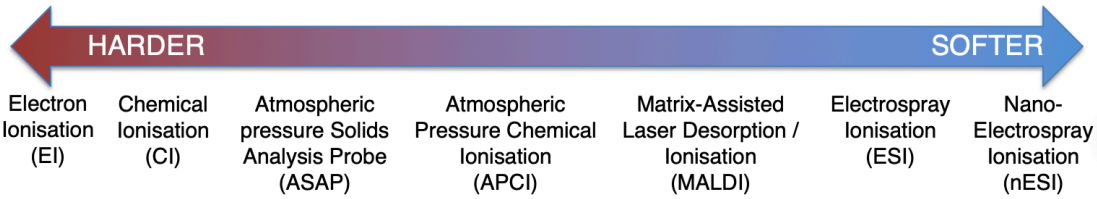

Figure 1.1. Various ionisation techniques ranked in order of 'hardness'.

1.2.1.1. Electrospray ionisation

Electrospray ionisation (ESI) is one of the 'softer' ionisation techniques and produces predominantly intact protonated molecules. This is beneficial for large, fragile molecules that would otherwise dissociate easily. ESI is utilised for both polar and ionic compounds, and with its ability to form ions with multiple charges, large molecules can be analysed in an appropriate *m/z* range for different instrument mass analysers. [13] Due to the way in which the sample is introduced to the instrument, ESI is ideally suited to be coupled with techniques such as LC and capillary electrophoresis. However, the use of buffers and salts, such as those commonly used in capillary electrophoresis, can greatly affect the ionisation processes, routinely creating $[M + Salt_n]^{n+}$.

The theory behind ESI can be broken down into three distinct stages; droplet formation, droplet shrinkage and ion desorption. First, analyte molecules dissolved in a polar solvent are sprayed through a capillary needle that has a high potential difference to a counter electrode creating a strong electric field. This causes charges to accumulate at the surface of

the liquid near the end of the needle, affecting the flow of droplets by forming a Taylor cone. [14] This process is represented in Figure 1.2.

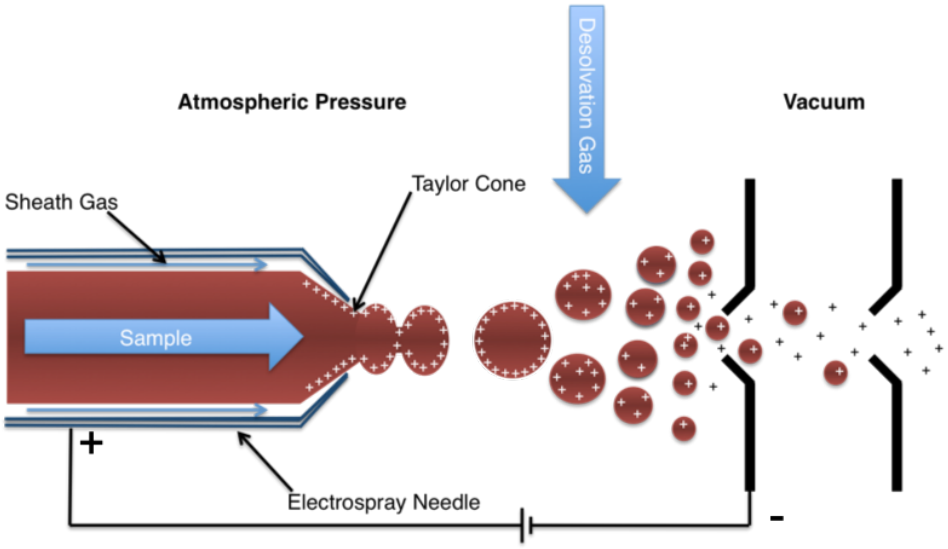

Figure 1.2. Diagram showing the electrospray process with a magnified view of the needle.

The use of a hot desolvation gas, usually nitrogen, encourages solvent evaporation from the droplet, increasing charge density until a point is reached where the surface tension of the droplet is exceeded by coulombic repulsion. This is known as the Rayleigh limit and can be defined by Equation 1.1. [15] Once the Rayleigh limit has been reached, a coulombic explosion, or fission occurs, which splits the droplet into smaller droplets. This process happens repeatedly until only a small amount of solvent remains, forming nanodroplets.

$$q_{Ry} = 8\pi(\varepsilon_0 \gamma R^3)^{1/2}$$

Equation 1.1. Rayleigh stability limit where q_{Ry} = charge (C), ε_0 = permittivity of vacuum ($C^2\ N^{-1}\ m^{-2}$), Υ = surface tension ($N\ m^{-1}$) and R = droplet radius (m).

Several different mechanisms can describe the ESI process, including the ion evaporation model (IEM), the charge residue model (CRM) and the chain ejection model (CEM). The CRM hypothesises that Rayleigh-charged solvent nanodroplets containing one analyte molecule continue to evaporate; as the last of the solvent shell evaporates, the charge held by the solvent transfers to the analyte leaving a charged analyte molecule. [16-19] This is the mechanism by which large molecules, such as proteins, are transported into the gas phase. [18-20] This is supported by the correlation between that the average charge-state of a protein following ESI and the Rayleigh charge of the smallest water droplet that could feasibly contain one protein molecule (Equation 1.1). [16, 19, 21, 22] This is further reinforced by molecular dynamics calculations which show proteins are held in the centre of a water droplet due to hydration at the protein surface. [23-25]

The IEM describes a process whereby the analyte, charged in solution with the aid of an organic acid, is directly desorbed from a small solvent droplet into the gas phase. This is achieved by solvated ions being ejected from a Rayleigh-charged nanodroplet due to the electric field surrounding it, with the ejection rate described by Equation 1.2. [19, 26, 27]

$$k = \frac{k_B T}{h} exp\left(\frac{-\Delta G^*}{k_B T}\right)$$

Equation 1.2. Transition state theory where k is the equilibrium constant, k_B is the Boltzmann constant, ΔG^* is the activations barriers height, T is the temperature and h is Planck's constant.

The initial IEM hypothesised that the activation barrier for ion ejection, pictorially shown in Figure 1.3, was due to attraction and repulsion of an ion's charge to the nanodroplets charge. However, the IEM has advanced following molecular dynamics modelling, focusing on droplets composed of water and methanol. [28] Rather than focusing on purely aqueous droplets, the mix of methanol *and* water was chosen due to the destabilising effect methanol has on droplet structure due to reduced hydrogen bonding and differing surface tension. [29, 30] Demixing, when a droplet is composed of water and methanol, has been shown to result in the outer layer of the droplet being composed of mainly methanol, giving one explanation as to why less hydrophobic analytes are more easily transported into the gas phase. [30-32] The IEM describes a process where the analyte ion remains connected to the droplet by a string of solvent molecules. This 'solvent bridge' eventually ruptures as the analyte ion is released into the gas phase. [28] This model is generally accepted as accurate for low molecular weight species, such as drugs [28, 33]. It also has been argued for larger molecules such as proteins, [34, 35] to which hybrids of IEM and CRM have been proposed. [36]

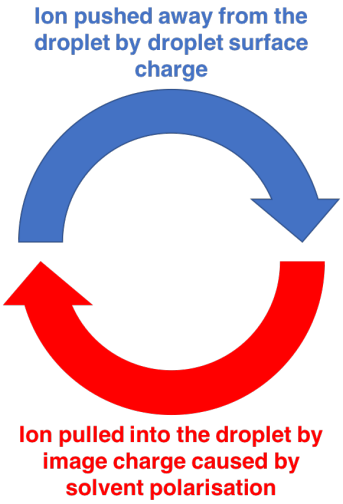

Figure 1.3. Initial IEM.

The CEM has been shown, by molecular dynamics calculations, [25, 37] to apply to proteins which have become unfolded, allowing many hydrophobic regions of the molecules to have access to solvent molecules. [38, 39] Whereas globular proteins can follow the CRM due to the majority of hydrophobic moieties being protected from solvent interaction, the increased accessibility of these groups in unfolded proteins result in the protein moving to droplet surface where one termini is ejected from the charged nanodroplet. Sequential ejection events then occur until the unfolded protein is free from the droplet in the gas phase. These three models are summarised in Figure 1.4. Following ionisation, ions are drawn into the mass spectrometer through influences of an electric field (typically applied to the entrance cone) and the vacuum of the instrument.

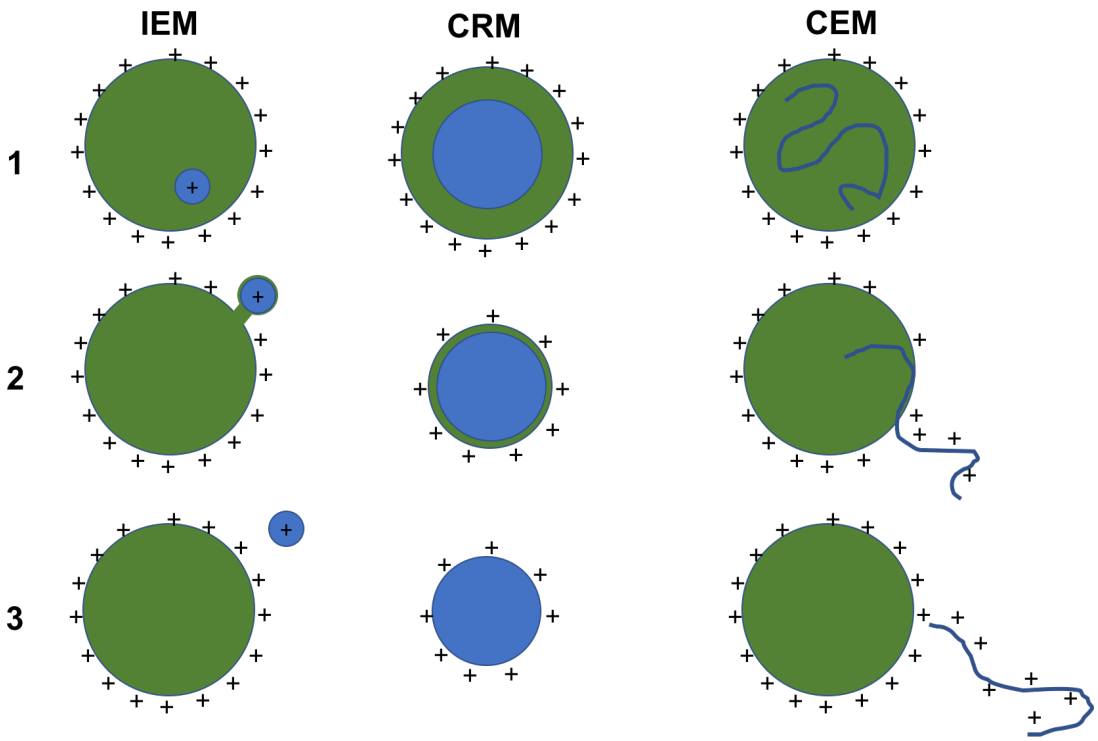

Figure 1.4. Representation of IEM, CRM and CEM.

1.2.2. Mass analysers

Mass analysers are utilised after the ionisation of analyte molecules has taken place. It is the device within the mass spectrometer that is responsible for separating ions in space or time by their mass-to-charge ratios (*m/z*). Many different varieties of mass analyser are available, all of which separate ions in a different way. The capabilities of a mass analyser can be measured and compared with the most important being sensitivity, resolving power (mass separation), mass accuracy and duty cycle. The different types used in this report are described below.

1.2.2.1. Quadrupoles

A simple quadrupole is a device made up of either four cylindrical, or four identically hyperbolic metal rods, with each opposing pair directly parallel to one another. The rods are connected in a circuit as shown in Figure 1.5 where one pair of rods has a potential of $(U + Vcos\ \omega t)$ and the other has a potential of $(-(U + Vcos\ \omega t))$ where U is a direct current (DC) voltage and Vcos ωt is a radio frequency (RF) voltage.

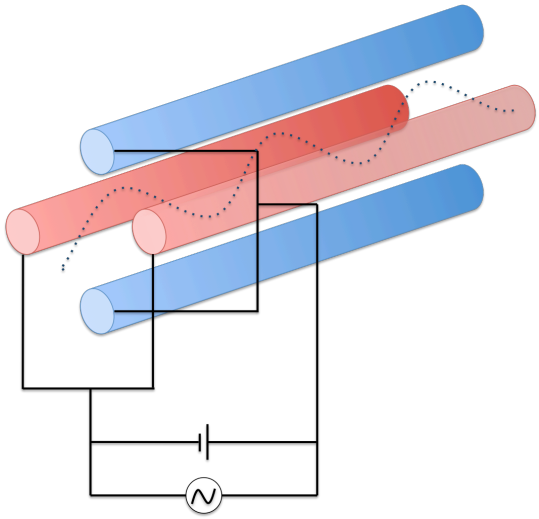

Figure 1.5. Quadrupole circuit diagram with an ion's path illustrated.

The RF voltages applied to each pair of rods have opposite polarities as they are out of phase with one another, but the same amplitudes, with a DC voltage superimposed. The RF voltage polarity switches between the two pairs of rods causing an oscillating electric field in the cavity between the poles. When an ion is introduced, it is alternately attracted to, and repelled from, opposite poles causing it to move in an oscillating motion through the centre of the quadrupole as seen in Figure 1.5. Depending on how the electric field is manipulated by way of a combination of RF and DC, an ion could collide with one of the poles causing it to become neutral and therefore not be transmitted to the detector. At a specific DC/RF, an ion of a particular *m/z* will be transmitted, therefore scanning the DC/RF will transmit every *m/z* in turn, producing a spectrum. The motion in which ions travel through a quadrupole is given by the general form of the Mathieu equation (Equation 1.3). [40-42]

$$\frac{d^2u}{d\xi^2} + (a_u - 2q_u \cos 2\xi)\, u = 0$$

Equation 1.3. Mathieu equation where a_u is a function of magnitude of a DC voltage, q_u a function of magnitude of AC voltage, and ξ is a dimensionless parameter of frequency multiplied by time divided by 2.

The way in which the electric field can be manipulated to allow ions of a particular *m/z* though the cavity can be seen in Figure 1.6, a plot of *a* (DC) and *q* (AC) from Equation 1.3, which shows the stability of different ions as a function of RF and DC voltages.

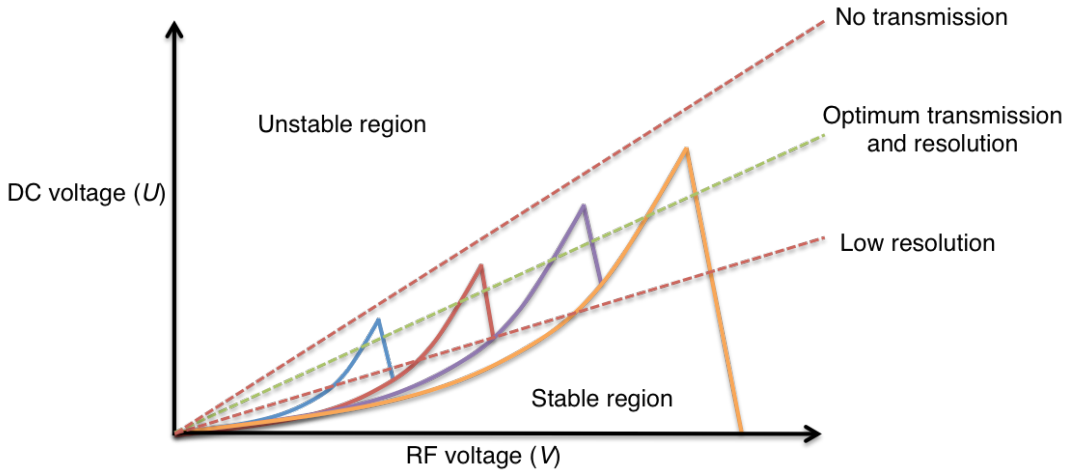

Figure 1.6. Ion stability diagram as a function of *U* and *V* inside a quadrupole.

In addition to being used as mass analysers, quadrupoles can serve other functions within a mass spectrometer such as ion guides and collision cells. To use a quadrupole as an ion guide, it is operated in RF only mode, which allows all ions to pass though the cavity without discrimination. The ThermoFinnigan LTQ-FT used for this work utilises a hexapole and an octapole, producing a quadrupolar field, to function as ion guides. The

quadrupoles in Waters qToF instruments can be tuned using settings for low mass (LM) resolution and high mass (HM) resolution to ensure all ions across a mass range can be equally transmitted. Figure 1.7 shows that LM and HM resolution can be tuned to ensure linearity in ion transmission across an *m/z* range.

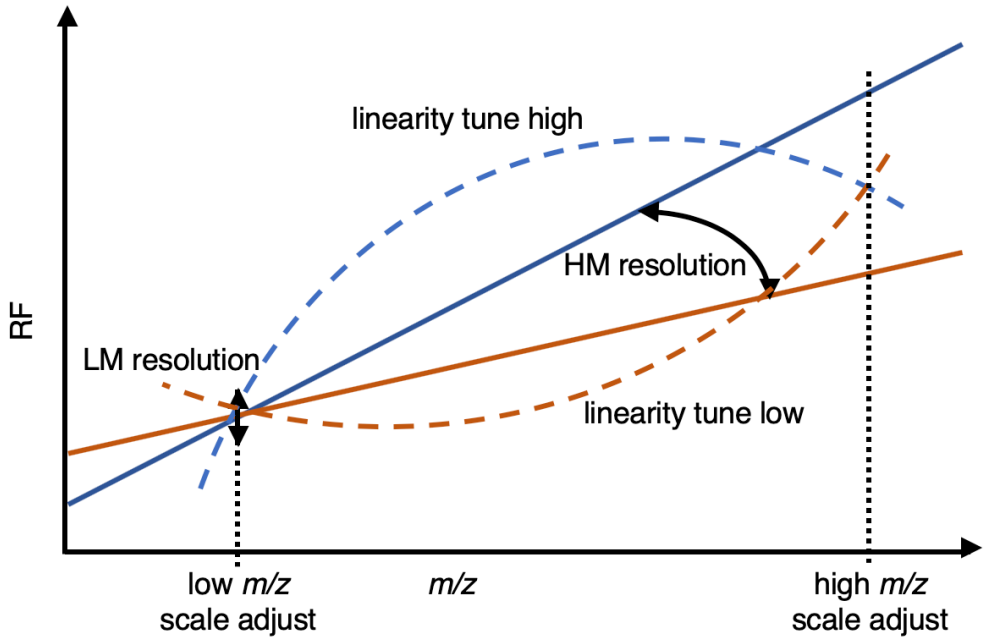

Figure 1.7. Pictorial representation of adjusting the LM and HM resolution settings on a Waters qToF mass spectrometer where the red and blue lines indicate the change in the RF versus *m/z*, determined by adjusting the LM and HM resolution settings to ensure linearity across an *m/z* range.

A quadrupole can also function as a collision cell for collision-induced dissociation (CID) in tandem mass spectrometry (MSMS), which will be further discussed in the MSMS section of this report.[40]

1.2.2.2. Ion traps

In ion traps, a packet of ions is trapped within the mass analyser and separated by an electric field caused by applying RF potentials. There are two major types of ion trap; the quadrupole ion trap (QIT), known as a 'Paul' trap or 3D trap and a subclass of this, the linear ion trap (LIT), sometimes called a 2D trap. Equation 1.3 (the Mathieu equation) equally applies to the motion ions in quadrupoles as to the motion of those within ion traps. Both types of trap work in generally the same way, but with a slightly different set-up. In a QIT, ions are trapped in a potential well between two hyperbolic end-cap electrodes with a hyperbolic ring electrode around the middle (Figure 1.8) by AC and DC electric fields.[43]

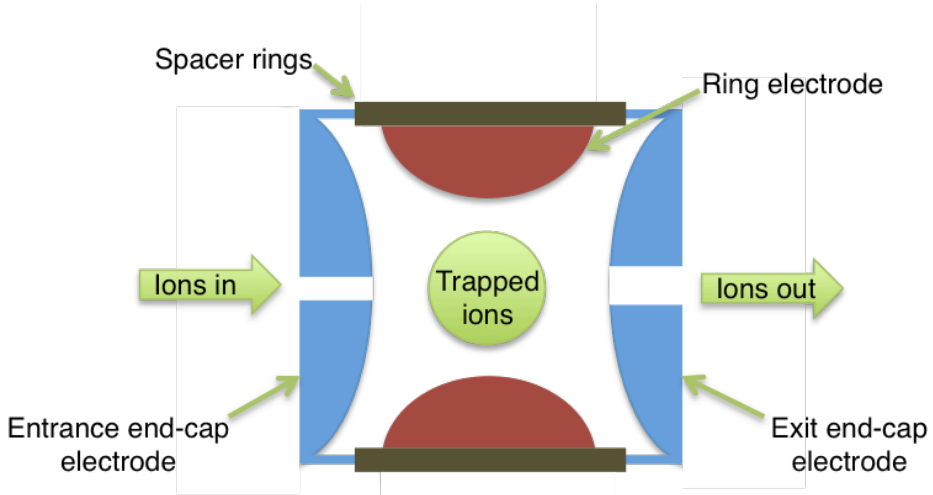

Figure 1.8. Quadrupole ion trap.

LITs function similarly to a quadrupole, with the addition of a DC voltage at either end-electrode that keeps ions within the mass analyser (Figure 1.9). These electrodes also focus ions before entering the quadrupolar region if the device is transmitting ions rather than trapping them. With both types of trap, ions trapped within the mass analyser repel each other. The longer

ions are stored, the larger their trajectory becomes, eventually causing ions to be lost. To avoid this, a pressure of around 0.13 Pa of helium is kept within the QIT, which helps to reduce the kinetic energy of the ions *via* collisions. [44],[45]

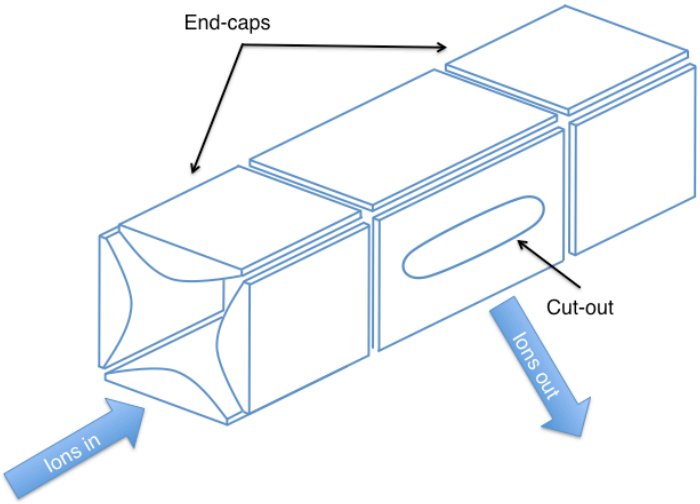

Figure 1.9. Linear ion trap.

To mass select and eject particular ions, the RF amplitude is increased while keeping the frequency constant. As shown in Figure 1.10, which is derived from Equation 1.4, the stability of ions within a trap can be calculated showing the point at which they become unstable. By increasing the acceleration voltage, *V*, ions move further along the q_z axis until they are no longer stable and are ejected from the ion trap. The means of separation comes from how higher mass ions have lower q values so become unstable later than lower mass ions. The ions will only move horizontally along the q_z axis as DC current is kept constant.

$$q_z = k\frac{V}{(m/e)}$$

Equation 1.4. Stability of an ion in a trap.

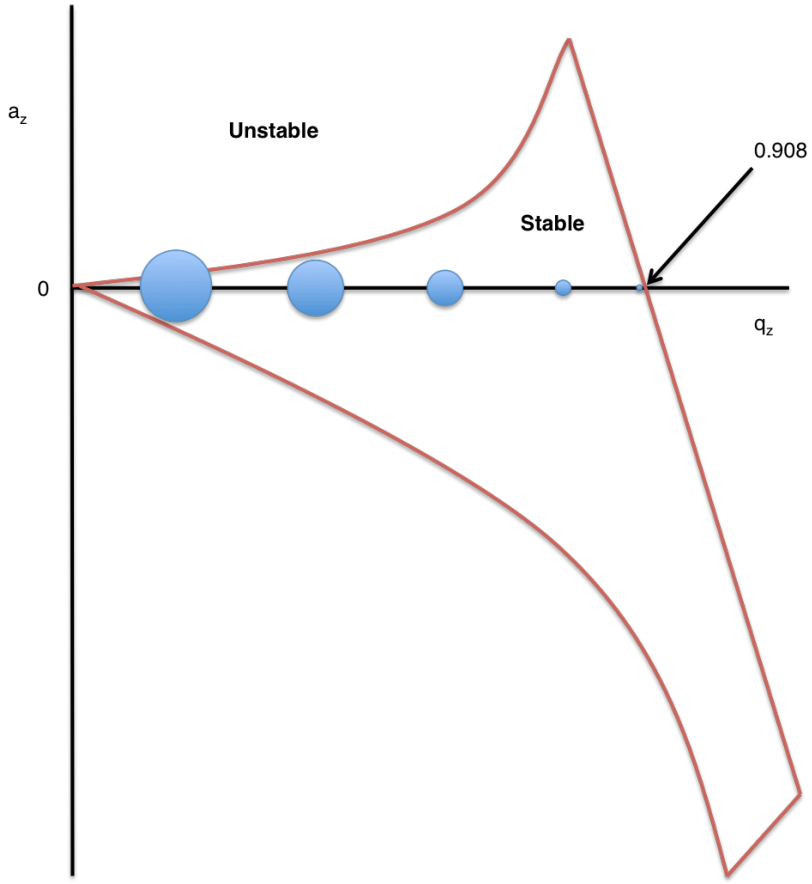

Figure 1.10. Stability diagram of ions within a trap.

By increasing the RF and DC voltages, all ions can be ejected from the trap in ascending *m/z* order, other than an ion of interest. This makes MS^n type experiments available, which are useful for gaining extra information about a certain ion. For ion excitation, an AC RF voltage that has constant frequency, but variable amplitude oscillates across the two end-caps, preventing ions from neutralising on the surface, while a driving AC voltage is applied to the ring electrode. This causes the ions to stay in the centre of the trap with a complex, oscillating motion, thereby causing ion collisions

with the helium already in the analyser. Figure 1.10 also demonstrates the stability of product ions, created from collisional dissociation, within the ion trap. Ions with a q_z exceeding 0.908 are not stable so will not be retained in the trap and will not be detected. This translate to product ions below one third of the precursor ion mass not being detected, thereby restricting the mass range and usefulness of this technique. [43],[44],[46] The ThermoFinnigan LTQ-FT uses a LIT before ions are transmitted to the Fourier transform-ion cyclotron resonance cell.

1.2.2.3. Time-of-flight

Time-of-flight (ToF) mass analysers separate ions spatially by way of the time it takes ions of a different *m/z*, but the same kinetic energy, to travel from one end of a field free region, known as a drift region, to the other (Figure 1.11).

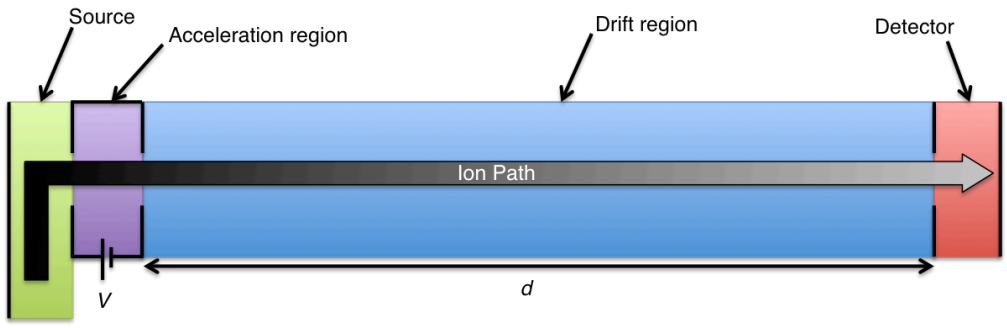

Figure 1.11. Time-of-flight mass analyser.

The same acceleration voltage (*V*) is applied to all ions, giving each ion the same kinetic energy regardless of mass. Equation 1.5 shows the relationship between kinetic energy (E_{kin}) given to an ion, its mass (*m)* and velocity (*v*).

$$E_{kin} = qeV = \frac{1}{2}mv^2$$

Equation 1.5. Where E_{kin} is kinetic energy, q is the number of charges on an ion, e is electron charge, V is the acceleration voltage, m is the mass of a particular ion and v is velocity (which is equal to distance divided by time).

This can be rearranged to give the particular velocity of an ion based on its mass-to-charge ratio as shown in Equation 1.6.

$$\frac{m}{q} = 2eVv^2$$

Equation 1.6. Rearranged form of Equation 1.5.

This can in turn be simplified further to Equation 1.7 by the removal of constants (as v is a function of distance and time, and the distance of the drift region is a constant) to give a proportional relationship between the mass-to-charge ratio of an ion and the time it takes to travel through the drift region. [47],[48]

$$\frac{m}{q} \propto t^2$$

Equation 1.7. Equation 1.6 with constants removed where t represents time.

The resolution of a ToF analyser can be improved by increasing the length of the drift region, allowing the ions more time to separate in their 'race' to the detector. Reflectrons, or ion mirrors, were developed to increase the effective flightpath of an ion without increasing the physical size of the

mass analyser. A reflectron is made up of a series of electrodes whose voltages increase in order to slow down and change the direction of the ions. This technique has the effect of further separating ions of different *m/z* as lower mass ions cannot enter the reflectrons electric field to the same extent as higher mass ions can, increasing the time heavier ions spend at the reflectron compared to lighter ions (Figure 1.12). Resolution is increased when utilising reflectrons as the effective path length of the ion is increased.

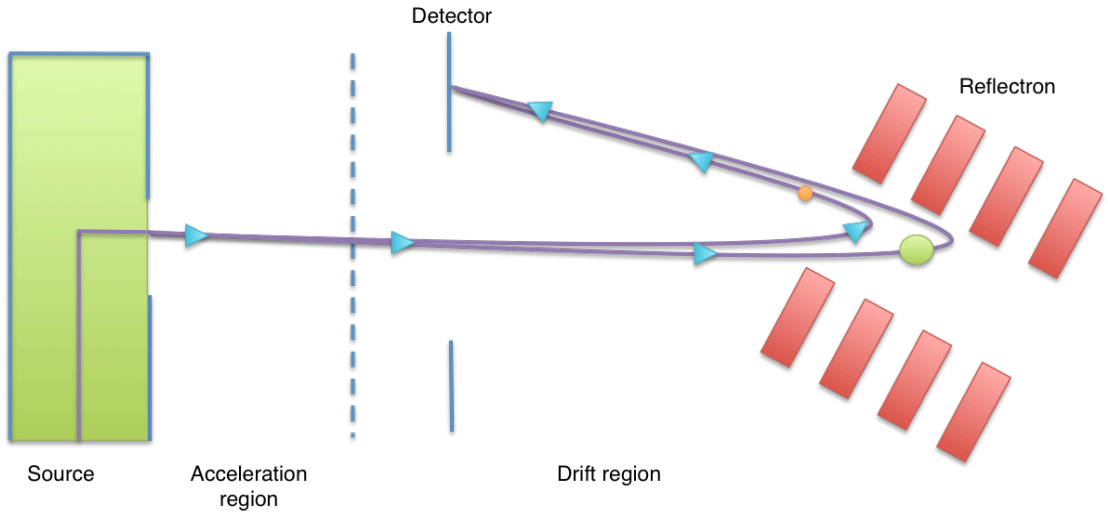

Figure 1.12. Diagram of different mass ions' path into a reflectron.

The Synapt G2-S uses orthogonal acceleration time-of-flight (oaToF) in order to allow ionisation techniques that produce a constant flow of ions, such as ESI, to be compatible. This is due to the fact that ToF analysers require a discrete packet of ions to enter the drift tube or flight tube, *i.e.* all ions need to start traveling at the same time. oaToF facilitates this by introducing the ions from the source at a 90° angle to the drift tube; a pulsed voltage is then applied opposite to the drift tube aperture, which forces the

required packet of ions into the acceleration region allowing analysis (Figure 1.12). This also has the effect of not allowing any molecules into the drift region, which reduces unwanted collisions. The use of reflectrons reduces energy aberrations between ions of the same *m/z* that were in slightly different spatial positions when energy was provided to accelerate the ions along the flight tube. Ions with higher kinetic energy will enter into the reflectron further than the ions of the same *m/z* with lower kinetic energy, thereby reducing energy aberrations. [49],[50]

1.2.2.4. Fourier transform ion cyclotron resonance

Fourier transform mass spectrometry (FTMS) is capable of very high resolution, sensitivity and mass accuracy. For the purposes of this report the cell contained with the ThermoFinnigan LTQ-FT will be discussed, although designs can vary from instrument to instrument. The basis behind a Fourier transform-ion cyclotron resonance (FT-ICR) instrument involves an FT-ICR cell inside a strong magnetic field. This is achieved by placing the cell within the bore of a 7 tesla superconducting magnet (SCM). Being a Penning ion trap, FT-ICR mass analysers separate ions while they are contained within the cell, based on the frequency at which an ion of a particular *m/z* precesses inside the cell. A high vacuum in the region of 1 x 10^{-9} mBar is maintained within the cell to stop ions colliding with gas molecules, although some FT-ICR designs facilitate rapid introduction and removal of gas as a basis for MSMS. Figure 1.13 depicts a FT-ICR cell made up of six electrodes. Those shown in red are the two trapping

electrodes that prevent ions leaving the cell using a DC voltage. Those shown in blue represent the excitation electrodes, with the green showing the detection electrodes. [51],[52],[53]

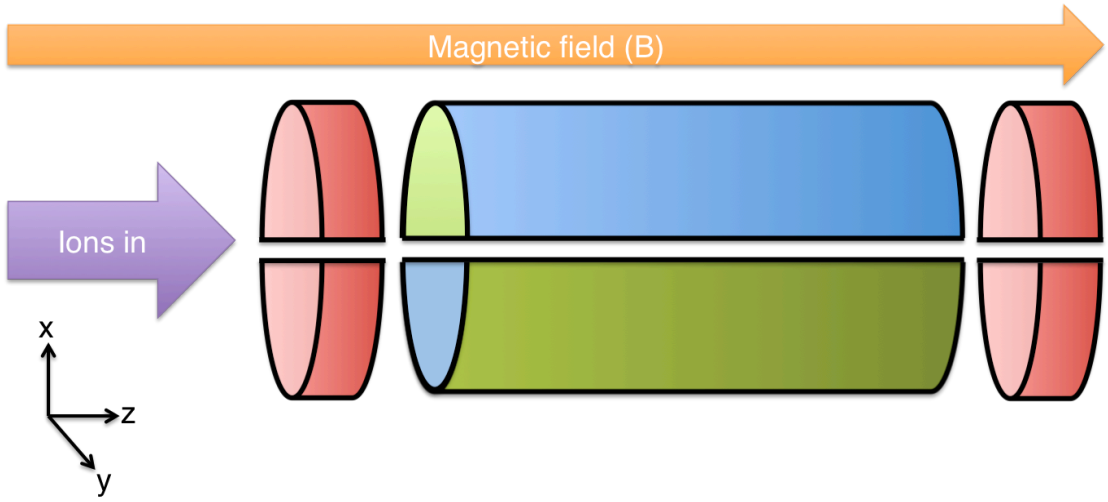

Figure 1.13. Open cylindrical FT-ICR cell.

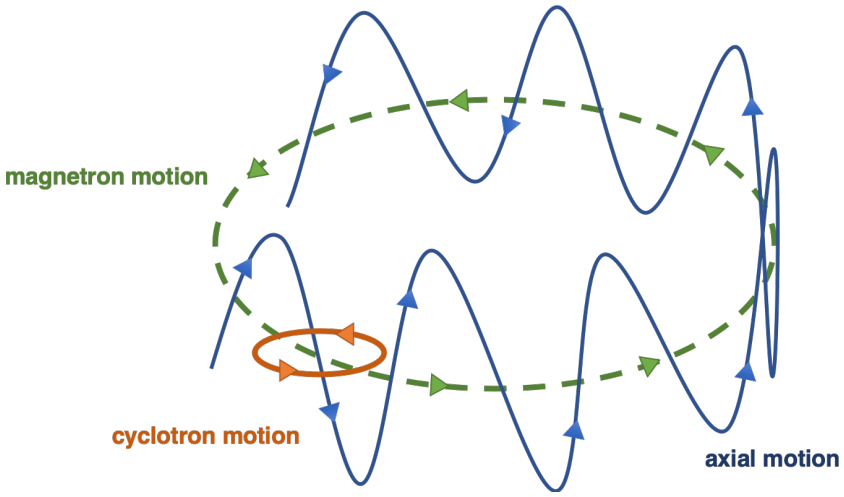

Figure 1.14. Motion of ions within an FT-ICR cell.

Ions within the FT-ICR cell have a complex motion caused by a combination of electric and magnetic fields made up of cyclotron, magnetron and trapping motions (Figure 1.14). The trapping, or axial

motion is a minimal movement along the z-axis between the two trapping electrodes. The cyclotron motion describes the movement of the ions in the x-y axis and is a periodic cyclic motion whereby frequency is specific to the *m/z* of an ion. Finally, the magnetron motion, which is of a much smaller frequency compared to cyclotron motion, also causes motion along the x and y-axis, and is superimposed on the cyclotron motion. Magnetron motion is intentionally reduced by way of injecting ions into the cell parallel to the magnetic field. When an RF voltage is applied across the excitation electrodes that match the ion cyclotron frequency of an ion contained within the cell, the radius of the flight path of the ion is increased, causing it to fly closer to the electrodes. As the newly excited ion passes a detection electrode, electrons are attracted to the ion moving towards the electrodes surface (for positive ions) and a signal is recorded. This works in the same way for negative ions, however, electrons are repelled by the negative ions, moving further away from the electrodes surface. This function occurs every time a cloud of ions pass close to the two detection electrodes, causing a sine wave to be collected. Around 100 charges (100 singly charged ions) are needed to make up the ion cloud to induce an image current. This is in contrast to detection in ToF or LIT where electron multipliers can record the signal of a single ion. If only one ion was excited at a time, data would be relatively simple to analyse, however, in an FT-ICR cell ions of different *m/z* are excited at the same time, as an excitation frequency range is used rather than a single excitation frequency. This results in the signal output becoming complex, requiring the application of the Fourier transform algorithm to obtain useable data. Once applied, this

produces a spectrum of cyclotron frequency versus intensity, which is converted using Equation 1.8, to a plot of *m/z* versus intensity. [53]

$$v_c = \frac{qB}{2\pi m}$$

Equation 1.8. Where v_c is cyclotron frequency, B is magnetic field strength, *m* is ion mass and *q* is the ion's charge.

1.2.3. Tandem mass spectrometry

1.2.3.1. Collision-induced dissociation

Collision-induced dissociation (CID) is one of the most commonly used fragmentation techniques. In the pharmaceutical industry, CID is used for studies ranging from structural elucidation to drug site binding studies. It is a vibrational dissociation technique that involves a collision between a precursor ion and a neutral target molecule such as Argon, Nitrogen or Helium, resulting in an activated ion. The collision brings about an increase in internal energy for the ion, which causes unimolecular decomposition. When an inelastic collision (kinetic energy is not conserved) occurs between an ion possessing high translational energy and a neutral target molecule, some of the ion's translation energy converts to the ions internal energy, leading to ion decomposition. [1] Using the centre-of-mass framework (com), where momentum equals zero, rather than the laboratory framework, this can be easily explained. By employing the laws of conservation of mass and of energy, the energy transfer that takes place

in collisional activation, as well as the kinetic energy released, can be determined. The whole system is considered so that the kinetic energies of both the ion and neutral target molecule are relative to one another. The centre-of-mass kinetic energy (KE_{com}) impacts upon the nature of the activation since it is relative to the total energy that is possible to be transferred from kinetic energy to internal energy. [54]

$$E_{com} = \left(\frac{N}{m_p + N}\right) E_{lab}$$

Equation 1.9. Describing how the centre-of-mass framework is linked to laboratory framework and how the masses of the precursor ion and neutral target molecule affect them, where E_{lab} = ion's kinetic energy, N = mass of neutral target molecule and m_p = mass of precursor molecule.

Equation 1.9 shows that the masses of both the neutral target molecule and of the precursor ion have a large affect in defining the CID process. Due to conservation of energy, any change in the relative translational energies of either molecule must be reflected in the resulting internal energy; this is known as collision endothermicity, q. The maximum amount of energy that can be converted from kinetic to internal energy (q_{max}) is directly proportional to the starting E_{com}. This means that q is affected by m_p so more of the kinetic energy of the ion can be converted with an increased ion size. However, E_{com} decreases as a function of the reciprocal of m_p which means that the bigger the molecule, the less internal energy will be available for fragmentation. [55] Unimolecular bond dissociation in a high vacuum environment is described in the quasi-equilibrium theory

(QET); energy can redistribute over all degrees of freedom (*i.e.* vibrational, electronic, rotational, and translational motion) therefore the molecular ion has an equal chance of being in every state. QET also postulates that the energy barrier between precursor and product ions is unidirectional, meaning fragmentation is not reversible. [56, 57] The Rice–Ramsperger–Kassel–Marcus (RRKM) theory states that a mechanism where collisional activation is followed by intramolecular vibrational relaxation results in a transition state leading to dissociation. [58, 59] Here, the rate of unimolecular dissociation and collisional activation are dependent on one another. At threshold energy, as internal energy is increased, dissociation rates are increased. Alternative dissociation pathways are produced by different molecules depending on the dissociation rate constant curve *(k(E)*) which is in turn dependant on the potential energy surface. [60]

The type of collision, whether it be elastic, inelastic or superelastic, can be determined by looking at the collision endothermicity as Table 1.2 describes. In a super-elastic collision, kinetic energy is increased at the expense of internal energy, which is not analogous to fragmentation as the internal energy must increase past the energy threshold of the molecule in order for fragmentation to occur. Elastic conditions will conserve the energy within the system, therefore causing no change to either kinetic or internal energy. With inelastic collisions, however, a decrease in kinetic energy occurs following a collision in the collision cell of a mass spectrometer, and once again due to conservation of energy, a proportional increase in internal energy transpires. [54],[1]

Collision endothermicity (*q*)	Collision type	Δ Kinetic energy	Δ Internal energy
Less than zero	Super-elastic	Increases	Decreases
More than zero	Inelastic	No change	No change
Equal to zero	Elastic	Decreases	Increases

Table 1.2. Collision endothermicities and the resulting collision type.

The general mechanism for CID, and other collisional activation methods such as surface induced-dissociation (SID), can be described as a two-part process with the first part being the activation, followed by unimolecular dissociation, which can be described by Equation 1.10 below. [1]

$$m_p{}^+ + N \rightarrow m_p{}^{+^*} \rightarrow m_f{}^+ + m_n$$

Equation 1.10. Mechanism for the collisional activation and dissociation of a precursor ion colliding with a target molecule, where m_p = mass of precursor ion, N = mass of the target molecule m_f = mass of the fragment and m_n = mass of the resulting neutral ion.

In order for fragmentation to occur in a time-scale congruent with the experiment, the threshold energy of the molecule must be surpassed; this is known as the kinetic shift. As expected, the more energy introduced (or the higher the kinetic shift), the shorter the time observed before fragmentation. CID collision energy can be classified as high collision energy, intermediate collision energy or low collision energy. These conditions are usually utilised depending on what type of instrument is

being used and the type of ions being fragmented. Although these values can be highly subjective and instrument dependant, for the purposes of this work Table 1.3 shows the typical mass spectrometer operating energy ranges for each category. The amount of energy used for the collision will affect the outcome of the experiment.

Approximate collision energy range (eV)	**Category**
1-100	Low energy collision
100-1000	Intermediate energy collision
> 1000	High energy collision

Table 1.3. Approximated range of CID collision energies.

Generally, instruments with a trapping device such as those with quadrupole ion traps (QIT), linear ion traps (LIT), and in Fourier-transform ion cyclotron resonance (FTICR) instruments, use low energy collisions as a means for ion dissociation. Low energy collisions are also used by instruments that use quadrupole devices as a collision cell, such as triple quadrupole (QqQ) and quadrupole time-of-flight instruments (qToF). In QqQ instruments, CID is brought about using the second quadrupole (q_2) as a collision cell. The lower case 'q' indicates that the second quadrupole is in RF only mode and no DC voltage is applied. This has the effect of accelerating all of the resonant ions that came from Q_1, through q_2 and into Q_3, most likely with multiple collisions occurring, usually with either Argon or Nitrogen as the collision gas. The benefit of using a QqQ instrument for

CID is that it has the ability to use various different scan modes, depending on the type of experiment required. Table 1.4 shows how each quadrupole can be used, along with the type of scan that results. In qToF instruments, the quadrupole is used like q_2 in triple quadrupole instruments when set to full scan mode.

Scan type	**Q_1**	**q_2**	**Q_3**
Full	Scanned	No gas	RF only mode
Product ion	Selected *m/z*	Gas	Scanned
Precursor ion	Scanned	Gas	Selected *m/z*
Selected reaction monitoring	Selected *m/z*	Gas	Selected *m/z*
Neutral loss	Scanned	Gas	Scanned

Table 1.4. Different scan modes available on a triple quadrupole mass spectrometer.

In some FTICR instruments, CID can be achieved in the FTICR cell in a similar manner, *i.e.* on-resonance, to the QIT method. Here the ions are subjected to a high amplitude AC potential at the exact cyclotron frequency of the precursor ion for around only 100 µs so as to not cause excess ion loss. This causes multiple collisions and results in dissociation. There is however a more common way in which CID can occur in FTICR mass spectrometers known as sustained off-resonance irradiation collision induced dissociation (SORI-CID). SORI-CID differs from the previous method by introducing a high amplitude AC potential just above the resonant cyclotron frequency of the precursor ion. This has the effect of causing the ions to orbit the FTICR cell in more erratic orbits where they

are constantly accelerating and decelerating in cycles. This reduces the translational energy of the ion which allows for a longer collision time, meaning more collisions can take place without significant ion loss. As this is much slower than before, some lower energy rearrangement reactions are favoured, giving rise to unexpected product ions. [61],[62],[63]

The pressure of the collision gas within the collision cell of an instrument is also an important factor when considering how CID takes place. It is evident that the higher the gas pressure, the higher the probability of an ion-neutral molecule collision, and also of multiple collisions, whether that be precursor ion-neutral molecule (Equation 1.11) or product ion-neutral molecule collision (Equation 1.12).

$$m_p{}^+ \overset{N}{\rightarrow} m_p{}^{+*} \overset{N}{\rightarrow} m_{f1}{}^+$$

Equation 1.11. Reaction for a product ion colliding with a neutral molecule, not dissociating, then colliding with another neutral molecule, activating and dissociating.

$$m_p{}^+ \overset{N}{\rightarrow} m_{f1}{}^+ \overset{N}{\rightarrow} m_{f2}{}^+$$

Equation 1.12. Reaction for a product ion colliding with a neutral molecule, activating and dissociating, then the resulting fragment colliding with a neutral molecule, activating and producing a second fragment ion.

Both Equations 1.11 and 1.12 can occur multiple times depending on gas pressure and the time allowed for CID by an individual instrument. For ions that prove difficult to fragment, increasing the pressure of the collision gas

can aid in dissociation by increasing the probability of multiple collisions as demonstrated in Equation 1.13. [64],[1]

$$\frac{I_0}{I} = e^{n\sigma L}$$

Equation 1.13. Equation for the collision cross section, where I and I_o represent beam intensities, n represents the number of gas molecules, σ is the collision cross section (Å^2 per atom) and L gives the length of the collision cell.

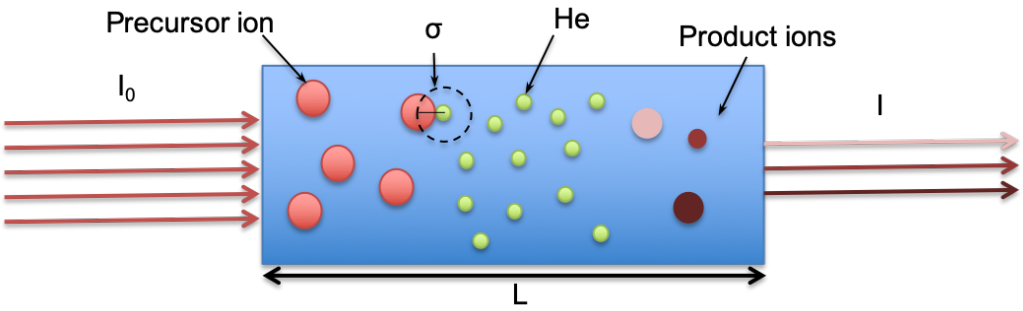

Figure 1.15. Pictorial representation of Equation 1.13.

High energy CID is limited to sector field and some ToF instruments, that have a high energy precursor ion beam. This gives the ions high translational energy within the collision cell, typically resulting in a single collision. In ToF instruments, dissociation can be increased by either locating the collision cell close to the ion source or by colliding ions with gas molecules in the flight tube under a low vacuum. This is unnecessary in a tandem ToF (ToF-ToF) where the collision cell is located between two flight tubes. [1]

1.2.3.2. Electron-capture dissociation

ECD is an electron-based dissociation technique that uses a low energy electron beam, typically 1-5 eV, to fragment multiply charged ions. An electron beam is produced from a cathode and electrons are introduced into the path of analyte ions. Low energy electrons can be captured by the ion, cancelling out one of the charges and creating an unstable intermediate $[M + nH]^{(n-1)+*}$, causing an increase in internal energy and inducing dissociation. The ECD dissociation mechanism is fundamentally different to that of CID because of the addition of an electronic excitation element due to the time-scale in which it occurs (around 10^{-14} s). As randomisation of internal energy does not take place before dissociation, direct bond cleave occurs, so it may not be the weakest bond in the ion that breaks. [65] In simple terms this means that different fragment ions may be produced compared to vibrationally dissociative techniques such as CID. [3] The irradiation time, the time that the ions are exposed to the electron beam, is longer than the time it takes for an ion to capture an electron. This is because there is only a small cross-section where the narrow electron beam can interact with the ion cloud, which causes ECD to have low efficiency. [1] Commercially, ECD is restricted to FT-ICR instruments, where ions and electrons are trapped within the cell. ECD is typically performed on large biomolecules such as proteins and peptides as they tend to be multiply charged and so can capture an electron but still remain charged, therefore detectable. It is necessary to briefly consider the

analysis of such ions in order to better understand the fundamentals of ECD.

Using CID in proteins and peptides, the CO-NH bond is predominantly cleaved, as it is generally the weakest, producing *b* and *y* type ions (Figure 1.16). This predictable dissociation allows for the identification of amino acid sequences. [66]

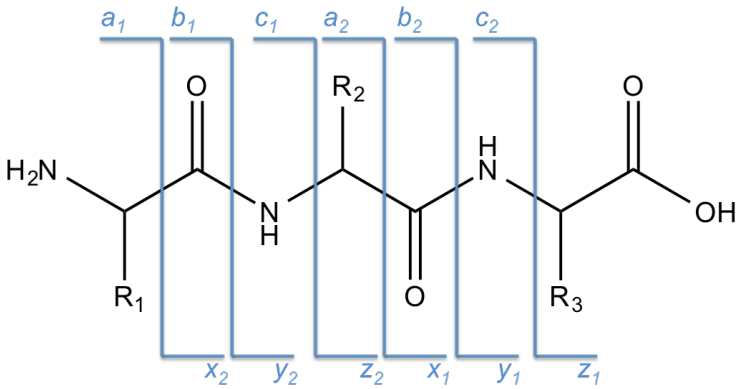

Figure 1.16. Standard nomenclature for common peptide cleavages. [67, 68]

When weakly covalently bound modifications need to be studied, CID is not particularly useful as these labile moieties tend to be cleaved from the ion. ECD has been utilised to study protein modifications because bond cleavage occurs before the redistribution of the internal energy of the ion, resulting in a different series of product ions than CID, retaining, for example, phosphates and glycans. [3] ECD produces *c* and *z·* type ions by non-specific homolytic cleavage of the N-C_α backbone (Figure 1.16) as well as dissociation of disulfide bridges. [69],[3]

Various mechanisms for ECD have been proposed, such as the Cornell method. (Figure 1.17) [70] Here, a charged group captures an electron, causing charge neutralisation which results in the repulsion of a hydrogen atom. An aminoketyl radical intermediate is then formed due to the adjacent carbonyl oxygen capturing the hydrogen radical which causes cleavage of the N-Cα bond.

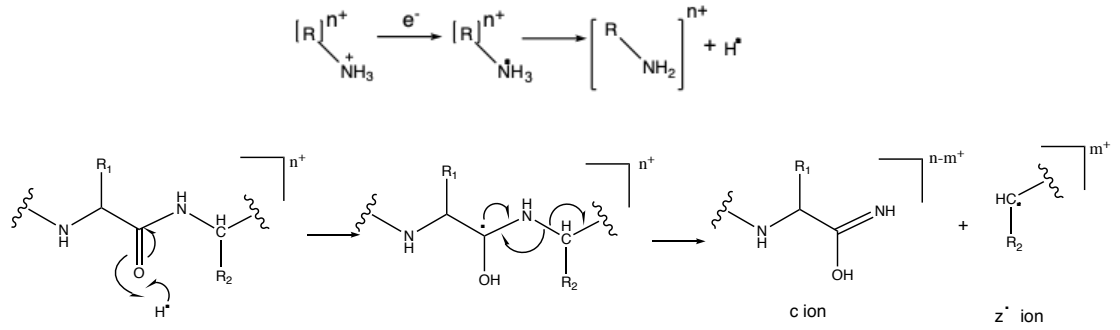

Figure 1.17. Cornell method.

An alternative mechanism for ECD is the amide-superbase mechanism (Figure 1.18), in which the electron is captured by the carbonyl group forming an anionic radical which cleaves the adjacent N-Cα bond. The negative charge is then neutralised by a different H^+. [71]

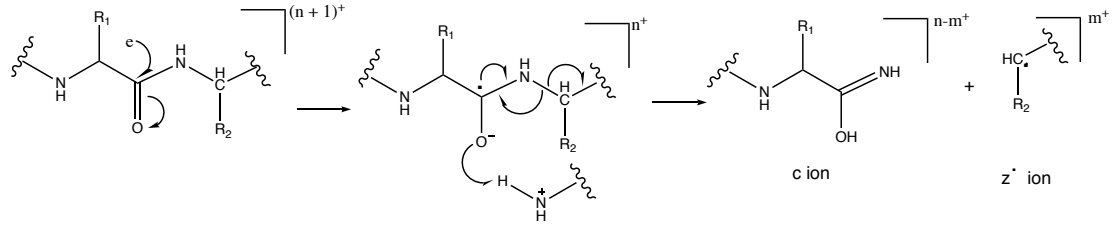

Figure 1.18. ECD amide-superbase mechanism.

A third mechanism was proposed in 2012 by Wodrich *et al.* termed the enol mechanism. [72] Here, heterolytic cleavage of the N-Cα bond (N-terminal

of the amide oxygen bond) occurs, as opposed to C-terminal homolytic cleavage in the superbase and Cornell mechanisms.

Secondary fragmentation in ECD is common, and achieved by the N-terminal carbon radical of the $z^{\cdot}$ product ion migrating, resulting in side chain loss (or partial loss). [73, 74] This same radical has been postulated to be involved in a free radical cascade mechanism, whereby several backbone cleavages can be induced by a single electron capture. [75] This was put forward following the observation of several backbone cleavages on a doubly protonated peptide where only one electron capture would be possible.

By increasing the energy of the electron beam, >5 eV, secondary fragmentation is observed producing not only *a*, *b*, *c*, *y*, and *z* type ions, but also ions resulting from R group losses. This is known as hot electron capture dissociation (hECD). [76, 77] The capture of an electron in hECD is two orders of magnitude lower than that of ECD, but the increased electron current offsets this, resulting in a similar degree of fragmentation. [70]

hECD has been more recently performed on small doubly charged pharmaceutical molecules. Prakash *et al.* carried out hECD on small doubly-charged ions, in comparison with CID and EID of the singly charged precursor ion, and found that many unique product ions were formed. [78] This is an important development for the pharmaceutical industry, as CID

may struggle to identify analogous ions that fragment in a similar way. If electron-based dissociation techniques can provide complimentary information to CID, this could allow for distinction and characterisation of analogous pharmaceutical molecules previously unavailable.

1.2.3.3. Electron-induced dissociation

EID has been developed from a technique named Electron Impact Excitation of Ions from Organics (EIEIO), which involves an electron beam of varying energy interacting with neutral analyte molecules causing ionisation to occur *via* electron impact (EI) depicted in Equation 1.14. [11, 79]

$$M + e^-_{(high\ energy)} \rightarrow M^{+\bullet} + 2e^-$$

Equation 1.14. Electron ionisation.

The energy of the electron beam is then reduced causing dissociation through the electronic excitation of the radical cation (Equation 1.15).

$$M^{+\bullet} + e^-_{(low\ energy)} \rightarrow M^{+*}$$

Equation 1.15. Electronic excitation of a radical cation.

This could typically be achieved in a FT-ICR instrument, as the magnetic field strength of a super-conducting magnet is needed to keep the ions in the path of the electron beam, although it has also been successfully

performed in a radio frequency ion trap. [11, 80] A combination of EIEIO and ECD was developed into a technique known as electron excitation dissociation (EED). EED involves a two-step process designed for the dissociation of ions produced using atmospheric ionisation techniques such as electrospray ionisation (ESI), *i.e.* singly charged even-electron cations. The first step of this process is to create a doubly charged ion by using a high-energy electron beam to induce secondary ionisation (Equation 1.16).

$$[M + H]^+ + e^-_{(high\ energy)} \rightarrow [M + H]^{2+\cdot} + 2e^-$$

Equation 1.16. Secondary ionisation using a high-energy electron.

In the second step, the electron that was removed from the ion is then recaptured producing a singly charged, electronically excited ion (Equation 1.17). [81] When each step was studied in peptides, the mechanism of EED was postulated. If the second step does not occur, only *b* and *y* type ions are produced which is thought to be the result of vibrational dissociation like in CID. When both stages occur, *b*, *c*, *y*, and *z* type ions are observed similar to the electronic dissociation seen in ECD. This suggests that both vibrational and electronic excitation can occur following electron irradiation.

$$[M + H]^{2+\cdot} + e^-_{(low\ energy)} \rightarrow [M + H]^{+*}$$

Equation 1.17. Electron capture of a low energy electron by a doubly charged radical cation.

EID is a single step development of EED that involves a high-energy electron beam (~10-25 eV) inducing dissociation on an ion. [82] In proteomics, EID has been shown to give comparable product ions to ECD of multiply charged ions as well as EED of singly charged ions. The mechanism for EID is more likely related to EED rather than ECD, as the capture of an electron by a singly charged ion would result in a neutral molecule. If the first stage of EED occurred (Equation 1.16), further electron interactions would likely need to occur before dissociation could take place. This is best explained by a 'fast' electron causing additional ionisation, followed by the capture of a 'slow' electron which would form a hydrogen deficient radical cation, causing fragmentation as in ECD. [83] This proposal, supported by the observation of doubly charged product ions produced by EID, but combined with the presence of product ions thought to be produced by vibrational techniques, suggests competitive dissociation pathways are present. [84] EID has been performed on a wide range of ions, including metal-ligand complexes, amino acids and pharmaceutical compounds, and has been shown to give complementary information to CID. [4, 85, 86] Recent developments in EID have also been shown to be capable of being carried out on an LC time-scale to allow for LC-MSMS. [87]

1.2.3.4. Electron-transfer dissociation

Electron-transfer dissociation (ETD) is a mechanism of fragmenting ions by way of an ion/ion interaction rather than more traditional collisions, such as CID (ion/neutral molecule interactions) or with ion/electron interactions as with ECD and EID. Hunt *et al.* discovered this technique by reacting multiply charged proteins and peptides with a radical anion in an ion trap, forming product ions similar to those formed in ECD. [88] A small, generally aromatic reagent molecule is ionised to form a radical anion that can interact with the precursor ion of interest, transferring an electron, which induces fragmentation. [89] This was originally achieved by way of negative chemical ionisation (CI) of anthracene performed at the opposite end of the instrument to analyte ion introduction of an ion trap instrument, and $[M + n+1H]^{n+1+}$ peptides and proteins formed by ESI. The use of a negative CI source located at the opposite end of the instrument to ion introduction cannot be used with high resolution mass analysers such as ToFs and orbitraps due to the position of the mass analyser at the rear, therefore alternative methods to produce radical anions have been developed. These include negative ion mode ESI to form $[M – H]^-$ with subsequent CID to form $[M]^{-\cdot}$ [90] and negative APCI using a nanoESI source, [91] both of which are used by ThermoFinnigan in LTQ-Orbitraps. A method in which ionisation by glow discharge to form radical anions, followed by positive mode ESI within the same source to form multiply charged analyte molecules, has been made commercially available by

Waters in their Synapt range of instruments. This method has been utilised for the work herein, and will be covered in more detail in Section 3.

Two reactions are possible following interaction of the ETD reagent radical anion and the multiply protonated analyte molecule as depicted in Figure 1.19.

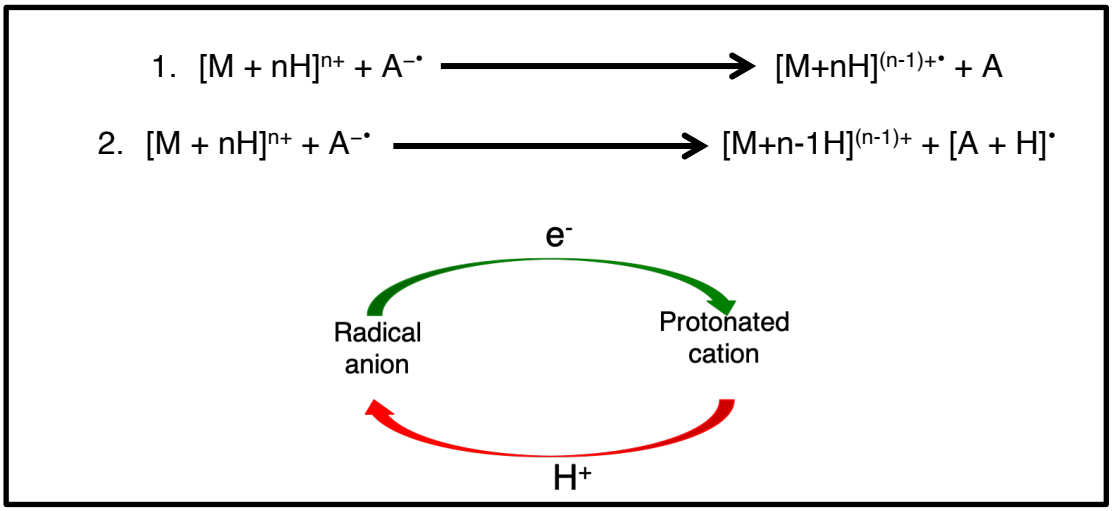

Figure 1.19. Two possible outcomes from an ETD experiment; 1. Electron-transfer from the reagent anion to the multiply protonated analyte and 2. Proton-transfer from the multiply protonated analyte to the reagent anion.

ETD only produces *c* and *z* type ions in peptides if electron-transfer is successful; if proton transfer (PTR) occurs, only *b* and *y* type ions are formed. [90, 91] The two main factors that influence a successful ETD reaction (*i.e.* the ability to form product ions as a result of electronic dissociation) are the charge density of the analyte cation, and the reagent anion used as an electron donor. The physiochemical properties of reagents that form the odd-electron anion have been shown to affect factors such as the number of product ions formed and the relative intensity

of products ions compared to the precursor ion in dissociation of multiply charged polypeptides. [92] The physiochemical properties of reagent ions (such as electron affinity, proton affinity and ionisation energy) have been considered in choosing appropriate molecules for use as ETD reagents for peptides and proteins. [93],[94] Reduced efficiency has been observed for ETD compared with ECD as the ion/ion interaction has a lower energy transfer than with ion/electron interactions possibly due to energy redistribution or collisional cooling. [95] For CI type anion formation, fluoranthene has been shown to give the highest ETD efficiency at around 40%; new reagents are still being investigated by the Coon group and others in the search for a molecule with lower electron affinities. [96] The physiochemical properties of the reagent anion have been shown to be an important driving factor in the competition between electron-transfer from the anion to the analyte cation, and proton-transfer between the analyte cation and reagent anion. Computational studies combined with experimental studies showed that low electron affinity of the reagent, and a low Franck-Condon factor between the radical anion and neutral reagent molecule, were key. [97, 98] Williams *et al*. investigated over 200 compounds for use as ETD reagents with the Synapt G2 using molecular modelling. They found the two reagents with the most favourable Franck-Condon factor and electron affinity were 1,4-dicyanobenene and 4-nitrotoluene, although around 50% of these reagents resulted in good ETD (low PTR levels). [99]

Another key aspect of ETD which has been developed is the overall duty cycle. For ETD where CI has been performed at the opposite end of the instrument to ion introduction to form reagent anions, the time scale of injection is typically 300 ms, which is concurrent for an LC-timescale. The first advent of alternative methods, namely the use of negative ion mode ESI with CID and atmospheric pressure chemical ionisation (APCI) methods, had a much longer duty cycle (around 800 ms) due to the polarity switching required in the instrument to allow ion transmission of both positive and negative ions. In fact, although the injection time on these instruments was faster than the CI method (200 ms), it took 300 ms for each polarity switch. This duty cycle has since been improved by the advent of the dual ESI source where the switching time in the LTC-Orbitrap has been reduced to 30 ms, giving an overall duty cycle of less than 300 ms. The CI method has also been developed on the LTC-Orbitrap ETD with injection times of less than 8 ms. [100] For the Waters Synapt QToF instruments, with the instrument set to a scan rate of 1 ETD spectrum/second, the ETD reagent refill time is generally optimal at 100 ms, (analytical duty cycle >90%) which is also applicable to an LC timescale as shown in Figure 1.20.

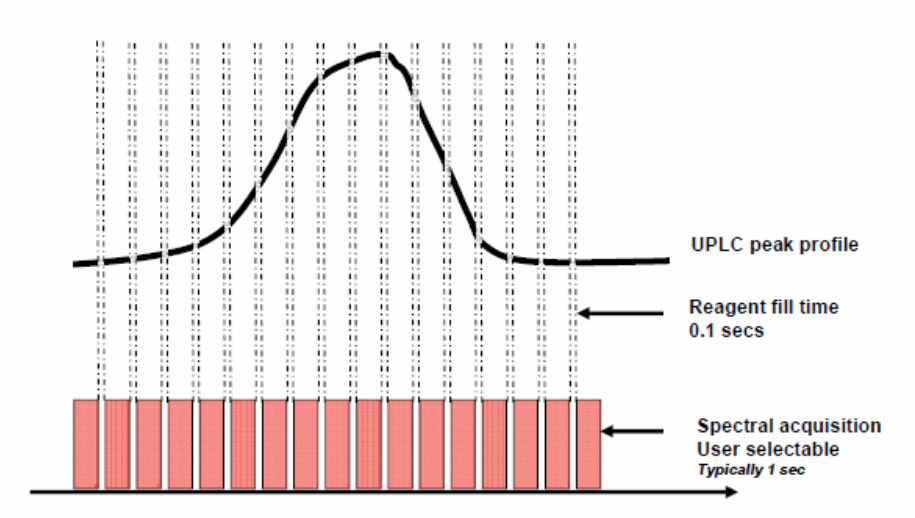

Figure 1.20. Duty cycle of ETD performed on a Waters Synapt QToF instrument. Figure supplied by Waters and used with permission. UHPLC is denoted by UPLC, which was copywritten by Waters.

The mechanism of ETD is similar to that of ECD as shown in Figure 1.21 below. [101]

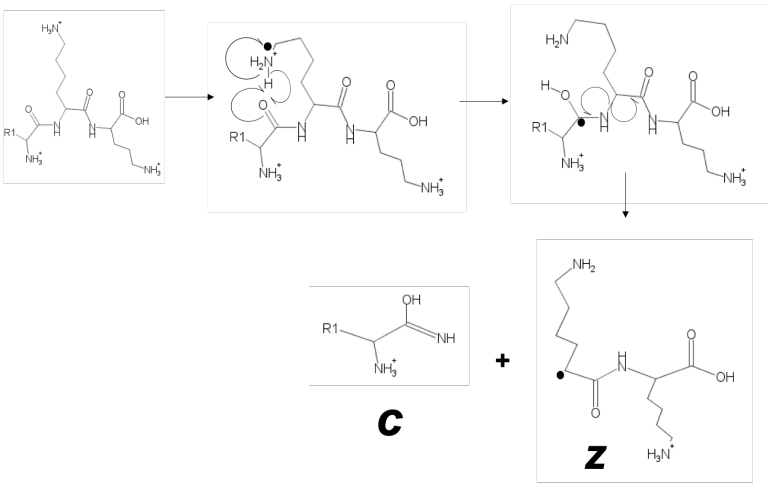

Figure 1.21. ETD mechanism.

ETD has been found to be useful in identifying post-translational modifications (PTM) in proteins and peptides much like ECD, such as phosphorylation and glycosylation, as these covalent bonds are not

cleaved during the mechanism. ETD is also used for characterising basic peptides, where *c* and *z* product ions are produced similar to other electronic dissociation techniques. ETD has the potential to be more widely used than ECD/EID as an FT-ICR instrument is not required, so ETD can be carried out on many cheaper and more widely available instruments such as ToFs, quadrupoles and ion traps. [102] ETD has only been utilised for multiply charged molecules, as it is thought that a minimum of two charges is needed for the technique to work, as a negative charge combined with a positive charge should result in a molecule, the same rational as with ECD. The higher charge density of an analyte (*i.e.* the more positive charges present) has been shown to result in more efficient ETD. [97] For peptides where charge density is low (*i.e.* $[M + 2H]^{2+}$), performing CID on intact $[M + 2H]^{+\cdot}$ has been shown to result in increased efficiency (*i.e.* higher abundance product ions compared with the precursor ion abundance) for *c* and *z* type ions in a quadrupole ion trap mass spectrometer, a technique named electron-transfer collisionally activated dissociation (ETcaD). [103]

EID has been shown to be capable of fragmenting singly charged ions, which was first thought to be unlikely due to charge neutralisation. ETD, for the first time, will be investigated for its ability to dissociate singly charged ions. ETD has been shown to be effective at characterising peptides with multiple protons, but little work, or no work for small molecules, has been conducted on observing differences in product ions created caused by changing the charge carrying species. This will be investigated by creating

salt adducted compounds using small, singly charged pharmaceutical molecules and subjecting the precursor ions to ETD. Proof of principle lies with similar studies conducted using EID on comparable compounds. [104]

1.2.3.5 Tandem mass spectrometry of salt-adducted ions and phosphorylated nucleotides

Not only has EID proved useful for the structural elucidation of protonated pharmaceutical compounds, but by the dissociation of sodium, potassium and ammonium adducts, complementary information has been gained compared with CID, allowing for more complete characterisation of these ions. [86] EID of protonated and ammonium-adducted precursor ions resulted in similar product ion spectra, with a small amount of additional structural information gained from the ammonium adduct. Generally, EID of the alkali metal-adducted precursor ions resulted in the formation of a greater number of unique product ions compared with the protonated and ammonium adducted precursor ions, with sodium-containing precursor ions providing the most structural information. [104] EID and CID of metal-adducted polyketide precursor ions also produced different product ion spectra with lithium-adducted precursor ions resulting in the most structural information. The EID and CID product ions formed were similar, although the most abundant product ions were formed by EID. [105] Chlorophyll-*a* has been dissociated by EID, CID and Infrared multi-photon dissociation (IRMPD), with EID shown to provide complimentary product ions to CID and IRMPD. The loss of $H^{\bullet}$ was a common assignment by EID, as well as fragmentation resulting in odd election species. [106] Electron detachment

dissociation (EDD) has been compared with CID and IRMPD of DNA and RNA, with EDD resulting in no secondary fragmentation and minimal base loss. The formation of Osmium (Os) bound product ions by EDD allowed for determination of the Os binding positions to DNA. [81, 107-111] A study utilising matrix-assisted laser/desorption ionisation (MALDI) of deoxy-oligonucleotides showed that by exchanging up to seven protons with sodium ions, backbone cleavages were greatly reduced, and the neutral loss of certain bases was increased with increasing sodium content. The loss of bases was thought to be due to protonation of an adjacent base with a higher proton affinity. Unique product ions were formed with the inclusion of sodium atoms, including a complex fragmentation pathway involving the loss of several central bases and recombination to form a product ion. [112]

Phosphorylated ions have predictable fragmentation by vibrational tandem mass spectrometric techniques, with the loss of phosphate groups primarily observed due to the labile nature of the bond. [113-117] CID of cyclic adenosine monophosphate (cAMP) analogues resulted in limited product ion formation, with the majority of product ions relating to cleavage between the ribose-phosphate and aminopurine groups. [113] The limited nature of product ions formed from CID for this type of ion has led to studies aimed at inducing bond cleavage at other locations of the ions, including the use of electron-based techniques. ECD of adenosine triphosphate (ATP) and analogous ions were shown to form complementary product ions to CID for doubly charged precursor ions. Unique to ECD, cross-ring

cleavage at the ribose moiety was observed along with several hydrated product ions formed by cross-ring cleavage at other groups. As CID also forms unique product ions, Liu *et al.* concluded that a combination of ECD and CID could be implemented to gain the maximum amount structural information for acidic metabolites. [118] Higher sequence coverage has also been gained by ECD of phosphopeptides ions containing up to four phosphorylation sites. [114] ECD of $[M + 2H]^{2+}$ peptides that contain varying numbers of phosphate groups demonstrated that lower sequence coverage was gained with increasing phosphorylation. The likely cause of this phenomenon is the formation of salt-bridges with amino acid side chains. [119] Characteristic losses observed by CID, such as H_2O, phosphate groups and phosphoric acid were not observed by ECD. [114]

1.3. Chemical supercharging in electrospray ionisation

ESI forms multiply charged ions that have been invaluable in mass spectrometry for a multitude of reasons. The production of ions at low *m/z* (high mass) enables the study of large molecules, such a proteins, peptides and polymers in mass spectrometry, which would otherwise be limited by the range of most mass analysers. Multiply charged ions are also crucial for certain types of tandem mass spectrometry such as ECD and ETD, where a single charge is neutralised by an electron to increase the internal energy of a precursor ion, resulting in dissociation. Supercharging, a technique first coined in 2000 by the Williams group, has become an emerging method of increasing the charge-state of an ion during the ESI

process, typically by the addition of 'supercharging reagents' (SCRs) to the ESI solution [120] or LC diluents. [121] Since its advent, several different methods to achieve this have come to light, including the addition of chemical additives to an ESI solution, the use of different solvents systems during ESI and optimising MS source parameters. [120] The mechanisms of supercharging are a hotly contested subject, with evidence unclear as to the exact mechanism, or mechanisms, of action. Much of the work carried out in this area has been performed on proteins, with limited research on polymers, peptides and small molecules. The mechanisms relating to the formation of protein charge-state distributions (CSDs) to protein unfolding have been shown to be dependent on several factors; solvent accessibility, Coulombic repulsions and protein conformation. In the solvent accessibility theory, it has been suggested that the folded tertiary structure of the protein leads to solvent having less access to basic and acidic groups making them less available to ionise. [122, 123] An alternative theory states that an unfolded protein can stabilise higher charge-states due to the increased distance of ionisable sites compared to folded structures, making the sites more likely to ionise. [123, 124] The final theory postulates that 'native-like' conformations cause charge neutralisation by intermolecular interactions. [125] Another factor that has been shown to affect the CSD of proteins is the number of collisions an ion undergoes after formation; more collisions lead to lower charge-states and can induce vibrational dissociation. [126] Different solvents have been shown to affect the CSD of proteins, with higher charge-states being produced when 50% of the solvent is made of methanol, acetonitrile and

isopropanol, compared with water alone. A correlation was shown between increasing gas-phase basicities of the organic fraction of the solvent and the charge-states produced, although Iavarone *et al.* comments that other physical properties, such as electron affinity and boiling point, could also be involved. [120] Protein supercharging has been studied by spraying from native conditions (buffered solutions) and from non-native/denaturing conditions (aqueous and organic solutions with or without the addition of acids).

1.3.1. Protein supercharging from denaturing conditions

When sprayed from denaturing conditions, mechanisms (such as increased droplet surface tension and protein unfolding) have been suggested to explain the increase in maximum charge (Z_{max}) and higher CSDs (Z_{avg}) observed when SCRs are added to an ESI solution. Surface tension of the ESI droplet has been proposed as an explanation to the phenomenon. When *m*-nitrobenzyl alcohol (*m*NBA) or glycerol is added to cytochrome C and myoglobin solutions made up of water, methanol and acetic acid, an increase in Z_{max} and Z_{avg} is observed by ESI. *m*NBA and glycerol have high surface tensions, a droplet with a high surface tension requires more charges to undergo Rayleigh fission, the higher surface charge density of the droplet leads to higher charge-state ions being formed, as described in Equation 1.18. It is important to note that due to solvent evaporation during the CRM model of ESI, the mature droplets are

composed mainly of the SCR due to their higher boiling points, termed enrichment.

$$q_R = z_r e = 8\pi(\epsilon_o \gamma R^3)^{1/2}$$

Equation 1.18. Rayleigh equation, where q_R is the total charge at Rayleigh limit, z_r is the charge radius, e is elementary charge, ϵ_o is permittivity of the vacuum, γ is solvent surface tension, and R is droplet radius.

Conformal changes in the protein are not thought to impact the observed Z_{max} and Z_{avg} as similar increases were demonstrated for four-residue peptides with no significant tertiary structure. [18, 120, 127, 128] The addition of higher levels of acetic acid were also investigated to rule out conformational changes, as more acidic solutions will increase protein denaturation. This decreased Z_{max} however, thought to be due to the lower surface tension and vapour pressure of acetic acid compared with water. [18, 129]

The theory of droplet surface tension is disputed by Grandori *et al.* who state that protein CSD is not limited by the surface tension of the droplet. The addition of isopropanol and 1,2-propylene glycol to solutions of ubiquitin, cytochrome C, lysozyme and myoglobin was investigated and the results compared with predicted CSDs using the Rayleigh equation. It was found that upon the addition of isopropanol, which has a lower surface tension that water, rather than the CSD decreasing to a lower *m/z*, a higher z_{max} and z_{avg} was observed. A bimodal CSD was produced, which the

author suggests is due to an equilibrium of folded and unfolded protein. This would suggest that, for these molecules, the main mechanism of action in supercharging is protein unfolding rather than an increase in droplet surface tension. [130, 131] Similar effects were observed when using higher desolvation gas flow rates to unfold the protein, while pH effects were shown not to affect CSD using varying concentrations of hydrochloric acid, formic acid and acetic acid. [131] The same research group later described that surface tension of the droplet may contribute to supercharging as the addition of DMSO increased z_{avg} of acid unfolded proteins. [132] The effects of pH were further investigated by Donald *et al*. who demonstrated that for a range of SCRs, strong acids reduce the supercharging effect where weak acids increase it. The reduction in supercharging is thought to be due to conjugate base anions neutralising charge sites. [133] The surface tension mechanism was further disputed when the SCR tetrahydrothiophene-1,1-dioxide (sulfolane) was added to a solution of cytochrome C. Positive and negative ESI were performed with an increase in z_{max} and z_{avg} only being observed in positive ESI. If surface tension was the main mechanism of action, it would be observed in both polarities as the Rayleigh equation (Equation 1.18) is independent of charge. The observation of significant sulfolane adduction to the protein led the author to suggest that the supercharging effect of sulfolane is caused by direct interaction with the protein. A similar observation was made when using glycerol as a SCR with myoglobin and ovalbumin. [134] Charge delocalisation, a process whereby polar solvents diffuse charge through large-scale dipole ordering, was proposed. This allows more

protonation sites to be accessible due to sulfolane molecules aligning at partial negative sites. This effectively neutralises the charge, with the charge found at the edge of the ordered solvation shell. This allows basic sites which would otherwise be unavailable for protonation to protonate by overcoming the electrostatic barrier. This was demonstrated with several analogous molecules to sulfolane. When the dipole moments were plotted, good correlation with the degree of supercharging was obtained, however the author comments that other factors are also involved. [135]

1.3.2. Protein supercharging from native conditions

Supercharging from native solutions has been investigated, with the most likely mechanism being protein unfolding in the droplet, as postulated by Grandori *et al*., demonstrating a correlation between the surface area of a protein and its average charge. [136] Williams *et al.* tested this hypothesis by comparing the effects of increasing the capillary temperature and the addition of SCRs. Both conditions increased z_{avg}, although the addition of 0.4% (3-nitrophenyl)methanol (commonly known as *m*-nitrobenzyl alcohol, *m*NBA) had more of an effect than high capillary temperature for both myoglobin and NtrC4-RC complex (a σ^{54} activator from *Aquifex aeolicus*). Denaturation in the droplet with the addition of *m*NBA is likely due to enrichment of *m*NBA in the droplet caused by evaporation of lower boiling point solvents. As *m*NBA has a lower vapour pressure than water (50.5 mN/m [128] compared with 71.99 mN/m at 25 °C [137]), the rate of

evaporative cooling is longer, so droplets have a higher temperature and life time. The resulting higher temperature then induces conformational changes of the protein, allowing more protonation sites to be accessible, thus producing higher charge-state ions. The author suggests that the similarity between spectra obtained by both methods leads to the conclusion that conformational changes in the droplet is the main mechanism of supercharging from native conditions. [138, 139] This is further supported by ion mobility studies that show higher charge-state proteins have a more unfolded conformation. [140] An interesting observation was that circular dichroism (CD) showed sulfolane directly destabilises myoglobin in high concentrations, leading the author to suggest the enriched ESI droplet could contribute to protein unfolding, although other mechanisms such as droplet surface tension may also play a role. [141] Similar studies have shown the same destabilising effect for anthrax toxin oligomers with *m*NBA and cytochrome C with sulfolane and 4-hydroxymethyl-1,3-diocolan-2-one. [142, 143] CD shows that no conformational changes were induced with the addition of 0.5% *m*NBA to a solution of myoglobin, further demonstrating that supercharging occurs in the MS source, rather than in solution. [144, 145] Further support is given to protein unfolding being the main mechanism behind native protein supercharging by the observation that chemically modifying myoglobin with more cross-links does not affect the CSD by ESI, but does dramatically reduce supercharging. [142, 146]

Chen *et al.* also compared the use of *m*NBA with capillary temperature denaturation. For myoglobin, DNA 12mer and cytochrome C, high capillary temperature did increase charge-state but much less than *m*NBA. When both high capillary temperature and SCR were used, less supercharging was observed than with *m*NBA alone. Due to this discrepancy, the author concludes completely different mechanisms are at work, with direct interaction between SCR and protein causing the supercharging effect, with charge delocalisation by dipolar moments of solvents as previously described for denaturing conditions. [147] One factor thought to limit protein supercharging is the level of proton-transfer from $[M + (n+1)H]^{(n+1)+}$ to either solvent molecules or molecules within the solvent, as solvents with high gas-phase basicities have been shown to reduce ion charging. [120, 139] For most SCRs this does not pose much of a problem as water has a lower gas-phase basicity than the SCRs. DMSO however has a higher gas-phase basicity than water so has been though to limit its use as a SCR. Williams *et al.* show that although low concentrations of (methylsulfinyl)methane (commonly known as dimethyl sulfoxide, DMSO) reduce protein charging, high concentrations increase both z_{max} and z_{avg} for a range of proteins. This shows that even when the SCR has a high gas-phase basicity, no significant proton-transfer limiting ion charging occurs. [145, 148] Another limiting factor to protein supercharging is the adduction of salt ions. Charging is shown to be reduced when 8 different salt ions are adducted to the protein, with CD and ion mobility showing different protein conformations with the addition of mM concentrations of salts. [149] Cassou *et al.* showed that by the addition of *m*NBA or sulfolane,

sodium adduction was reduced for ten small (8.6-29 kDa) proteins containing mM concentrations of NaCl. It is proposed that this is due to the SCRs binding to sodium ions, reducing the number of Na cations available for adduction to the proteins. [150]

An alternative supercharging mechanism, termed a charge trapping mechanism (CTM), has been informed by molecular dynamics calculations and focuses on myoglobin being released from nanodroplets containing water, water/*m*NBA and water/sulfolane (Figure 1.22). [151] A notable approximation is the use of Na^+ rather than H^+. This is because to accurately model the behaviour of protons, high level density functional theory (DFT) or quantum mechanical calculations would need to be used. However to achieve this on a system as large as nanodroplets is not currently feasible. Another exception from these calculations was the effect of an electric field during the ESI process. It was shown that without the use of SCRs, Na^+ is ejected *via* the IEM, reducing the number of charges in the droplet. The protein then enters the gas phase following the CRM. When a SCR is added to the droplet composition, the SCR forms a shell at the edge of the nanodroplet, partially inhibiting the ejection of Na^+ into the gas phase as Na^+ is not as permeable though the hydrophobic shell of SCR. When all the water has evaporated, a droplet containing exclusively myoglobin, SCR and Na^+ remains. The sodium then preferentially binds to the protein, likely at carboxylate groups, until protein desorption occurs, at which time some Coulombically driven protein unfolding occurs, leaving a highly-charged protein molecule. [151] Good agreement between the

calculated charge-state, and experimentally observed charge-state of myoglobin [149] was shown. However, this does not account for lack of supercharging seen when protein conformation was confined by the addition of chemical cross-links to inhibit protein unfolding. [142, 146]

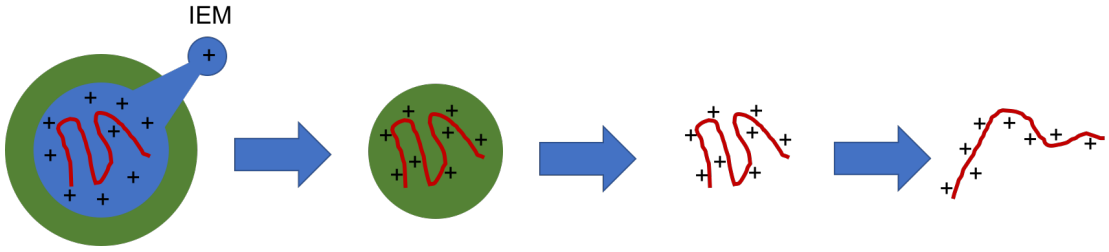

Figure 1.22. Visual representation of CTM.

Supercharging has proven to be useful for many proteomic applications. For both positive and negative ion top-down and bottom-up peptide sequencing, the addition of SCRs has enabled more efficient ECD, ETD, EDD, and complementary CID and IRMPD spectra by fragmenting higher charge-state precursor ions, leading to higher sequence coverages being obtained. [108, 152-159] An increase in the cleavage of disulfide bonds was also observed, generating higher sequence coverage of proteins with multiple disulfide linkages. [160] The use of SCRs has also been demonstrated for HDX kinetics studies. Here, the SCR takes the place of the acid quench step, as the high boiling point of the SCR causes droplet heating, leading to protein unfolding as measured by ion mobility. [155]

Other methods of supercharging protein have also recently emerged. Chemically modifying proteins by addition of functional groups such as

amine groups, have been shown to increase Z_{max} and Z_{avg} by increasing the number of protonation sites available. [161] Electrothermal supercharging, where the capillary temperature is increased in native mass spectrometry has also been shown to increase Z_{max} and Z_{avg}, thought to be due to thermal denaturation of proteins while inside the capillary. [162-165] Salt adduction with trivalent metal ions such as La^{3+} increases protein charging. CD data showed no measurable difference in protein conformation, although ion mobility showed the higher charge-state ions were in a more unfolded conformation. [166] Finally, the O'Connor group has designed a source whereby chemical ionisation of CH_4 to form the 'superacid' CH_5^+ increases Z_{avg} for various proteins by proton-transfer to the protein. [167]

1.3.3. Supercharging non-protein molecules

Fewer studies have been performed using SCRs for non-protein molecules. As previously mentioned, peptides have been shown to exhibit the same increase in z_{max}, even when the size of the peptide makes conformation changes negligible. [108, 152-159, 168] Synthetic polymers such as polyethylene glycol (PEG) have been studied and form higher z_{avg} when sprayed from methanol solutions containing 20% *m*NBA, with these trends being consistent with surface tension dependant charging. z_{avg} is reduced however, when sprayed from water with 1% *m*NBA. This is thought to be due to PEG forming more extended conformations in

methanol than in water. A shift in molecular weight distribution is also noted with the addition of *m*NBA towards lower molecular weight. [18, 128]

1,n-Diaminoalkanes were studied when sprayed from water and methanol with 5% *m*NBA. 1,12-Diaminoalkane generally forms $[M + 2H]^{2+}$ by ESI, where z_{avg} was higher in water than in methanol, but as with PEG, the addition of *m*NBA to water reduced z_{avg} whereas it was increased when *m*NBA was added to methanol. From aqueous solutions 1,5-diaminoalkane was the smallest chain to form $[M + 2H]^{2+}$. N-N distances of less than 10.1 Å resulted in only low relative intensities of $[M + 2H]^{2+}$. This distance is lower than allowed by the Rayleigh equation for a water droplet where z_R = 2. It is suggested that the water droplet could be forming a dumb-bell shape around the charges which would have a larger diameter than a sphere.

A methanol droplet where z_R=2 would have 19 Å distance, which is 2 Å larger than n=12. $[M + 2H]^{2+}$ in methanol was not expected as it is not allowed by the Rayleigh equation as two charges cannot get that close together in a methanol droplet. Explanations for this observation include fluctuations in charges around equilibrium positions on the droplet, stabilisation of a nano-droplet by the analyte molecule or by non-spherical droplets. The same relationships cannot be drawn for *m*NBA and methanol due to differential evaporation rates of the two components. Interestingly, z_{avg} drops abruptly as N-N distance goes below 14.2-17 Å, a similar charge distance for droplets of only *m*NBA (z_R=14.4). As the CRM is proposed to

apply to large molecules, [169] and the IEM does not support the observed formation of $[M + 2H]^{2+}$, the author suggests a dynamic IEM model where one end of molecule is desorbed and charge reorganisation at the droplet surface results in protonation at the other end of the molecule. [18] This is analogous to the asymmetric droplet fission process observed for large ESI droplets in which small droplets are emitted from a larger droplet with the small droplets carrying away a disproportionate fraction of charge. [170]

Although the majority of proposed supercharging mechanisms involve protein unfolding/denaturation, this does not account for the increase in doubly protonated diaminoalkanes observed by Iavarone *et al.* as small molecules have no significant tertiary structure. [18] To further investigate the effect of SCRs on small molecules, a selection of molecules with varying structures and functional groups have been investigated with a selection of SCRs (Chapter 3.3).

1.4. Waters research enabled software (WREnS)

Waters research enabled software (WREnS) is a software development tool which allows the control of instrument parameters in Waters' mass spectrometers. Custom scripts can be written in order to dynamically control a wide range of instrument settings based on the read back of a selected mass range. As previously mentioned (Section 1.2.3.5), efficient ETD relies on a constant balance between ETD reagent anion and precursor cation of 1×10^6 : 5×10^4. During LC-MS, the intensity of the

precursor ion changes during peak elution, reducing the efficiency of ETD. To overcome this, optimisation of different instrument parameters was evaluated with custom WREnS scripts in an attempt to increase ETD efficiency during LC-MS (Chapter 3.4).

1.5. Ion mobility Separation

Ion mobility is not a new technique, with references seen as far back as the 19th century. [171] The first ion mobility experiments that resemble what could be recognised as analogous to modern experiments were conducted in the 1950's and 1960's by McDaniel *et al.* [172] The basis of ion mobility is to move ionised molecules through a tube filled with a known volume of gas by way of a DC electric field. Resolution in ion mobility, as with mass spectrometry, can be described by Equation 1.19.

$$Rp = \frac{x}{\Delta x}$$

Equation 1.19. Ion mobility resolution equation where Rp is resolving power, x is the dimensional location of the measurement (*i.e.* drift time) and Δx is full width of the peak at half maximum height.

In ion mobility, this can be estimated by Equation 1.20. [173]

$$\frac{x}{\Delta x} \approx \sqrt{\frac{LEze}{16k_BTln2}}$$

Equation 1.20. Approximation of Rp in ion mobility where L is drift tube length, E is applied electric field, *z* is ion charge, e is elementary charge, k_B is Boltzmann's constant and T is temperature. [173]

Ion separation in ion mobility occurs by Ω/z, where Ω is collisional cross section and z is ion charge. CCS can be thought of as a relationship between size and shape; the area presented by one molecule for collision with the centre of another. The number of collisions an ion has with the drift gas will be determined by the ions CCS, therefore, the larger the ion, the more it will be hindered by the drift gas atoms, therefore separating ions based on their CCS. [174] Currently, there are five main types of ion mobility; traveling-wave ion mobility spectrometry (TWIMS); field-asymmetric waveform ion mobility separation (FAIMS), (which is also known as differential-mobility separation (DMS)); drift-time ion mobility spectrometry (DTIMS); aspiration ion mobility spectrometry (AIMS) and trapped ion mobility spectrometry (TIMS). For the scope and purposes of this work more detail will be given only to TWIMS, as this is the only technique utilised herein.

1.5.1. Traveling-wave ion mobility separation (TWIMS)

TWIMS is commercially available in both the Waters Synapt and Vion instrument classes and is a low resolution, high sensitivity method. The TWIMS device is an ion guide comprising of a series of stacked ring electrodes in an orthogonal orientation to the direction of ion transmission as shown in Figure 1.23. [175]

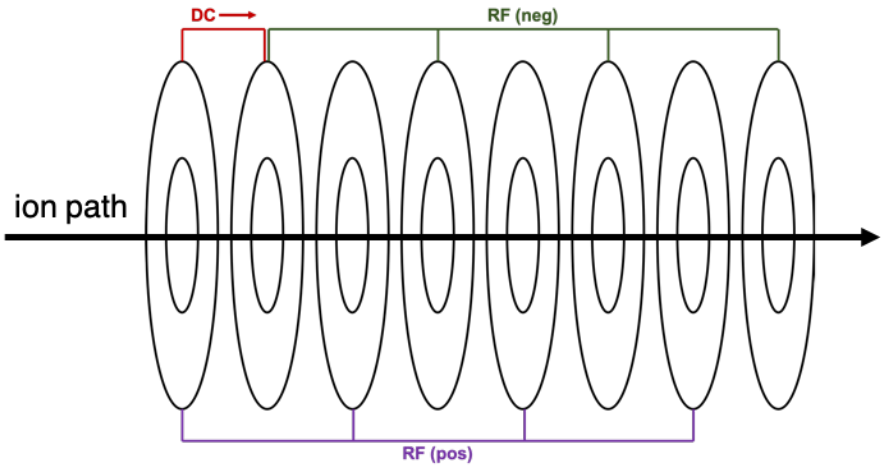

Figure 1.23. Traveling-wave ion mobility separation device.

Separation of ions is achieved by the effect of two factors within the TWIMS device. Firstly, as with DTIMS, by the collisions of ions with drift gas atoms, usually He or N_2. Secondly, by the use of positive and negative RF voltages applied to alternate ring electrodes. This provides potential wells in which ions are trapped thereby reducing unintentional ion diffusion between electrodes during transmission. A DC is then applied to a pair of ring electrodes, as shown in Figure 1.23. The DC is switched to adjacent electrodes in a continuous fashion resulting in a pulse that pushes the ions through the TWIMS device, resulting in collisions with drift gas atoms. Not all ions are propelled at the front of the wave however; those with less mobility (*i.e.* larger size or lower charge) will collide with more drift gas atoms and fall behind the wave front, giving mobility separation. In this case, collisional cross sections of ions can be determined by Equation 1.21.

$$\Omega = z \times F \times {t_d}^B$$

Equation 1.21. Drift time equation for TWIMS where Ω is collisional cross section, z is charge, B and F are constants which must be experimentally determined and t_d is drift time.

TWIMS boasts high sensitivity; this is due to ion accumulation and ion trapping by the traveling wave. Although a low resolution technique, recent improvements in Vion instruments have been made by increasing IMS cell pressure, T-wave amplitude and using a helium entry gas which keeps ions in a tighter cloud prior to separation.

2. Methods and materials

2.1. Sample preparation

Unless otherwise stated, all samples were made up to 1 µg/mL in a 0.1% formic acid (Sigma Aldrich) solution of 50:50 acetonitrile (Fisher Scientific): water. In order to increase salt adduction, 12 mM solutions of NaCl were made up of 0.1% formic acid in 50:50 acetonitrile : water was used. 1 µL of a 1 mg/mL analyte solution was then added to 1 mL of the salt solution. Where dissolution was not immediate, a vortex mixer was employed until dissolution was complete.

2.2. Synapt G2-s

The Synapt G2-S (Waters corporation, UK) comprises of various interchangeable sources, of which the ESI and ETD sources were used in this work along with the TriWave collision cell and oaToF mass analyser. For ETD, the reagent molecule is ionised by glow-discharge, where crystalline reagent molecules are vaporised, then flow through a hollow discharge electrode with the assistance of a make-up gas. A discharge of around -300 V then occurs between the electrode and the ion block, producing an electron-rich plasma from the nitrogen in the source. This results in the formation of radical anion which goes on to interact with analyte ions in the trap region of the TriWave (Figure 2.1).

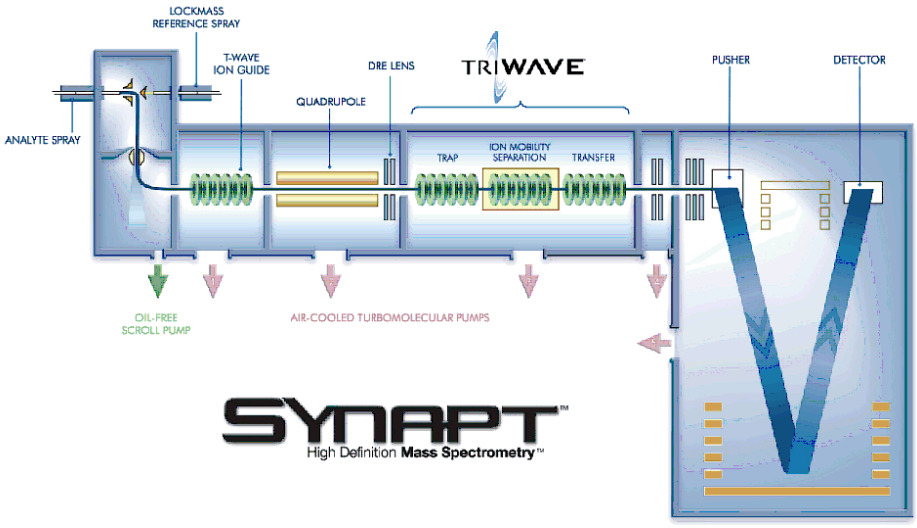

Figure 2.1. Synapt G2-S schematic used with permission. [176]

2.2.1. Dynamic range enhancement (DRE) lens

The dynamic range enhancement (DRE) lens is positioned after the quadrupole and before the TriWave as shown in Figure 2.1. The purpose of the DRE lens is to increase the dynamic range of the mass spectrometer without adversely affecting resolution; that is to say allowing both high and low abundance ions to be detected without ion saturation occurring. This is achieved by quickly alternating the voltage applied to the DRE lens between a high and low value. While in high transmission mode, full transmission of ions is allowed, whereas in low transmission mode, only around 2% of ions are transmitted. An algorithm then detects ion signals which have become saturated during high transmission mode, and stiches in data from low transmission mode. The resulting mass spectrum then

includes both high and low abundance ions and overcomes to issues of ion saturation. This is pictorially represented in Figure 2.2.

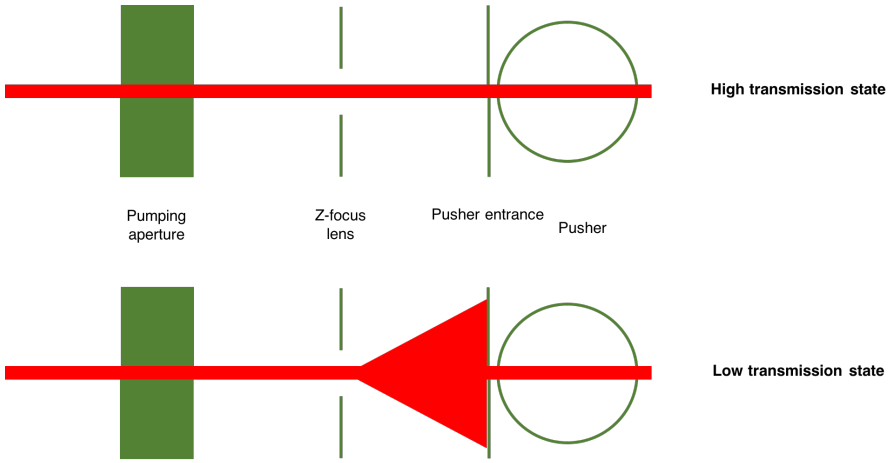

Figure 2.2. Schematic of working DRE lens.

2.2.2. TriWave

The TriWave region of the Synapt G2-S (Figure 2.3) is where dissociation and ion mobility takes place and is comprised of three separate traveling wave ions guides which use RF voltages for ion confinement. There are three regions within the TriWave; the trap cell, the ion mobility separation (IMS) cell and transfer cell. In MSMS experiments, CID can take place in the trap or transfer cells, whereas ETD can only occur in the trap cell. In CID experiments, the trap and transfer cells contain argon which is used as the collision gas to which precursor ions collide. During ETD experiments, the trap cell is where reagent anions and analyte cations come into contact.

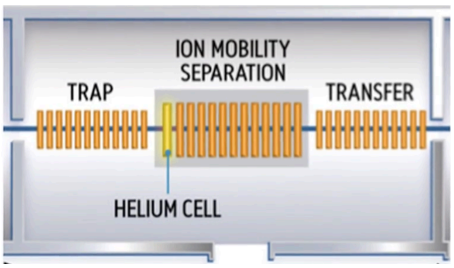

Figure 2.3. TriWave region of the Synapt G2-S. [176]

IMS, the separation of ions drifting through a gas while under the influence of an electric field, is achieved by utilising the TriWave as a whole. The trap accumulates ions before releasing them into the IMS cell, enabling 100% duty cycle in IMS experiments. In the IMS cell, a travelling wave propels the ions through helium gas where a series of low energy gas collisions and 'roll over' events, in which ions roll over the traveling wave, results in ions becoming separated based on their mobility within the cell, relating to an ions physical size and shape. Finally, the transfer cell guides the now separated ions into the qToF mass analyser.

2.2.3. Synapt G2-S Instrument parameters

Unless otherwise stated, samples were introduced into the mass spectrometer *via* direct infusion set at a flow rate of 5 µL/min. Standard ESI parameters are shown in Table 2.1.

Parameter	Setting
Capillary voltage	2 kV
Sampling cone voltage	40 V
Source offset	30 V
Source temperature	150 °C
Desolvation gas temperature	350 °C
Cone gas flow rate	100 L/h
Desolvation gas flow rate	600 L/h
Nebuliser gas pressure	6 bar

Table 2.1. Synapt G2-S Standard ESI settings.

The Synapt G2-S utilises a separate ESI capillary for lockspray ionisation. This is a reference compound which is ionised at time points throughout the experiment. This is used as an internal calibrant which enables improved accurate mass measurements. The reference compound used for all work conducted herein was leucine encephalin, a peptide chain of 5 amino acids. The lockspray source parameters were set each time; the instrument was set to give an ion signal of $5x10^4$ ion intensity. For CID experiments, the collision energy was optimised on a compound-to-compound basis using a range of 15-30 eV.

For ETD experiments, unless otherwise stated, the source settings were set as shown in Table 2.2 with a diagram of the ETD source block shown in Figure 2.4.

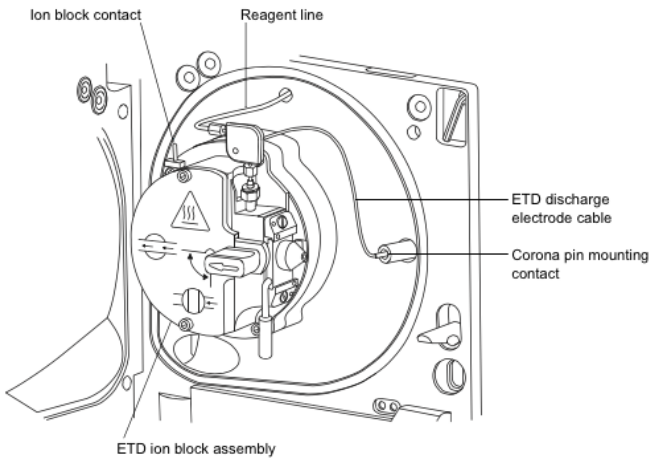

Figure 2.4. Synapt G2-S ETD source block used with permission. [176]

ESI parameters	**Setting**
Capillary voltage	1.5 kV
Sampling cone voltage	20 V
Source offset	30 V
Source temperature	150 °C
Desolvation gas temperature	200 °C
Cone gas flow rate	100 L/h
Desolvation gas flow rate	300 L/h
Nebuliser gas pressure	6 bar
Glow-discharge parameters	
Discharge current	60 µA
Sampling cone	0 V
Source offset	30 V
Source temperature	150 °C
Make up gas flow rate	36 mL/min

Table 2.2. Synapt G2-S source settings for ETD.

For all ETD experiments, the reagent anion used was *p*-nitrotoluene. The trap section of the TriWave was setup as shown in Table 2.3.

Trap Parameter	Setting
Wave velocity	350 m/s
Wave height (to inhibit ETD)	1.5 V
Wave height (to induce ETD)	0.2 V
Trap gas flow rate	20 mL/min
Transfer gas flow rate	2.2 mL/min

Table 2.3. Synapt G2-S ETD trap settings.

2.3. LTQ-FT

The LTQ-FT (ThermoFinnigan corporation, Germany) has an ESI source, and uses a linear ion trap and an FT-ICR cell (7 tesla superconducting magnet) as mass analysers, with the latter also acting as a detector (Figure 2.5).

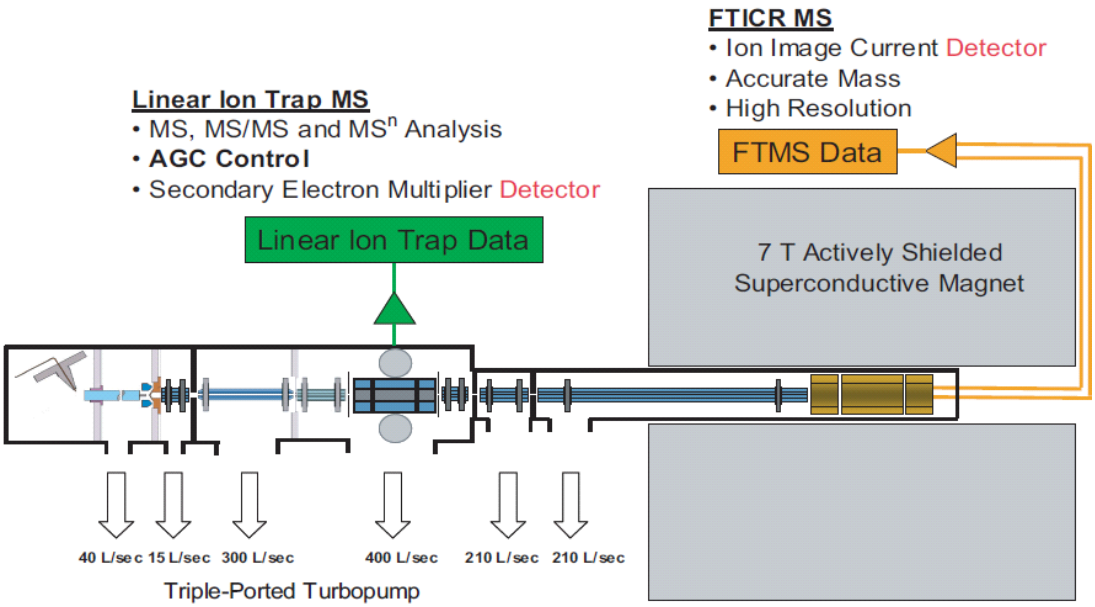

Figure 2.5. LTQ-FT schematic. [177]

2.3.1. LTQ-FT Instrument parameters

The samples were introduced using direct infusion at 5 µL/min by means of a syringe pump. The ESI source parameters were set as shown in Table 2.4.

Parameter	Setting
Spray voltage	4 kV
Capillary voltage	30 V
Capillary temperature	350 °C
Tube lens voltage	100 V
Sheath gas flow rate	5-15 arbitrary units
Auxiliary gas flow rate	5-10 arbitrary units
Sweep gas flow rate	5-10 arbitrary units

Table 2.4. Standard LTQ-FT source parameters.

For ECD and EID experiments, the indirectly heated dispenser cathode was used to generate electrons between 5-30 eV for 70 ms for EID, 1-5 eV for ECD and 5-30 eV for hot ECD (hECD).

3. Results and discussion

3.1. Characterisation of phosphorylated small molecules by collisional and electron based tandem mass spectrometry

MSMS of phosphorylated ions generally results in predicable CID product ion spectra due to the labile nature of the phosphate bond. The limited information obtained from performing CID on the phosphorylated organic drug molecule fostamatanib, has led to an investigation into methods to induce increased fragmentation for this molecule. AMP, ADP and ATP are smaller phosphorylated molecules that also form limited product ions by CID and thus provide a good system to understand the effect of phosphorylation. These simple molecules allowed for a fundamental study while still being applicable to fostamatanib. The tandem mass spectrometric behaviour of these phosphorylated small molecules has been studied by CID and EID. Precursor ions were observed with differing numbers of sodium atoms associated with the ion; the tandem mass spectrometric behaviour of these ions was also investigated. As an outcome of this research, the paper "Ball, A. T., Prakash, A. S., Bristow, A. W. T., Sims, M. & Mosely, J. A. Characterisation of phosphorylated nucleotides by collisional and electron-based tandem mass spectrometry. *Rapid Communications in Mass Spectrometry.* **30** (19), 2155-2163, (2016)" was published.

3.1.1. Results and discussion

Unless otherwise stated, all work was carried out on a ThermoFinnigan LQT-FT instrument. Further experimental details can be found in Section 3.3.

3.1.1.1 Terminology

For all data in this chapter, the charge-state of precursor ions was 1+. These ions can, however, be named in several ways. For clarification, the following terminology for precursor ions has been used:

- Protonated molecule: ions that contain only C, H, N, O and P atoms, and have an increased mass of 1 *m/z* above the neutral mass and therefore must be protonated.
- Monosodium ion: ions that could either be a sodiated molecule with OH groups, *or* a protonated molecule that contains one ONa group.
- Disodium ion: protonated molecule that contains two ONa groups *or* a sodiated molecule that contains one ONa group and one OH groups.
- Trisodium ion: protonated molecule that contains three ONa groups *or* a sodiated molecule that contains two ONa groups and one OH group.

3.1.1.2. EID and CID of protonated AMP, monosodium AMP and disodium AMP

Only one product ion was formed as a result of CID of protonated AMP (Figure 3.1.1a), to give a peak at *m/z* 136.0617 formed by cleavage at **A**, $[C_5H_6N_5]^+$ (-0.2 ppm error) as shown in Figure 3.1.2. CID of monosodium AMP (Figure 3.1.b) resulted in more MSMS data, with the sodium-containing product ion, formed again by cleavage at **A**, *m/z* 158.0436,

$[C_5H_5N_5Na]^+$ (-0.5 ppm). Fragmentation at **B** was also observed forming the sodium-containing product ion at *m/z* 234.9978, $[C_5H_9O_7PNa]^+$ (0.0 ppm). This data gives an insight as to where the sodium atom can be located on monosodium AMP; both halves of the precursor ion are seen to retain the sodium atom showing that the sodium atom is located at both sites on different instances of the ion. By comparing the relative peak intensities of the production ions, this data supports the postulation that the phospho-ribose moiety has a higher affinity for the sodium cation compared with the proton. Product ions at *m/z* 250.0934 and 272.0753 were also formed by cleavage at **C**, $[C_{10}H_{12}N_5O_3]^+$ and it's sodium-containing counterpart $[C_{10}H_{11}N_5O_3Na]^+$ (-0.4 and -0.3 ppm respectively). By comparing the relative intensity of these two product ions, this data also indicates the preferred location of the sodium cation is on the phosphate group: This is because the relative abundance of the product ion with the sodium atom present on the phosphate group is higher than the relative intensity of the product ion that does not have the sodium atom present. CID for disodium AMP (Figure 3.1.1c) gave less MSMS information, with only the loss of water observed, *m/z* 374.0235, $[C_{10}H_{11}N_5O_3Na]^+$ with an error of -0.3 ppm. This suggests that the precursor ion of disodium AMP is inherently more stable than protonated AMP or disodium AMP as the same amount of collision energy was applied to each precursor ion.

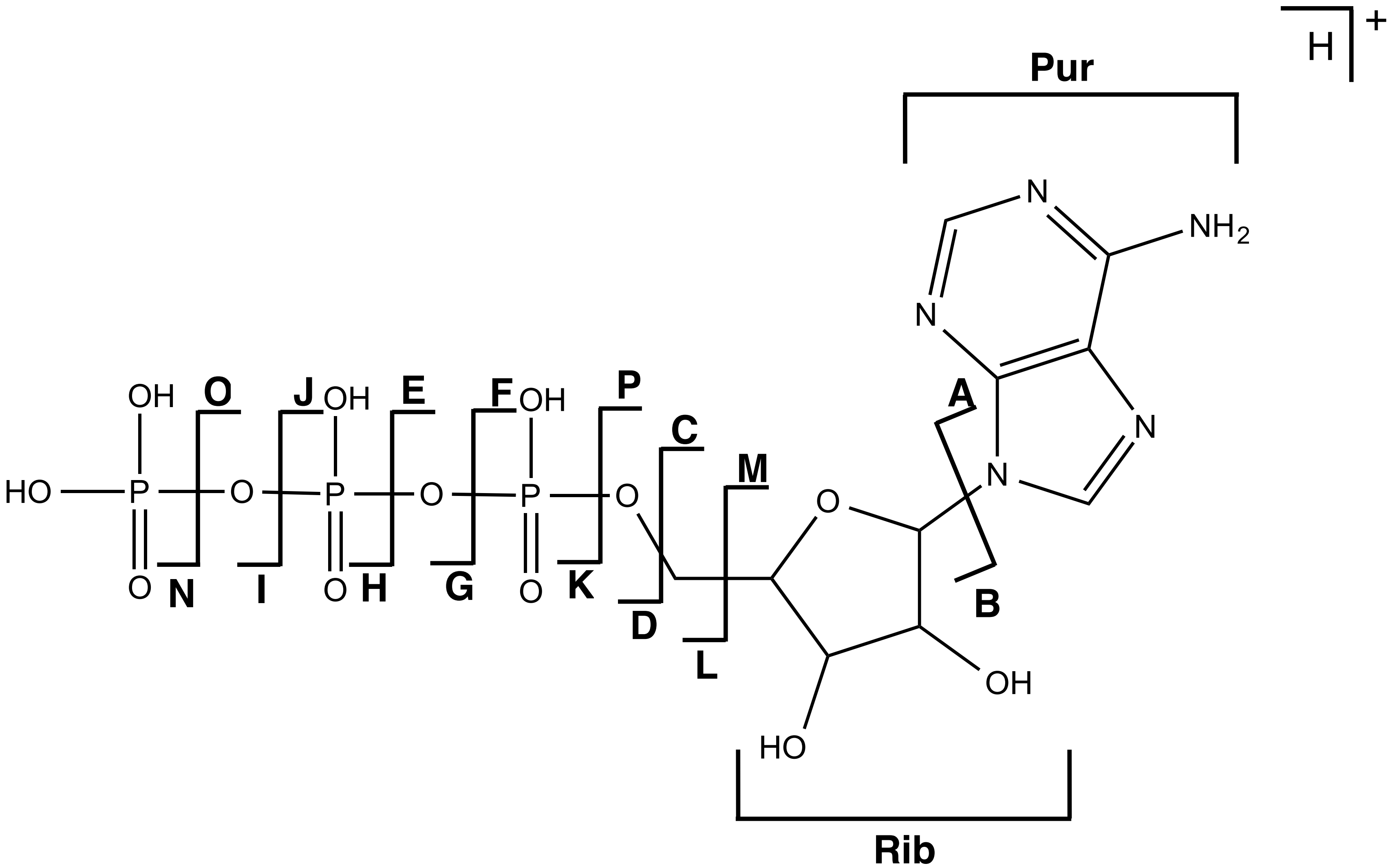

Figure 3.1.2. Diagram given for protonated ATP describing the nomenclature used to indicate a particular bond cleavage and corresponding product ion, plus the terminology used to discuss cleavage involving the purine (Pur) and ribose (Rib) regions. By extension, this diagram also applies to AMP and ADP and the mono, di and trisodium species.

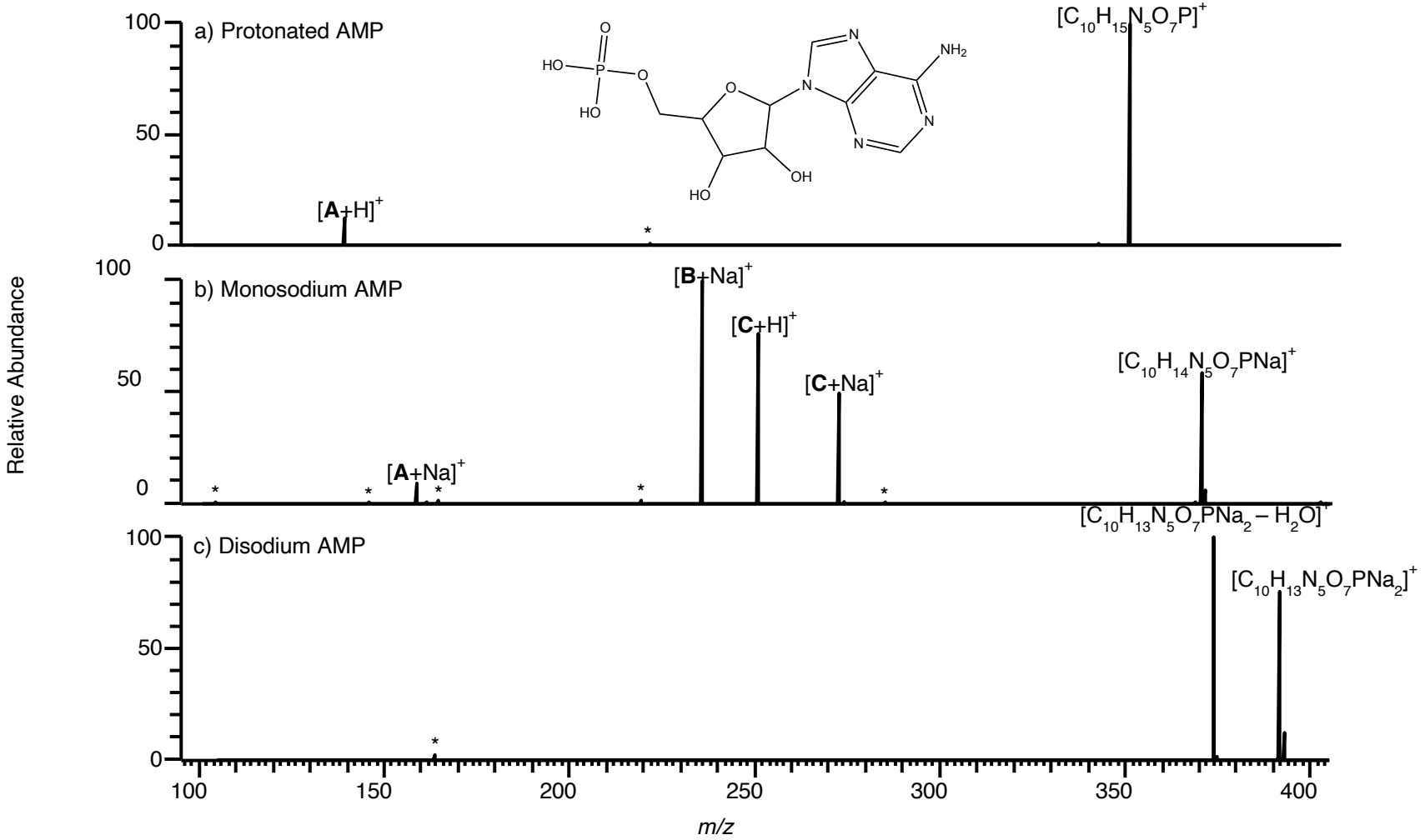

Figure 3.1.1. LTQ-FT CID of precursor ions with an overall single charge for a) protonated AMP, b) monosodium AMP and c) disodium AMP. A full list of *m/z* values and corresponding molecular formulae are given in Appendix 8.1.1-3 * indicates instrument noise.

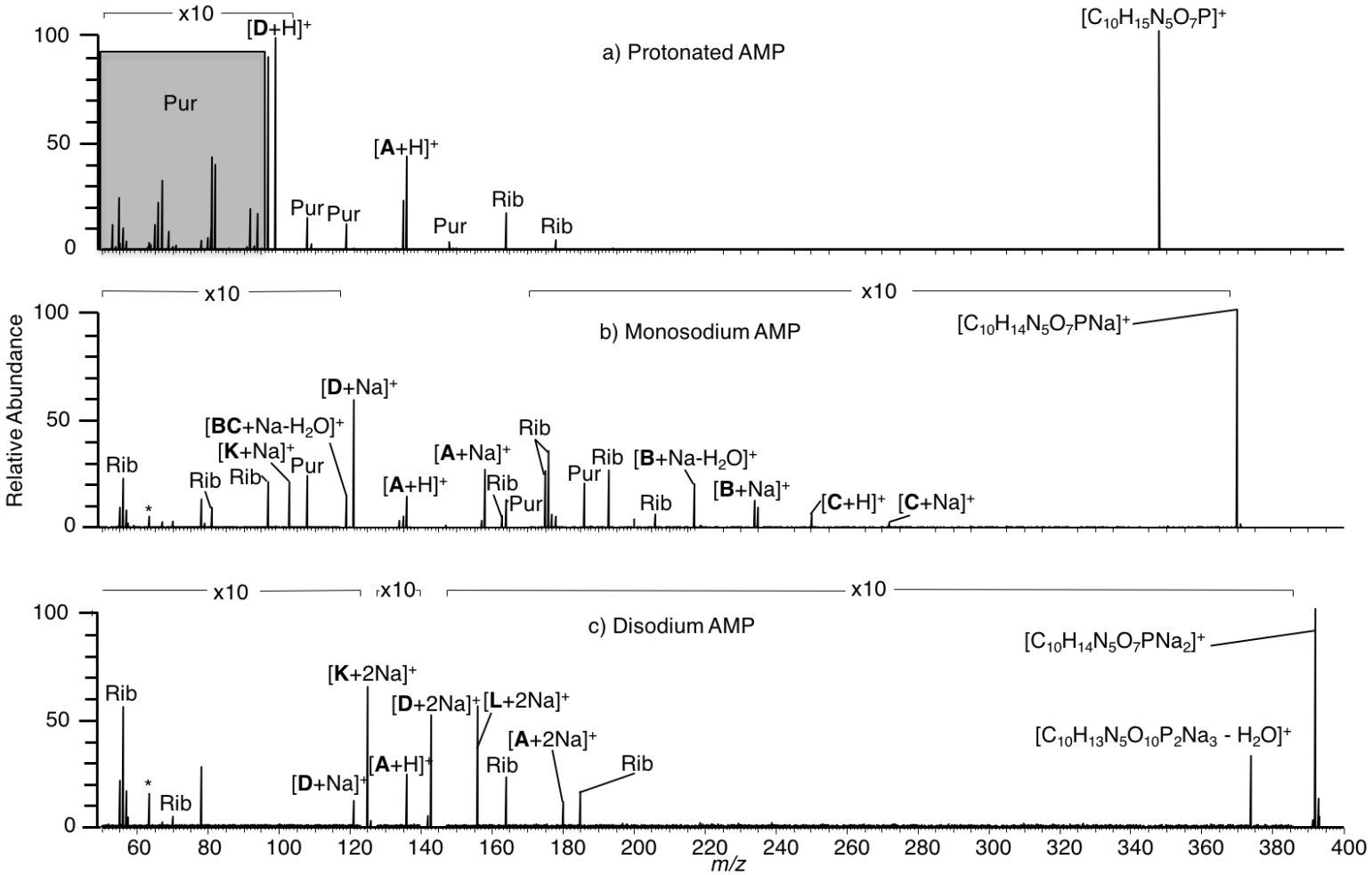

Figure 3.1.3. EID of precursor ions with an overall single charge for a) protonated AMP, b) monosodium AMP and c) disodium AMP. A full list of *m/z* values and corresponding molecular formulae are given in Appendix 8.1.1-3. * indicates instrument noise.

When EID was performed on protonated AMP (Figure 3.1.3a), a greater number of product ions were formed (Figure 3.1.3), with over 80% of these forming by cleavage at the aminopurine moiety. Cross-ring cleavages at the aminopurine (**Pur**) and ribose (**Rib**) groups were only observed for protonated AMP by EID. This concurs with a previous study by Liu *et al.* where cross-ring cleavage was only observed by ECD for the ribose group on metabolite ions such as AMP. [118] By examining the product ions formed by cleavage at **A** and **D** (*m/z* 136.0618, $[C_5H_6N_5]^+$, 0.0 ppm and *m/z* 98.9841, $[H_4PO_4]^+$, -0.4 ppm respectively), it can be deduced that the phosphate or aminopurine moiety can retain the proton. There is a shift in product ion formation when monosodium AMP undergoes EID (Figure 3.1.3b), with over 75% relating to the ribose moiety. There are fewer cross-ring cleavages at the aminopurine compared with EID of protonated AMP, with an increased number of product ions pertaining to cleavage across the ribose ring, indicating that the sodium may be located closer to this part of the molecule. Product ions observed by EID of both protonated AMP and monosodium AMP include **A**, which is seen in its protonated and monosodium form (*m/z* 136.0618, $[C_5H_6N_5]^+$, 0.1 ppm and *m/z* 158.0438, $[C_5H_5N_5Na]^+$, 0.4 ppm respectively) and **D** which is only observed in monosodium form (*m/z* 120.9661, $[H_3PO_4Na]^+$, 0.1 ppm). From these data it can be inferred that the phosphate moiety has a higher affinity for the sodium cation. The ribose group is also able support the sodium cation, as demonstrated by the product ion formed by cleavage **BC** seen in both protonated and monosodium versions (*m/z* 97.0284, $[C_5H_5O_2]^+$, -0.1 ppm and *m/z* 119.0104, $[C_5H_4O_2Na]^+$, 0.1 ppm). Interestingly, cleavage **BC** was

not observed by EID of protonated AMP, meaning that the inclusion of the sodium cation in this locale of the precursor ion is required to form the product ion at *m/z* 119.01. Compared to EID of protonated and monosodium AMP, fewer product ions where observed when disodium AMP underwent EID (Figure 3.1.3c). Overall, when comparing the EID product ion spectra for protonated, monosodium and disodium AMP, it can be observed that increased bond cleavage at the phosphate moiety occurs for disodium AMP, with over half of all product ions relating to this section of the precursor ion. Another difference between EID of these three precursor ions is that cross-ring cleavage is only observed across the ribose group for disodium AMP, whereas protonated and monosodium AMP have cross-ring cleavages across the ribose *and* aminopurine rings. Both the phosphate group, and the aminopurine group are seen to support both sodium cations, as demonstrated by the product ions formed by cleavages **D**, **L** and **A**. **D** is formed containing one and two sodium cations (*m/z* 120.9661, $[H_3PO_4Na]^+$, -0.1 ppm and *m/z* 142.9481, $[H_2PO_4Na_2]^+$, 0.0 ppm respectively) and **L** is only observed containing two sodium cations (*m/z* 155.9559, $[CH_3PO_4Na_2]^+$, 0.1 ppm). Conversely, **A** is observed containing zero and two sodium cations (*m/z* 136.0618, $[C_5H_6N_5]^+$, 0.1 ppm and *m/z* 180.0257, $[C_5H_4N_5Na_2]^+$, 0.3 ppm). As the two product ions deriving from the phosphate moiety are only seen to contain sodium cations, whereas the aminopurine derived product ions are still observed in a protonated form, these data would suggest that the aminopurine moiety has a higher proton affinity than the phosphate group, and that the phosphate group has higher sodium affinity. Estimated pKa values for each

nitrogen group (Figure 3.1.4) in the aminopurine moiety are given in Table 3.1.1. This estimation shows the likely location of the proton to be on N_1.

Position	pK_a
N_1	3.92
N_3	1.58
N_7	0.55
N_9	-
N_{10}	-6.38

Table 3.1.1. pKa values for AMP calculated by MarvinSketch 17.18.0. The calculations are based on empirically calculated partial charge distribution, and the modelling of intramolecular hydrogen bonds. Ionisation constants are also taken into consideration in the algorithm, calculated using ionisation site-specific regression equations. [178]

The location of the proton at the aminopurine group is supported by a study by Turecek *et al.* who showed by density functional theory (DFT) calculations (a method of modelling atoms and molecules using computational quantum mechanical modelling) the most thermodynamically stable location of a proton in adenine was at N_1 (Figure 3.1.4). [179] At the low pH of the ESI solution, deprotonation of one or both OH groups on the phosphate is also likely, allowing O^{-} $^{+}$Na to form. [180]

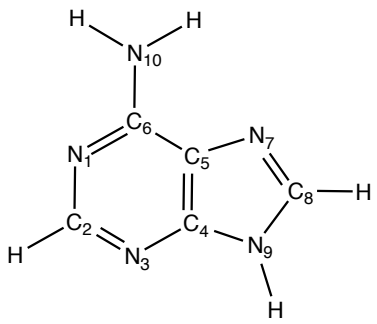

Figure 3.1.4. Nomenclature for adenine atoms.

This postulation is further supported by reports of cation-π interactions which have been observed for ions including tryptophan and other aromatic ions. Cation-π interactions are non-covalent molecular interactions between a cation such as Na^+ and the face on an electron rich π system, such as that offered by a benzene ring. Here it was shown that in the gas phase, cations including sodium can bind tightly to aromatic moieties of the ions investigated. [181, 182] Another interesting observation is that the disodium AMP precursor ion lost water following EID (*m/z* 374.0236, $[C_{10}H_{11}N_5O_6PNa_2]^+$, 0.1 ppm), a product ion observed by CID, but not in studies utilising ECD. This supports the work by Nguyen *et al.* that concludes some vibrational dissociation occurs during the EID process. [4] Although for all precursor ions EID provided enhanced MSMS structural information when compared with CID, for both types of dissociation, the most detailed *and* useful product ion spectra were produced when the monosodium species was fragmented. As can be seen in Table 3.1.2 (a summary of product ions observed for protonated AMP, monosodium AMP and disodium ATP) dissociation is directed towards the phosphate group as more sodium cations are included in the precursor ion. A possible rationale for this in CID is that when only a sodium atom is present on the ion, some level of steric stress is put on the linear structure of AMP. This will affect the bond energy of the constrained structure reducing the energy required to fragment the constrained bonds. In EID, the position of the sodium atom will affect the location of electronic integration for both secondary ionisation by fast electrons, and slow electron capture to form the electronically excited singly charged ion during the EID process. The

data suggest that this process yields the most EID structural information when only one sodium atom is present.

Compound	Adduct	Cleavages from EID	Cleavages from CID
AMP	**H**	Purine(15), Ribose(2), **A**, **D**	**A**
	Na	Purine(4), Ribose(8), **M**, **A**, **A***, **B***, [**B***-H_2O], [**BC***-H_2O], **D***, **K***, **M***	**A**, **C**, **B***, **C***
	2Na	Ribose(4), **A***, **D***, **A****, **D****, **K****, **L****	-H_2O
ADP	**H**	Purine(8), Ribose(4), **A**, **C**, **D**, **E**	[**C**-H_2O], [**E**-H_2O], **E**
	Na	Purine(2), Ribose(14), **A**, [**BC**-H_2O], **M**, **A***, **B***, [**B***-H_2O], **BE***, **BF***, **D***, **K***, **L***	**C**, **F**, **B***, **BF***, [**B***-H_2O], **D***
	2Na	Ribose(7), **A**, **M**, **A***, **B***, [**B***-H_2O], **BE***, **BF***, **D***, **G***, **H***,**K***, **L***, **G****	**B****, [**B****-H2O], **BF****, **D****, **F****
	3Na	Ribose(3), **A**,**G**, **F****,**G****, **H****, **D*****, **K*****	-H_2O, **F****
ATP	**H**	Purine(5), Ribose(4), **A**, **BC**, [**BC**-H_2O], **G, H**, **I**	**E**, **K**, [**K**-H_2O]
	Na	Purine(3), Ribose(7), **A**, **BC**, **C**, **G**, **I**, **B***, [**B***-H_2O], **BF***, **BK***, **D***, **G***, **I***, **JB***, **K***, **L***, **N***	**B***, [**B***-H_2O], **C***, **J***
	2Na	Purine(1), Ribose(11), **A**, **C**, **A***, **I***, **G***, **B****, [**B****-H_2O], **D****, **F****, **G****, **H****, **I****, **J****, **JB****, **K****, **L****, **N****	**B****, [**B****-H_2O], **D****, **J****
	3Na	Purine(2), Ribose(8), **A**, **A***, **A****, **F****, **G****, **H****, **I****, **N****, **B*****, [**B*****-H_2O], **D*****, **G*****, **H*****, **I*****, **J*****, **JB*****, **K*****, **L*****,	**B*****, [**B*****-H_2O], **J*****, **JB*****

Table 3.1.2. Summary of product ions formed by CID and EID for all precursor ions. * denotes the sodium content for each product ion: * = 1; ** = 2 and *** = 3.

3.1.1.3. EID and CID of protonated ADP, monosodium ADP, disodium ADP and trisodium ADP

Analogous results can be seen when comparing CID of protonated, monosodium and disodium AMP with their ADP counterparts (Figure 3.1.5), again with the monosodium precursor ion producing the richest product ion spectrum. This could be steric stress due to intramolecular forces caused by the presence of a sodium atom on the ion. When protonated ADP underwent CID (Figure 3.1.5a), the only product ions formed were a result of cleavage at either of the phosphate groups; this is expected due to the labile nature of the phosphate bonds. [113-117] As mentioned above, CID of monosodium ADP (Figure 3.1.5b) generated a slightly more diverse product ion spectrum, with the loss of aminopurine and loss of aminopurine and water observed by cleavage **A**/**B** (*m/z* 314.9642, $[C_5H_{10}O_{10}P_2Na]^+$, 0.0 ppm). The neutral loss of the aminopurine group and one phosphate group formed the monosodium internal product ion **BF** (*m/z* 216.9874, $[C_5H_7O_6PNa]^+$, 0.0 ppm). The expected product ions caused by fragmentation at the phosphate groups are also present, with **F** corresponding to the neutral loss of one phosphate group and **D** corresponding to the charged loss of both phosphate groups, both in their monosodium form (*m/z* 352.0414, $[C_{10}H_{12}N_5O_6PNa]^+$, 0.0 ppm and *m/z* 200.9324, $[H_4P_2O_7Na]^+$ -0.2 ppm respectively). As the diphosphate group is only observed as a product ion by CID of monosodium ADP, it is likely that the location of the sodium cation on this moiety has a stabilising effect. Figure 3.1.5c shows the product ion spectrum for disodium ADP, which is similar to the spectrum produced by CID of monosodium ADP, with the

exceptions that ions are in their disodium form and cleavage at **C**, observed by CID of monosodium ADP, was not observed. For the disodium ADP precursor ion, only phosphate-containing product ions were formed. Unlike AMP, ADP is also observed as a trisodium species. When this underwent CID (Figure 3.1.5d), very few product ions were generated. Cleavage at **F** (*m/z* 374.0241, $[C_{10}H_{11}N_5O_6PNa_2]^+$ 1.1 ppm) resulted in the same product ion observed by CID of monosodium ADP and disodium ADP, however a sodium cation is lost along with the phosphate group suggesting that the third sodium cation is in the form of ONa on the end phosphate group. The only other product ion observed is loss of water, which has only been formed by CID of trisodium ADP. Product ions which are only formed by CID of monosodium ADP and disodium ADP all contain sodium cations, suggesting that sodium has a destabilising effect on the phosphate bonds.

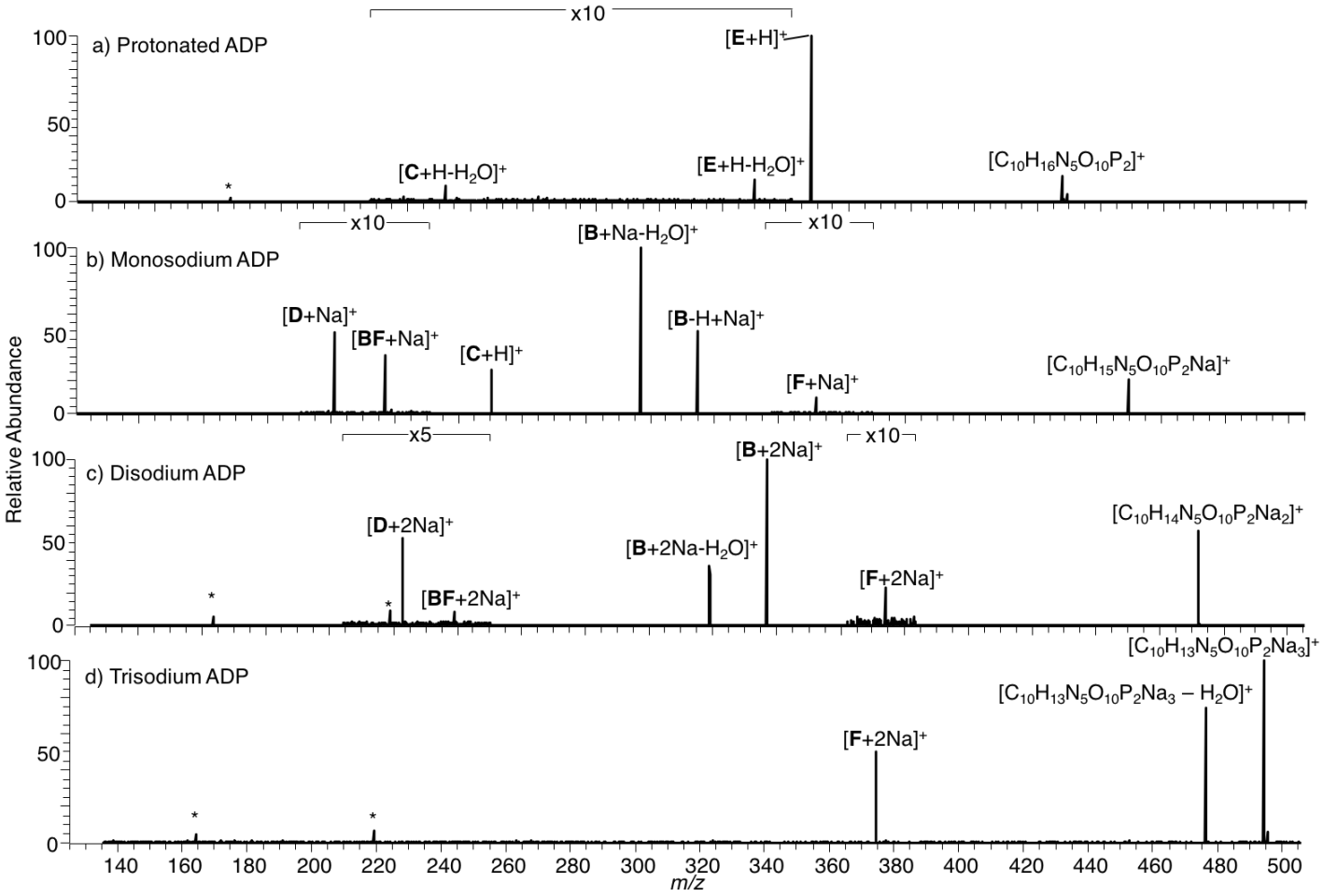

Figure 3.1.5. CID of precursor ions with an overall single charge for a) protonated ADP, b) monosodium ADP, c) disodium ADP and d) trisodium ADP. A full list of *m/z* values and corresponding molecular formulae are given in Appendix 8.1.4-7. * indicates instrument background.

Akin to AMP, EID of ADP (Figure 3.1.6) formed much richer product ion spectra when compared with the corresponding CID spectra. For EID of protonated ADP (Figure 3.1.6a), the vast majority of product ions relate to extensive cleavage at and across the aminopurine group by way of cross-ring cleavages not seen by CID. Other cross-ring cleavages at the ribose group were also observed, as with EID of protonated AMP, and some product ions resulting from dissociation of the phosphate backbone were also formed. As the majority of product ions include some part of the aminopurine group, it is highly likely that the proton resides on that group, likely on N_1 (Figure 3.1.4) as previously discussed. For EID of monosodium ADP (Figure 3.1.6b), the majority of product ions were formed by cross-ring cleavages across the ribose ring, with fewer product ions being formed by cleavage across the aminopurine group; this is directly comparable to EID of monosodium AMP. Where product ions contained part, or all of the phosphate backbone, the sodium cation was always retained. Sodium was also retained by the product ion formed by cleavage at **A** (*m/z* $[C_5H_5N_5Na]^+$, 0.1 ppm) pertaining to the charged loss of the aminopurine group, as well as by the lone ribose product ion, resulting from cleavage **BC**-H_2O (*m/z* 119.0103, $[C_5H_4O_2Na]^+$, 0.1 ppm). This shows that both the aminopurine and ribose groups are able to support either a proton, or a sodium cation, whereas the sodium cations affinity for the phosphate group means that formation of a protonated adduct is not favourable. Figure 3.1.6c shows the EID product ion spectrum for disodium ADP, with dissociation along the phosphate back and at the ribose group being most prevalent. Product ions formed by cross-ring cleavage across the ribose group were less

numerous, with increased fragmentation of the phosphate region of the ion when compared to EID of the monosodium and disodium species. Analogous to EID of monosodium ADP, product ions containing all, or part of the phosphate group always retained at least one sodium cation, with only two product ions not including this moiety. These data further support the postulation made above that the location of the sodium cation, or cations, direct fragmentation to different regions of the precursor ion. Limited cleavage of trisodium ADP (Figure 3.1.6d) was observed as a result of EID with, for the first time, no cross-ring cleavages being induced. Product ions were generally formed by dissociation at the phosphate group, with these product ions always retaining one or two sodium cations. This may be because, with three sodium cations located on the precursor ion, the phosphate groups higher sodium affinity means the probability of two or more sodium cations being located here as -ONa groups are much more likely than having the sodium cations residing on any other sub-species. That is to say, in a collection of these ions, the Na will not all be in fixed locations; there is a small possibility that there is a distribution of locations. It follows that if there is a higher concentration of sodium cations at the phosphate group, EID would be directed to this region of the ion. Another piece of supporting evidence for this explanation is the formation of a product ion relating to a single phosphate group as a trisodium species (**G**, *m/z* 164.9300, $[HPO_4Na_3]^+$, 0.2 ppm) showing that three sodium cations can be stable on a single phosphate group. As no other group of the precursor ion has been seen to support three sodium cations, it follows that the phosphate group has a higher sodium affinity. The aminopurine group

can, however, support two sodium cations, demonstrated by the product ion formed by cleavage at **A** (*m/z* 180.0260, $[C_5H_4N_5Na_2]^+$, 1.9 ppm). Whereas the only example of a product ion containing the ribose sub-species was produced by cleavage at **F** (*m/z* 374.0259, $[C_{10}H_{11}N_5O_6PNa_2]^+$, 5.2 ppm), which although does contain two sodium cations, also includes a phosphate group, supporting at least one of the sodium cations.

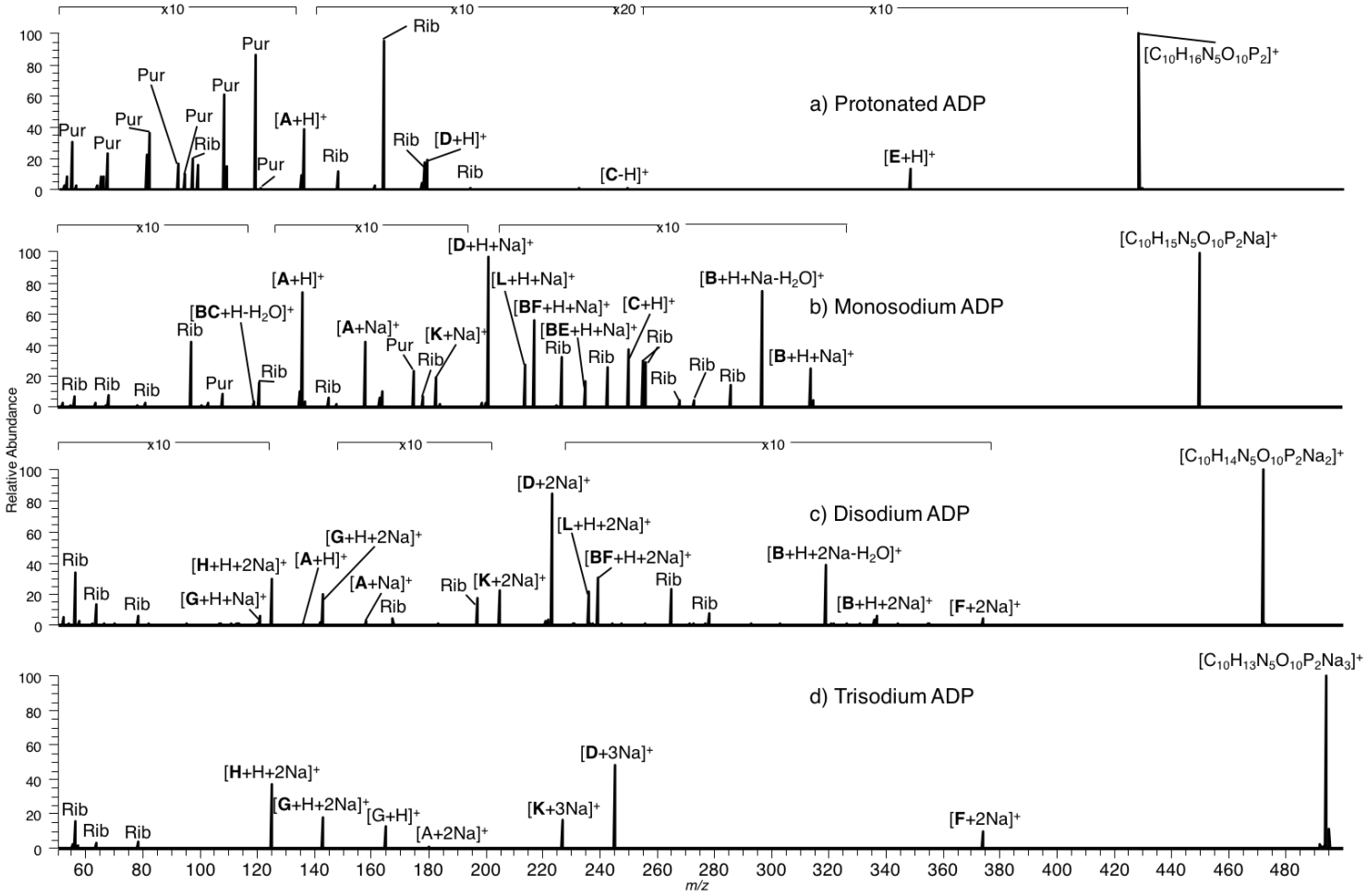

Figure 3.1.6. EID of precursor ions with an overall single charge for a) protonated ADP, b) monosodium ADP, c) disodium ADP and d) trisodium ADP. A full list of *m/z* values and corresponding molecular formulae are given in Appendix 8.1.4-7. * indicates instrument noise.

3.1.1.4. EID and CID of protonated ATP, monosodium ATP, disodium ATP and trisodium

Product ion spectra generated by CID for all ATP precursor ions (Figure 3.1.7) were comparable with CID for AMP and ADP precursor ions. CID of protonated ATP (Figure 3.1.7a) resulted in a predictable MSMS spectrum, with cleavage at the labile phosphate bonds only. [113-117] Collisional dissociation of monosodium ATP did, however, induce cleavage **B** and **B**-H_2O (*m/z* 394.9304, $[C_5H_{11}O_{13}P_3Na]^+$, -0.2 ppm and *m/z* 376.9199, $[C_5H_9O_{12}P_3Na]^+$ -0.1 ppm respectively), relating to the neutral loss of the aminopurine moiety and the aminopurine moiety with water, which was not observed by CID of protonated ATP. These data suggest that the presence of sodium in the precursor ion affects the stability in this region of the ion. As this was not observed by CID of monosodium AMP or monosodium ADP, the length of the phosphate backbone would seem to play a role. As has previously been noted, the most likely location of the sodium cation is on the phosphate backbone. Perhaps the addition of another phosphate group changes the structural conformation of the precursor ion in the gas phase, causing the backbone to wrap around the ribose ring, allowing the sodium cation to interact with the aminopurine group enabling the cleavage observed. The same cleavages at **B** were also observed for CID of the disodium ATP and trisodium ATP precursor ions, with all sodium cations being retained in the product ion. Cleavage at **JB** (*m/z* 340.9176, $[C_5H_6O_9P_2Na_3]^+$, 0.4 ppm), pertaining to the concurrent loss of the aminopurine group and one phosphate group was formed by CID of

trisodium ATP. CID did not result in this bond cleavage for any of the other precursor ions studied; this is likely caused by a combination of the conformation of ATP when three sodium cations preside on the precursor ion and of the interaction of the three sodium cations with the phosphate and aminopurine group. Ion mobility data recorded with the Waters Synapt G2-S (Section 3.1.1.5) shows that whereas ADP has an increased collisional-cross section (CCS) for the trisodium species compared with the disodium species, ATP has a small reduction in CCS for the trisodium species compared with the disodium species, clearly showing that conformational differences, caused by the additional phosphate group, occur between to trisodium ADP and trisodium ATP.

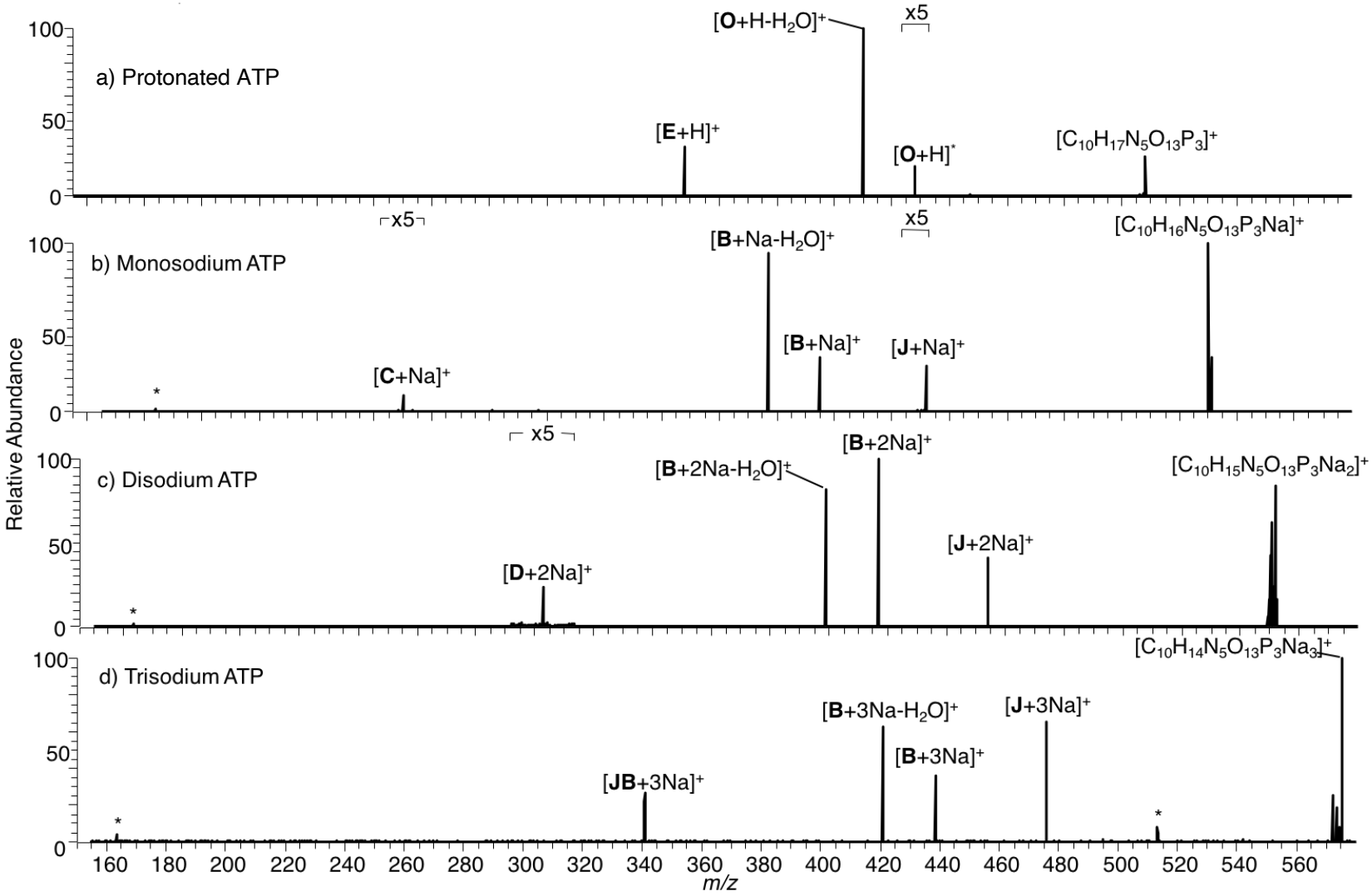

Figure 3.1.7. CID of precursor ions with an overall single charge for a) protonated ATP, b) monosodium ATP, c) disodium ATP and d) trisodium ATP. A full list of *m/z* values and corresponding molecular formulae are given in Appendix 8.1.8-11. * indicates instrument noise.

EID of protonated ATP (Figure 3.1.8a) resulted in fewer product ions relating to the aminopurine group when compared with EID of protonated AMP and protonated ADP; the addition of a third phosphate group increases the pKa of that region of the ion, thereby changing where the charges are located, altering how the electron interacts with the ion as a whole. [181, 183] The product ion resulting from cleavage **BC** (*m/z* 119.0103, $[C_5H_5O_2]^+$, 0.1 ppm) was formed, which has only previously been observed by EID of monosodium precursor ions. Again, this suggests the addition of a third phosphate group alters the EID mechanism. When monosodium ATP underwent EID (Figure 3.1.8b) the monosodium product ion formed by cleavage at **A** was not produced. The most reasonable explanation for this is that the addition of a third phosphate group biases the location of the sodium cation, *i.e.* no sodium atoms are associated with the aminopurine moiety. An increased number of product ions were formed relating to cross-ring cleavage at the aminopurine group for EID of trisodium ATP (Figure 3.1.8d) when compared with EID of monosodium ATP and disodium ATP (Figure 3.1.8c). This is probably because when three sodium atoms are contained within the ATP precursor ion, there is a higher probability that one of the sodium cations will reside on the aminopurine moiety, directing fragmentation towards this region. As this was not observed for trisodium ADP, perhaps a more likely explanation for this is that the third phosphate group on the precursor ion changes the conformation of the ion in the gas phase, allowing greater interaction of a sodium cation residing on the end phosphate group with the aminopurine ring. Ion mobility studies (Section 3.1.1.5) showed a small decrease in CCS

from disodium ATP to trisodium ATP, whereas from disodium AMP to trisodium AMP, a 11 $Å^2$ increase in CCS was observed. This would suggest that the third phosphate group in ATP allows the trisodium ion to adopt a different conformation than trisodium ADP, supporting this hypothesis. The polydentate nature of the phosphate group, *i.e.* the ability for a single sodium cation to interact with multiple moieties on the phosphate group, could contribute to this, especially where multiple phosphate groups are present. This could be confirmed with molecular modelling which could provide further insight, but such experiments were out of the timeframe and focus of this project.

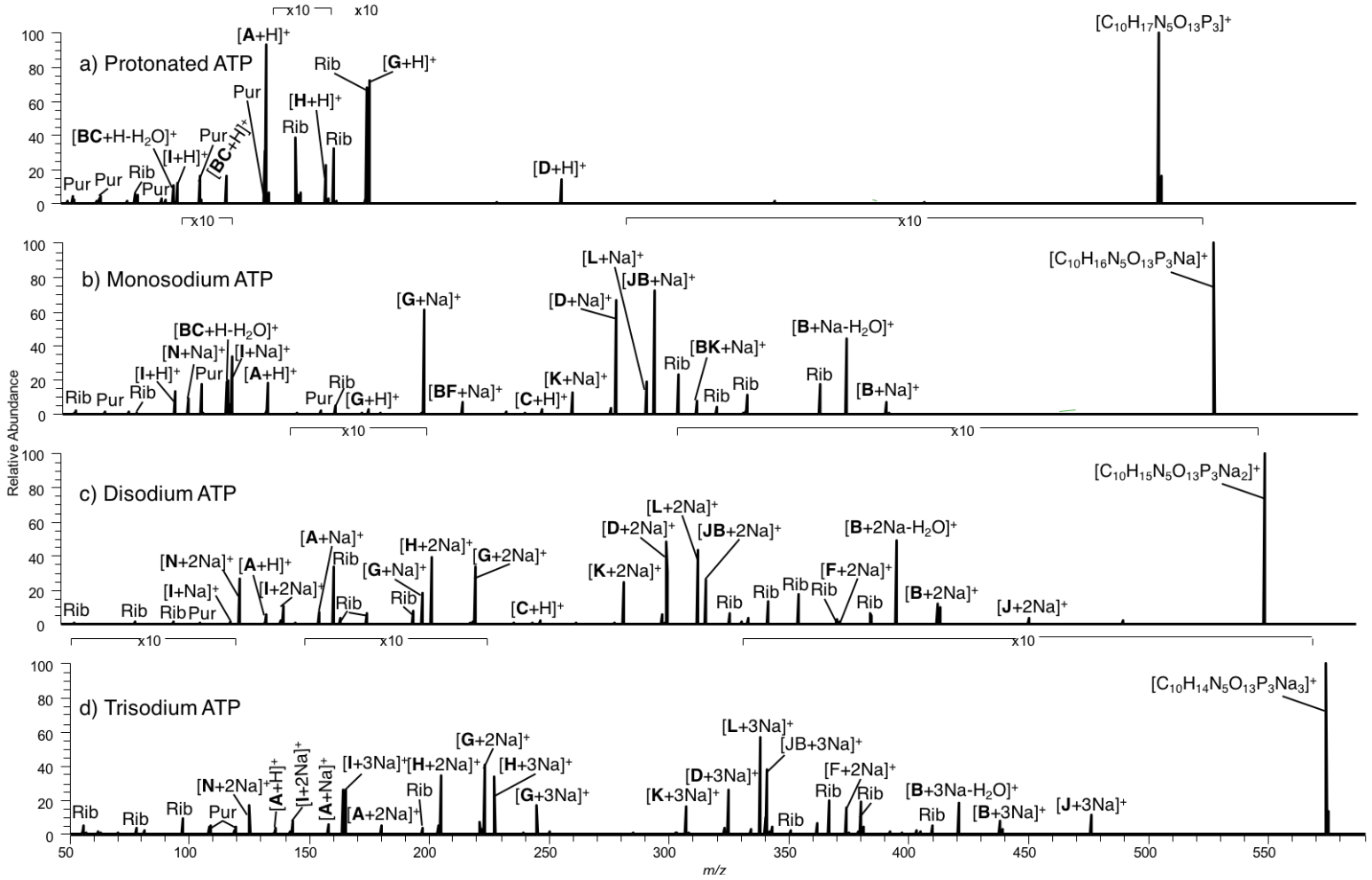

Figure 3.1.8. EID of precursor ions with an overall single charge for a) protonated ATP, b) monosodium ATP, c) disodium ATP and d) trisodium ATP. A full list of *m/z* values and corresponding molecular formulae are given in Appendix 7.1.7-11. * indicates instrument noise.

For all nucleotide precursor ions, EID gave much richer product ions spectra when compared with CID. CID predominantly induced cleavage at the phosphate group, which was expected, as collisional dissociation generally breaks the weakest bond in the precursor ion, and phosphate bonds are known to be labile. [113-117] CID product ion spectra were not seen to be greatly affected by the number of sodium cations present in the precursor ions. This was not the case for EID, where differing numbers of sodium cations had a definite effect on the product ions formed. The locations where the sodium cations are thought to reside directs electronic-induced bond dissociation, producing unique product ions for the majority of nucleotides tested. No major differences between EID product ion spectra where one, two or three phosphate groups were included in the precursor ion, were observed. This is not the case for CID product ion spectra, where the increased number of phosphate groups resulted in a larger number of product ions, as has been previously observed. [113] EID of protonated species, irrespective of the number of phosphate groups contained within the precursor ion, generally formed product ions by cleavage at and across the aminopurine group, giving evidence that this is where the proton tends to reside. This is supported by the fact that at an acidic pH, like the conditions used in this study, the site of protonation is shown to be at the aminopurine ring. [181, 183] The monosodium precursor ions formed the majority of product ions by fragmentation of the ribose group by EID, whereas EID of the disodium and trisodium precursor ions resulted in most cleavage occurring at the phosphate groups. This is

exemplified in Figure 3.1.8 for ATP precursor ions. When dictating which precursor ions resulted in the most informative product ion spectra;

(i) EID on any of the precursor ions gave more comprehensive structural information than CID.

(ii) EID of the monosodium species for AMP and ADP gave the greatest number of product ions for these two nucleotides, generating information useful for characterisation across the entirety of the precursor ions likely due to differences in electronic interactions during the EID process.

(iii) ATP proved to be different, with the trisodium species resulting in the greatest number of product ions. This is less useful than for AMP and ADP precursor ions however, with the vast majority of product ions being formed by cleavage at the phosphate backbone.

(iv) For ions analogous to AMP, ADP and ATP, it would seem sensible to generate a product ion spectra of monosodium species by EID to gain the most diagnostically useful MSMS data.

Targeted study of different regions of the precursor ion is also possible, depending on whether a protonated, monosodium, disodium or trisodium species is isolated and fragmented, as shown in Figure 3.1.9.

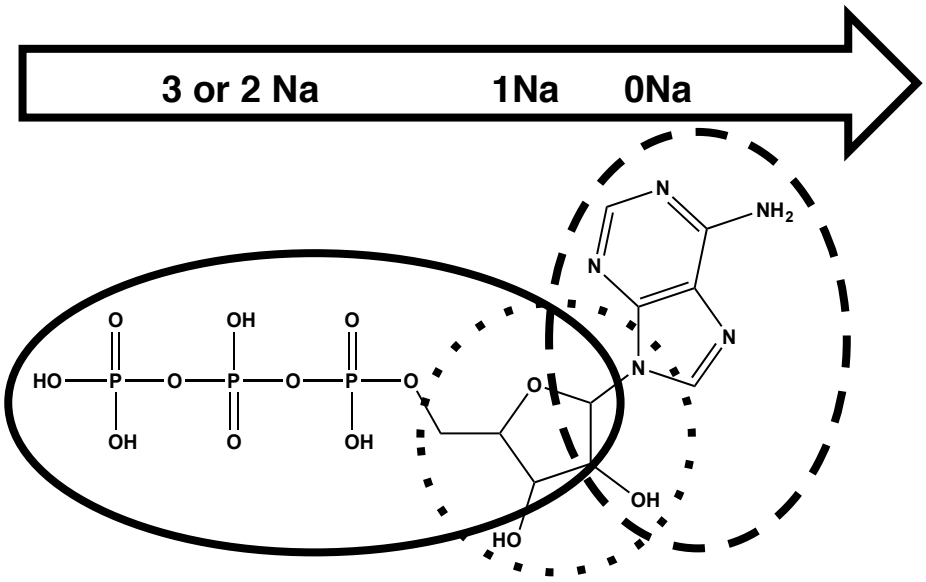

Figure 3.1.9. An ATP molecule has been used here to demonstrate the main regions of fragmentation that the ATP ions undergo with EID. For protonated ATP the main regions of fragmentation are shown by the dashed lines, for monosodium ATP the dotted line and for di and trisodium ATP the solid line. By extension, this diagram also applies to AMP and ADP.

3.1.1.5. Ion mobility of ATP, ADP and AMP

To test whether the conformation of ATP precursor ions alters depending on differing numbers of cations, the CCS of protonated ATP, monosodium ATP, disodium ATP and trisodium ATP were measured using TWIMS on a Waters Synapt G2-S, with the data externally calibrated using poly-DL-alanine (Figure 3.1.10 and 3.1.11, and Table 3.1.3). There is an increase from 130.64 ± 0.01 $Å^2$ to 135.91 ± 0.01 $Å^2$ in the CCS of protonated ATP to monosodium ATP. This is expected as the addition of a sodium cation would increase the CCS of the ATP ion. This trend could be expected to continue with a similar increase in CCS for each additional sodium atom on the ion. However, the CCS does not alter as more sodium cations are

associated with the ion. This suggests that as more sodium is adducted to the ATP ion, the conformation of ATP is becoming more folded and less linear, *i.e.* although there is a greater mass to the ion, a more folded shape means the CCS is not increased. An alternative explanation is that monosodium ATP could have a larger CCS than protonated ATP due to the sodium causing the phosphate chain to elongate. The lack of change in CCS from monosodium ATP as more sodium is added could then be caused by the structure becoming more folded. If this was the case, it may explain why monosodium AMP and ADP provided richer EID product ion spectra than protonated AMP and ADP; the less folded structure allows for more of the ion to interact with electrons during the EID process. The CCS data for all precursor ions of AMP ADP and ATP are shown in Table 3.1.3.

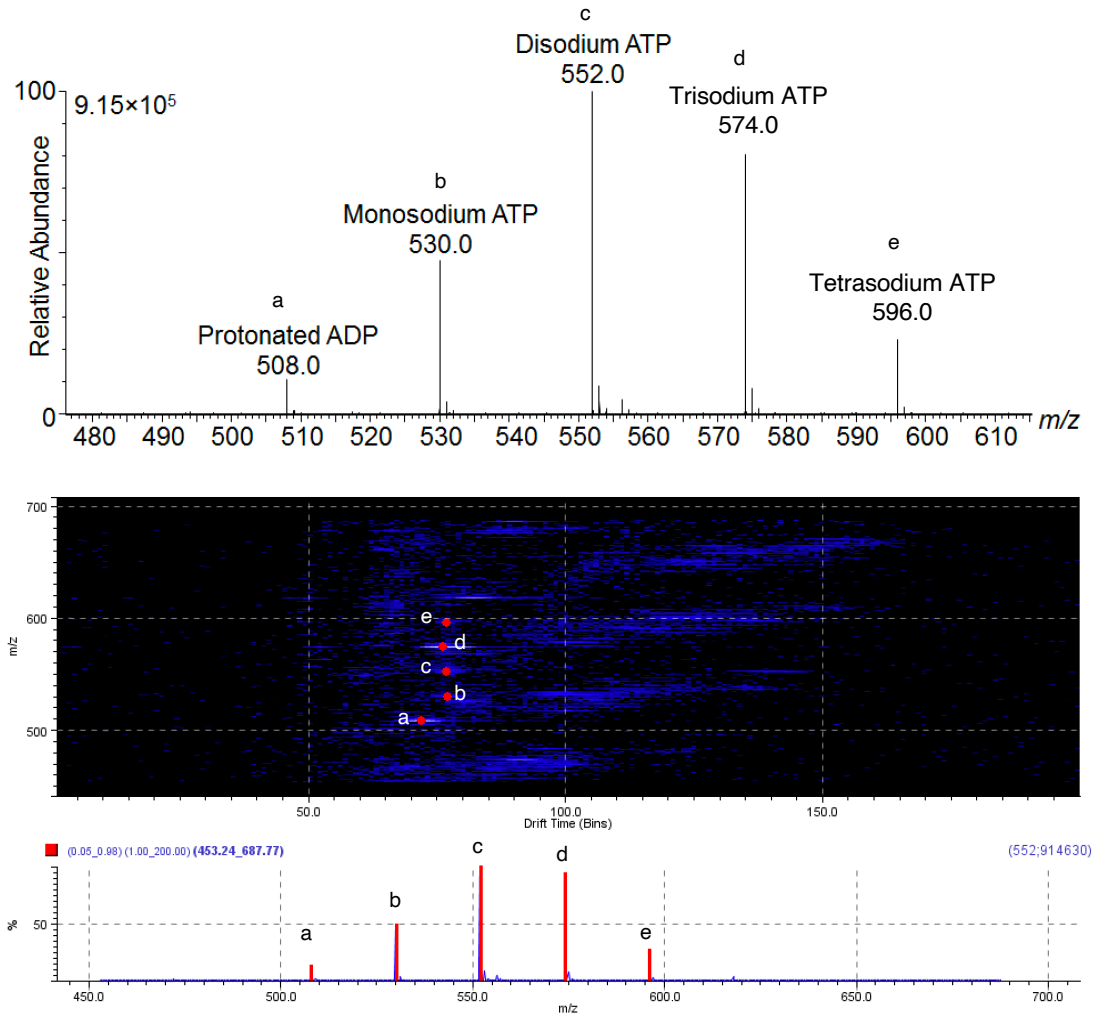

Figure 3.1.10. ATP mass spectrum and mobilogram, where **a** is protonated ATP, **b** is monosodium ATP, **c** is disodium ATP, **d** is trisodium ATP and **e** is tetrasodium ATP. The drift time of each ion was measured through the IMS cell of the Waters Synapt G2-S, the CCS was then calculated by DriftScope 2.4 software based on the velocity of the ion, the electric field applied to the drift tube, the drift time (or mobility) of the ion, and the length of the drift tube, as described in Section 1.6.1.

Molecule	Species	Observed *m/z*	CCS Experiment 1 (Å^2)	CCS Experiment 2 (Å^2)	CCS Experiment 3 (Å^2)	CCS Average (Å^2)	CCS Error (Å^2)
AMP	**Protonated**	348.1	104.85	105.05	105.08	104.99	0.1
	Monosodium	370.1	110.49	110.66	110.73	110.63	0.1
	Disodium	392.0	113.18	113.34	113.42	113.31	0.1
	Trisodium	414.0	122.74	123.01	123.05	122.93	0.2
ADP	**Protonated**	428.0	119.62	119.65	119.64	119.64	0.02
	Monosodium	450.0	126.53	126.57	126.60	126.57	0.04
	Disodium	472.0	121.05	121.09	121.11	121.08	0.03
	Trisodium	494.0	127.48	127.49	127.54	127.50	0.03
ATP	**Protonated**	508.0	130.64	130.65	130.64	130.64	0.01
	Monosodium	530.0	135.91	135.89	135.91	135.91	0.01
	Disodium	552.0	135.51	135.56	135.56	135.54	0.03
	Trisodium	574.0	134.64	134.68	134.68	134.66	0.02
	Tetrasodium	595.9	135.16	135.16	135.14	135.15	0.01

Table 3.1.3. Observed AMP, ADP and ATP ions with drift-times and CCS values.

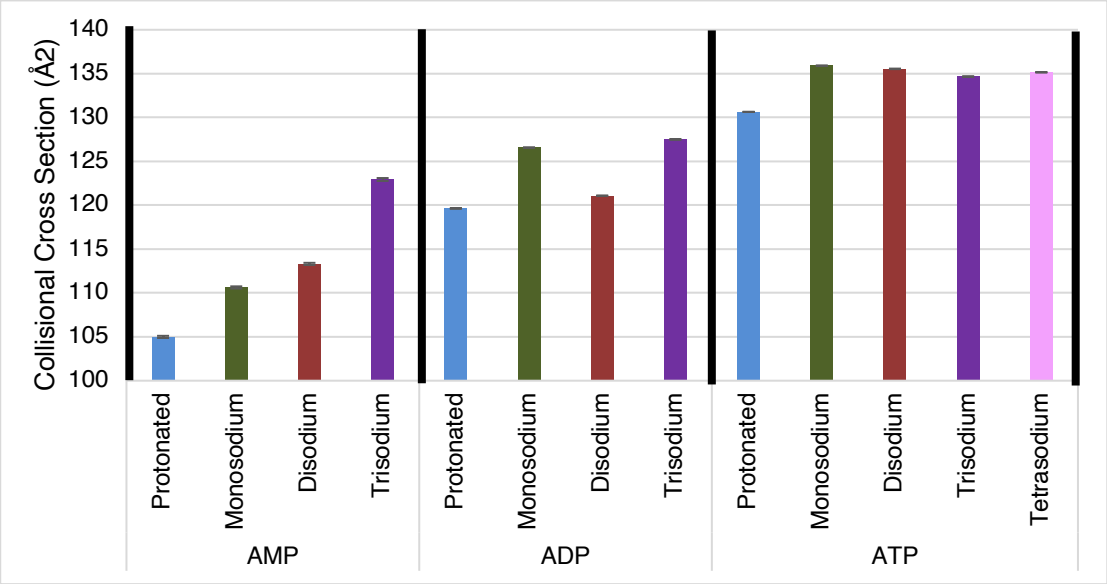

Figure 3.1.11. AMP, ADP and ATP vs CCS, triplicate results with standard deviation error bars.

As seen in Figure 3.1.11, when TWIMS was performed on AMP, an increase in CCS was observed for ions containing one and two sodium compared with the protonated species. The initial increase in CCS from 104.99 ± 0.1 $Å^2$ to 110.63 ± 0.1 $Å^2$ for AMP with zero sodium to AMP with one sodium is consistent with the same increase observed for ATP. The CCS of AMP ions containing two sodium atoms was 113.31 ± 0.1 $Å^2$, only 2.68 ± 0.1 $Å^2$ larger than monosodium AMP. This smaller increase could be due to the AMP ion becoming slightly more folded compared to the monosodium form under the influence of an additional sodium cation. This differs from the change in CCS from monosodium ATP (135.91 ± 0.01 $Å^2$) to disodium ATP (135.54 ± 0.03 $Å^2$) which was a slight decrease of 0.37 ± 0.04 $Å^2$. This is likely because the additional phosphate groups on ATP can fold around the structure more than the single phosphate group on AMP.

For ADP (Figure 3.1.11), the data would suggest that a conformational change occurs to the ion from protonated ADP to monosodium ADP. The CCS increases from 119.64 ± 0.02 $Å^2$ for protonated ADP to 126.57 ± 0.04 $Å^2$ for monosodium ADP, an increase of 6.93 ± 0.04 $Å^2$, which is larger than the equivalent change for ATP and AMP. Disodium ADP has a reduced CCS compared with monosodium ADP, likely due to the phosphate group folding around the ion. This trend is not observed for ATP but could be explained by the phosphate group already folding to some extent in the protonated species. This is supported by the lack of change in product ion spectra for ATP ions compared with ADP ions for different precursor ions. Trisodium ADP seems to have a similar conformation to disodium ADP, with the increase in CCS of 6.4 ± 0.03 $Å^2$ being explained by the additional sodium cation as seen of AMP, which is supported by both precursor ions having similar product ion spectra for CID and EID (Figures 3.1.5 and 3.1.6).

3.1.1.6. EID and CID of protonated fostamatanib, monosodium fostamatanib and disodium fostamatanib

Applying the knowledge gained from the study on phosphorylated nucleotides, fostamatanib (Figure 3.1.12), a small pharmaceutical molecule of interest, has been studied in a similar way, to observe whether

the same targeted dissociation is available on phosphorylated pharmaceutical ions.

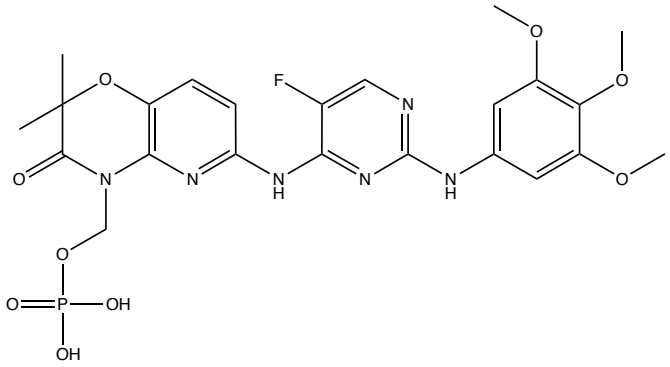

Figure 3.1.12. Structure of fostamatanib.

CID of protonated fostamatanib (Figure 3.1.13a) resulted in cleavage at **A** (*m/z* 483.1792, $[C_{23}H_{24}N_6O_5F]^+$, 1.1 ppm) relating to the neutral loss of the phosphate group, as shown in Figure 3.1.14. Cleavage **A** was also observed by CID of monosodium fostamatanib (Figure 3.1.13b), which was seen with and without the sodium cation (*m/z* 505.1621, $[C_{23}H_{23}N_6O_5FNa]^+$, 2.8 ppm and *m/z* 483.1799, $[C_{23}H_{24}N_6O_5F]^+$, 2.6 ppm respectively). Cleavage **B** (*m/z* 493.2500, $[C_{22}H_{23}N_6O_5FNa]^+$, 2.8 ppm) was observed, which relates to the loss of the methyl-phosphate group with the product ion retaining the sodium cation. These data show that the sodium cation cannot only be stabilised by the phosphate group, but also by another moiety on the precursor ion. As cleavage **B** was not observed by CID of protonated fostamatanib, this suggests the sodium atom stabilises the bond between the phosphate group and methyl group. CID of disodium fostamatanib (Figure 3.1.13c) only induced cleavage **B**, with only one sodium atom being retained; this would imply that only one sodium cation can be retained by the phosphate group, unlike the nucleotide ions, where

evidence showed the sodium could be located elsewhere. Applying the knowledge gained from AMP, ADP and ATP, it is possible to predict that EID of fostamatanib will offer more diagnostically useful information compared with CID, and that by dissociating the protonated, monosodium and disodium precursor ions, complementary information can be gained.

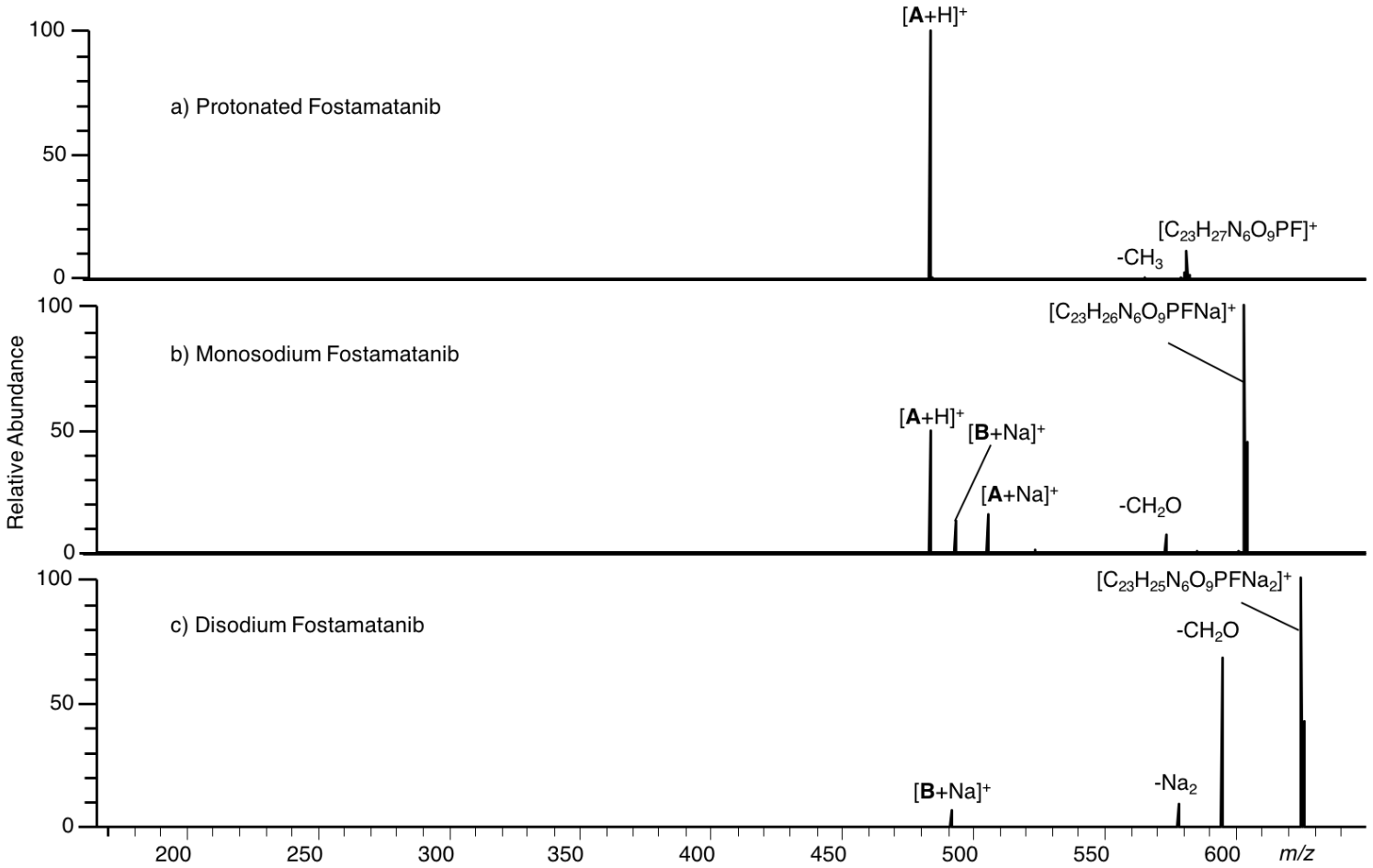

Figure 3.1.13. CID of precursor ions with an overall single charge for a) protonated fostamatanib, b) monosodium fostamatanib and c) disodium fostamatanib. A full list of *m/z* values and corresponding molecular formulae are given in Appendix 8.1.12-14. * indicates instrument noise.

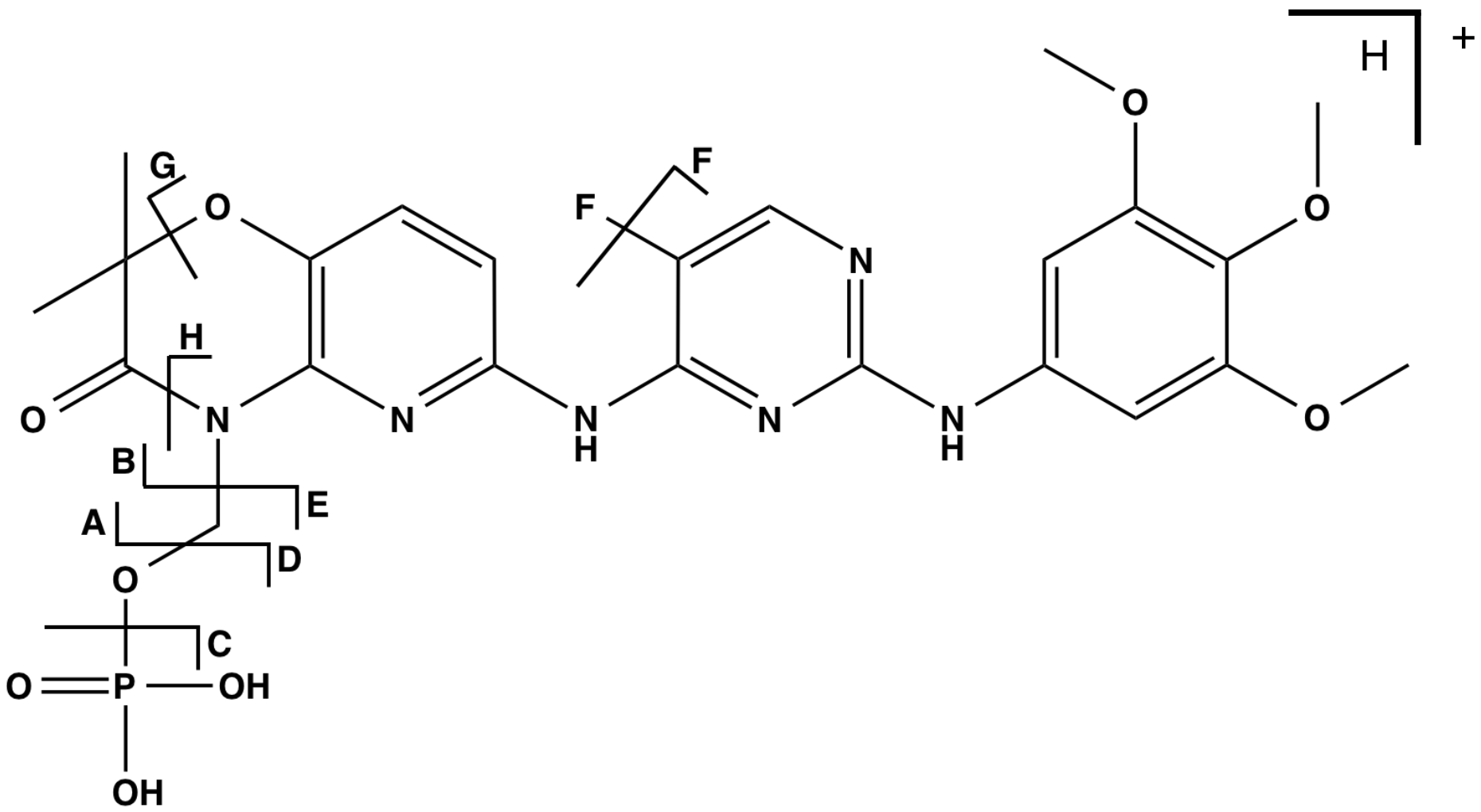

Figure 3.1.14. Diagram given for protonated fostamatanib describing the nomenclature used to indicate a particular bond cleavage and corresponding product ion. By extension, this diagram also applies to the monosodium and disodium species.

EID of protonated fostamatanib (Figure 3.1.15a) resulted in more product ions than CID, with bond cleavage mainly observed at the alkyl chain connected to the phosphate group. This would suggest that the proton resides in close proximity to the alkyl chain connected to the phosphate group. Cross-ring cleavage was observed for the first time for this ion, across the morpholin-3-one ring, **BGH**, (*m/z* 402.1436, $[C_{18}H_{19}N_6O_4F]^+$, -2.2 ppm). This is comparable to EID of the nucleotide precursor ions, where cross-ring cleavage was only observed by EID, and agrees with previous work. [118] Loss of the phosphate group, (**A**, *m/z* 483.1792, $[C_{23}H_{24}N_6O_5F]^+$, 1.1 ppm) and HF (**AF**, *m/z* 463.1730, $[C_{23}H_{23}N_6O_5]^+$, 1.3 ppm) were common along with loss of methyl groups (*m/z* 565.1252, $[C_{22}H_{23}O_9N_6PF]^+$, 1.7 ppm and *m/z* 453.1324, $[C_{21}H_{18}N_6O_5F]^+$, 1.5 ppm), methoxy group (*m/z* 439.1529, $[C_{21}H_{20}N_6O_4F]^+$, 1.0 ppm) and water (*m/z* 562.1381, $[C_{23}H_{24}O_8N_6PF]^+$, 1.6 ppm). Other product ions relating to complex rearrangements of the precursor ion were also observed. When EID was performed on monosodium fostamatanib (Figure 3.1.15b), less product ions were formed than for protonated fostamatanib, with limited differences in the cleavages induced. The only unique peaks relate to small neutral losses of a methoxy group (*m/z* 573.1288, $[C_{22}H_{24}N_6O_8PFNa]^+$, 3.3 ppm), the methyl-phosphate group (*m/z* 493.1620, $[C_{22}H_{23}N_6O_5FNa]^+$, 2.8 ppm) and loss of $C_2H_6O_5PNa$ (*m/z* 439.1535, $[C_{21}H_{20}N_6O_4F]^+$, 2.3 ppm). The loss of the phosphate group is observed, with the precursor ion both retaining (*m/z* 505.1621, $[C_{23}H_{23}N_6O_5FNa]^+$, 2.8 ppm) and not retaining the sodium atom (*m/z* 483.1787, $[C_{23}H_{24}N_6O_5F]^+$, 2.6 ppm), again demonstrating that the sodium atom resides on a distribution of locations

on the precursor ion. Figure 3.1.15c shows the EID product ion spectrum for disodium fostamatanib. No cross-ring cleavage was observed, and fragmentation was limited to the phosphate moiety. **C** (*m/z* 124.9375, $[PO_3Na_2]^+$, -0.1ppm) and **D** (*m/z* 142.9481, $[H_2PO_4Na_2]^+$, 0.1 ppm) were observed for the first time; the phosphate group was only seen to retain a charge with the inclusion of two sodium atoms (for both CID and EID).

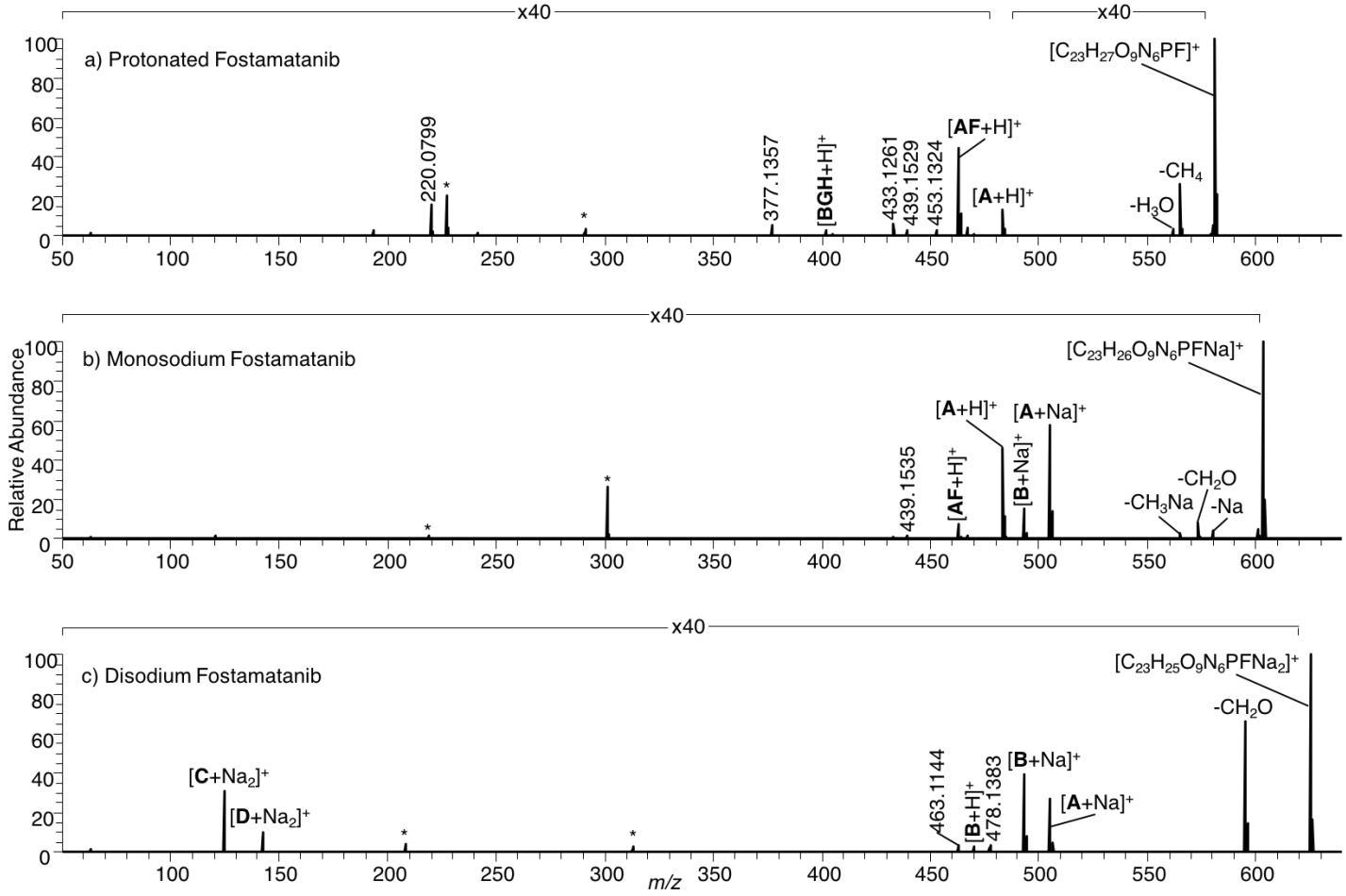

Figure 3.1.15. EID of precursor ions with an overall single charge for a) protonated fostamatanib, b) monosodium fostamatanib and c) disodium fostamatanib. A full list of *m/z* values and corresponding molecular formulae are given in Appendix 7.1.12-14. * indicates instrument noise.

A trend relating to the origin of unique product ions, depending on sodium content, was observed following EID of fostamatanib, analogous to EID of AMP, ADP and ATP. When two sodium atoms were present in the precursor ion, peaks relating predominantly to the phosphate moiety were produced, and when zero and one sodium atom was present, cleavage was mainly limited to the alkyl-morpholine region. Rather than gaining useful information across the entire ion by sequentially performing EID on precursor ions with different numbers of sodium cations, only limited differences in bond cleavages were observed. Although this is useful if studying the phosphate region of fostamatanib, no new product ions relating to cleavages in other regions of the ion were obtained.

3.1.1.7. Ion mobility of protonated fostamatanib, monosodium fostamatanib and disodium fostamatanib

The CCS of protonated, monosodium and trisodium fostamatanib were measured as shown in Table 3.1.4. Comparing protonated fostamatanib to monosodium fostamatanib, the CCS decreased from 164.43 ± 0.2 $Å^2$ to 151.30 ± 0.1 $Å^2$ which suggests the structure becomes much more folded. From monosodium fostamatanib to disodium fostamatanib there is a smaller decrease in CCS of 3.10 ± 0.1 $Å^2$. This data could explain the reduced fragmentation by EID observed; as the conformation of the ion is becoming more folded, less of the structure is able to interact with electrons

during the EID process. Additionally, if the structure is more folded, there may be more steric stress on certain bonds, reducing the energy required to dissociate a bond, which could explain why more CID product ions were formed for monosodium fostamatanib compared with protonated fostamatanib.

Species	Observed *m/z*	CCS 1 (Å^2)	CCS 2 (Å^2)	CCS 3 (Å^2)	CCS Average (Å^2)	CCS Standard Deviation
Protonated	581.1616	164.33	164.28	164.69	164.43	0.2
Monosodium	603.1444	151.18	151.45	151.27	151.30	0.1
Disodium	625.1205	148.18	148.14	148.26	148.20	0.06

Table 3.1.4. Observed fostamatanib ions with drift-times and CCS values.

3.1.2. Conclusions

With EID of Fostamatanib, the same targeted dissociation across the entire ion was not possible, as observed for EID of the nucleotide precursor ions. This could be because, if the location of the sodium atoms is directing EID, it is likely that all three sodium atoms are located at the phosphate group. EID of fostamatanib resulted predominantly in fragmentation close to the phosphate group. As electrons from the EID process generally interact, and cause fragmentation close to the proton, the most likely position of the proton on [fostamatanib + H]$^+$ is a moiety in close proximity to the phosphate group. This differs from the nucleotide ions, where EID of [AxP + H]$^+$ resulted in fragmentation predominantly at the aminopurine group,

suggesting the proton resides at the opposite end of the ions to the phosphate group. For AMP, ADP and ATP, one could easily shift fragmentation across the molecule by changing where the electron from the EID process interacted; the attraction to the proton and the sodium cation or cations biased where the electron ended up and so targeted fragmentation could be achieved. With fostamatanib, the only way this could be feasible would be to attach a group, similar in pKa to the aminopurine group on AMP, ADP and ATP. When studying phosphorylated ions, this study indicates that the most diagnostic and prolific tandem mass spectrometric information can be gained by performing EID on a monosodium species.

3.2. Characterisation of small pharmaceutical molecules by electron-transfer dissociation

For the first time, electron-transfer dissociation has been successfully performed on doubly protonated pharmaceutical molecules. Both electron-transfer and proton-transfer has been observed for a selection of ions, with the product ion spectra resulting from electron-transfer offering the most useful information. For the majority of ions tested, information complementary to CID was produced, useful in aiding structural elucidation studies.

3.2.1. Results and discussion

3.2.1.1. ETD and CID of cediranib

Cediranib is a small molecule of pharmaceutical interest which was developed by AstraZeneca as an anti-cancer chemotherapeutic agent. It was chosen for study due to the formation of $[cediranib + H]^+$ and $[cediranib + 2H]^{2+}$ following ESI. The vibrational dissociation of $[cediranib + H]^+$ and $[cediranib + 2H]^{2+}$ (Figure 3.2.1) have been well documented, with more bond cleavages observed due to the higher internal energy of the doubly protonated precursor ion. [78] This is explained by RRKM theories of unimolecular dissociations, as covered in Section 1.2.3.1. [58-60] For a direct comparison, the CID product ion spectrum is shown in Figure 3.2.2e and Figure 3.2.2f, with peak assignments available in the appendix. ECD of $[cediranib + 2H]^{2+}$ and EID of $[cediranib + H]^+$ have also been studied previously, with complementary product ions to CID being formed (Section 1.2.3.2 and 1.2.3.3). [86, 104] In order to compare the product ion spectra, ECD of $[cediranib + 2H]^{2+}$ can be seen in Figure 3.2.2c and EID of

[cediranib + H]$^+$ in Figure 3.2.2d, with peak assignments also found in the appendix.

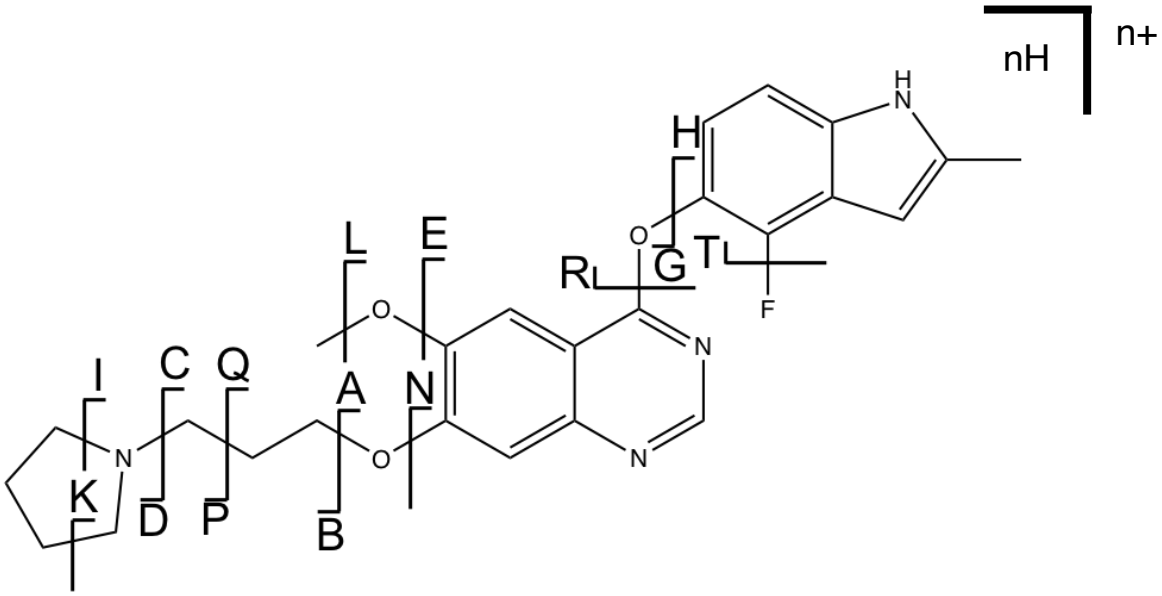

Figure 3.2.1. Cediranib with cleavage sites relating to Figure 3.2.2.

Following on from the successful application of EID on singly charged ions, there is the potential for ETD, an alternative electron-based dissociation technique, to be applied to the study of singly charged molecules. In order to investigate this, a 1 μg/mL solution of cediranib made up in 0.1% formic acid in 50:50 water : acetonitrile, was directly infused into a Waters Synapt G2-S in ESI mode. [Cediranib + H]$^+$ was isolated by the quadrupole and ETD performed in the trap region of the TriWave using *p*-nitrotoluene anion as the ETD reagent. Figure 3.2.2b shows the product ion spectrum from this experiment.

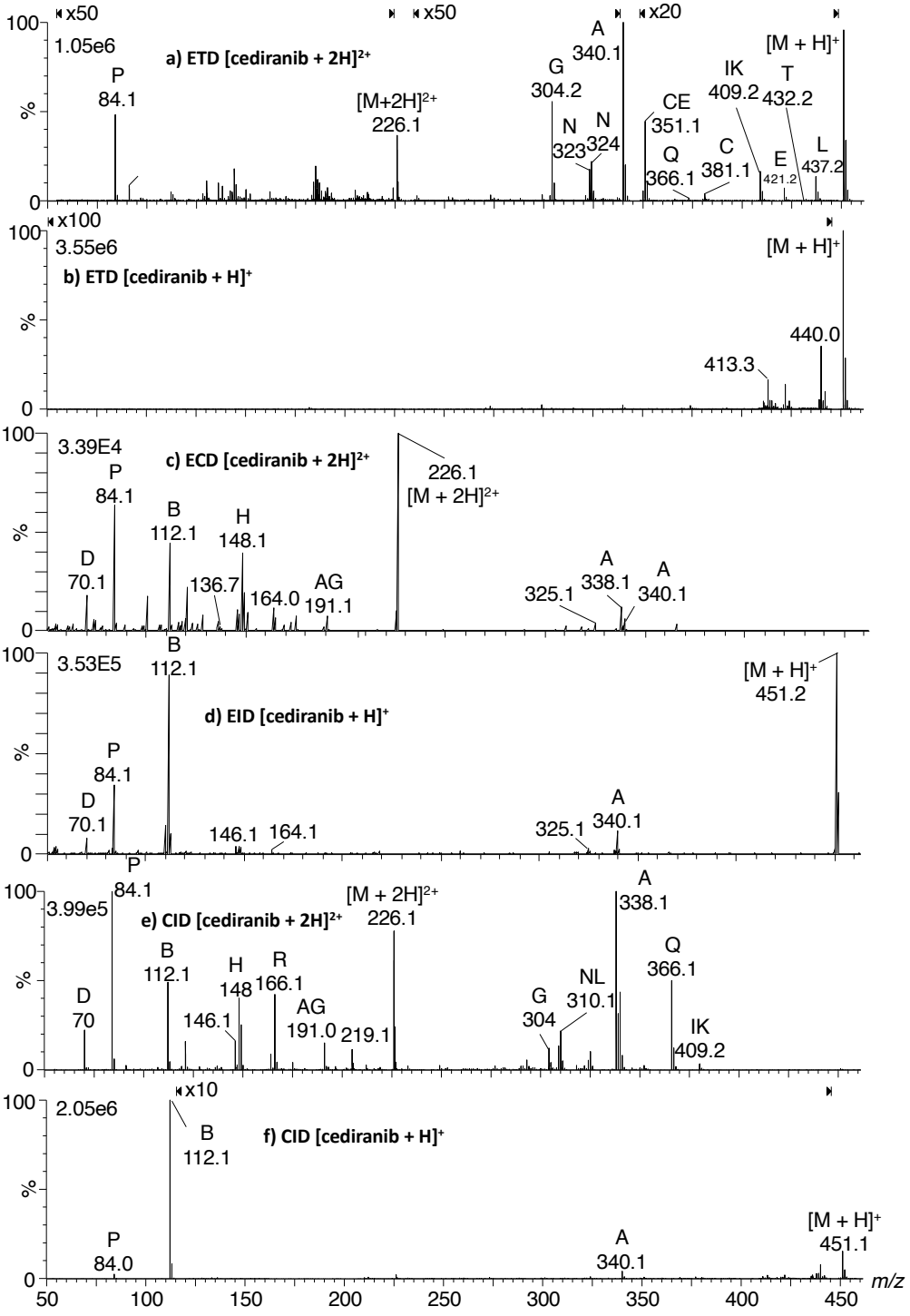

Figure 3.2.2. Cediranib MSMS for a) $[M + 2H]^{2+}$ ETD, b) $[M + H]^{+}$ ETD, c) $[M + 2H]^{2+}$ hECD, d) $[M + H]^{+}$ EID, e) $[M + 2H]^{2+}$ CID and f) $[M + H]^{+}$ CID.

No significant fragmentation was induced following ETD of $[cediranib + H]^+$. The low abundance ions seen from *m/z* 413.3 to 440.0 could not be assigned by accurate mass and are likely noise or impurities. The reasoning for ETD not successfully forming product ions for $[cediranib + H]^+$ could be that any electrons transferred to $[cediranib + H]^+$ would simply neutralise the ions. In EID, a 'fast' electron causes secondary ionisation with a 'slow' electron then being captured to form an electronically excited precursor ion inducing fragmentation, whereas, the electron transferred in ETD is done by way of a chemical reaction and is unlikely to cause secondary ionisation. Due to cediranib forming both $[cediranib + H]^+$ and $[cediranib + 2H]^{2+}$ by ESI, ETD was performed on $[cediranib + 2H]^{2+}$ with the product ion spectrum shown in Figure 3.2.2a.

ETD of $[cediranib + 2H]^{2+}$ was, for the first time, successfully performed. Proton-transfer was observed following the interaction of the *p*-nitrotoluene radical anion with the doubly protonated cediranib (Reaction 3.2.1). This was determined by the mass of the singly charged cediranib peak at *m/z* 451.2139 corresponding to $[cediranib + H]^+$ (-0.6 ppm) and the peak at *m/z* 452.2134 corresponding to the ^{13}C isotopologue, with the relative abundance of the ^{13}C peak concurrent with this assignment. If a small amount of $[cediranib + 2H]^{+\cdot}$ were produced, the Synapt G2-S does not have the 7.5×10^5 resolving power required to separate the two species.

$$[M + 2H]^{2+} + [pNT]^{-\bullet} \rightarrow [M + H]^{+} + [pNT + H]^{\bullet}$$

Reaction 3.2.1. Doubly protonated species reacting with a *p*-nitrotoluene radical anion, resulting in proton-transfer.

The product ions formed by ETD are for the most part a combination of those seen by CID and ECD. Like ECD, ETD formed product ions not observed by CID, suggesting that an electronic dissociation mechanism similar to ECD is taking place, alongside a vibrational mechanism. [78, 84] A unique product ion formed by cross-ring cleavage at the pyrrolidine ring (**IK**) is seen to occur by ETD (*m/z* 409.1678, $[C_{22}H_{22}N_4O_3F]^+$, 0.5 ppm). Although cross-ring cleavage by CID has been observed, it is rare and generally formed by MS^n experiments, where product ions undergo further collisions resulting in ion activation and dissociation, whereas this type of bond dissociation is common for electronic mechanisms. This suggests an electronic mechanism is occurring alongside vibrational dissociation. [118] Other unique product ions observed by ETD include two product ions likely formed by cleavage **L** and **E** at the methoxy region of the ion as shown in Figure 3.2.3 (*m/z* 437.1968 and 421.2010, $[C_{24}H_{26}N_4O_3F]^+$ and $[C_{24}H_{26}N_4O_2F]^+$, -4.8 ppm and -7.1 ppm respectively).

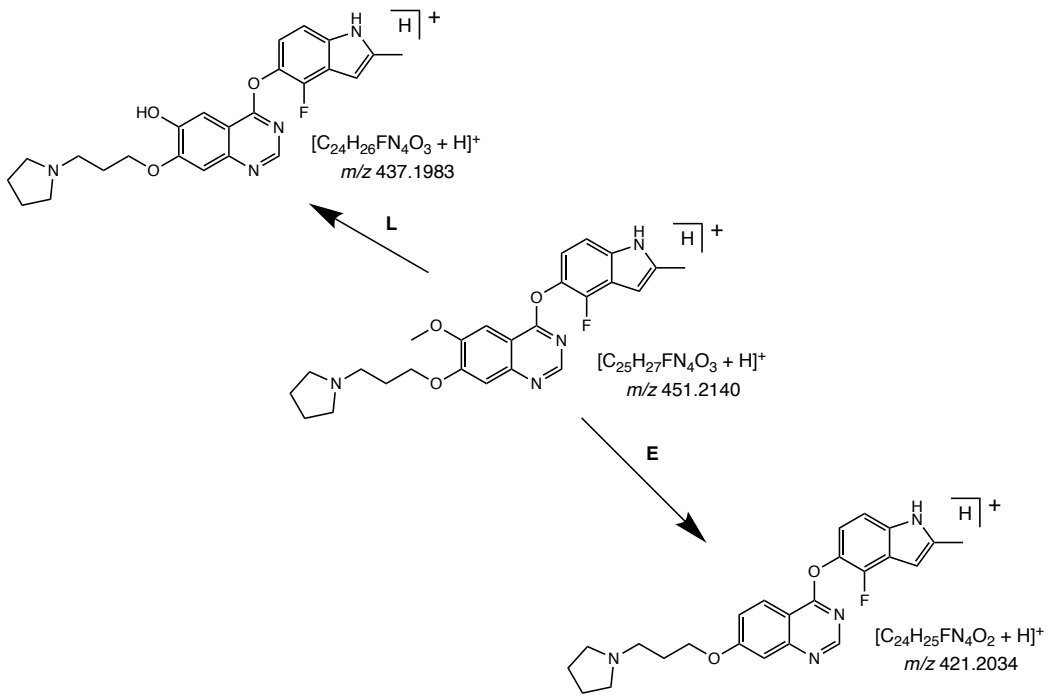

Figure 3.2.3. Fragmentation tree for formation of **L** and **E** from [cediranib + 2H]$^{2+}$ following proton-transfer to the ETD reagent radical anion forming [cediranib + H]$^{+}$.

There is evidence of a two-step process, with proton-transfer occurring followed by vibrational dissociation. This is supported by the relative peak intensities of *m/z* 338.0938 (Figure 3.2.4) and 340.1086 (Figure 3.4.5) relating to cleavage at **A** (-0.9 ppm and -1.8 ppm respectively). The CID and ECD product ion spectra for [M + 2H]$^{2+}$ cediranib both result in an approximately 3:1 relative peak intensity ratio of *m/z* 338.0938 to *m/z* 340.1086, whereas when the same precursor ion undergoes ETD, *m/z* 340.1086 is formed exclusively. If these data are compared with CID and EID of [M + H]$^{+}$ cediranib, only the product ion at *m/z* 340.0886 is observed for cleavage at **A**. This strongly suggests that proton-transfer, followed by dissociation, is taking place. Conversely, the reciprocal fragment (*m/z* 112.1121) is not formed by ETD where this ion was observed by CID of [cediranib + H]$^{+}$. It is likely that both these ions are formed by CID of

[cediranib + H]$^+$ as sites at either end of the molecule could be protonated. This would suggest that proton transfer is always taking place from the propylpyrrolidine arm, resulting in neutralisation of that moiety prior to fragmentation.

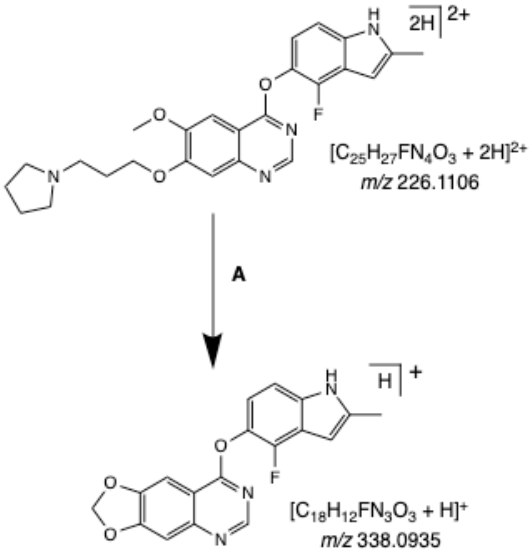

Figure 3.2.4. Proposed fragmentation tree for formation of **A** for CID of [cebiranib + 2H]$^{2+}$

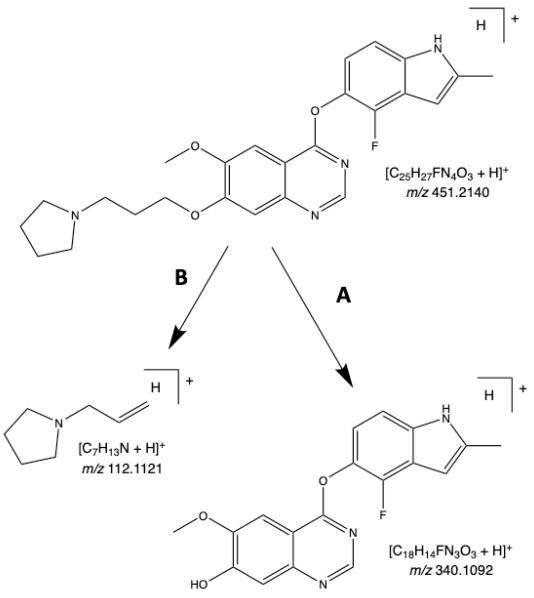

Figure 3.2.5. Proposed fragmentation tree for formation of **A** and **B** for CID of [cebiranib + H]$^+$.

3.2.1.2. ETD and CID of AZD9291

When ETD is performed on $[AZD9291 + 2H]^{2+}$ (Figure 3.2.6), the competitive nature of proton-transfer verses electron-transfer is exemplified, with an obvious mix of both occurring (Reaction 3.2.1 and 3.2.2), as can be seen by observing the charge reduced precursor species, with *m/z* 500.2767 relating to the $[AZD9291 + H]^{+}$ species (-1.4 ppm) and *m/z* 501.2846 relating to the $[AZD9291 + 2H]^{+}$ species (-0.8 ppm) (Figure 3.2.7).

$$[M + 2H]^{2+} + pNT^{-\bullet} \rightarrow [M + 2H]^{+\bullet} + pNT$$

Reaction 3.2.2. Doubly protonated species reacting with a *p*-nitrotoluene radical anion resulting in electron-transfer.

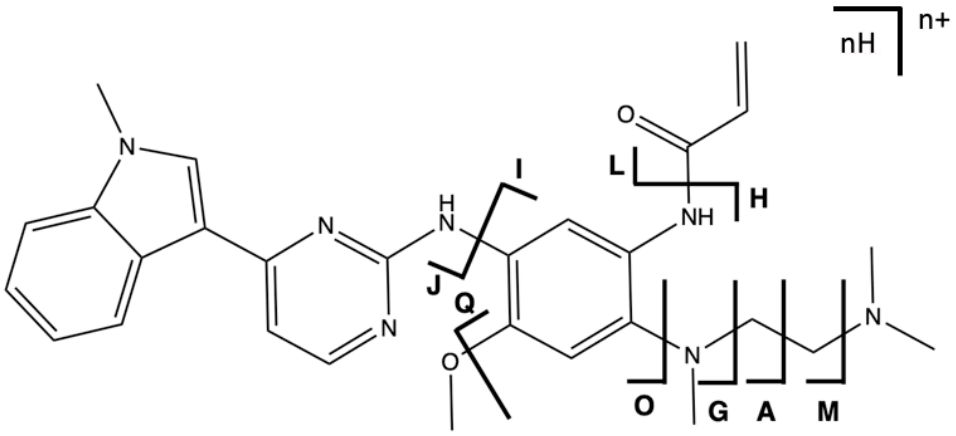

Figure 3.2.6. AZD9291 with cleavage sites relating to Figure 3.2.8.

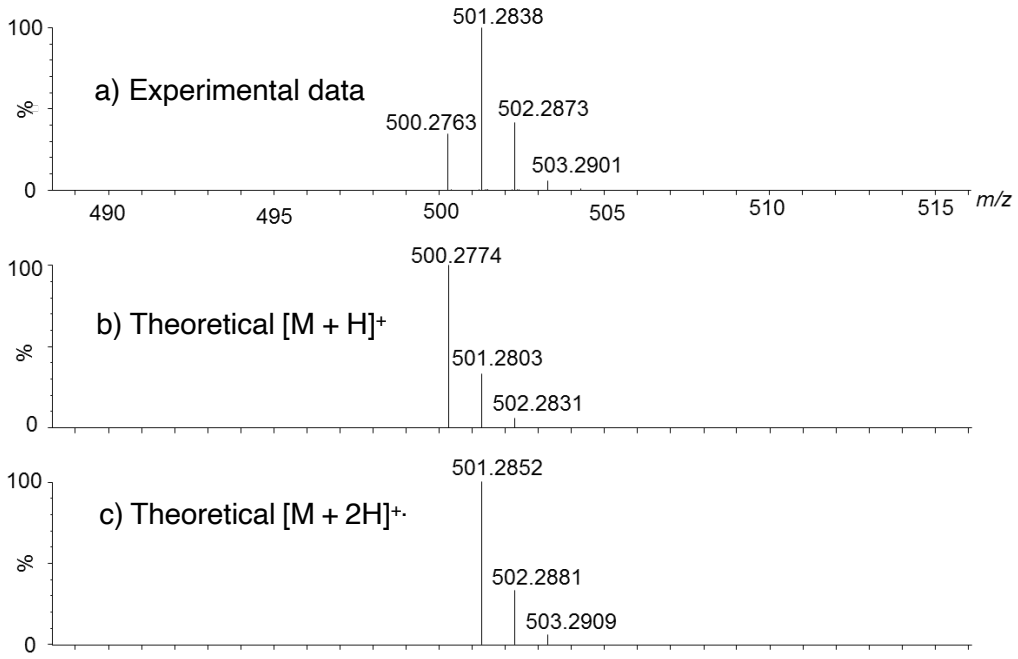

Figure 3.2.7. Model and experimental data showing the mix of electron-transfer and proton-transfer following ETD of $[AZD9291 + 2H]^{2+}$ resulting in $[AZD9291 + 2H]^{+\cdot}$ and $[AZD9291 + H]^{+}$ where a) experimental data showing the isotopic profile around the mass of singly protonated AZD9291, b) theoretical isotopic profile of $[AZD9291 + H]^{+}$ and c) theoretical isotopic profile of $[AZD9291 + 2H]^{+\cdot}$. This data confirms the presence of both $[AZD9291 + H]^{+}$ and $[AZD9291 + 2H]^{+\cdot}$, meaning both proton-transfer from $[AZD9291 + 2H]^{2+}$ to $[p\text{NT}]^{-\cdot}$ And electron-transfer from $[p\text{NT}]^{-\cdot}$ To $[AZD9291 + 2H]^{2+}$ occurs.

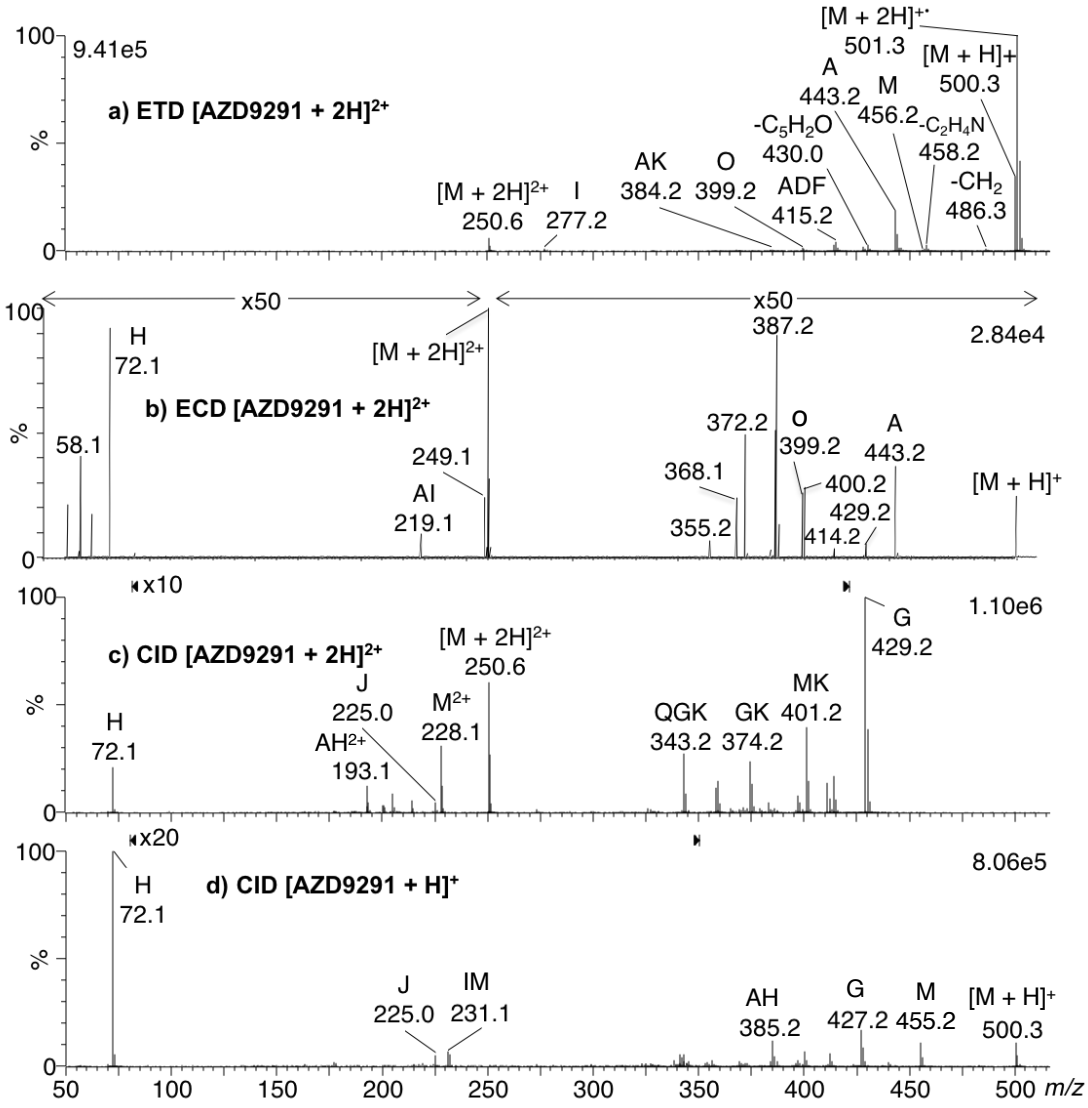

Figure 3.2.8. AZD9291 MSMS a) $[AZD9291 + 2H]^{2+}$ ETD, b) $[AZD9291 + 2H]^{+}$ ECD, c) $[AZD9291 + 2H]^{2+}$ CID and d) $[AZD9291 + H]^{+}$ CID.

ETD and CID of $[AZD9291 + 2H]^{2+}$ and CID of $[AZD9291 + H]^{+}$ form product ions unique to each technique, with all ions formed by ECD of $[AZD9291 + 2H]^{2+}$ also observed by *either* ETD or CID (Figure 3.2.8a-d). ETD resulted in loss of C_2H_2N (Figure 3.2.8a) (*m/z* 458.2481, $[C_{26}H_{30}N_6O_2]^{+}$, -0.9 ppm) and is likely the result of a complex rearrangement. The product ion relating to cleavage **I** (*m/z* 277.1798, $[C_{15}H_{23}N_3O_2]^{+}$, -0.4 ppm) was also only observed by ETD (Figure 3.2.9), whereas cleavage **J** (*m/z* 225.1131,

$[C_{13}H_{13}N_4]^+$, -4.0ppm), observed only by CID is formed by the same bond cleaving, but with the other half of the precursor ion retaining the charge showing mechanistic differences between the two techniques.

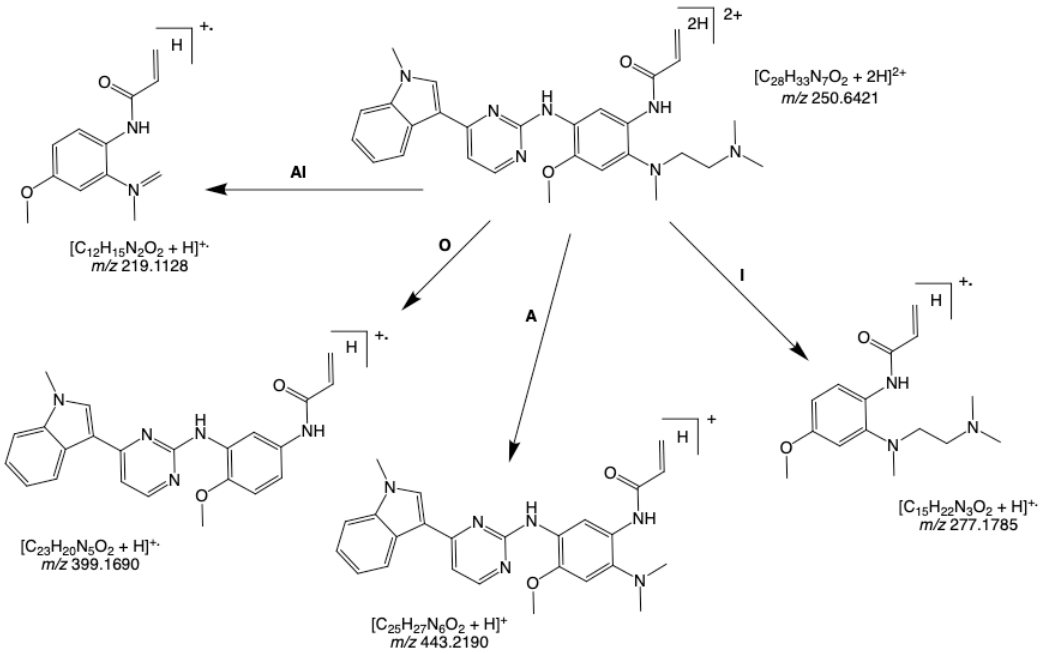

Figure 3.2.9. Proposed fragmentation tree for formation of **A, Al, O** and **I** for ETD of $[AZD9291 + 2H]^{2+}$.

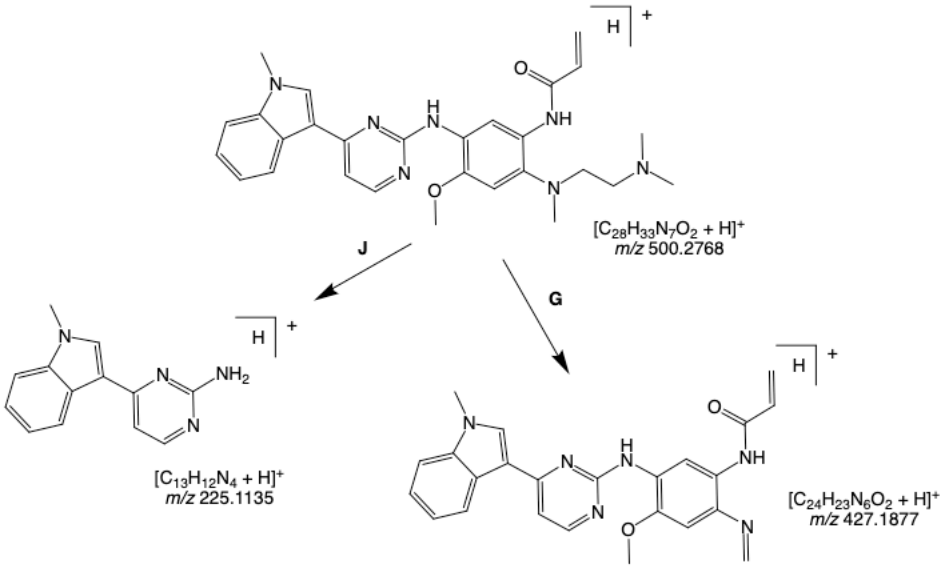

Figure 3.2.10. Proposed fragmentation tree for formation of **J** and **G** for CID of $[AZD9291 + H]^+$.

Unique to ETD and ECD was extensive cleavage along the tetramethylethane-1,2-diamine group, with cleavages **A** and **O** (*m/z* 443.2188, $[C_{25}H_{27}N_6O_2]^+$, -1.5 ppm and *m/z* 399.1699, $[C_{23}H_{21}N_5O_2]^+$, 1.0 ppm respectively), suggesting that this region of the molecule is liable to protonate (Figure 3.2.9). Heavy fragmentation in this area of the precursor ion is further supported by cleavage **AI** (*m/z* 219.1138, $[C_{12}H_{15}N_2O_2]^+$ 2.3 ppm) which is also only formed by ETD and ECD, with some secondary fragmentation taking place (Figure 3.2.9). As all three ions are only formed by ECD and ETD, it would suggest that these ions are the result of an electronic dissociation mechanism.

A peak at *m/z* 374.1777 was only observed by CID of $[AZD9291 + 2H]^{2+}$. Exact mass measurement suggests this peak corresponds to $[C_{21}H_{22}N_6O]^+$ with -2.7ppm error and is proposed to result from a complex rearrangement rather than simple bond-cleavages annotated in Figure 3.2.3. In comparison to CID of $[AZD9291 + 2H]^{2+}$, CID of $[AZD9291 + H]^+$ resulted in limited fragmentation, again highlighting the need for development of small molecule dissociation techniques. A unique product ion formed by cleavage at **G** (*m/z* 427.2142, $[C_{24}H_{23}N_6O_2]^+$, -1.2 ppm) is observed by CID of $[AZD5672 + H]^+$ (Figure 3.2.10)). Although this bond was cleaved by CID of $[M + 2H]^{2+}$, it was always combined with another bond dissociation occurring concurrently. These data demonstrate that complementary product ion spectra can be generated for a single molecule, by varying the dissociation technique used and the charge-state of the precursor ion

fragmented. Purely comparing ETD and CID of $[AZD9291 + 2H]^{2+}$, 78% of the number of product ions formed as a result of ETD were unique and had never been observed for this ion. Bond dissociation was mainly concentrated around the central benzene ring which is surrounded by heteroatoms (likely protonation sites). CID of $[AZD9291+ 2H]^{2+}$ resulted in a much richer product ion spectrum compared with CID of $[AZD9291 + H]^{+}$, which has been previously noted as being due to the doubly protonated molecule being a higher energy species. [58-60] Table 3.2.1 shows a summary of product ions useful for the characterisation of this ion, along with the techniques by which they were generated. CID and ETD both produce unique product ions, whereas those formed by ECD were also formed by ETD. ECD does however have the benefit of being a more efficient technique (due to higher electron energy, trapping times and interaction time) with respect to product ion formation when compared with ETD, but has the drawback of requiring expensive FT-ICR or orbitrap instruments for high resolution data. [95, 184]

Product ion (*m/z*)	Cleavage	CID	ECD	ETD
225.0	J	✓	×	×
427.2	G	✓	×	×
443.2	A	×	✓	✓
399.2	O	×	✓	✓
219.1	AI	×	✓	✓
458.2	$-C_2H_2N$	×	×	✓
277.2	I	×	×	✓

Table 3.2.1. Summary of AZD9291 product ions formed by different dissociation techniques.

As AZD9291 resulted in a mix of proton-transfer and electron-transfer following interaction with *p*-nitrotoluene radical anions, an experiment to determine whether instrumental parameters could be optimised to bias either reaction, was performed. For this experiment, the source settings were set to form analyte precursor ions with an absolute intensity of 5×10^4 counts per push and ETD reagent anions with an absolute intensity of 1×10^6 counts per push. Trap wave height was optimised as this parameter controls how closely the analyte cation and the ETD reagent anion are squeezed together in the trap region of the TriWave, and was tested over the range of 0.5 V to 0.1 V (Table 3.2.2), with the maximised efficiency seen at 0.2 V. The size of the analyte cations is proportional to the wave height, therefore the wave height optimised for small molecules (0.2 V) is smaller than that generally used for larger peptides (0.4 V). Although the intensity of product ions were altered, the difference in proton-transfer and electron-transfer was negligible. The trap gas flow rate (used for collisional cooling of ions) was also investigated over the range of 10 mL/min to 40 mL/min. Although this did not greatly change the ratio of electron-transfer to proton-transfer reactions occurring, product ions thought to be a result of vibrational dissociation were reduced in abundance at lower flow rates. This is to be expected as if more gas is present in the trap, the ions have more chance of a collision, therefore being more likely to result in vibrational dissociation. Modifications to the wave velocity setting, which controls the speed of the traveling wave through the TriWave and therefore the ion/ion reaction time was tested at different velocities. However

changing from 300 ms was not seen to have significant effect on the product ion spectra.

		$[AZD9291 + H]^+$ Intensity	**$[AZD9291+ 2H]^{+\cdot}$ Intensity**	**Ratio ET to PT**
Trap Wave Height (V)	0.1	1.70E+05	5.52E+05	3.2
	0.2	**2.74E+05**	**8.92E+05**	**3.3**
	0.3	4.23E+05	1.31E+06	3.2
	0.5	2.76E+05	7.48E+05	2.7
Trap Wave Velocity (ms)	**200**	**2.96E+05**	**1.06E+06**	**3.6**
	300	**2.98E+05**	**1.06E+06**	**3.6**
	400	2.12E+05	7.41E+05	3.5
	500	1.49E+05	4.98E+05	3.3
Trap gas flow rate (mL/min)	10	3.58E+05	9.98E+05	2.8
	20	2.88E+05	1.01E+06	3.5
	30	**1.89E+05**	**6.72E+05**	**3.6**
	40	9.53E+04	3.20E+05	3.4

Table 3.2.2. ETD parameters with resulting peak intensities for $[AZD9291 + H]^+$ and $[AZD9291 + 2H]^{+\cdot}$ ET = electron transfer, PT = proton transfer with the numbers in bold showing optimum parameters.

The parameters which gave the most efficient ETD for AZD9291, and therefore used for all future ETD on small molecules were a trap wave height of 0.2 V, a trap wave velocity of 300 ms and a trap gas flow rate of 30 mL/min.

3.2.1.3. ETD and CID of AZD5672

$[AZD5672 + 2H]^{2+}$ (Figure 3.2.11) was formed by chemical supercharging ESI (See Chapter 3.3). Interaction with the *p*-nitrotoluene anion resulted in proton-transfer occurring (Reaction 3.2.1). As with ETD of $[cediranib + 2H]^{2+}$, ETD of $[AZD5672 + 2H]^{2+}$ (Figure 3.2.12a) resulted in limited cleavages.

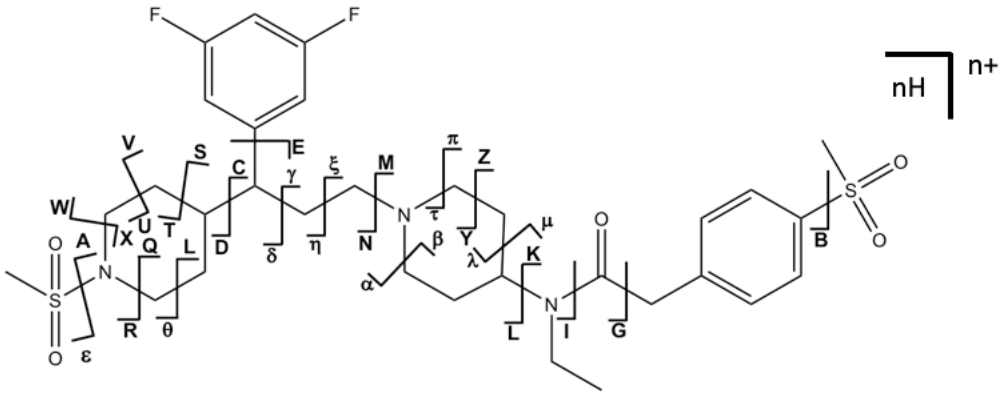

Figure 3.2.11. AZD5672 with cleavage sites relating to Figure 3.2.8.

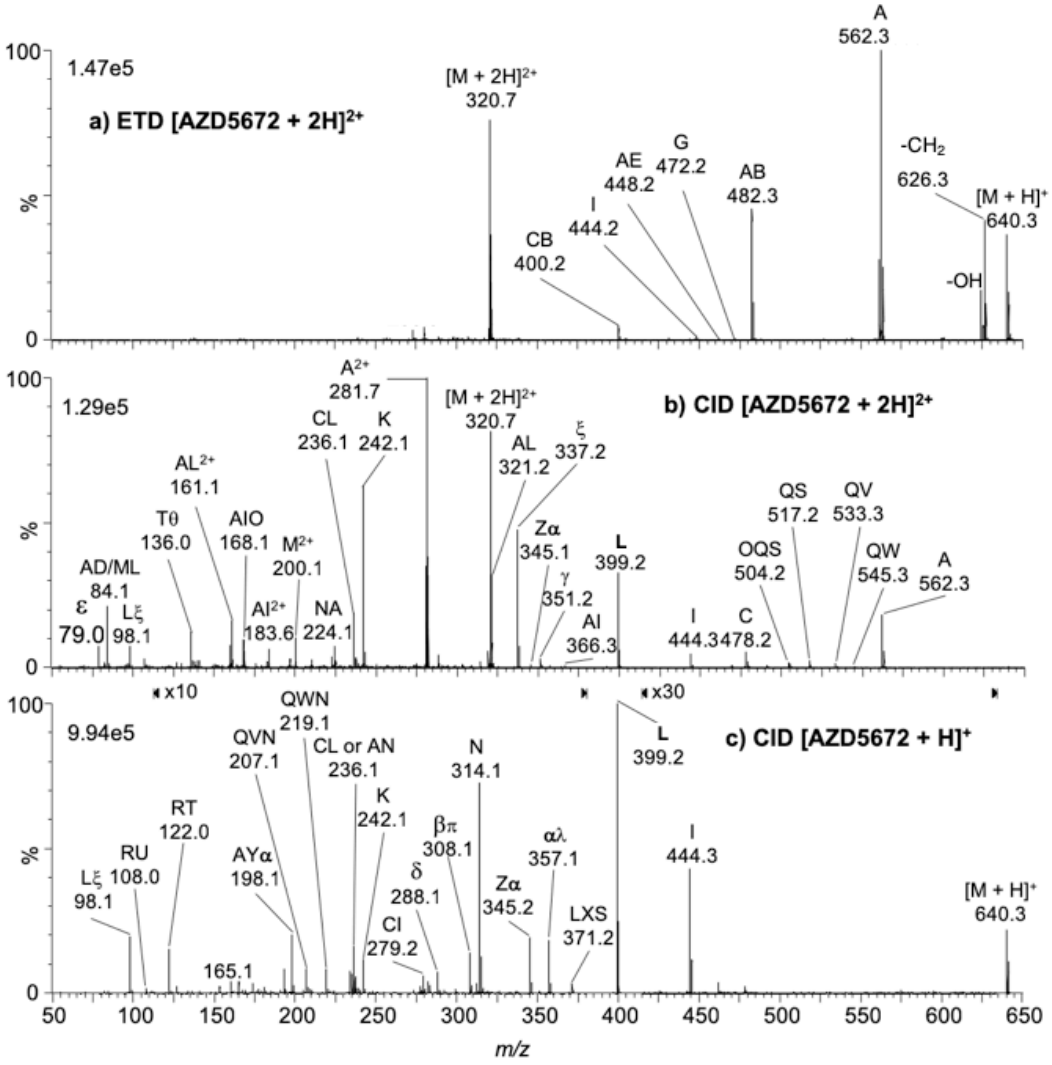

Figure 3.2.12. AZD5672 MSMS for a) $[M + 2H]^{2+}$ ETD, b) $[M + 2H]^{2+}$ CID and c) $[M + H]^{+}$ CID showing limited bond cleavage by ETD, with many more product ions being formed by CID.

A small neutral loss of $-CH_2$ was observed resulting in *m/z* 626.2531 ($[C_{30}H_{42}N_3O_5F_2S_2]^+$, 0.5 ppm) as was the loss of -OH at *m/z* 624.2731 ($[C_{31}H_{44}N_3O_4F_2S_2]^+$, 0.5 ppm). Although these product ions are unique to ETD, they are of limited use for characterisation purposes. Cleavage **AB** (Figure 3.2.13), the loss of both hydrosulfonylmethane groups, was also only observed by ETD (*m/z* 482.2974, $[C_{29}H_{38}N_3OF_2]^+$, -1.9 ppm). This is interesting as although cleavage **A** might be expected being close to a

possible protonation site, **B** seems less likely. Cleavage **A** or **B** occurs concurrently to cleavage **E** (Figure 3.2.13), the loss of the difluorobenzene ring (*m/z* 448.2619, $[C_{24}H_{38}N_3O_3S]^+$, -1.8 ppm). The only other unique ion produced by ETD was *m/z* 472.2444 relating to cleavage at **G** ($[C_{23}H_{36}N_3O_3F_2S]^+$, 0.6 ppm). CID of $[M + 2H]^{2+}$ resulted in many more product ions compared with ETD, with cleavages observed across the entire ion. The generation of this product ion spectrum is also novel, as this is the first time $[AZD5672 + 2H]^{2+}$ has been formed. For this ion, the data shows that for the most complete characterisation of AZD5672, CID of $[M + 2H]^{2+}$ should be performed. While proton-transfer is the dominating reaction, product ion spectra produced by ETD may be of limited use.

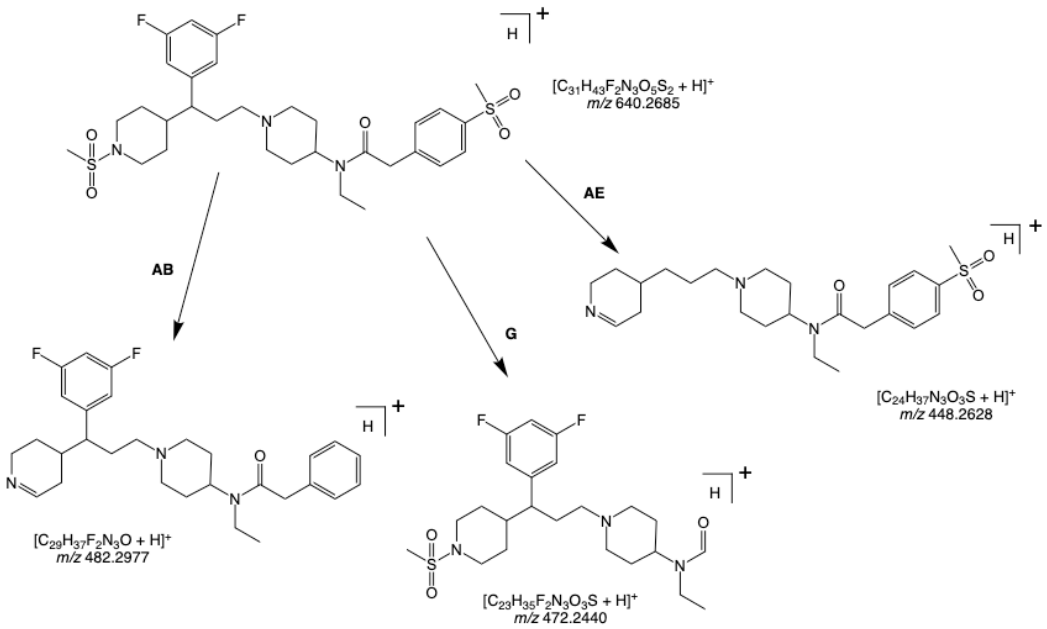

Figure 3.2.13. Fragmentation tree for formation of **G**, **AB** and **AE** from $[AZD5672 + 2H]^{2+}$ following proton-transfer to the ETD reagent radical anion forming $[AZD5672 + H]^+$.

3.2.1.4. ETD and CID of [1,1'-Biphenyl]-3,3',4,4'-tetramine

The interaction of [3,3-diaminobenzidine + 2H]$^{2+}$ (Figure 3.2.14) with *p*-nitrotoluene resulted in proton-transfer (Reaction 3.2.1, Figure 3.2.15).

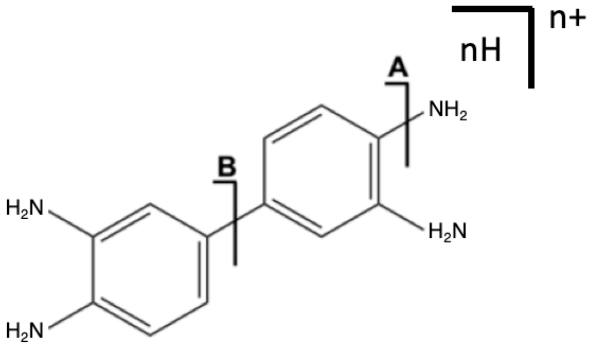

Figure 3.2.14. [1,1'-Biphenyl]-3,3',4,4'-tetramine (3,3-diaminobenzidine, DAB) with cleavage sites relating to Figure 3.2.15.

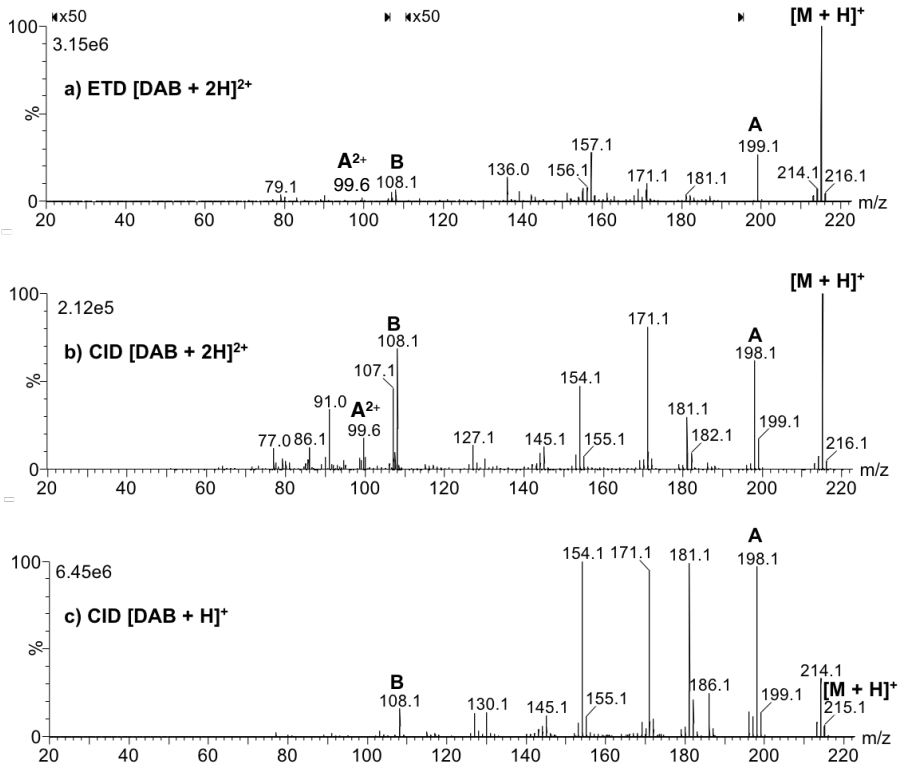

Figure 3.2.15. 1,3-diaminobenzidine MSMS a) $[M + 2H]^{2+}$ ETD, b) $[M + 2H]^{2+}$ CID and c) $[M + H]^{+}$ CID. Product ions in the ETD spectrum that appear 1 Da heavier than their counter-parts in the CID spectra are an artefact of the ETD process, where the addition of H· is observed.

The main product ions observed by ETD are very similar to those formed by CID of both [1,3-diaminobenzidine + $2H]^{2+}$ and [1,3-diaminobenzidine + $H]^{+}$. This is the same relationship observed for other analytes whose doubly protonated molecules underwent proton-transfer following interaction with *p*-nitrotoluene. Loss of NH_2· (*m/z* 199.1097, $[C_{12}H_{13}N_3]^{+\cdot}$, 1.5 ppm) is observed by ETD, whereas CID results in loss of NH_3 (*m/z* 198.1016, $[C_{12}H_{12}N_2]^{+}$, 1.0 ppm). There is a mechanistic difference here between CID and ETD, showing that a non-vibrational mechanism is occurring following the proton-transfer ETD process. Cleavage at **B** (Figure 3.2.16, *m/z*

108.0607, $[C_6H_8N_2]^+$, 5.6 ppm) is observed, however the mass accuracy of this product ion is larger than for others due to the proximity of another product ion which has less than 0.01 Da mass difference. These two peaks are not isotopically resolved, so when using Waters' MassLynx data processing tools to generate accurate mass, centroided data from the continuum data was recorded, the centring of the data is non-optimal, resulting in poor accurate mass.

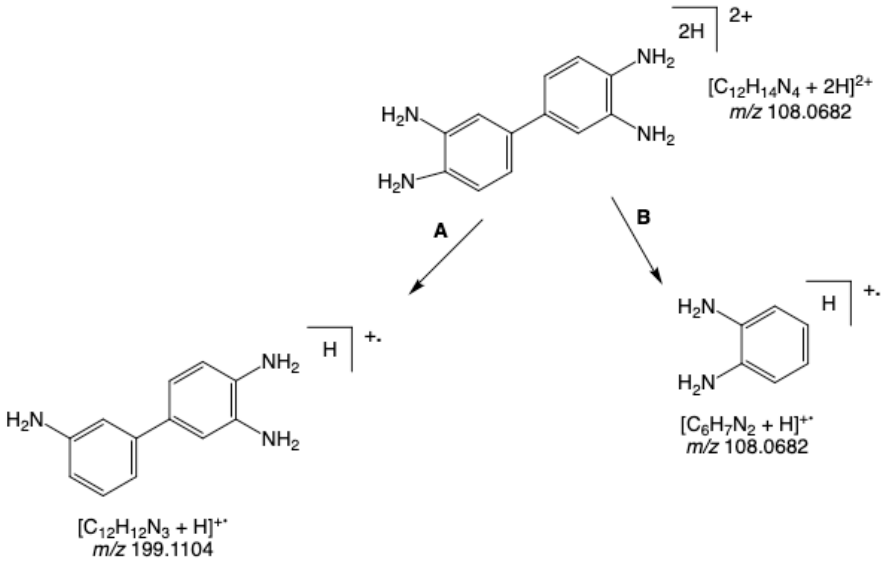

Figure 3.2.16. Proposed fragmentation tree for formation of **A** and **B** for ETD of [DAB + 2H]$^{2+}$.

The lack of *m/z* 154.0709 ($[C_{11}H_8N]^+$, -0.6ppm) in the ETD tandem mass spectrum, which is observed in both CID spectra is interesting, and again shows mechanistic differences. Instead, *m/z* 157.1003 ($[C_{12}H_{13}]^+$, -1.3 ppm) is observed by ETD, but not by CID. The difference here is a rearrangement of one of the benzene rings to include a nitrogen with CID, whereas with ETD, a bipyridyl structure is formed as shown in Figure 3.2.17. This could be further evidence for an electronic type mechanism,

where vibrational mechanisms occur on a relatively slow time scale allowing for rearrangement of the benzene ring to include a nitrogen. An electronic mechanism happens on a much faster timescale, perhaps not allowing for this rearrangement, and therefore resulting in the bipyridyl ring; a stable carbocation at *m/z* 157.1003. [185-187]

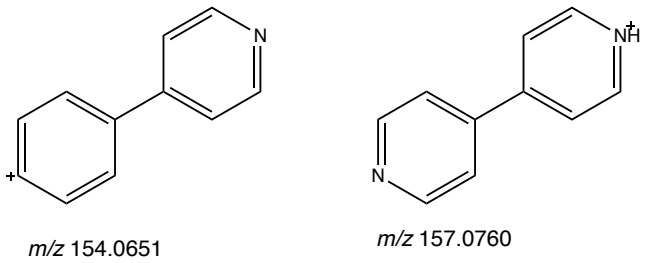

m/z 154.0651 *m/z* 157.0760

Figure 3.2.17. Proposed structures of product ions at *m/z* 154.0709 and *m/z* 157.1003.

3.2.1.5. ETD and CID of chloroquine

ETD of [chloroquine + 2H]$^{2+}$ (Figure 3.2.18) was successfully performed. (Figure 3.2.19a).

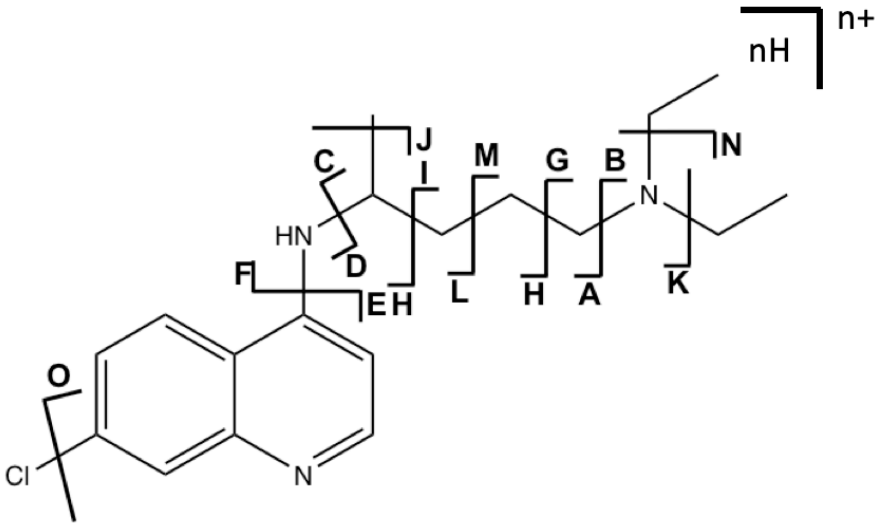

Figure 3.2.18. Chloroquine with cleavage sites relating to Figure 3.2.14.

Following interaction with the *p*-nitrotoluene radical anion, proton-transfer was seen to exclusively occur (Reaction 3.2.1).

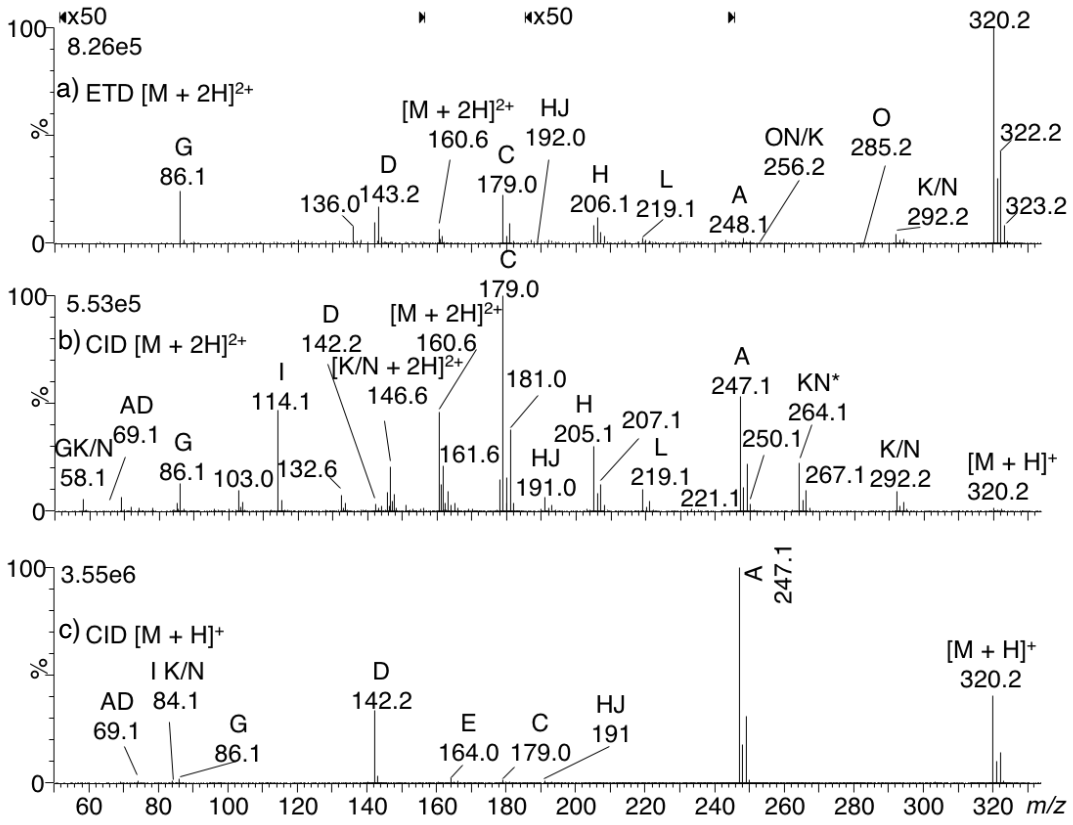

Figure 3.2.19. Chloroquine MSMS for a) $[M + 2H]^{2+}$ ETD, b) $[M + 2H]^{2+}$ CID and c) $[M + H]^{+}$ CID. Product ions in the ETD spectrum that appear 1 Da heavier than their counter-parts in the CID spectra are an artefact of the ETD process, where the addition of H· is observed.

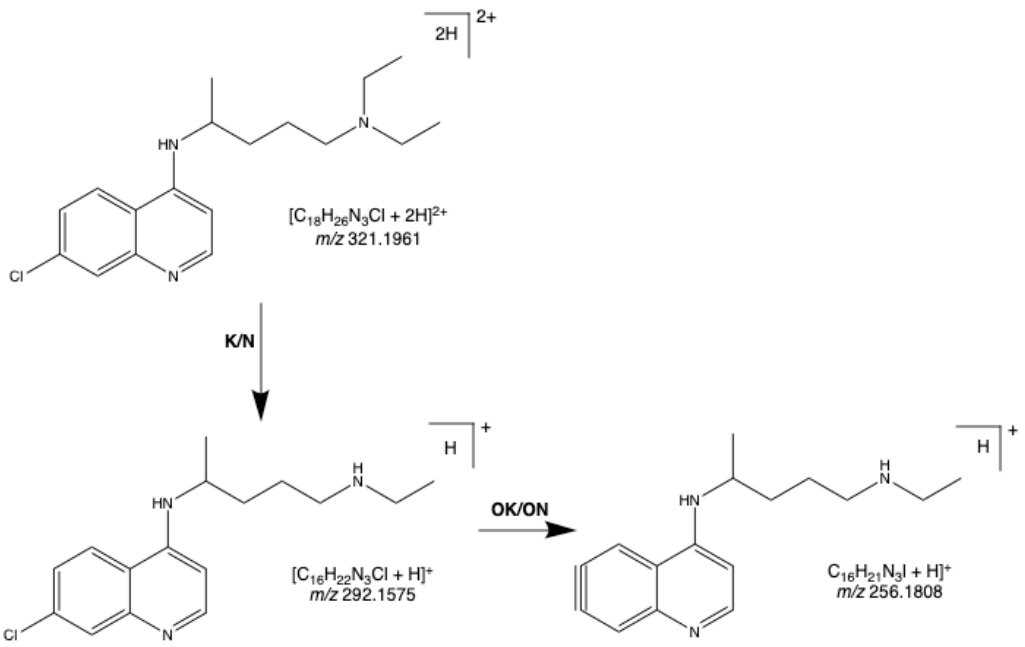

Figure 3.2.20. Proposed fragmentation tree for formation of **K/N** and **OK/ON** for ETD of $[DAB + 2H]^{2+}$.

ETD of [chloroquine + 2H]$^{2+}$ formed two unique product ions, both relating to loss of the chlorine atom, cleavage **O** (*m/z* 285.2238, $[C_{18}H_{27}N_3]^+$, 11.6 ppm error) and **OK** or **ON** (*m/z* 256.1756, $[C_{16}H_{22}N_3]^+$, -22.6 ppm error) which may be charge remote fragmentation. (Figure 3.2.20) [95] This is interesting, as chlorine has a delta negative charge due to the electrons in its outer shell. This is an important observation, as it suggests that the inclusion of a halogen in the precursor ion could play a role in retarding the electron-transfer process and making it more energetically likely to lose one of the protons from the doubly protonated molecule. This is supported by the fact that both cediranib and AZD5672 both underwent proton-transfer, with both containing a halogen, whereas AZD9291, which does not contain a halogen underwent electron-transfer. Another possible train of thought is the electronegative halogen attracts one of the protons on the

doubly protonated molecule, and then cleaves from the ion as HCl but a larger sample of molecules would be required to follow this further. CID of [chloroquine + 2H]$^{2+}$ (Figure 3.2.19b) formed significantly more product ions compared with CID of [chloroquine + H]$^{+}$ (Figure 3.2.19c) with the majority of bonds across the ion being fragmented.

3.2.2. Conclusions

For the first time, ETD has been performed on small doubly protonated molecules. Like ETD of peptides, a competitive reaction of proton-transfer and electron-transfer was observed, with anecdotal evidence of interaction with heteroatoms influencing the result. No fragmentation was observed when ETD was performed on $[M + H]^+$, most likely due to the lack of a fast electron to cause secondary ionisation, as postulated in EID. ETD is known to be affected by the charge density of the precursor ion (*i.e.* the number of charges per ion), and in peptides, ETD of $[M + 3H]^{3+}$ and $[M + 4H]^{4+}$ have been shown to be more efficient than $[M + 2H]^{2+}$ in terms of the relative abundance of product ions compared with the relative abundance of the precursor ion. [92-94] This is an important observation, as even though all precursor ions studied here only formed $[M + 2H]^{2+}$, observable and diagnostic product ions were formed.

When electron-transfer occurs, many unique product ions are formed. If proton-transfer occurs, the resulting product ion spectra are largely comparable to those produced by CID. Overall, these data show that for small doubly protonated molecules, complementary product ion spectra can be generated by using CID and ETD, which can aid structural elucidation, particularly for molecules where breaking a ring provides the key piece of information. These unique peaks are likely formed by electronic dissociation. However, with the resolution available on the Synapt G2-S, the isotopic profile of $[M + H]^+$ prevents a confident confirmation. This could be determined by further study using a FT-ICR

instrument with 1 x 10^6 resolving power. By using ETD alone, product ions formed as a result of probable electronic and vibrational dissociation mechanisms can be formed, technically making this is a more useful technique. However, the low abundance of many product ions observed by ETD make CID more practical. Previous theories about the competitive nature of proton-transfer and electron-transfer as discussed in the introduction have been supported. [93, 96, 98, 100, 188] These data show that instrument parameters have a limited effect on this competition, and that the physiochemical properties, such as electron and proton affinities and Franck-Condon factors of the analyte ions, are the driving factor. In proteins and peptides, the ideal characteristics for the reagent anion would be a low electron affinity, and Franck-Condon factors between the anion and the equivalent neutral not being too low. [97] The reagent used in this study was *p*-nitrotoluene which has been shown to meet these criteria, leading the most likely explanation of the observed cases of proton-transfer occurring in favour of electron-transfer, being due to the low charge density of the precursor ions, or analyte specific (*e.g.* halogen content) differences.

3.3. Supercharging small organic molecules

Chemical supercharging has been previously studied for the analysis of proteins and polymers. It has been shown that the addition of supercharging reagents (SCRs) to an ESI solution can bias the charge-state distribution toward higher charge-states. [120] When studying MSMS of small organic ions, it has been shown that diagnostically relevant information can be generated by fragmenting both $[M + H]^+$ *and* $[M + 2H]^{2+}$, with efficiency and increased pathways being linked to charge. [104, 127, 189] In this chapter, a range of SCRs have been tested for the study of small organic ions. Section 3.3.1.3.-3.3.1.9. shows a selection of the data collected, along with observations of note. Section 3.3.1.10. summarises the data, in order to make the discussion in Section 3.3.1.11. more accessible.

3.3.1. Results and discussion

3.3.1.1. Addition of SCRs to ESI solution

The instrument was set-up as shown in Figure 3.3.1, with analyte and SCR being introduced into the ion source *via* a dual syringe pump connected to a T-piece.

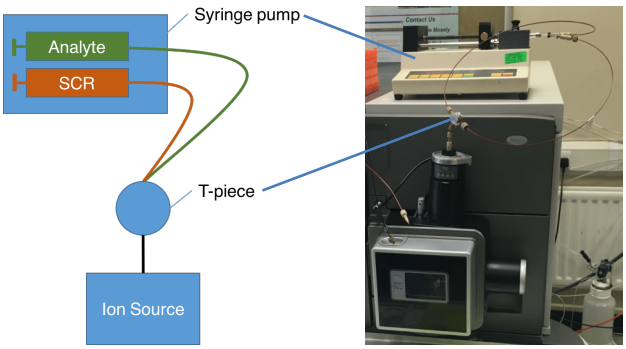

Figure 3.3.1. Inlet configuration for SCR experiments where analyte and SCR are introduced into the source at the same time using a dual syringe pump connected to a T-piece which flows directly into the ESI needle.

Table 3.3.1 show the 7 small molecules of pharmaceutical interest chosen for study. The SCRs studied were informed by previous work performed on peptides, proteins and polymers with the range of concentrations tested for each SCR are shown in Table 3.3.2. The analytes concentration was 1 μg/mL made up in 0.1% formic acid in 50:50 water : acetonitrile. As two syringes are flowing, a 50% dilution in the T-piece takes place resulting in an analyte concentration of 0.5 μg/mL. Data were collected for 1 minute with a scan rate of 1 scan per second.

Compound	Structure	Monoisotopic Mass (Da)
Cediranib	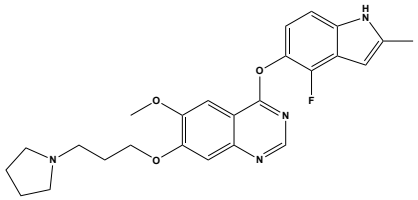	450.2067
AZD9291	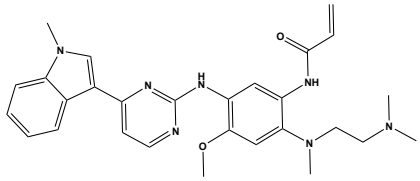	499.2696
AZD5672	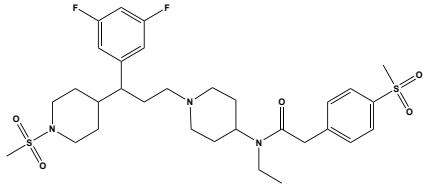	639.2612
Fostamatanib	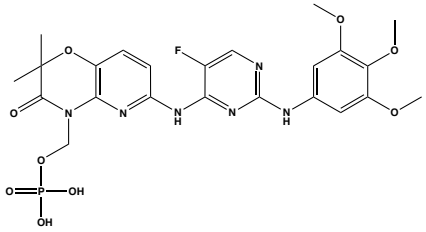	580.1483
AZD2171 BQ **Indole**	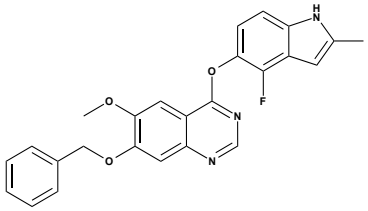	429.1489
AZD5672 **Bisamide**	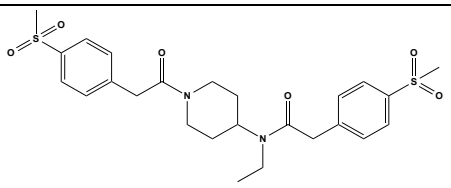	520.1707
AZD5672 **Precursor**	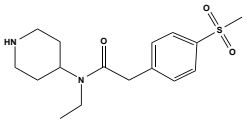	324.1508

Table 3.3.1. Analyte molecules chosen for study.

Compound	Structure	Monoisotopic Mass (Da)	Concentration (μg/mL)	Acidity at 25°C (p*K*a)	Density (g cm^{-3})	Boiling Point (°C at 760 mmHg)	Surface Tension of pure liquid (dyne cm^{-1})
(3-nitrophenyl)methanol (m-nitrobenzyl alcohol, *m*NBA) [120, 190]	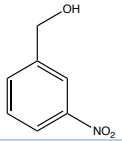	153.0426	0 – 19.5 μg/mL	13.61 [179]	1.3 [191]	402.2-409.5 [191]	57.0 ± 3.0 [192]
2-(3-nitrophenyl)ethan-1-ol (*m*NPEA) [139]	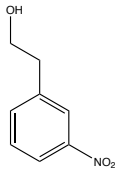	167.0582	0 – 10.4 μg/mL	14.47 [178]	1.3 [192]	281.3 ± 23.0 [192]	51.6 ± 3.0 [192]
3-nitrobenzonitrile (*m*NBN) [139]	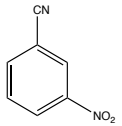	148.0273	0 – 3.9 μg/mL	-	1.3 [192]	311.0 [191]	58.2 ± 5.0 [192]
Tetrahydrothiphene 1,1-dioxide (Sulfolane) [139]	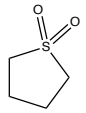	120.0245	0 – 40 μg/mL	12.9 [193]	1.3 [191]	285.0 [191]	35.6 ± 3.0 [192]
Thiophen-2(*5H*)-one (Thiophenone) [143]	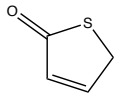	99.9983	0 – 10 μg/mL	-	1.4 [192]	322.5 ± 15.0 [192]	67.6 ± 5.0 [192]
Hydroxymethyl-1,3-dioxolan-2-one (Glycerol-1,3-carbonate) [143]	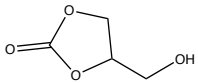	118.0266	0 – 2 μg/mL	14.57 [178]	1.4 [192]	353.9 ± 15.0 [192]	44.2 ± 3.0 [192]
(methylsulfinyl)methane (Dimethyl sulfoxide, DMSO) [132]		78.0139	0 – 60.5 μg/mL	-	1.1 [191]	189.0 [191]	43.7 ± 3.0 [192]

Table 3.3.2. SCRs tested and their relevant physiochemical properties.

3.3.1.2 Optimising ion source settings for $[M + 2H]^{2+}$

Ion source settings were optimised on an analyte-to-analyte basis. An example of how optimisation was performed using AZD5672 and sulfolane (1 μL/mL) is shown in Figure 3.3.2. The ratio of absolute intensity of $[M + 2H]^{2+}$: $[M + H]^{+}$ was compared when source parameters were set to different values (shown on the x-axis as n : 1). The source parameters plotted represent the extremes manufacture recommended settings.

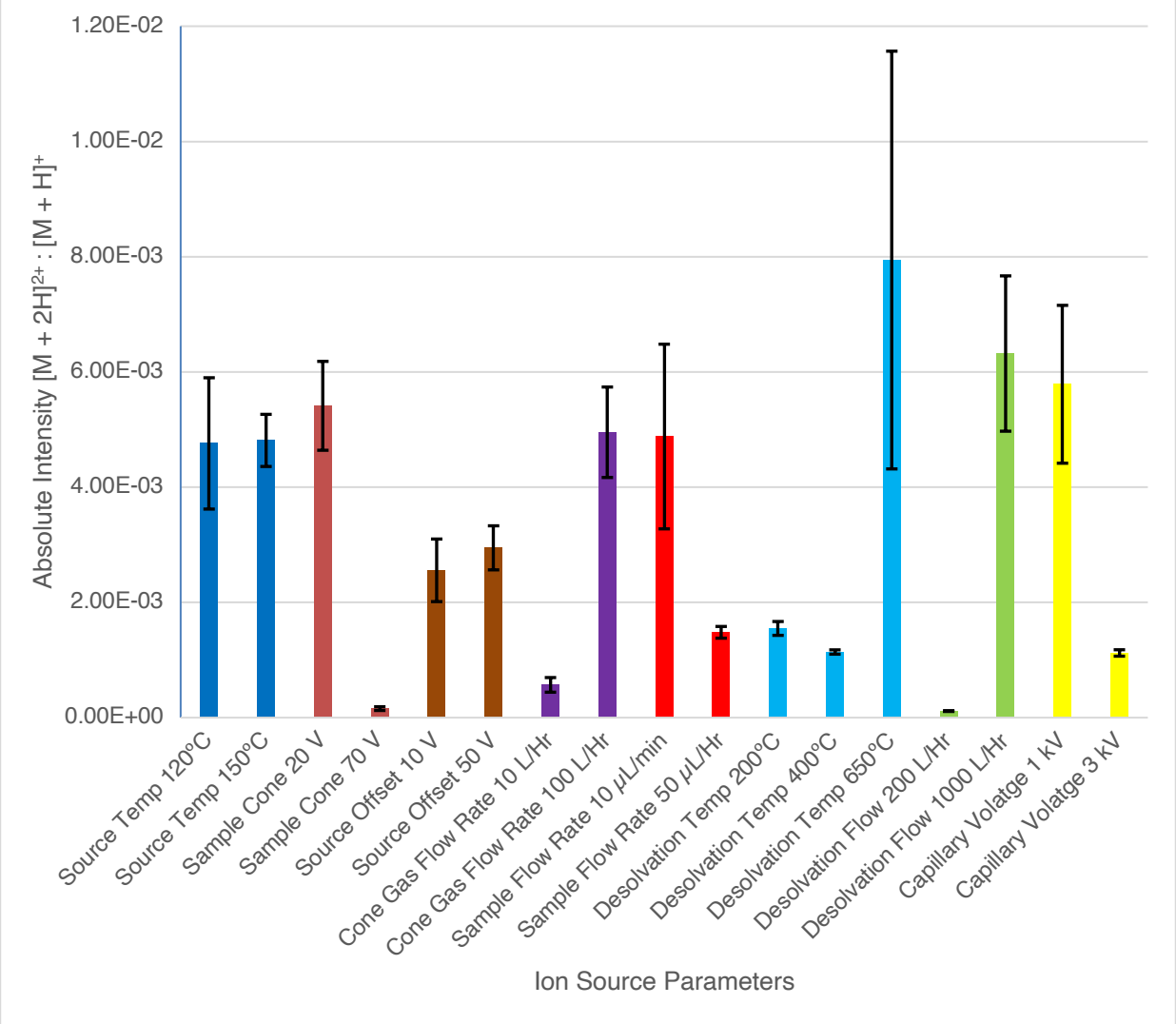

Figure 3.3.2. Effect of individual source parameters on the ratio of absolute intensity of $[M + 2H]^{2+}$: $[M + H]^{+}$ for AZD5672. Error bars were calculated from the standard deviation of 3 repeat measurements.

When comparing the different settings for each parameter, source temperature and source offset voltage showed little effect on the relative formation of $[M + 2H]^{2+}$. At the higher sample cone and capillary voltages it is likely that in-source fragmentation causes charge reduction from $[M + 2H]^{2+}$ to $[M + H]^{+}$, leading to a lower ratio of $[M + 2H]^{2+}$: $[M + H]^{+}$. Although the lower sample flow rate was shown to give a higher ratio of $[M + 2H]^{2+}$: $[M + H]^{+}$, a stable spray could not always be achieved with a stable flow rate of 10 μL/min so this was set at the lowest setting where a stable spray was consistently generated (20 μL/min). All analogous experiments were performed with a range of supercharging reagents (Table 3.3.2) and with seven analytes (Table 3.3.1). Parameters which were optimal for the different analytes, regardless of SCR are given in Table 3.3.3. Although similar results were observed for all analytes tested with all SCRs, desolvation temperature, flow rate, and capillary voltage were seen to have different affects for each analyte. Different SCRs had no affect and this likely has more to do with the affinity of each molecule to doubly protonate. Table 3.3.4 shows the optimised source parameters used for the four analytes observed as $[M + 2H]^{2+}$.

Source Parameter	Setting
Source Temperature (°C)	150
Sample Cone Voltage (V)	20
Source Offset Voltage (V)	10
Cone Gas Flow Rate (L/Hr)	100
Sample Flow Rate (μL/min)	20

Table 3.3.3. Optimum global ion source parameters to promote $[M + 2H]^{2+}$ formation.

Source Parameter	Cediranib	AZD9291	AZD5672	Fostamatanib
Desolvation gas temperature (°C)	200	650	650	200
Desolvation gas flow (L/hr)	300	600	600	250
Capillary voltage (kV)	1	2	2	1

Table 3.3.4. Analyte specific optimum ion source parameters to promote $[M + 2H]^{2+}$ formation.

A comparison of desolvation gas temperature settings for AZD5672 is shown in Figure 3.3.3 to confirm precursor ions are not adversely affected by factors such as thermal decomposition. The spectra show that the higher desolvation temperature had an enhancing effect on the ionisation of all ions formed. A small increase in the level of dissociation is noted by observing *m/z* 399.2053 ($[C_{20}H_{29}N_2O_2F_2S]^+$, -1.8 ppm), a product ion only observed by CID of $[AZD5672 + 2H]^{2+}$ of AZD5672 (See Section 3.2.1.3). The increase in the formation of $[M + 2H]^{2+}$ (875%, Figure 3.3.2) at the higher desolvation temperature is more than the increase in formation of $[M + H]^+$ (66%). It is possible that the increase in formation of $[M + H]^+$ is in part the result of charge stripping of $[M + 2H]^{2+}$. No adverse effects, other than a small increase in dissociation, were observed by the use of a higher desolvation temperature setting.

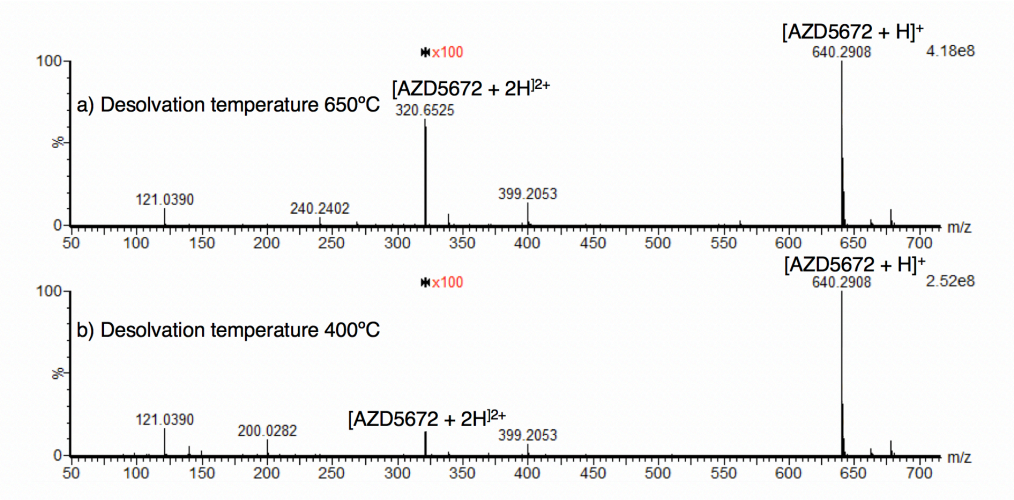

Figure 3.3.3. Stacked spectra of AZD5672 with 1.3 μg/mL sulfolane with desolvation temperature set to a) 650°C and b) 400°C.

3.3.1.3. (3-nitrophenyl)methanol as a SCR

The addition of (3-nitrophenyl)methanol (commonly known as m-nitrobenzyl alcohol, *m*NBA) to the ESI solution, resulted in the formation of $[M + 2H]^{2+}$ for cediranib, AZD9291 and AZD5672 only, from the seven compounds tested. ESI of cediranib and AZD9291 form $[M + 2H]^{2+}$ without any SCR, but a change in the ratio of absolute intensity of $[M + 2H]^{2+}$ to $[M + H]^{+}$ was observed (Figures 3.3.4 and 3.3.5). Figure 3.3.4 shows the relationship between the concentration of *m*NBA and the ratio of relative intensity of $[M + 2H]^{2+}$ to $[M + H]^{+}$ for cediranib. The errors were calculated based on the standard deviation between three measurements.

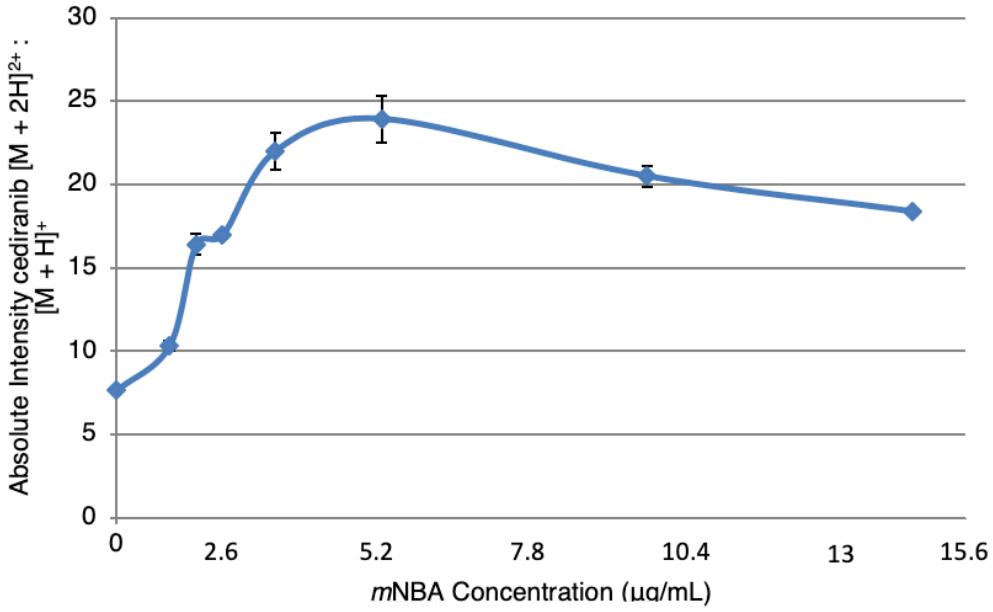

Figure 3.3.4. Effect of *m*NBA concentration on relative ion intensity ratio of $[M + 2H]^{2+}$ **:** $[M + H]^{+}$ for cediranib plotted for three repeated measurements.

Initially, when a low concentration of *m*NBA was added to the ESI solution, more $[M + 2H]^{2+}$ cebiranib was formed compared with $[M + H]^{+}$. The concentration that produced the highest ratio of $[M + 2H]^{2+}$ **:** $[M + H]^{+}$ is 5 µL/mL. When a greater concentration than 5 µL/mL was used the ratio slowly reduced, which is shown to be due to ion suppression of the analyte species by $[m\text{NBA} + H]^{+}$ (Figure 3.3.6).

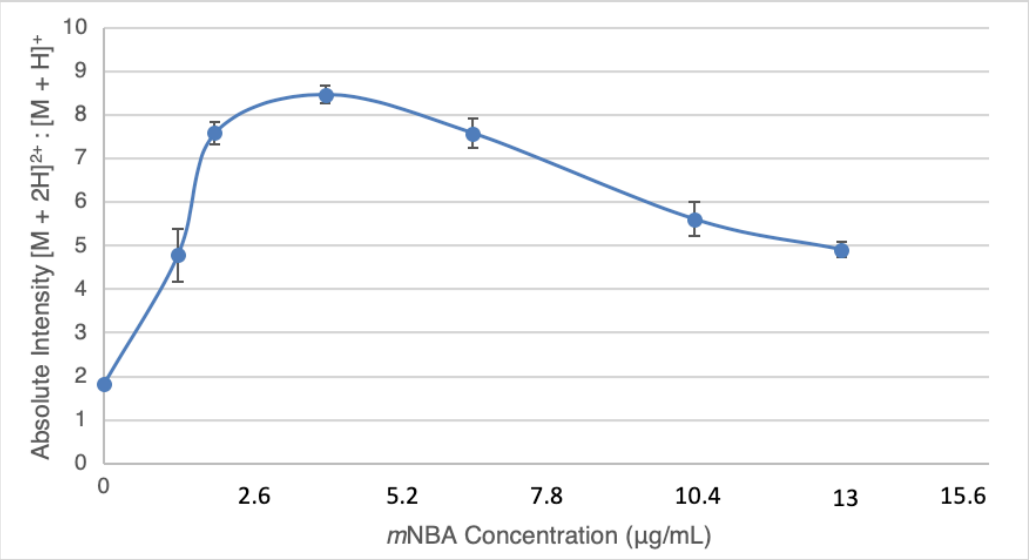

Figure 3.3.5. Effect of *m*NBA concentration on relative ion intensity ratio of $[M + 2H]^{2+}$ **:** $[M + H]^{+}$ for AZD9291.

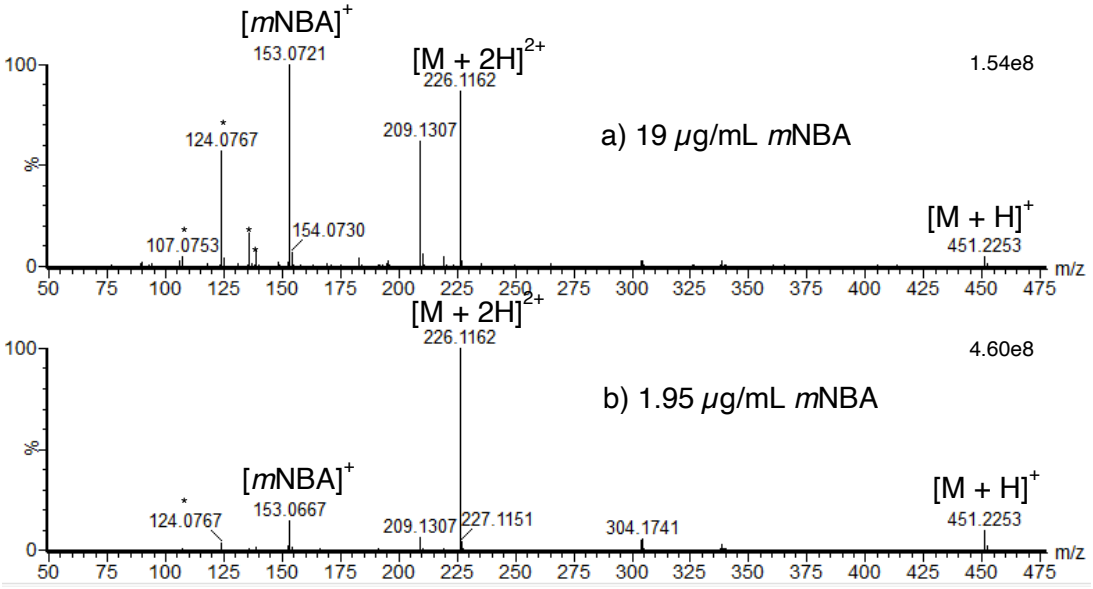

Figure 3.3.6. Comparison of cediranib spectra averaged for one minute with a) 19 µg/mL and b) 1.95 µg/mL *m*NBA. *Denotes likely impurities in the *m*NBA solution. Mass accuracy of $[m\text{NBA}]^{+}$ is poor in a) due to ion saturation.

The ratio of $[M + 2H]^{2+}$ **:** $[M + H]^{+}$ AZD9291 with changing concentration of *m*NBA is shown in Figure 3.3.5. AZD9291 is normally observed as $[M + 2H]^{2+}$ and $[M + H]^{+}$, yet the ratio of double to singly charged ion abundance

can be seen to change as a function of SCR concentration. The same relationship observed for cediranib is clear here for AZD9291, with $[M + 2H]^{2+}$: $[M + H]^{+}$ increasing with the initial addition of *m*NBA, reaching the maximum ratio of 8.5 at 3.9 µg/mL *m*NBA then decreasing.

AZD5672 is usually only observed as $[M + H]^{+}$, although by optimising ion source parameters a low abundance $[M + 2H]^{2+}$ was formed. This required desolvation temperature and flow rate to be set much higher than standard source settings (650°C and 600 L/hr respectively). The addition of *m*NBA increased the intensity of $[M + 2H]^{2+}$ relative to $[M + H]^{+}$ as shown in Figure 3.3.7. This is interesting, as requirement of a high desolvation temperature and flow rate suggest droplets need to evaporate faster to form $[M + 2H]^{2+}$, however the addition of *m*NBA to the ESI would slow droplet evaporation due to the increased boiling point of the droplet composition.

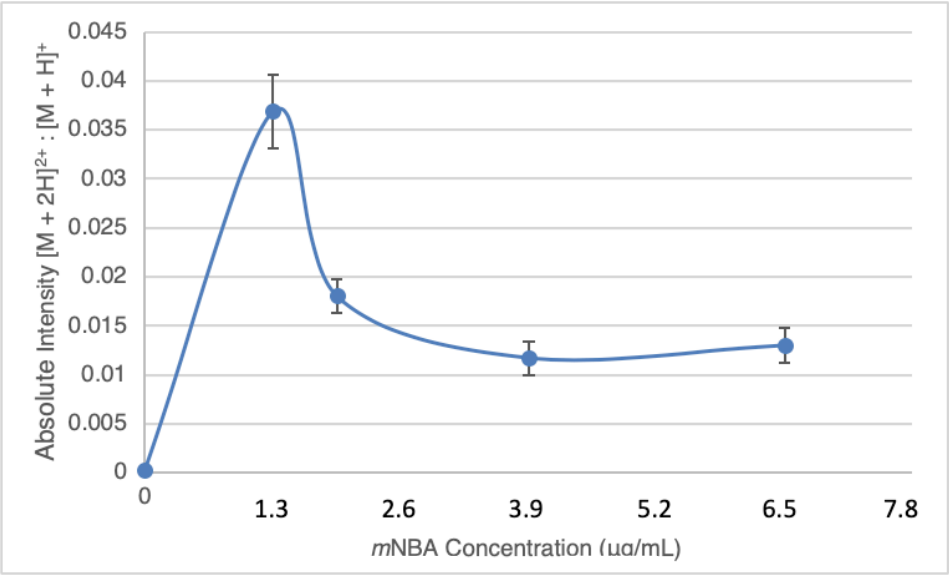

Figure 3.3.7. Effect of *m*NBA concentration on relative ion intensity ratio of $[M + 2H]^{2+}$: $[M + H]^{+}$ for AZD5672.

In contrast to cediranib and AZD9291, AZD5672 has a very low ratio of $[M + 2H]^{2+}$: $[M + H]^{+}$. Although the benefit of only reaching a maximum ratio of 0.037 may not be obvious, this produced enough of an increase in the signal-to-noise ratio for $[M + 2H]^{2+}$ to enable this ion to be cleanly isolated for MSMS. Figure 3.3.8a shows a typical mass spectrum for AZD5672 without the addition of any SCR. Signal-to-noise is poor around *m/z* 321.6 which would lead to difficulties in clean isolation. Figure 3.3.8b shows that when 1.3 μg/mL of *m*NBA is included in the ESI solution, a suitable signal-to-noise ratio for MSMS is achieved.

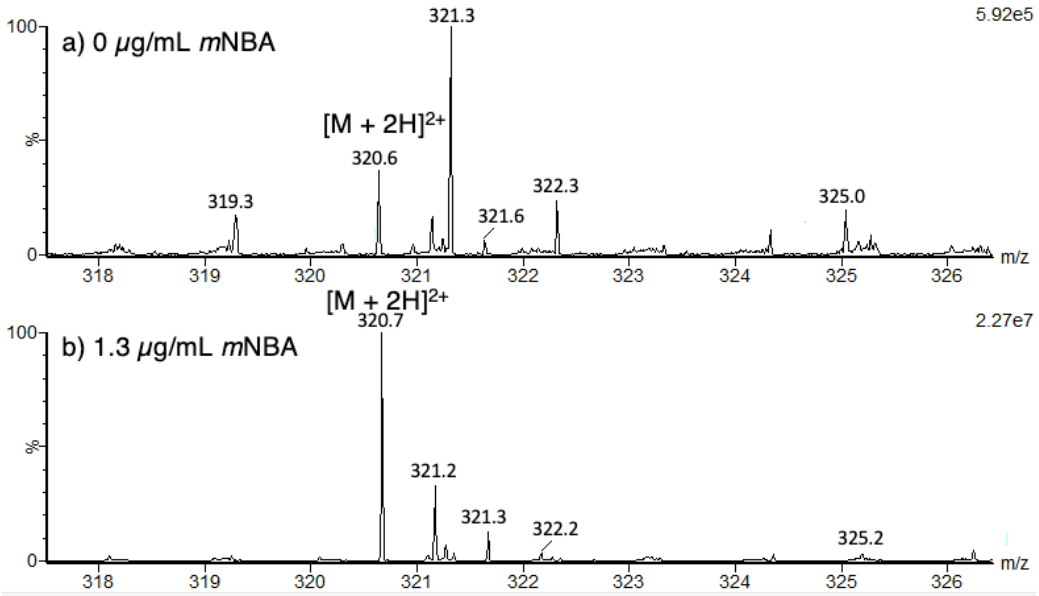

Figure 3.3.8. Mass spectra for AZD5672, focusing on *m/z* of $[M + 2H]^{2+}$ AZD5672 when a) no SCR is added and b) 1.3 μg/mL *m*NBA is added to the ESI solution. Continuum data is displayed above so peak shape can be assessed, therefore the data is non-lockmass corrected (*i.e.* not accurate mass measurement data).

The percentage increase in the ratio of $[M + 2H]^{2+}$: $[M + H]^{+}$ for cediranib, AZD9291 and AZD5672 is shown in Figure 3.3.9. This shows that *m*NBA

had the largest effect on the formation of AZD5672 and AZD9291 $[M + 2H]^{2+}$ with respect to $[M + H]^{+}$, and that 1.3-2.6 μg/mL *m*NBA has an enhancing effect on the formation of $[M + 2H]^{2+}$ with respect to $[M + H]^{+}$ for all three analytes.

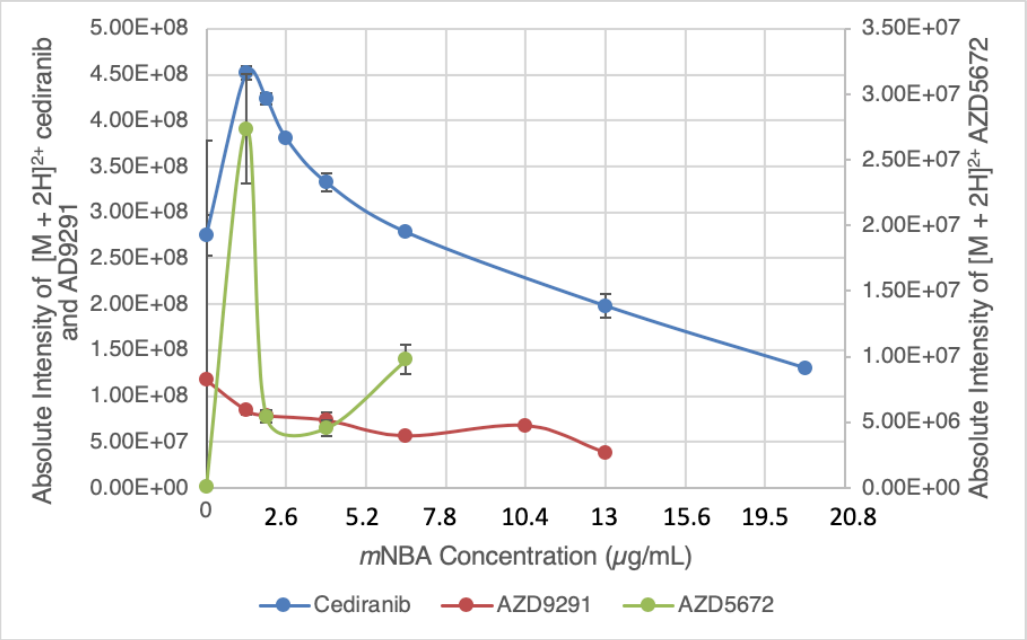

Figure 3.3.9. Percentage increase in ratio of $[M + 2H]^{2+}$: $[M + H]^{+}$ for AZD5672 (left y-axis), cediranib and AZD9291(right y-axis) with a range of *m*NBA concentrations.

The absolute intensity of $[M + 2H]^{2+}$ is an important factor when performing certain types of MSMS, such as ETD, as a stable and suitable peak intensity is required. Figure 3.3.10 shows the relative peak intensities of $[M + 2H]^{2+}$ for cediranib, AZD9291 and AZD5672 with varying concentrations of *m*NBA. In terms of ion abundance, cediranib formed more $[M + 2H]^{2+}$ with 1 μL/mL of *m*NBA rather than 5 μL/mL; the concentration at which the ratio between the double and singly protonated species was most biased towards $[M + 2H]^{2+}$. For AZD9291, the greatest $[M + 2H]^{2+}$ abundance was

obtained in the absence of *m*NBA from the ESI solution, whereas the ratio between $[M + 2H]^{2+}$ and $[M + H]^{+}$ was greatest for 3.9 μg/mL *m*NBA. For AZD5672, the greatest abundance of $[M + 2H]^{2+}$ and the greatest ratio between singly and doubly protonated molecules was at 1 μL/mL *m*NBA. One explanation for this is that the formation of $[M + 2H]^{2+}$ is greatest with low concentrations of *m*NBA, but with the formation of $[M + H]^{+}$ also being enhanced. The latter could be due to charge stripping occurring from $[M + 2H]^{2+}$ to $[M + H]^{+}$ by thermal decomposition. There are supporting protein studies where it was noted that enrichment of SCR in late-stage nanodroplets causes less evaporative cooling due to the increased vapour pressure of SCR compared with standard solvents. [18, 151] The higher temperature of the droplets can then induce thermal decomposition of the analyte, which results in charge stripping. [194] Evidence for thermal dissociation for small molecules when *m*NBA is added to the ESI solution is given in Figure 3.3.5 which shows an increase in the product ions, such as *m/z* 304.1741, at greater concentrations of *m*NBA. At greater concentrations, ion suppression, as previously noted, could be responsible for the discrepancy between the ratio of $[M + 2H]^{2+}$: $[M + H]^{+}$ and the absolute intensity of $[M + 2H]^{2+}$ for cediranib.

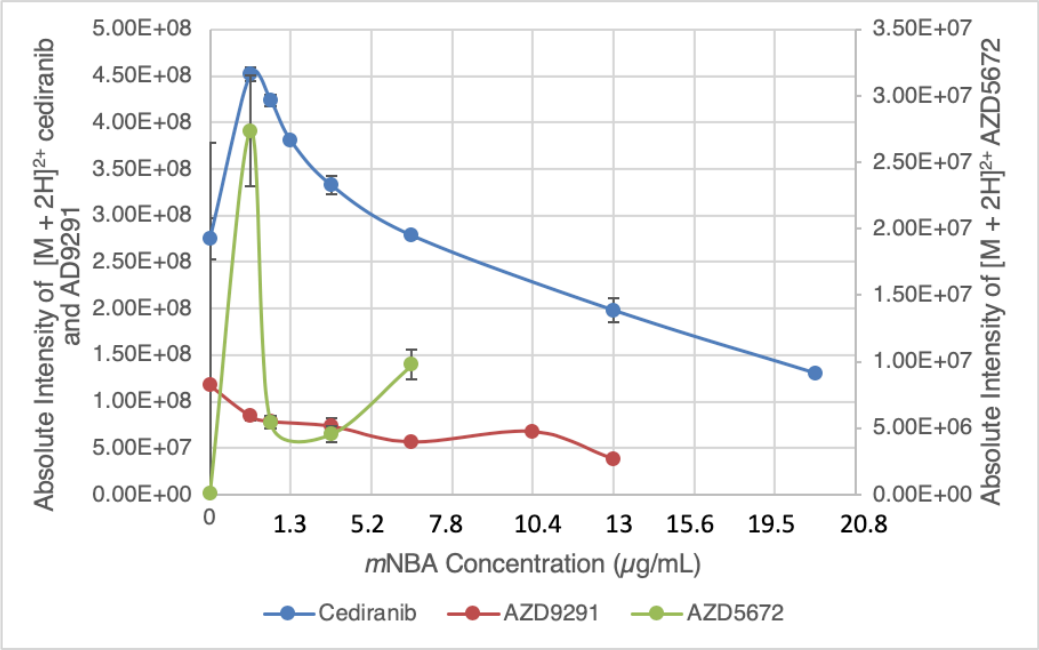

Figure 3.3.10. Absolute intensity of $[M + 2H]^{2+}$ cediranib, AZD9291 and AZD5671 for a range of *m*NBA concentrations.

Figure 3.3.11 shows the absolute intensity of $[M + H]^{+}$ for cediranib, AZD9291 and AZD5672 over the same concentration range of 0-19.5 μg/min *m*NBA. For cediranib and AZD9291 1.3 μg/mL *m*NBA produced the greatest abundance of $[M + H]^{+}$, the same relationship observed for $[M + 2H]^{2+}$. This is likely due to small concentrations of *m*NBA aiding in the protonation of cediranib. This is probably owing to an increased surface tension of ESI droplets, creating higher charge density within the droplet, making the ionisation process in general more efficient. Williams *et al.* noted similar observations for diaminoalkanes where *m*NBA aided in ionisation of both $[M + H]^{+}$ and $[M + 2H]^{2+}$. [18] The increase in abundance of $[M + 2H]^{2+}$ AZD5672 at 6.5 μg/mL *m*NBA is not fully understood, and requires further study.

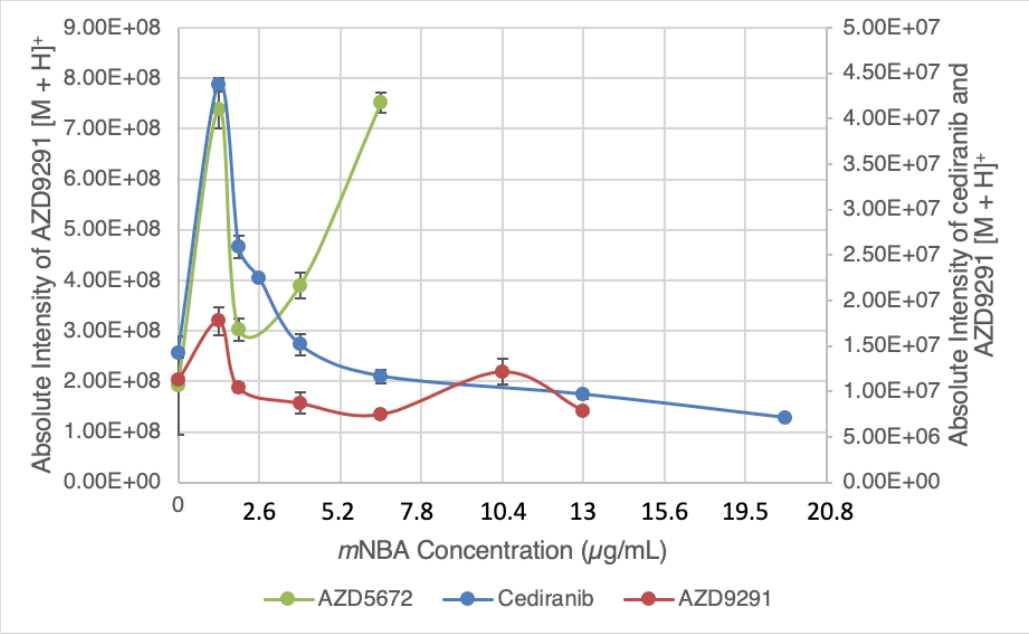

Figure 3.3.11. Absolute intensity of $[M + H]^+$ cediranib and AZD9291 (right y-axis) and AZD5671 (left t-axis) for a range of *m*NBA concentrations.

3.3.1.4. 3-nitrobenzonitrile as a SCR

The addition of 0.65 μg/mL 3-nitrobenzonitrile (commonly known as *m*-nitrobenzyl nitrile, *m*NBN) to the ESI solution initally increased the ratio of $[M + 2H]^{2+}$: $[M + H]^+$ for cediranib as shown in Figure 3.3.12. This is a much smaller increase in the ratio than was observed for *m*NBA indicating that *m*NBA has an increased supercharging effect than *m*NBN for this analyte. The concentration of *m*NBA and *m*NBN that gave the highest percentage in $[M + 2H]^{2+}$: $[M + H]^+$ for cediranib was 0.65 μg/mL, although for *m*NBN this increase (16.1%) is much smaller than for *m*NBA (213%). The effect of *m*NBN on the ratio of $[M + 2H]^{2+}$: $[M + H]^+$ AZD9291 is similar to that observed with the addition of *m*NBA (Figure 3.3.12) with the trend closely matching. *m*NBA effected the ratio of $[M + 2H]^{2+}$: $[M + H]^+$ AZD9291 more than *m*NBN, going up to a maximum ratio of 8.5 with 3.9 μg/mL whereas

*m*NBN achieved a ratio of 7.5 with 1.95 μg/mL. In the case of [AZD9291+ 2H]$^{2+}$ with optimal source settings, the doubly protonated species is the most abundant ion making the increased ratio for *m*NBA compared with *m*NBN less beneficial. For AZD9291 the highest percentage ratio increase (1547.6%) was observed when 1.95 μg/mL *m*NBN was added to the ESI solution. However, there is limited difference between the percentage ratio increase when 1.95 μg/mL *m*NBN was used compared with that observed when 0.65 μg/mL *m*NBN was added to the ESI solution (1353.7%). A similar effect was observed for AZD5672 with *m*NBA as with *m*NBN (Figure 3.3.12) with trend plots closley matching. Like AZD9291, *m*NBA induced the formation of more [M + 2H]$^{2+}$ compared to [M + H]$^{+}$ than *m*NBN. The concentration of *m*NBN required to gain the highest ratio of [M + 2H]$^{2+}$: [M + H]$^{+}$ was lower than with *m*NBA; a ratio of 0.037 at 1.3 μg/mL for *m*NBA compared to a ratio of 0.028 with 2.6 μg/mL of *m*NBN. The greatest increase in the percentage ratio of AZD5672 [M + 2H]$^{2+}$: [M + H]$^{+}$ was observed when 2.6 μg/mL *m*NBN was used (8725.2%), compared to 0.65 μg/mL for cediranib and 1.95 μg/mL for AZD9291. Consequently, *m*NBN may not be a useful choice as a SCR for small molecules as an overlap in concentrations of *m*NBN could not be chosen that would effectively supercharge all molecules. This is further supported by the observation that the only molecule where the formation of [M + 2H]$^{2+}$ is increased by the use of *m*NBN was AZD5672 (Appendix Figure 7.3.1). Possible fundamental reasons for this will be discussed Section 3.3.1.9.

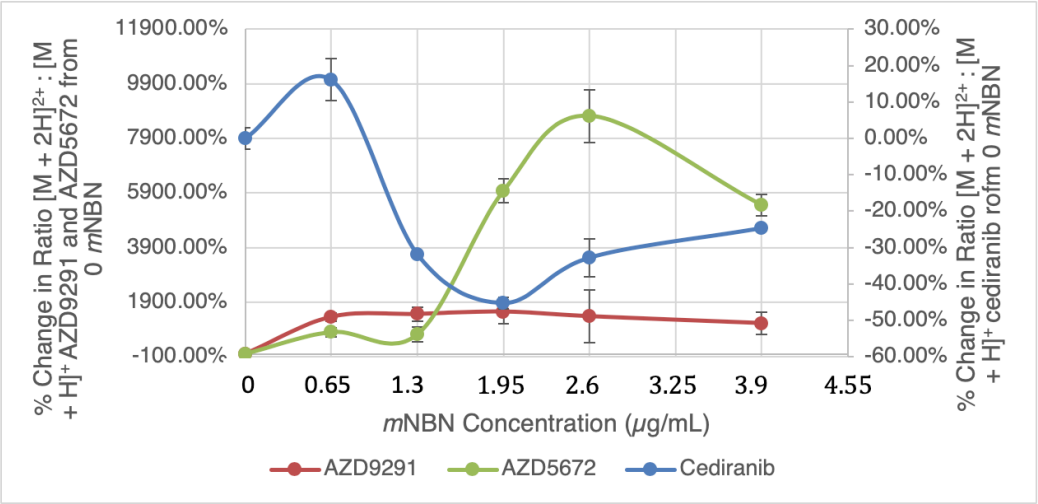

Figure 3.3.12. Percentage increase in ratio of $[M + 2H]^{2+}$: $[M + H]^{+}$ for cediranib (right y-axis), AZD5672 and AZD9291 (left y-axis) with a range of *m*NBN concentrations.

3.3.1.5. 2-(3-nitrophenyl)ethan-1-ol as a SCR

Figure 3.3.13 shows the percentage change in the ratio of absolute intensity of $[M + 2H]^{2+}$: $[M + H]^{+}$ for the three analytes with varying concentrations of 2-(3-nitrophenyl)ethan-1-ol (commonly known as *m*-nitrophenyl alcohol, *m*NPEA). The biggest percentage change in the ratio of double to singly protonated molecules was seen for AZD5672; a 1303.8% increase with 2.6 μg/mL *m*NPEA. For AZD9291, the percentage change in ratio initially increases by 233.0% with 1.3 μg/mL of *m*NPEA, and then continues to rise slowly with the addition of more *m*NPEA. *m*NPEA had no beneficial on the formation of $[M + 2H]^{2+}$ cediranib with respect to the percentage change of $[M + 2H]^{2+}$: $[M + H]^{+}$.

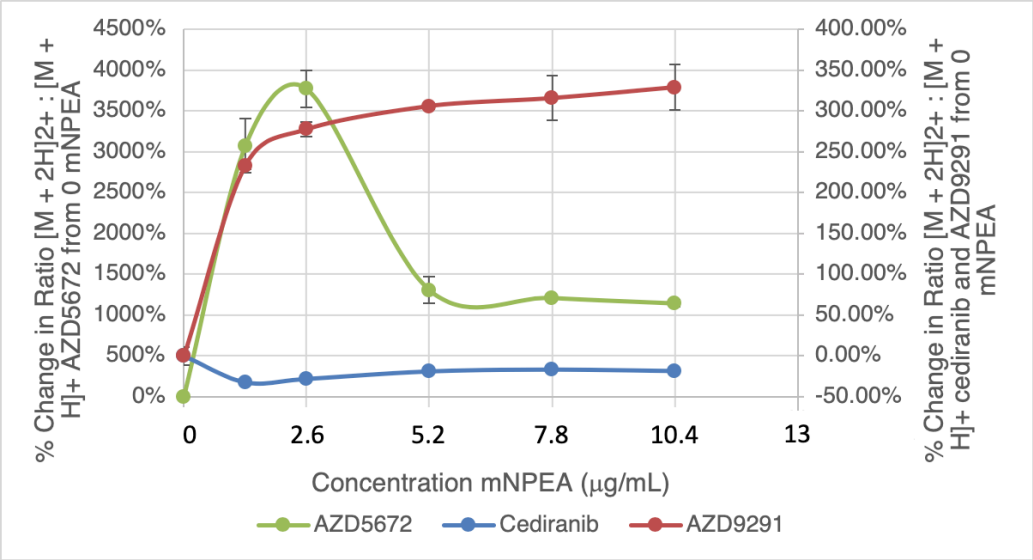

Figure 3.3.13. Percentage increase in ratio of $[M + 2H]^{2+}$: $[M + H]^{+}$ for cediranib, AZD5672 and AZD9291 with a range of *m*NPEA concentrations.

The absolute intensity of $[M + 2H]^{2+}$ for cediranib, AZD9291 and AZD5672, it becomes clear that *m*NPEA only has an enhancing effect on the formation of $[AZD5672 + 2H]^{2+}$. The trend for AZD5672 closely matches that of the increase in percentage ratio of double to singly protonated species (Figure 3.3.14). For cediranib and AZD9291, the highest abundance of $[M + 2H]^{2+}$ was formed when no *m*NPEA was added to the ESI solution.

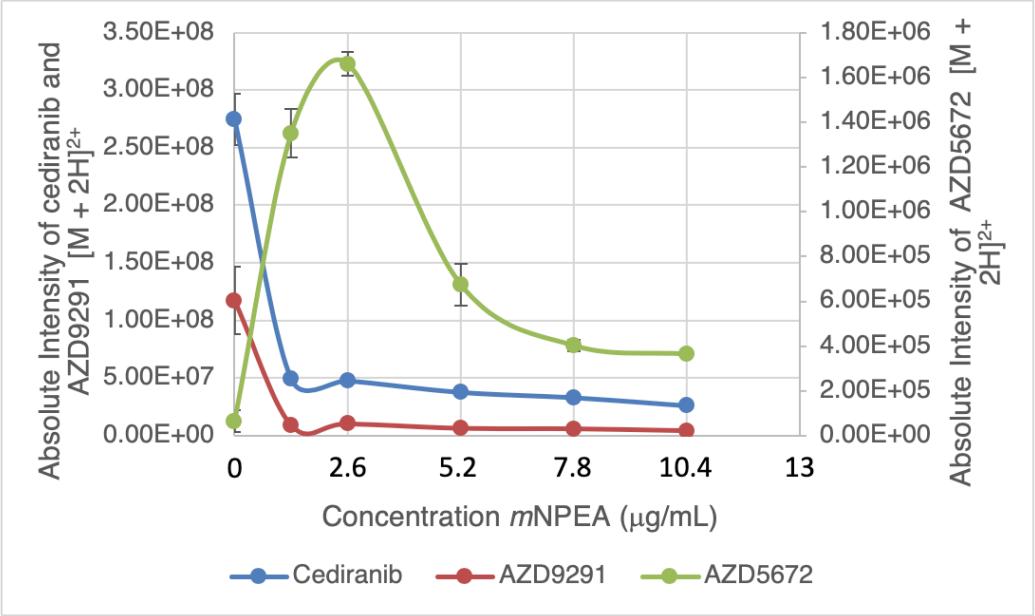

Figure 3.3.14. Absolute intensity of $[M + 2H]^{2+}$ cediranib, AZD9291 and AZD5671 for a range of *m*NPEA concentrations.

Figure 3.3.15 shows that increasing concentrations of *m*NPEA made little difference to the intensity of $[AZD5672 + H]^{+}$, making it an ideal SCR for this analyte as low concentrations can be used, reducing ion suppression and carryover. When examining Figures 3.3.14 and 3.3.15, an explanation for the percentage increase in ratio of $[M + 2H]^{2+}$: $[M + H]^{+}$ AZD9291 is observed. The abundance of both $[M + 2H]^{2+}$ and $[M + H]^{+}$ are both lower when *m*NPEA is present, compared with the absence of *m*NPEA in the ESI solution. As $[M + H]^{+}$ abundance reduces to a greater degree than $[M + 2H]^{2+}$, an increase in the ratio of single to doubly protonated species was observed. Figures 3.3.14 and 3.3.15 show that $[M + 2H]^{2+}$ and $[M + H]^{+}$ cediranib are less abundant with any concentration of *m*NPEA, with intensities of both species reducing at a similar rate. These data suggest

that *m*NPEA is not a suitable SCR for small molecules due to the dramatically different effects observed on only three analytes.

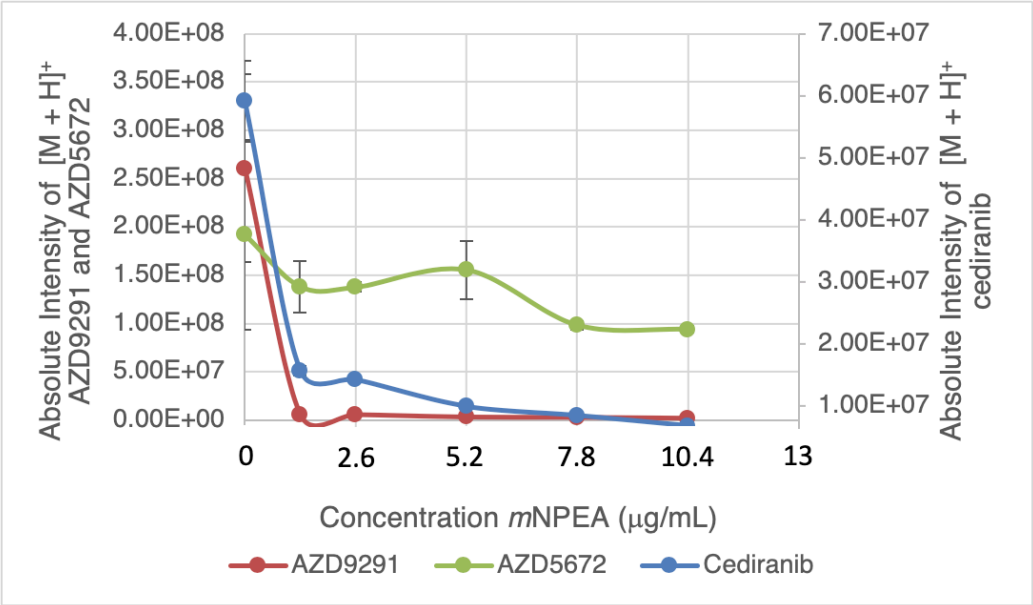

Figure 3.3.15. Absolute intensity of $[M + H]^+$ cediranib, AZD9291 and AZD5671 for a range of *m*NPEA concentrations.

3.3.1.6. Tetrahydrothiphene 1,1-dioxide as a SCR

Figure 3.3.16 shows the relationship between the percentage change in ratio of $[M + 2H]^{2+}$: $[M + H]^+$ and varying concentrations of Tetrahydrothiphene 1,1-dioxide (commonly known as sulfolane). The ratio of double to singly protonated AZD5672 initially increased by 1794.7% when 1 µg/mL sulfolane was added to the ESI solution. The ratio then decreases as greater concentrations of sulfolane are introduced, due to ion suppression (Figure 3.3.17) as shown for *m*NBA (Figure 3.3.6).

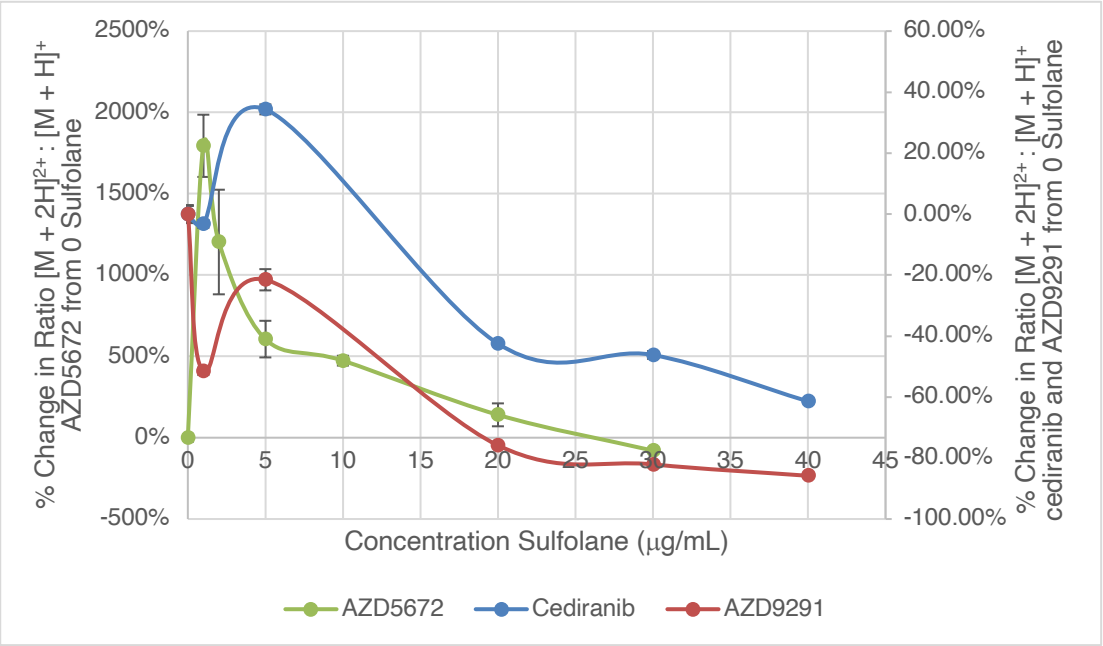

Figure 3.3.16. Percentage increase in ratio of $[M + 2H]^{2+}$: $[M + H]^{+}$ for cediranib, AZD5672 and AZD9291 with a range of sulfolane concentrations.

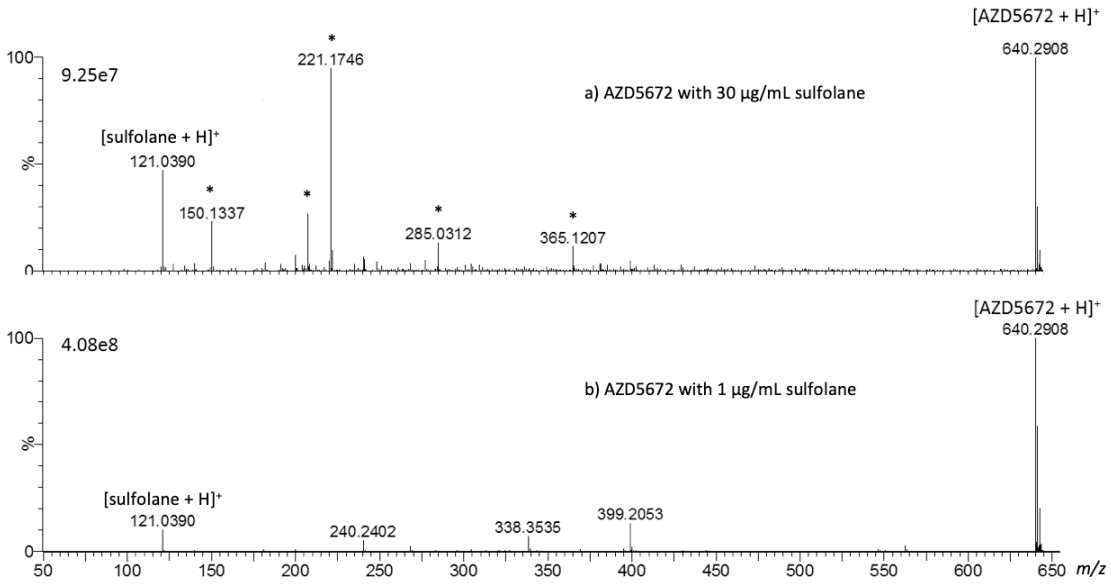

Figure 3.3.17. Comparison of AZD5672 spectra with a) 30 µg/mL and b) 1 µg/mL sulfolane. * likely impurities in sulfolane.

The same ratio of $[M + 2H]^{2+}$: $[M + H]^{+}$ for cediranib decreases when 1 μg/mL sulfolane was used, but when 5 μg/mL sulfolane was added to the ESI solution, a 34.4% increase was observed. This is a relatively small change with little benefit for this analyte. The ratio of $[M + 2H]^{2+}$: $[M + H]^{+}$ AZD9291 was lower for every concentration of sulfolane tested.

As with *m*NPEA, the only analyte that showed an increase in the formation of $[M + 2H]^{2+}$ with the addition of sulfolane was AZD5672. $[M + 2H]^{2+}$ cediranib and AZD9291 abundances were greater when in the absence of sulfolane in the ESI solution likely due to ion suppression (Appendix Figure 7.3.2). The abundance $[AZD5672 + H]^{+}$ remained largely with the addition of sulfolane; the same relationship observed for *m*NPEA (Appendix Figure 7.3.3). The intensity of $[cediranib + H]^{+}$ reduces significantly with the presence of 1 μg/mL sulfolane; this decrease is to a greater degree compared with $[M + 2H]^{2+}$ cediranib which accounts for the increase in the percentage change of the ratio of $[M + 2H]^{2+}$: $[M + H]^{+}$. The peak intensity for double and singly protonated species of AZD9291 were shown to reduce in the presence of sulfolane. As with *m*NPEA, the disparity in SC effects on the small molecules tested do not make it an ideal choice for enhancing the formation of $[M + 2H]^{2+}$ of small molecules.

3.3.1.7. Thiophen-2(*5H*)-one) as a SCR

Figure 3.3.18 shows the percentage change in the ratio of $[M + 2H]^{2+}$: $[M + H]^{+}$ for cediranib, AZD9291 and AZD5672 with changing concentrations of Thiophen-2(*5H*)-one) (commonly known as thiophenone). 5 μg/mL thiophenone induced a 1804.2% increase in the ratio of double to singly charged cediranib. The ratio of $[M + 2H]^{2+}$: $[M + H]^{+}$ for AZD9291 and AZD5672 was approximately 1500 times lower when thiophenone was added to the ESI solution; likely the result of ion suppression.

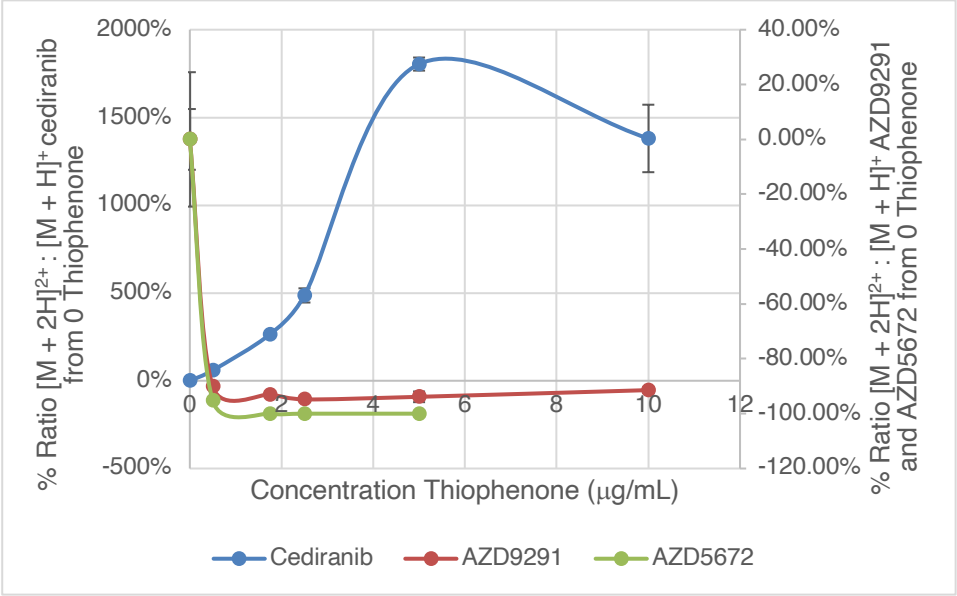

Figure 3.3.18. Percentage increase in ratio of $[M + 2H]^{2+}$: $[M + H]^{+}$ for cediranib, AZD5672 and AZD9291 with a range of thiophenone concentrations.

For all analytes, purely the presence of thiophenone resulted in a lower abundance of $[M + 2H]^{2+}$ (Appendix Figure 7.3.4), which indicates the thiophenone acts to increase the abundance of $[M + H]^{+}$, albeit to a lesser extent for cediranib, showing thiophenone is not a suitable SCR for small

molecules. When examining the change in abundance of $[M + H]^+$ and of $[M + 2H]^{2+}$ individually, the same relationship observed for sulfolane was seen with $[M + 2H]^{2+}$ decreasing in abundance at every concentration of thiophenone, but to lesser degree than $[M + H]^+$ for cediranib resulting in the ratio increase observed in Figure 3.3.18.

3.3.1.8. Hydroxymethyl-1,3-dioxolan-2-one as a SCR

Figure 3.3.19 shows the effect different concentrations of Hydroxymethyl-1,3-dioxolan-2-one (commonly known as glycerol-1,2-cabonate) has on the percentage change in the ratio of $[M + 2H]^{2+}$: $[M + H]^+$ for cediranib, AZD9291 and AZD5672. There is an initial increase in the percentage change of this ratio for AZD5672 of 141.6% with 0.1 μg/mL glycerol-1,2-cabonate, with the percentage change in the ratio reducing at higher concentrations. Glycerol-1,2-cabonate reduced the percentage change in $[M + 2H]^{2+}$: $[M + H]^+$ AZD9291 at all concentrations examined. ESI of cediranib with 2 μg/mL glycerol-1,2-cabonate resulted in a 10.9% increase in the ratio of double to singly protonated species.

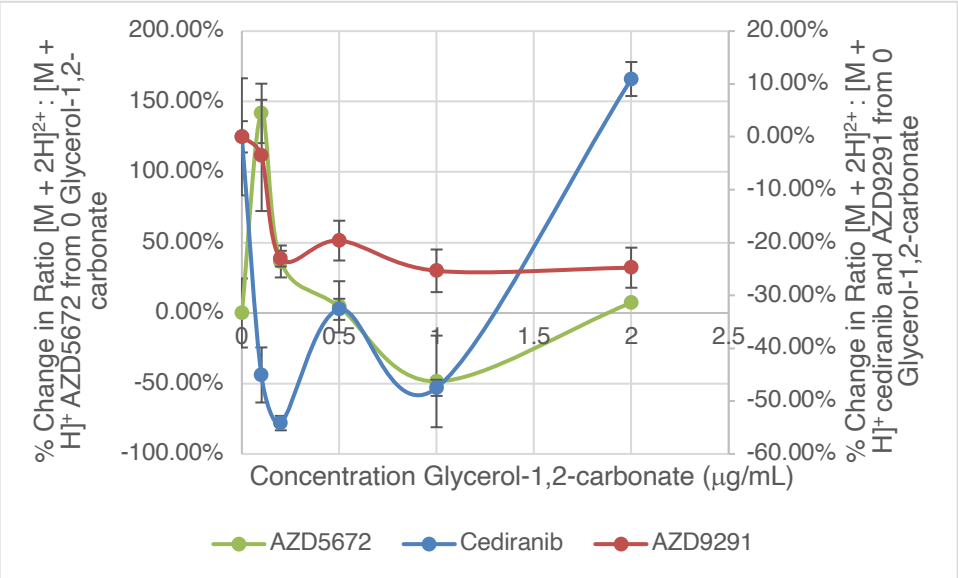

Figure 3.3.19. Percentage increase in ratio of $[M + 2H]^{2+}$: $[M + H]^{+}$ for cediranib, AZD5672 and AZD9291 with a range of glycerol-1,2-carbonate concentrations.

Glycerol-1,2-cabonate only increased the intensity of $[M + 2H]^{2+}$ AZD5672 (Appendix Figure 7.3.5). Unique to this SCR, the intensity of $[M + H]^{+}$ was not seen to significantly alter at any concentration of glycerol-1,2-cabonate for any analyte (Appendix Figure 7.3.6).

3.3.1.9. (methylsulfinyl)methane as a SCR

(Methylsulfinyl)methane (commonly known as dimethyl sulfoxide, DMSO) showed no supercharging effects for any of the small molecules tested as shown for cediranib in Figure 3.3.20 and AZD9291 and AZD5672 in Appendix Figure 7.3.7-9. This contrasts with studies by Sterling *et al.* where it was shown that with the addition of 5% DMSO, protein charge distribution was increased. [148] This is likely due to the supercharging effect induced

by DMSO being caused mainly by protein unfolding, allowing more protonation sites to be accessed. [148]

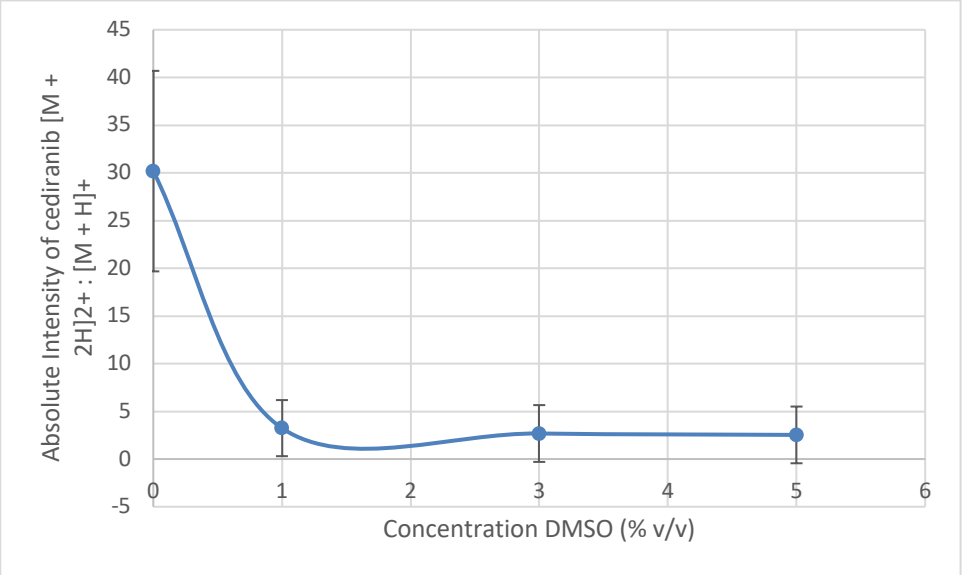

Figure 3.3.20. Ratio of the absolute intensity of $[M + 2H]^{2+}$: $[M + H]^{+}$ cediranib for a range of DMSO concentrations.

3.3.1.10. Results Summary

Out of all the molecules tested, only cediranib, AZD92921 and AZD5672 were seen to form $[M + 2H]^{2+}$ as shown in summary Table 3.3.5. Of these three molecules, cediranib and AZD9291 formed $[M + 2H]^{2+}$ without the addition of any SCR.

Molecule	*m*NBA	*m*NBN	Thiophenone	*m*NPEA	Glycerol-1,2-carbonate	Sulfolane	Absence of SCR
Cediranib	✔	✔	✔	✔	✔	✔	✔
AZD9291	✔	✔	✔	✔	✔	✔	✔
AZD5672	✔	✔	✗	✔	✔	✔	✗
AZD2171 BQ Indole	✗	✗	✗	✗	✗	✗	✗
AZD5672 Bisamide	✗	✗	✗	✗	✗	✗	✗
Fostamatanib	✗	✗	✗	✗	✗	✗	✗
AZD5672 Precursor	✗	✗	✗	✗	✗	✗	✗

Table 3.3.5. Summary table showing whether $[M + 2H]^{2+}$ was observed with the addition of SCRs.

Figure 3.3.21 shows the absolute intensity of $[cediranib + 2H]^{2+}$ with the addition of each SCR at a range of concentrations. These data suggest that *m*NBA performs best as a SCR for cediranib, producing the greatest increase in the absolute intensity of $[cediranib + 2H]^{2+}$ at a concentration of 1.3 μg/mL.

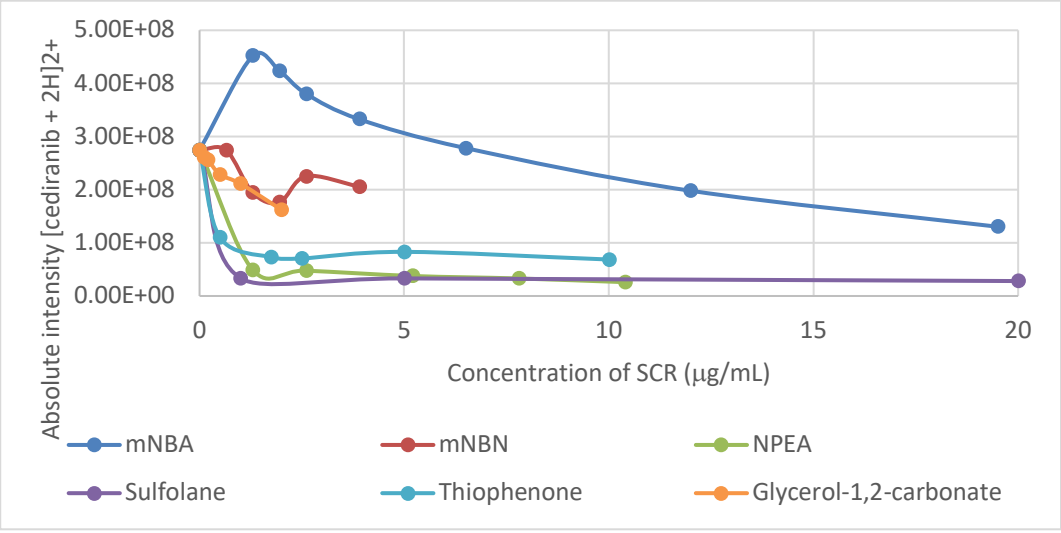

Figure 3.3.21. Absolute intensity of $[M + 2H]^{2+}$ Cediranib with SCRs.

For AZD9291, the addition of every SCR reduced the absolute intensity of $[AZD9291 + 2H]^{2+}$ as shown in Figure 3.3.22. This perhaps differs from cediranib due to the ionisation efficiencies of $[M + 2H]^{2+}$ and the SCRs themselves.

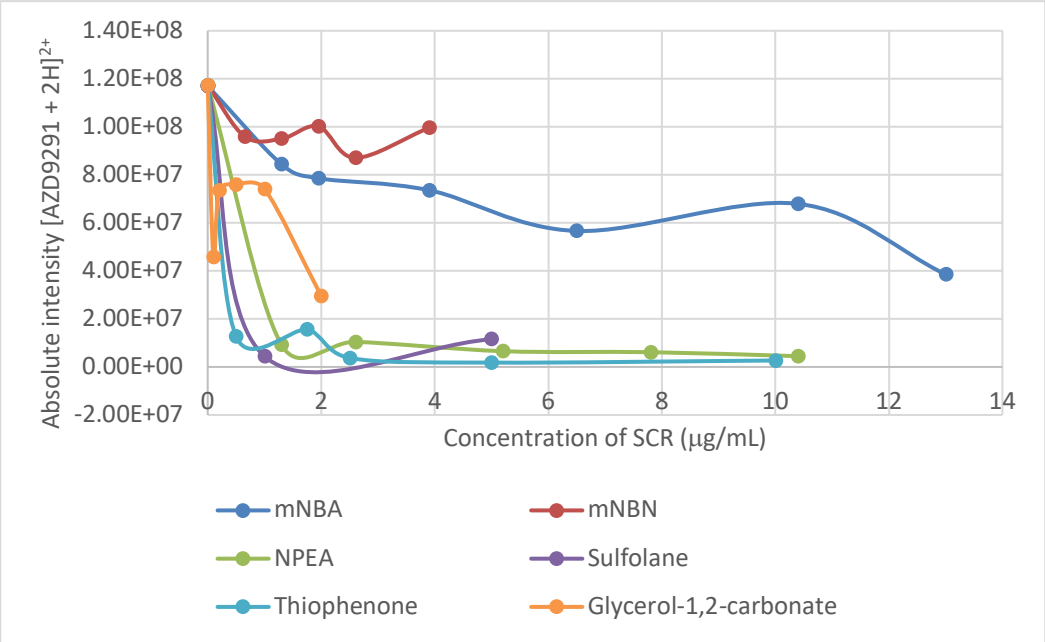

Figure 3.3.22. Absolute intensity of $[M + 2H]^{2+}$ AZD9291 with SCRs.

The absolute intensity of $[AZD5672 + 2H]^{2+}$ with varying concentrations of each SCR is shown in Figure 3.3.23. 1.3 µg/mL *m*NBA resulted in the highest abundance of $[AZD5672 + 2H]^{2+}$ as with cediranib. Unlike cediranib and AZD9291 which naturally formed $[M + 2H]^{2+}$ SCRs *m*NBA, *m*NBN, sulfolane, glycerol-1,2-carbonate and *m*NPEA had a beneficial effect on the formation of $[AZD5672 + 2H]^{2+}$, although *m*NBN was the only SCR other than *m*NBA that induced formation of a suitable abundance of $[M + 2H]^{2+}$ for isolation and MSMS.

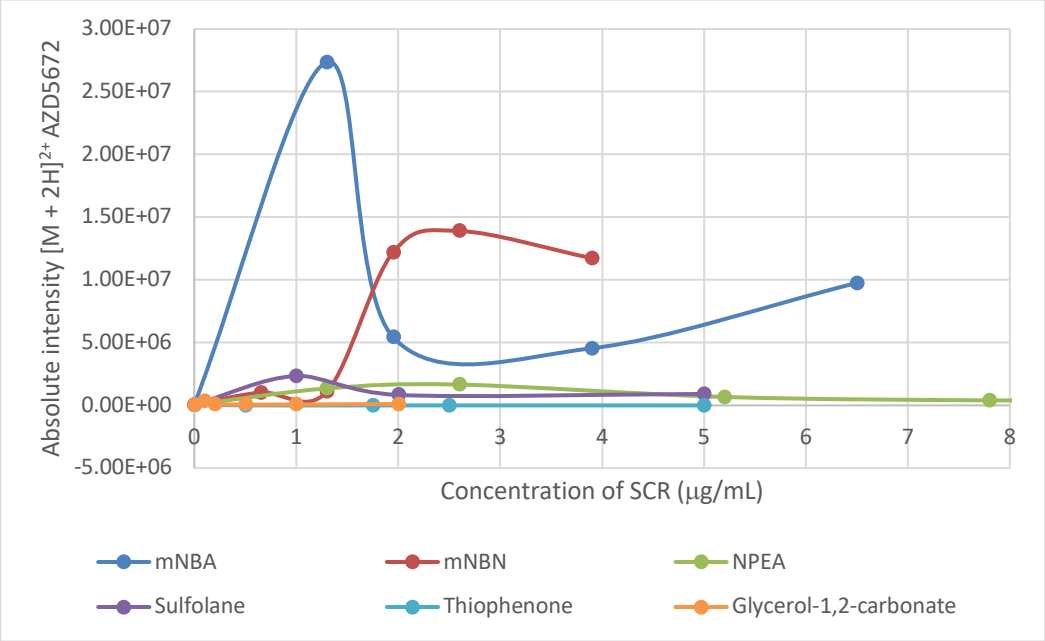

Figure 3.3.23. Absolute intensity of $[M + 2H]^{2+}$ AZD5672 with SCRs.

3.3.1.11. Discussion

Of the small molecules tested, only cediranib, AZD9291 and AZD5672 repeatably formed $[M + 2H]^{2+}$ with the addition of SCRs. Fostamatanib did form $[M + 2H]^{2+}$ with the addition of 130 μg/mL *m*NBA to the ESI solution as shown in Figure 3.3.24. At lower concentrations of *m*NBA, no [fostamatanib + 2H]$^{2+}$ was formed. The high concentration of *m*NBA required to induce formation of [fostamatanib + 2H]$^{2+}$ is impractical due to source contamination by *m*NBA discussed below.

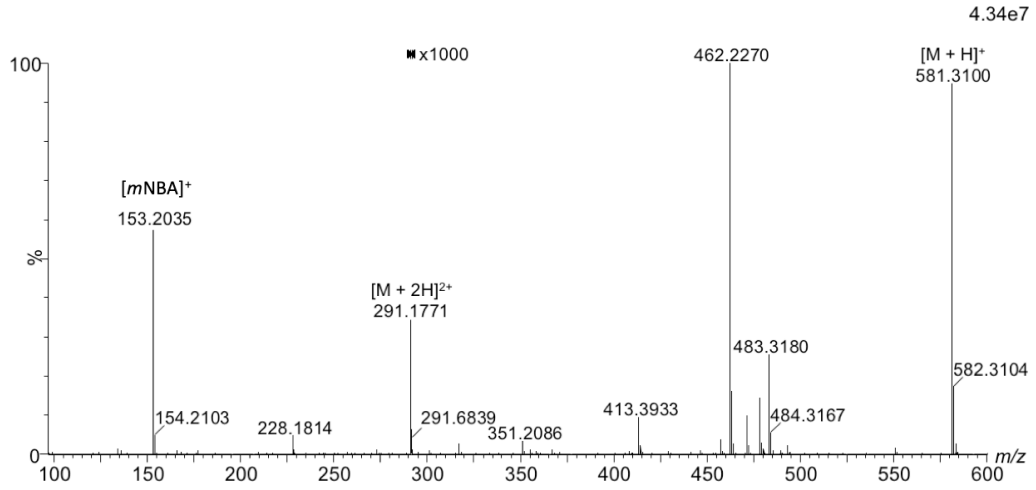

Figure 3.3.24. Mass spectrum of fostamatanib with 130 μg/mL *m*NBA.

AZD2171 BQ indole, AZD5672 bisamide and AZD5672 precursor did not form $[M + 2H]^{2+}$ which is likely due to the lack of favourable protonation sites on the molecules. As shown by Williams *et al.* (and discussed in detail in Section 1.4) the distance between protonation sites needs to be at least 10.9 Å in order for protonation to occur on both sites. [18] Although the distances between potential protonation sites for these molecules is not known, when comparing the distances between the possible protonation sites of cediranib, AZD9291 and AZD5672 to AZD2171 BQ indole, AZD5672 bisamide or AZD5672 precursor, it is one possible reason why $[M + 2H]^{2+}$ was not formed (Table 3.3.1).

Several mechanisms for supercharging have been suggested in the literature for proteins and peptides as discussed in Section 1.4. In terms of how these can be applied to small molecules, the increase in ESI droplet surface tension is likely one contributor to supercharging of small molecules. SCRs have high boiling points compared with the ESI solvents

resulting in enrichment in mature ESI droplets. The droplets higher surface tension compared with droplets with no SCR require more charges to be present before Rayleigh fission occurs, causing greater charge density in the droplet (Equation 1.1). It follows that these more charge dense droplets increase the likelihood of protonation occurring on more sites of the molecule. [190] If the surface tension mechanism was the main driving force behind small molecules supercharging, it would be expected that the SCRs with the highest surface tension or boiling point would lead to the greatest supercharging effect. These data do not overwhelmingly support this. However, as *m*NBA gave the best results with regards to formation of $[M + 2H]^{2+}$ which has a surface tension of 57.0 ± 3.0 dyne cm^{-1} [192] which although at the higher end of the scale with regards to those tested in this study (Table 3.3.2), both *m*NBN and thiophenone have higher surface tensions (58.2 ± 5.0 and 67.6 ± 5.0 dyne cm^{-1} respectively, which following enrichment *via* evaporation of solvent in the ESI process would effectively be the surface tension of the droplet make-up [192]). Although *m*NBN acted well as a SCR, thiophenone generally had a negative effect on the formation of $[M + 2H]^{2+}$. Thiophenone did however give promising results for cediranib, with the ratio of $[M + 2H]^{2+}$: $[M + H]^{+}$ increasing. On further examination however, this was due to $[M + H]^{+}$ being more suppressed than $[M + 2H]^{2+}$.

The charge trapping mechanism proposed by Konnerman *et al.* describes a process where the SCR forms a shell around the ESI droplet which reduces the loss of cations *via* IEM from the aqueous core due to low

permeability of cations though the hydrophobic layer. [151] As with the surface tension mechanism, this would result in a charge dense droplet leading to higher charge-state ions. The lack of an increase in salt adduction on the newly formed ions, as shown in Figure 3.3.25 for AZD5672 with *m*NBN for sodium and potassium adducts would suggest this is not the case. If salts are being trapped within the droplet, more salt adduction would be expected, whereas generally for all molecules, a decrease is observed (Appendix Figure 7.3.10). The observation of lower abundance of salt adducted ions agrees with some studies performed on proteins where a reduction in salt adduction was also noted, and proposed to be due to SCR binding the salt ions. [150] Equally, the mechanism involving charge delocalisation, whereby polar solvents diffuse charge through large-scale dipole ordering by SCR molecules aligning at partial negative sites, allowing more protonation sites to be accessible by delocalising negative charges and overcoming the electrostatic barrier, would result in SCR adduction on small molecules as seen in proteins, which was not observed. [135]

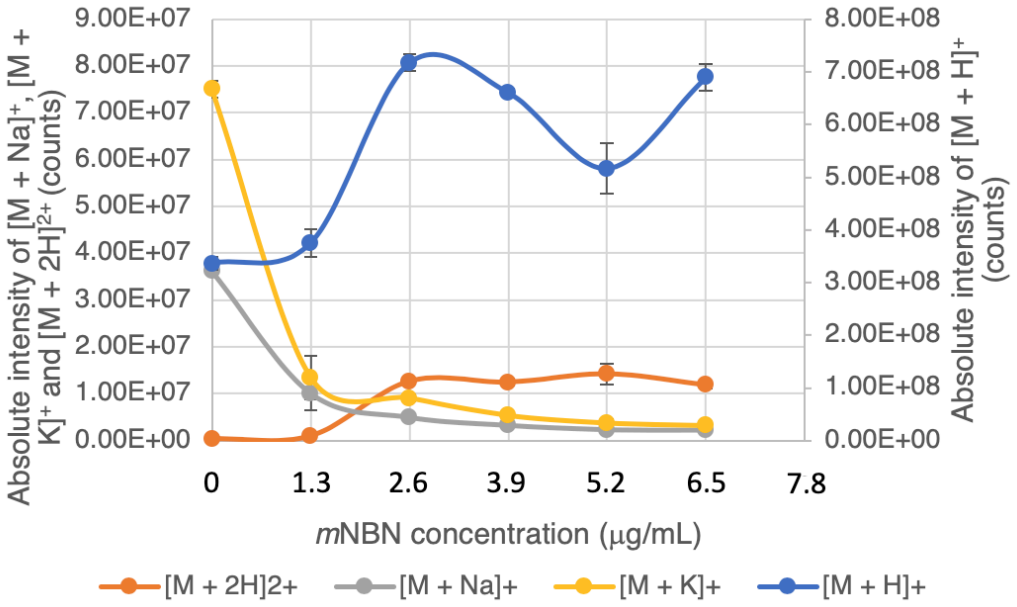

Figure 3.3.25. Absolute intensity of [AZD5672 + Na]$^+$ and [AZD5672 + K]$^+$ with varying concentrations of *m*NBN.

Chemical protein unfolding, or denaturation, is also a working hypothesis for a supercharging mechanism: some SCRs, including *m*NBA, have been shown to cause protein denaturation in high concentrations, SCR enrichment in mature ESI droplets results in high concentrations of SCR, causing chemical denaturation allowing more protonation sites to be available. [137] This does not translate well to the small molecules tested due to a lack of higher order structure. For this reason, thermally induced unfolding or denaturation in which mature ESI droplets enriched in SCR undergo less evaporative cooling due to high SCR boiling points, resulting in higher droplet temperature causing thermal denaturation is equally unlikely. This could, however, account for the increase in dissociation products noted above for cediranib in Figure 3.3.5, as the high droplet temperatures could induce thermal decomposition. [162-165] The effect of changing pH was investigated by Grandori *et al.* by the use of different

acids in the ESI solution and was shown to have no effect in proteins, making this unlikely to have an effect on small molecules supercharging. [131] Finally, the dynamic IEM where one end of a molecule is desorbed from the ESI droplet followed by charge reorganisation at the droplet surface allows protonation at the other end of the molecule, could very well apply, although no evidence either way was provided by the experiments conducted herein. [18]

A practical implication of using SCRs is source contamination. At concentrations over around 2 μL/mL for each SCR, a high degree of carryover was observed. This is likely due to their high boiling points, a property common to all SCRs tested. Especially difficult to remove from the source was *m*NBA, which is unsurprising as this has the highest boiling point of the SCRs tested at 402.2-409.5°C, although maintaining the highest possible ion source temperature overnight allowed for the majority of the SCR signal to dissipate.

3.3.2. Conclusions

$[M + 2H]^{2+}$ was not observed for several of the small molecules tested with any SCR. This is most likely due to the lack of available protonation sites on those particular molecules. *m*NBA performed the best as a SCR for small molecules. The main differentiator in physiochemical properties from the other SCRs tested is the high boiling point of *m*NBA, with both the surface tension and density not considerably different from other

supercharging reagents. This suggests that the main mechanism for supercharging in small molecules is related to the concentration of SCR left in droplets following solvent evaporation. However, strong memory effects were observed with the use of *m*NBA making it hard to remove from the instrument. Even so, from this study, *m*NBA is the recommended SCR at a concentration of 1.3 μg/mL for small molecules (with available protonation sites), with scope to optimise for different reagents. Another interesting point to come out of this study is that optimisation of source parameters, such as desolvation temperature and flow rate, makes a great deal of difference in formation of $[M + 2H]^{2+}$, and should be a first port of call before SCRs are utilised.

3.4. Coupling supercharged electrospray ionisation with electron-transfer dissociation and optimising for an LC timescale

For efficient ETD, a balance between the absolute intensity of the analyte ions and of the ETD reagent ions needs to be maintained at a ratio that was experimentally determined to be between 6×10^3 to 3×10^4 analyte intensity : 1×10^6 ETD reagent intensity. When coupling ETD to LC, there is an inherent problem: as the analyte elutes from the column, the concentration varies causing the abundance of ions formed by ESI to change. In this chapter, two methods have been investigated to attempt to maintain the ratio of ions required for efficient ETD. The first dynamically controls the capillary voltage of the ion source whilst the second dynamically controls the dynamic range enhancement (DRE) lens, which is located before the TriWave region of the instrument.

3.4.1. Results and discussion

3.4.1.1. Optimising analyte : reagent ratio

In order to determine the optimum ratio of analyte cation : ETD reagent anion, direct infusion of substance P (500 pmol/μL) was performed with the capillary voltage being set to different values to produce a range of $[\text{substance P} + 3\text{H}]^{3+}$ (*m/z* 450) ion abundance (Figure 3.4.1).

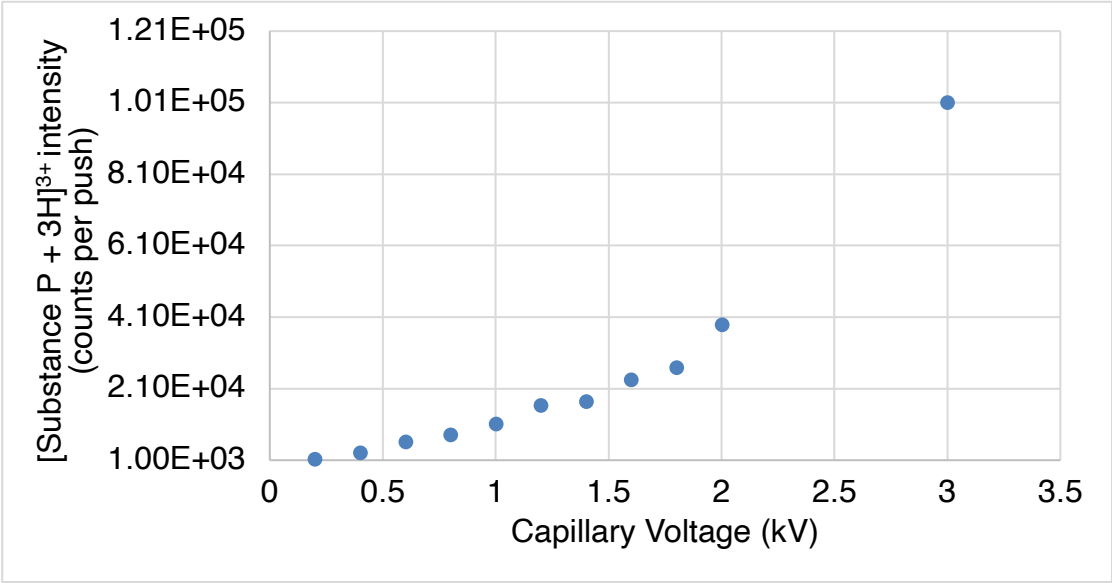

Figure 3.4.1. Absolute Intensity of [substance P + 3H]$^{3+}$ for a single scan at a range of capillary voltages. Counts per push relates to the intensity produced by the number of ions that hit the detector per push, which is aligned to scan time, in this case, 0.5 seconds.

ETD was then performed on the resultant [substance P + 3H]$^{3+}$ whilst the ETD reagent anion was maintained at a constant absolute intensity of 1×10^6 counts per push. This represents the maximum intensity that could be achieved for the ETD reagent anion, *p*-nitrotoluene, from the glow discharge source. The ETD efficiency calculated as described in Equation 3.4.1.

$$ETD\ efficiency = \frac{\sum(c\ and\ z\ product\ ion\ intensities)}{\sum(all\ ion\ intensities)}$$

Equation 3.4.1. ETD efficiency calculation.

In order to perform this calculation, data was processed firstly by 'automatic peak detection', a method of centring continuum peaks to produce centroid data, and secondly by performing a 'TOF transform', which collapses

charge states and isotopes into representative singly charged peaks. This process is shown in Figure 3.4.2 where a) is the raw spectrum, b) is the spectrum after automatic peak detection, and c) is the spectrum after TOF transformation. ETD product ion nomenclature is shown in Figure 3.4.3.

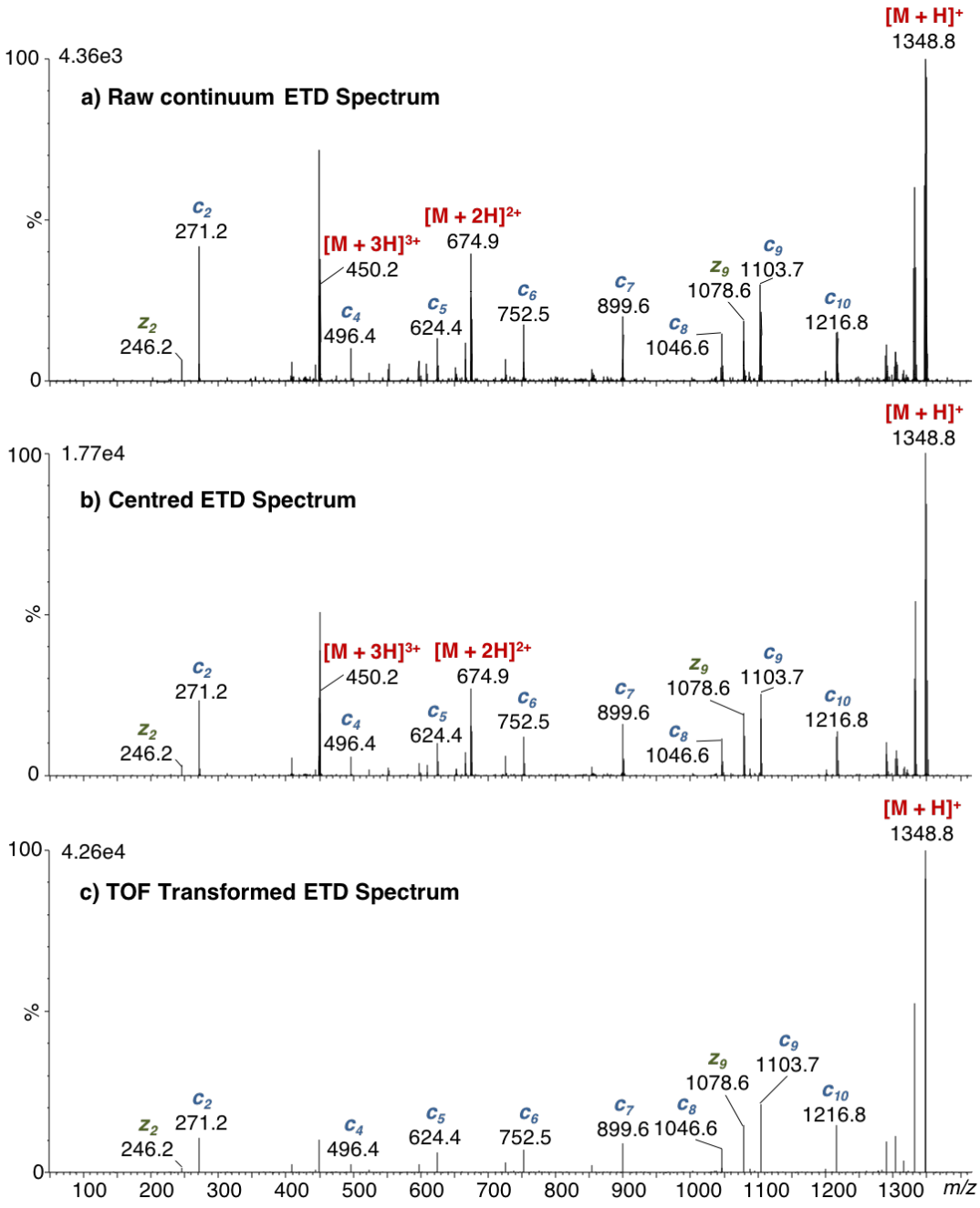

Figure 3.4.2. Example of data processing following acquisition of ETD data, from a) a raw ETD product ions spectrum to b) a centred centroid spectrum, to c) a TOF transformed spectrum, where isotopes and charge states have been collapsed in a single, representative peak.

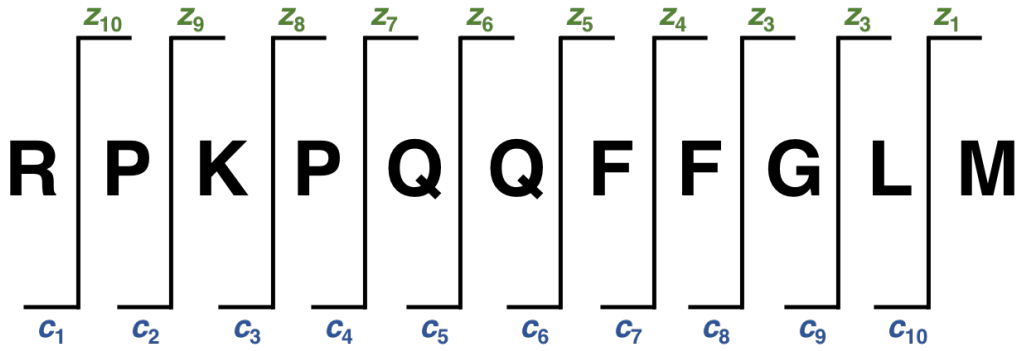

Figure 3.4.3. Electronic dissociation product ion annotation for peptides. [68]

Figure 3.4.4 shows the ETD efficiency of [substance P + 3H]$^{3+}$ at varying precursor ion intensities.

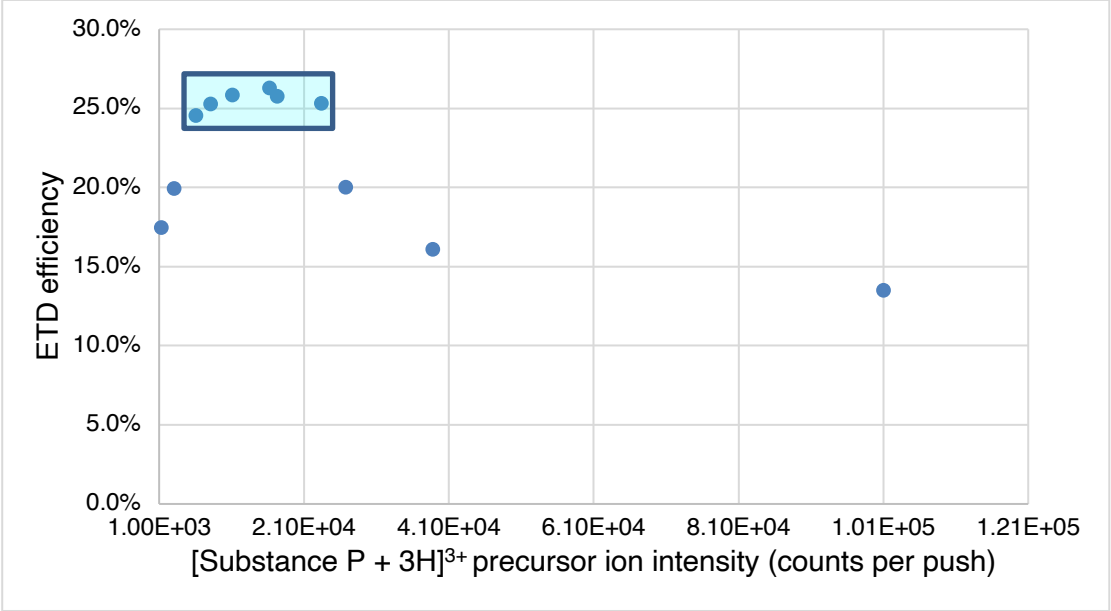

Figure 3.4.4. ETD efficiency against the absolute intensity of isolated [Substance P + 3H]$^{3+}$, for 60 scans (averaged) when the ETD reagent intensity was held at 1×10^6 counts per push. The highlighted points indicate the precursor ion intensity where the highest ETD efficiency was observed.

The most efficient ETD was observed when the precursor ion was at an absolute intensity of between 1.2-2.0x10^4 counts per push. Here, ETD efficiency was at 25.8%, although the efficiency of ETD plateaued when

the precursor ion was between 6.01×10^3 to 2.34×10^4 counts per push, as per the highlighted region in Figure 3.4.4. Beyond a product ion intensity of 2.34×10^4 counts per push of analyte ion, efficiency falls.

The efficiency of ETD would be very high if the intensity of one *c* or *z* type ion is much greater than the sum of all other peaks, but the information about the sequence of a peptide would be limited, *i.e.* efficiency does not equal sequence coverage. Therefore, along with ETD efficiency, the extent to which the ETD fragmentation covers the whole ion is an important factor to take into consideration. The ETD coverage for a series of precursor ion intensities is shown in Figure 3.4.5.

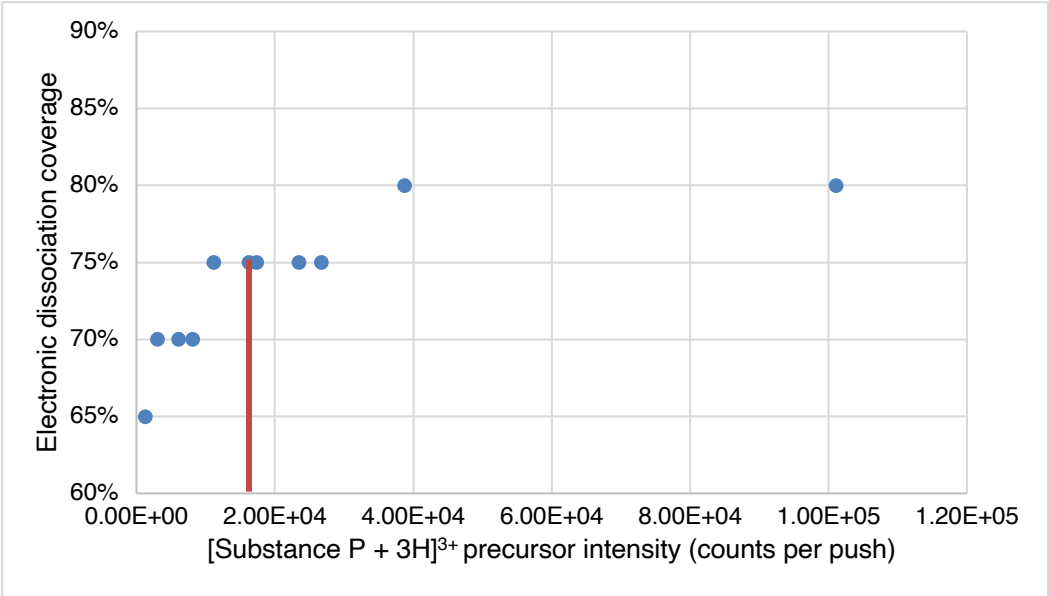

Figure 3.4.5. Electronic dissociation coverage verses $[Substance\ P + 3H]^{3+}$ precursor ion intensity (counts per push). The red line denotes where ETD was at the greatest efficiency ($1.73x10^4$ counts per push).

The greatest peptide sequence coverage was when the ETD efficiency was near maximal. One extra ETD fragment ion was formed when a higher abundance of precursor ions reacted with the ETD reagent. Ion z_{10}, 133.0

m/z, was detected at 60 counts per push and 148 counts per push when 3.87×10^4 counts per push and 1.01×10^5 counts per push of precursor ions were generated, which had previously not been observed. This is likely due to the inefficiency of the ions' formation, requiring a higher abundance of precursor ion in order for sufficient z_{10} to be generated and therefore detected. In addition to *c* and *z* ions, some *b* and *y* ions were detected, their occurrence attributed to vibrational dissociation. Vibrational activation of ions is caused by the energy given to ions at different stages of their journey through the mass spectrometer, for example as they travel through the StepWave, or at the initial point of ionisation. The unintentional vibrational fragmentation coverage can be plotted as a function of capillary voltage as shown in Figure 3.4.6. As one might expect, at higher capillary voltages, more vibrational fragmentation is induced. At the capillary voltage range in which ETD was most efficient, vibrational dissociation coverage is between 40-50%.

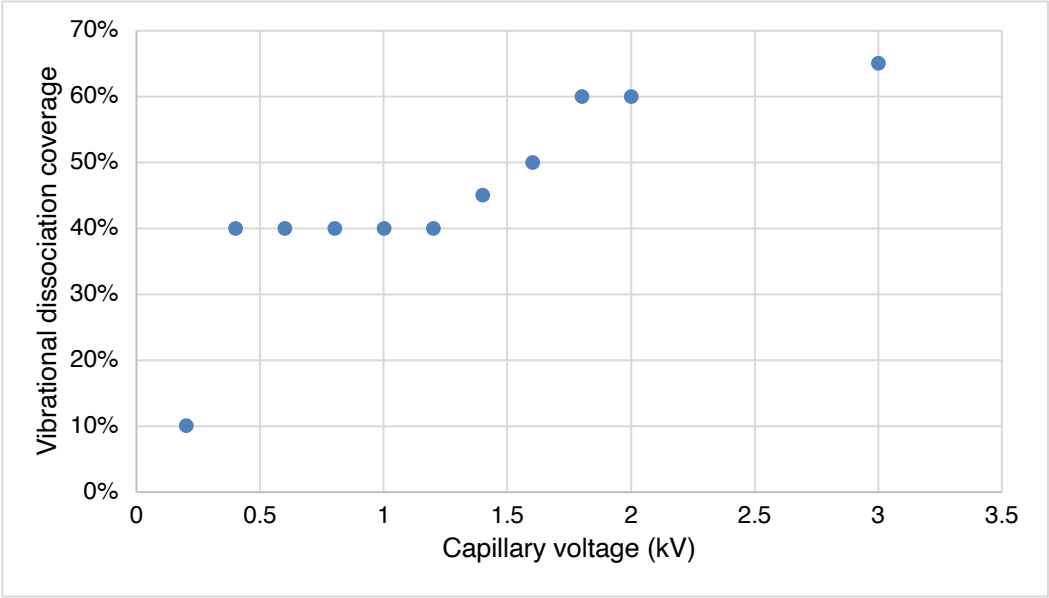

Figure 3.4.6. Vibrational dissociation coverage verses capillary voltage (kV).

3.4.1.2. Trapping ETD

Having established the optimum ratio of analyte to reagent, to further improve ETD efficiency from 25.9%, an alternative setup was explored. Instead of using conventional trap DC settings in glow discharge mode where trap DC voltage parameters were set to a negative value allowing the ETD reagent anions to pass through, the trap DC voltage parameters were set to a positive value which instead traps the reagent anions. This allows them to accumulate just before the trap region of the TriWave. When the instrument then switches polarity mid-acquisition, the positive values become negative, allowing the accumulated ETD reagent anions into the trap to react with the precursor cations. This cannot be achieved by simply increasing the number of ETD anions produced in source, as ionisation is already maximised. Figure 3.4.7 shows the comparison of ETD of substance P with and without trapping the anions just prior to the trap region of the TriWave.

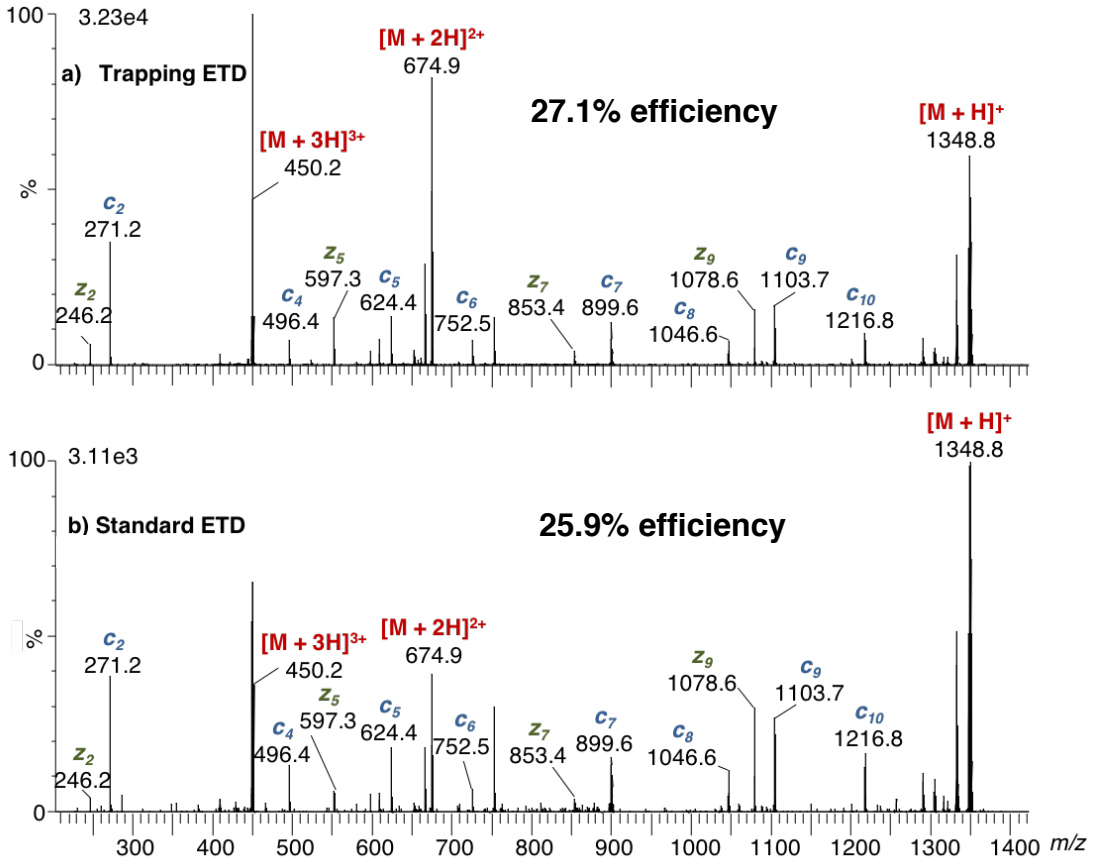

Figure 3.4.7. ETD product ion spectra for substance P using a) trapping ETD and b) standard ETD. All spectra were an average of 60 scans.

When tested on substance P, ETD efficiency increased to 27.1% as compared to 25.8%, with an increase in product ion peak intensity observed (Figure 3.4.7). The increased efficiency is likely due to the combination of a greater number of anions available to interact in the trap, and also an increase in time where interactions between cations and anions can occur. Although only a modest increase of 1.3%, the inherently low efficiency of ETD (as discussed in Section 1.2.6) means that any small increase in efficiency should not be taken lightly and can prove very useful in the application of ETD. A prime example of this is z_7 at *m/z* 853.4 (Figure 3.4.8). In non-trapping ETD, z_7 has poor signal-to-noise so is difficult to differentiate from background peaks, whereas in trapping ETD, this peak

has a clear improvement in signal-to-noise enabling confident assignment as a product ion. As a result, this setup will be used for the remainder of this work.

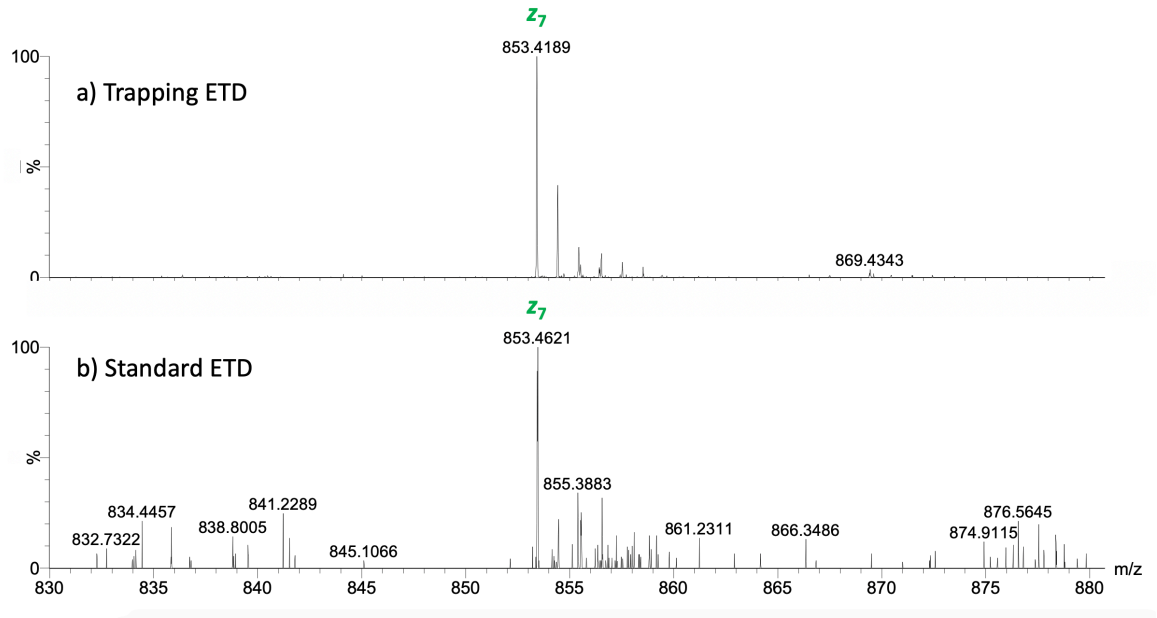

Figure 3.4.8. Substance P product ion z_7 following a) trapping ETD and b) standard ETD.

3.4.1.3. LC-ETD

2 pmol/µL substance P was injected onto an Acquity UHPLC BEH C_{18} 1.7 µm 2.1 x 50 mm column running a 10 minute gradient (Appendix Table 7.4.1). An LC-ETD method was set up to isolate [substance P + 3H]$^{3+}$ (*m/z* 450), and initiate ETD by lowering the trap TriWave height to 0.2 V. The results from this experiment are shown in Figure 3.4.9.

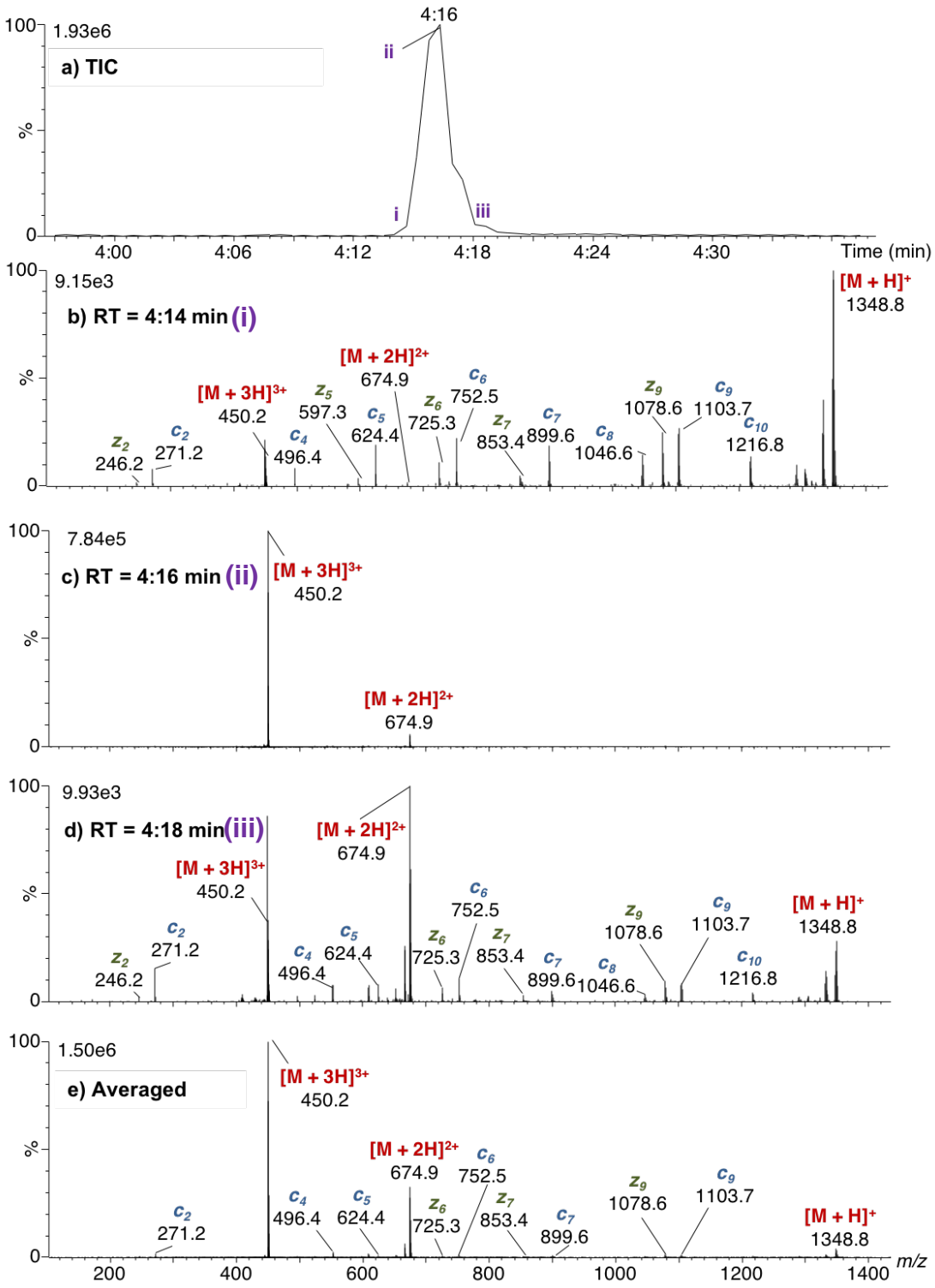

Figure 3.4.9. a) TIC and LC-ETD product ion spectra of $[M + 3H]^{3+}$ substance P, each a single scan at RT = b) 4:14 min, c) 4:16 min d) 4:18 min and e) averaged LC peak (9 scans, which is typical for ETD peptide data).

ETD was calculated to have an efficiency of 34.5% at (**i**), the onset of the eluting substance P (Figure 3.4.9b) and an efficiency of 19.7% at (**iii**)

(Figure 3.4.9d) at the conclusion of the substance P peak. At the apex of eluting substance P, (**ii**) (Figure 3.4.9c) the efficiency dropped to 0.4%. This is attributed to the intensity of the precursor ion rising above 2.34×10^4 counts per push, thereby reducing the efficiency of ETD as previously demonstrated. When this peak is averaged, as would be standard practice for data processing, the ETD efficiency is 6.8% (Figure 3.4.9e). This is because there are more scans across the peak with poor ETD efficiency, however, as suitable ETD efficiency was achieved at the start and end of the substance P LC peak elution, there are clear opportunities to optimise ETD efficiency across the entire peak.

The efficiency of LC-ETD is known to be generally low. As previously established, the absolute intensity ratio of multiply positively charged analyte molecule to ETD reagent anion must be kept at a constant. As an LC peak elute from the column into the mass spectrometer, the intensity of the analyte ions changes, resulting in inefficient ETD. There are several reasons why efficiency is an important factor when considering MSMS techniques: If the efficiency of product ion formation is too low, product ions will be difficult to assign, due to their signal-to-noise, as demonstrated in Figure 3.4.8. As well as the difficulty in manual assignment of peaks, come the difficulty of automatic peak via software packages such as Thermo's BioPharmaFinder, and Waters' BioPharmaLynx and UNIFI. These software packages all use peak detection, based on calculations of ion intensity and signal-to-noise. Product ions are then assigned by the software based on factors such as accurate mass measurements and ion

isotope ratios. This currently poses a problem for automatic assignment of LC-ETD data, as with low efficiency comes low product ion abundance and poor signal-to-noise, sometimes leading to poor accurate mass measurements. By increasing the efficiency of LC-ETD, both manual and automatic peak assignment of product ion spectra will be less challenging.

3.4.1.4. LC-ETD with dynamic capillary voltage

The need to maintain a fixed ratio of analyte cation to ETD reagent anion has been established in Section 3.4.1.1. This can be achieved manually by lowering the capillary voltage, resulting in a reduction in the abundance of precursor analyte ions to a level commensurate with efficient ETD as shown in Figure 3.4.1, and would provide a possible solution to the poor ETD efficiency observed in Figure 3.4.4. WREnS (Waters research enabled software) was used to monitor the intensity of the precursor ion and adjust the capillary voltage on-the-fly. By this means the ion abundance could be controlled dynamically within the timeframe of the LC peak elution so that the precursor ion peak intensity could be detuned at its maximum elution time in an effort to maintain the ratio of analyte to ETD reagent ions. This involves programming WREnS to step down the capillary voltage as the monitored peaks start to become more intense (to a pre-set minimum), and also to step up the capillary voltage as the peaks start to drop off in intensity, as visualised in Figure 3.4.10. The WREnS script is given in appendix.

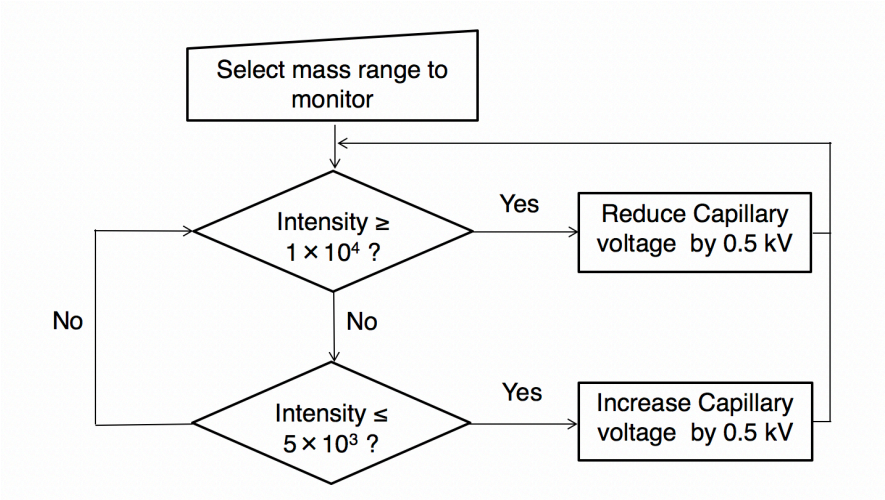

Figure 3.4.10. Visualisation of dynamic capillary voltage control *via* WREnS. Script can be seen in Appendix Script 7.4.1.

The data shown in Figure 3.4.11 results from stepping down the capillary voltage from 3 to 0.2 kV.

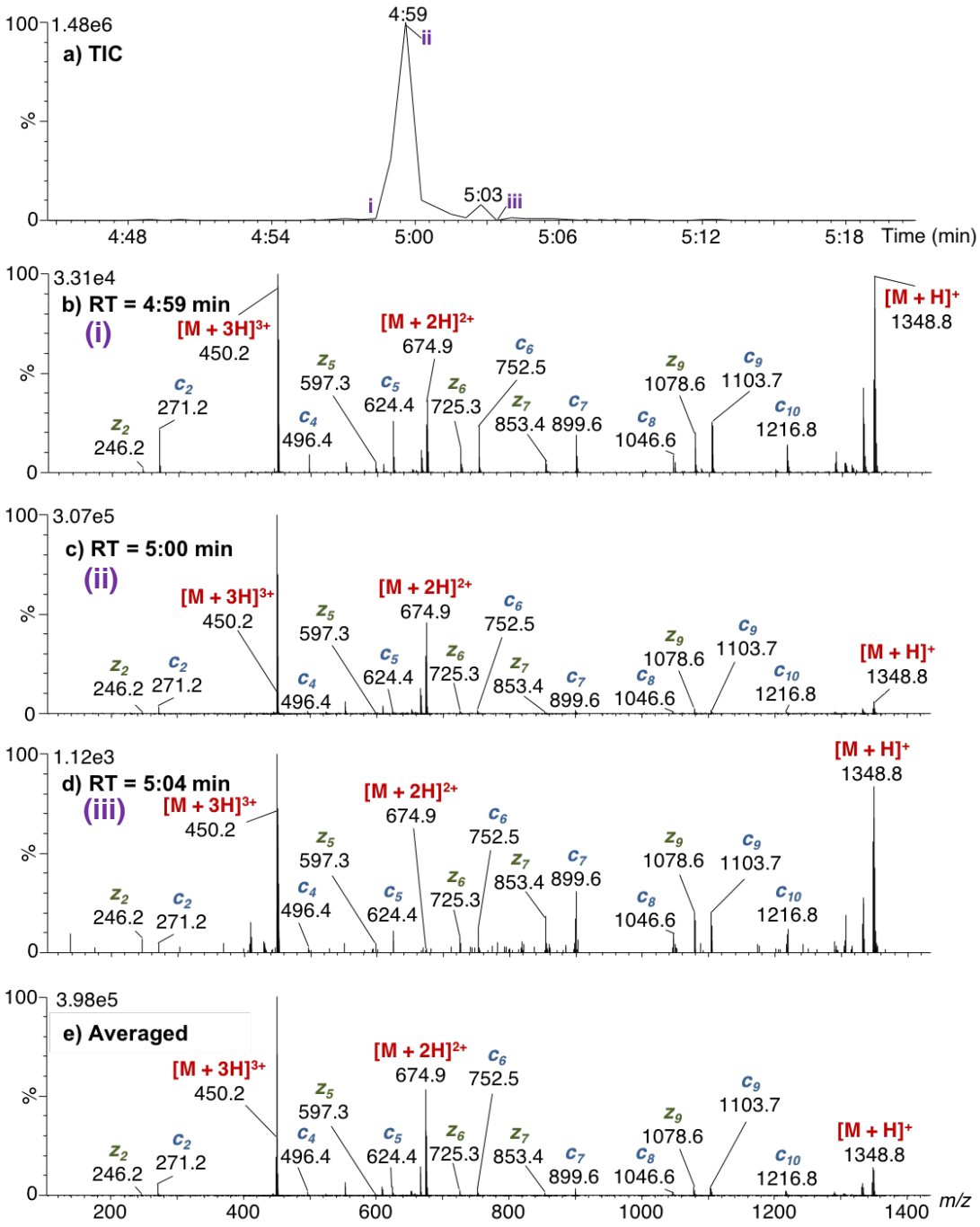

Figure 3.4.11. a) TIC, LC-ETD product ion spectra of $[M + 3H]^{3+}$ substance P, each a single scan at retention time (RT) = b) 4:59 min c) 5:00 min d) 5:04 min and e) averaged LC peak (9 scans) using WREnS to dynamically control capillary voltage from 3 to 0.5 kV.

ETD efficiency for (i) Retention time (RT) = 4:59 min, (ii) RT = 5:00 and (iii) RT = 5:04 as shown in Figure 3.4.11 was calculated as 27.4%, 10.4% and 21.2% respectively as shown in Table 3.4.1.

Experiment	ETD efficiency (i)	ETD efficiency (ii)	ETD efficiency (iii)	ETD efficiency (averaged peak)
LC-ETD	32.4%	0.4%	19.7%	6.8%
WREnS LC-ETD (capillary voltage)	27.4%	10.4%	21.2%	14.6%

Table 3.4.1. ETD efficiencies for substance P at (i) the start of the LC peak, (ii) the apex of the LC peak and (iii) the end of the LC peak.

This improved ETD efficiency at the apex of the peak by 10% and although a significant improvement, 10.4% efficiency is still low compared with the start and end of the LC peak. High ETD efficiency was maintained at the start and end of the peak, and when the mass spectra averaged across the peak the ETD efficiency calculated was 14.7% (Figure 3.4.11e), an improvement on the 6.8% obtained with dynamic control of the capillary voltage. Despite lowering the capillary voltage to 0.5 kV, the peak intensity at *m/z* 450.2 for $[M + 3H]^{3+}$ only dropped to 3.1 x 10^5 counts per push and not 1.73 x 10^4 counts per push proven to be required in Section 3.4.1.1. Whilst sufficient to improve ETD efficiency, there remained scope to improve this yet further.

3.4.1.5. LC-ETD with dynamic DRE control

A second approach was explored to overcome limitation identified with dynamic control of the capillary voltage. The DRE lens was chosen as this is designed to be used to control analyte abundance for accurate mass

measurement purposes as described in Section 3.2.1. Rather than controlling the number of molecules which are ionised, the DRE lens attenuates the number of analyte ions that are allowed into the TriWave region of the mass spectrometer. WREnS was used to trigger the DRE attenuation only when the instrument was in positive mode, *i.e.* forming analyte cations, therefore the number of ETD reagent anions allowed into the trap was not adversely affected. An additional improvement to the WREnS script was going straight to the minimum DRE lens voltage after the trigger intensity of 1 x 10^4 was reached. Once the precursor ion intensity drops below 5 x 10^3, the DRE lens setting reverts to 99.9% transmission. This methodology aligns with how DRE lens settings are utilised for accurate mass measurement purposes during the standard operation of the instrument. This can be visualised in Figure 3.4.12.

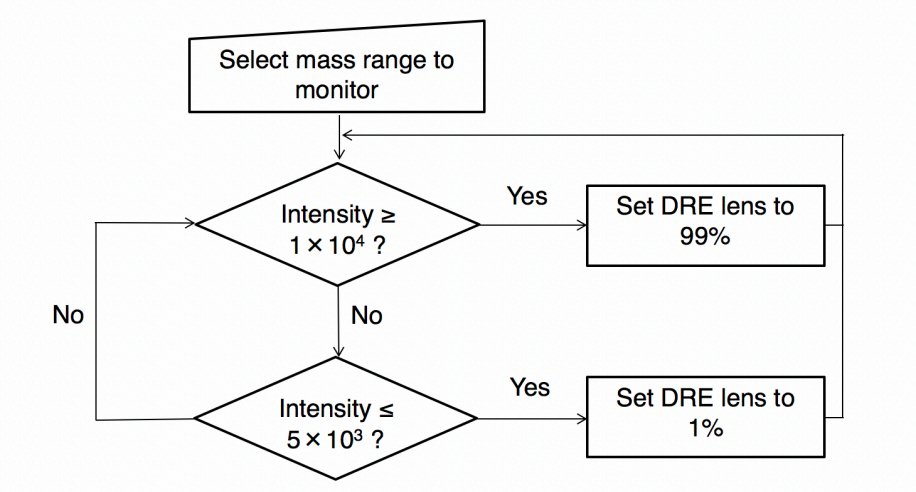

Figure 3.4.12. Visualisation of DRE lens control *via* WREnS. Script can be seen in Appendix Script 7.4.2.

Figure 3.4.13 shows the result of this approach, with ETD efficiency for (i) RT = 4:46 min, (ii) RT = 4:47 and (iii) RT = 4:52 as shown in Figure 3.4.13 being 32.7%, 24.8% and 29.6% respectively.

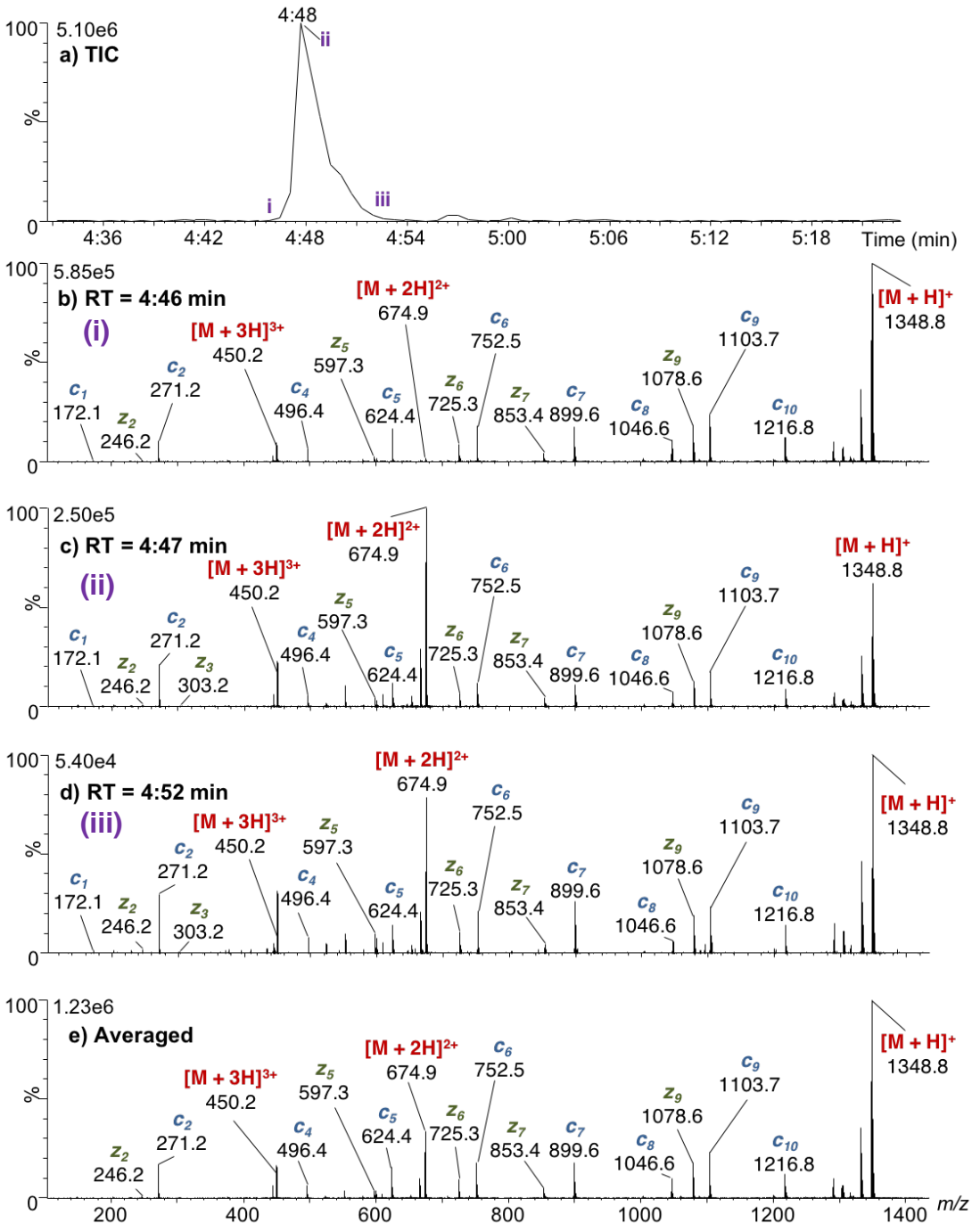

Figure 3.4.13. LC-ETD product ion spectra of $[M + 3H]^{3+}$ substance P, each a single scan at RT = a) TIC, b) 4:46 min c) 4:47 min d) 4:52 min and e) averaged LC peak (9 scans) using WREnS to dynamically control the DRE lens setting from 99.9% to 1%.

At the apex of the LC peak, ETD efficiency has increased by 24.4% compared with standard LC-ETD. The ETD efficiency for the averaged peak (Figure 3.4.13e) was 31.1%, a vast improvement of 24.3% compared with standard ETD as shown in Table 3.4.2.

Experiment	ETD efficiency (i)	ETD efficiency (ii)	ETD efficiency (iii)
LC-ETD	32.4%	0.4%	19.7%
WREnS LC-ETD (capillary voltage)	27.4%	10.4%	21.2%
WREnS LC-ETD (DRE lens setting)	32.7%	24.8%	29.6%

Table 3.4.2. ETD efficiencies for substance P at (i) the start of the LC peak, (ii) the apex of the LC peak and (iii) the end of the LC peak for LC-ETD, WREnS LC-ETD using capillary voltage to control analyte ion abundance and WREnS LC-ETD using the DRE lens to control analyte ion abundance.

3.4.1.6. Summary of LC-ETD using capillary voltage and dynamic DRE control

Figure 3.4.14 shows the resultant product ion spectra for standard LC-ETD, WREnS LC-ETD utilising capillary voltage to control precursor ion intensity and WREnS LC-ETD using the DRE lens to control precursor ion intensity. The ETD efficiencies were calculated for the summed spectra across the entire LC peak (11 scans), their ETD efficiencies are given in Table 3.4.3.

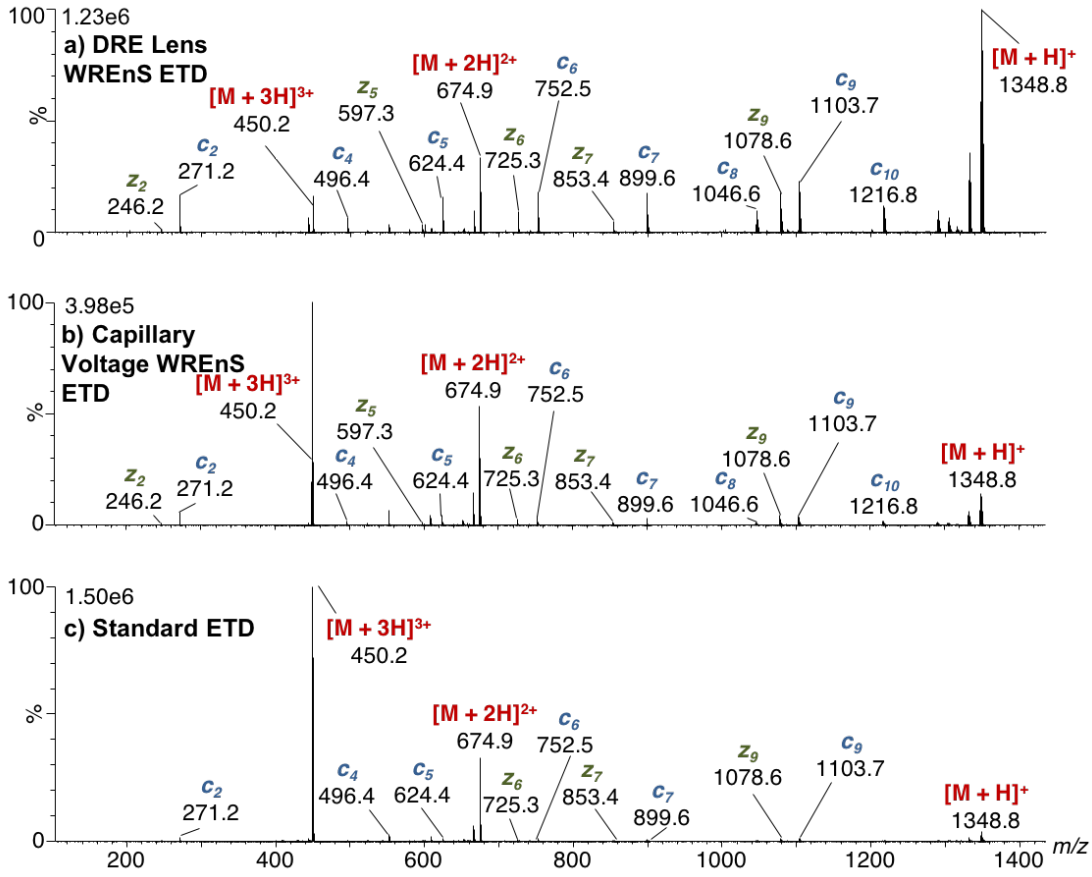

Figure 3.4.14. Averaged ETD product ion spectra summed across the entire LC peak for a) WREnS LC-ETD using the DRE lens to control precursor ion intensity, b) WREnS LC-ETD utilising capillary voltage to control precursor ion intensity and c) standard LC-ETD (9 scans).

Experiment	ETD efficiency	ETD coverage	Vibrational efficiency	Vibrational coverage
LC-ETD	6.8%	75%	0.1%	50%
WREnS LC-ETD (capillary voltage)	14.7%	70%	0.2%	55%
WREnS LC-ETD (DRE lens setting)	31.1%	75%	1.1%	70%

Table 3.4.3. ETD efficiencies and coverages for substance P for spectra summed across an entire LC peak and contributions from vibrational dissociation.

Figure 3.4.14 shows the increase in ETD efficiency has translated to an increase in the abundance of product ions and improved signal-to-noise. The product ions in 3.4.14a, compared with 3.4.14c are more clearly differentiated from the background signal, which would allow for automated peak detection and assignment of peaks by software. Furthermore, although for known peptide analytes the fragmentation by ETD can be predicted, for unknown peptide analytes, or small molecules, it is important that the product ions are clearly distinguishable from the background. No new product ions were formed using any WREnS approach, although very low abundance product ions, such as z_{10}, c_{10} and c_8 were more easily distinguishable from the background. The difference between 75% and 70% ETD coverage is a single product ion, c_1 which is not observed by WREnS LC-ETD when the capillary voltage is used to control analyte ion intensity. The c_1 ion is very low abundance in all ETD product ion spectra, so makes little difference to overall efficiency. Figure 3.4.15 shows the coverage achieved using the DRE lens WREnS script, which is the same as for standard LC-ETD and minus the c_1 ion for the capillary voltage WREnS scripted ETD.

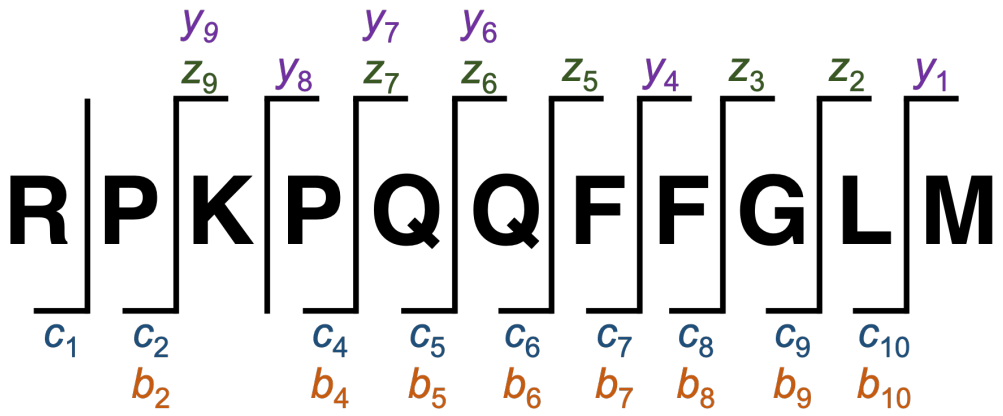

Figure 3.4.15. ETD fragmentation resulting from dynamically controlling the DRE lens based on precursor ion peak intensity with *b* and *y* ions resulting from unintentional vibrational dissociation.

It should be noted that singly charged product ion z_4 at *m/z* 450.2063 has a mass difference from the ^{13}C isotope of [substance P + 3H]$^{3+}$ of 0.04 Da, and due to the low abundance of product ions, compared with the abundance of unreacted [substance P + 3H]$^{3+}$, the resolution of the instrument is not sufficient to resolve the two peaks. ETD spectra for substance P contain a number of *b* and *y* ions with 70% sequence coverage as shown in Figure 3.4.15. *b* and *y* ions are commonly the result of vibrational dissociation. In these experiments, the intensity of the *b* and *y* ions increased compared with the intensity of the precursor ions in parallel with the *c* and *z* ions. This is likely due to the reduced abundance of precursor ion due to DRE attenuation before the TriWave. This suggests the *b* and *y* ions are being formed after the DRE lens. The reduced abundance of precursor ion in relation to *b* and *y* ions results in a higher calculated efficiency.

3.4.1.7. Effect of reverse-phased chromatography solvent gradients on ETD reagent ion intensity

In order to further improve and manage the ratio of ETD reagent ion intensity to analyte ion intensity during LC, the effect of solvent gradient on the ETD reagent ion signal was investigated by monitoring *m/z* 137.0477, as shown in Figure 3.4.16.

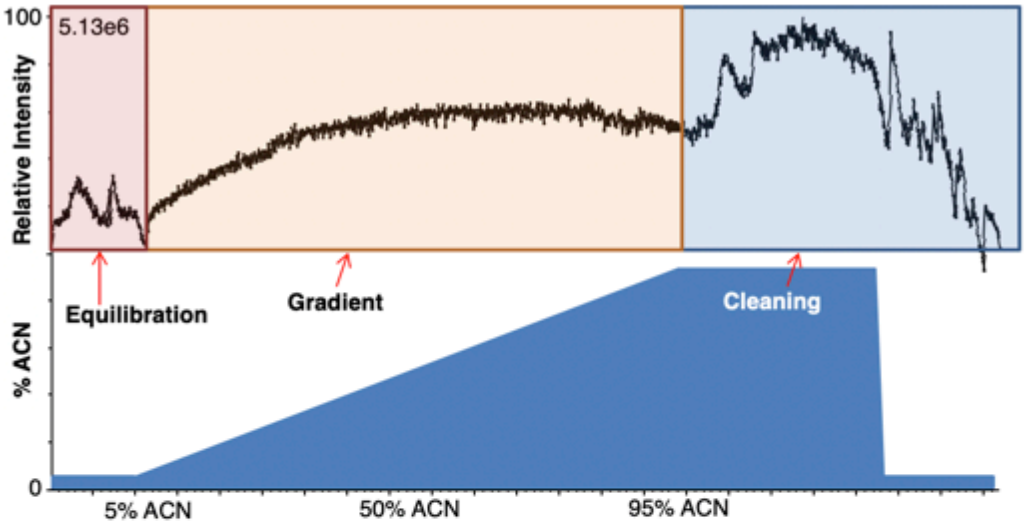

Time (s)	Flow Rate (µL/mL)	% H_2O	% Acetonitrile
0	0.2	95	5
2	0.2	95	5
15	0.2	5	95
20	0.2	5	95
20.5	0.2	95	5
22	0.2	95	5

Figure 3.4.16. EICC of *m/z* 137, 1,4-nitrotoluene over the course of an LC gradient.

The change in intensity of [*p*-nitrotoluene]$^{-\cdot}$ as the reversed phase LC gradient changed from aqueous solvent conditions to organic was

calculated to be 20.6% and is likely due to the glow discharge reaction being more efficient in high acetonitrile conditions, compared with a high aqueous environment at the start of an LC gradient. This has repercussions for LC-ETD, as analyte ions which elute at higher organic solvent ratios may fragment more efficiently by ETD due to the increased number of ETD reagent anions available to react in the trap. As an example, substance P elutes at around 45% acetonitrile, meaning there would be little effect of reduced availability of ETD reagent, however, early eluting peaks may have less ETD reagent available to react. The ideal ratio of analyte precursor cation abundance to ETD reagent anion was shown to be 1.73 x 10^4 : 1 x 10^6. If there was a 20.6% drop in ETD reagent anion abundance, the optimised analyte cation abundance would also drop to 7.94 x 10^5. A possible solution to this would be to alter the WREnS script to have different trigger intensities depending on where in the gradient the precursor ions elute.

3.4.1.8. LC-ETD of Bovine Serum Albumen digest

To further study the effect of solvent environment during the ETD stage, dynamic control of the DRE lens was utilised while running a trapping ETD experiment on a BSA digest, a complex mixture of peptides that vary in abundance, observed charge state and chemical nature and elute over a wide retention time range. The LC gradient employed can be seen in Table 7.4.2 in the Appendix. Five peptides with very different retention times and ion abundances were chosen, four $[M + 3H]^{3+}$ peptides and one $[M + 2H]^{2+}$

peptide. ETD efficiencies were calculated on a standard LC-ETD (no WREnS control) as shown in Table 3.4.4.

Peptide	Retention Time (min)	Charge State	Theoretical Monoisotopic Uncharged Mass (Da)	ETD Efficiency	ETD Coverage
C*C*TKPESER	8.9 (4.5 % ACN)	3	1167.4537	3.7%	81%
HLVDEPQNLIK	35.1 (17.6 % ACN)	2	1304.7089	0.1%	35%
SLHTLFGDELC*K	44.3 (22.2 % ACN)	3	141.6864	2.5%	86%
LFTFHADIC*TLPDTEK	48.6 (24.3 % ACN)	3	1906.9135	0.7%	73%
HPYFYAPELLYYANK	54.6 (27.3 % ACN)	3	1887.9196	1.8%	82%

Table 3.4.4. ETD efficiencies for 5 BSA tryptic peptides on a standard LC-ETD analysis.

To improve ETD efficiency for each of these peptides, the WREnS script was altered to include delay times, which correspond to the retention time of each peptide. The targeted *m/z* range is shifted to monitor each peptide after different delay times, which allows the DRE setting to change for different peptides at different RTs as shown in Figure 3.4.17.

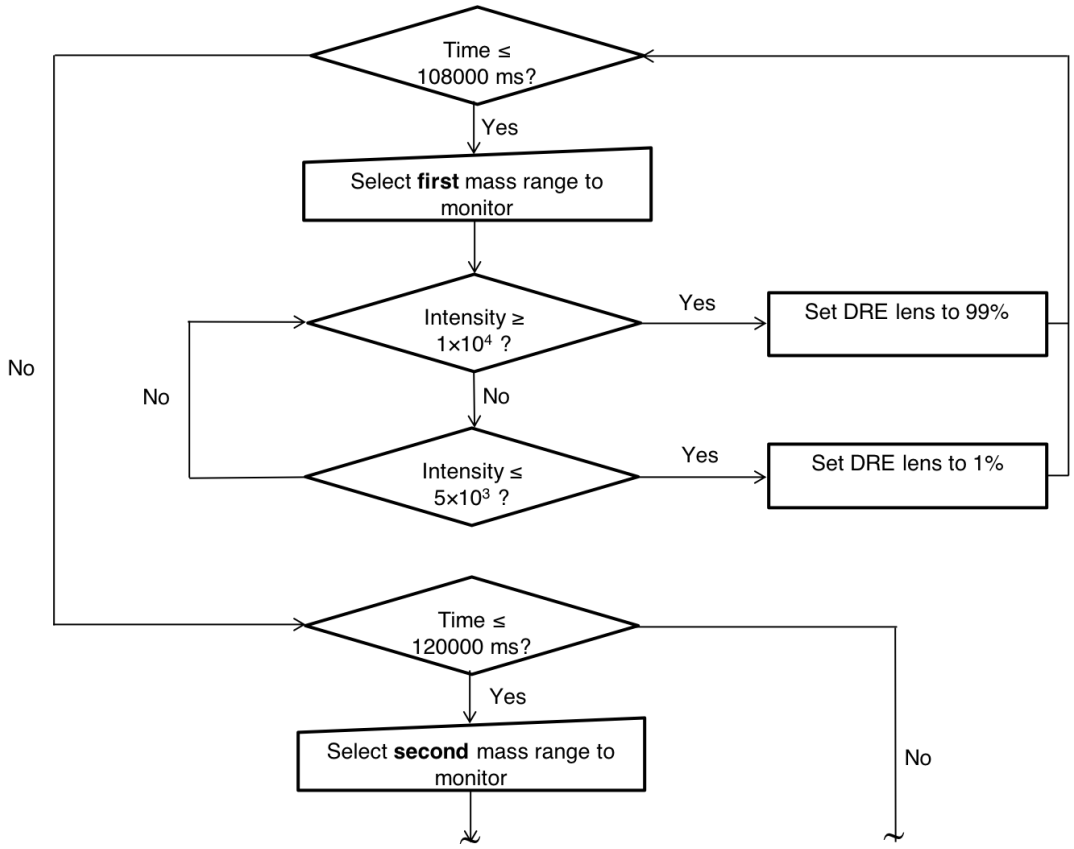

Figure 3.4.17. Visualisation of DRE lens control *via* WREnS using RT as target for mass range. Script can be seen in Appendix Script 7.4.3.

By this method, the DRE lens voltage changed automatically for each peptide as a function of analyte ion abundance, allowing for the precursor ion intensity to be reduced as required. To determine the retention time windows, the BSA digest was first analysed without WREnS. Figure 3.4.18a shows the chromatogram of a BSA peptide using the same precursor ion intensities to trigger the DRE lens script and DRE lens voltages informed by the analysis of substance P in Section 3.4.2.5. The DRE setting reverted to 99.9% too quickly, resulting in several iterations of DRE settings changing from 99.9% to 1% resulting in too many scans to have a precursor ion which is too strong for efficient ETD. This is

exemplified in Figure 3.4.18a. At **i**, the DRE lens setting of 1% is triggered as expected, however at **ii**, the intensity of precursor ion falls below 5×10^3 which results in the DRE setting reverting to 99.9%. This has the effect of causing inefficient ETD at **iii**, before the DRE setting is again set to 1% for the remainder of the most intense section of the peak elution. When averaging the LC peak, too many scans with a DRE lens setting of 99.9% results in low ETD efficiency.

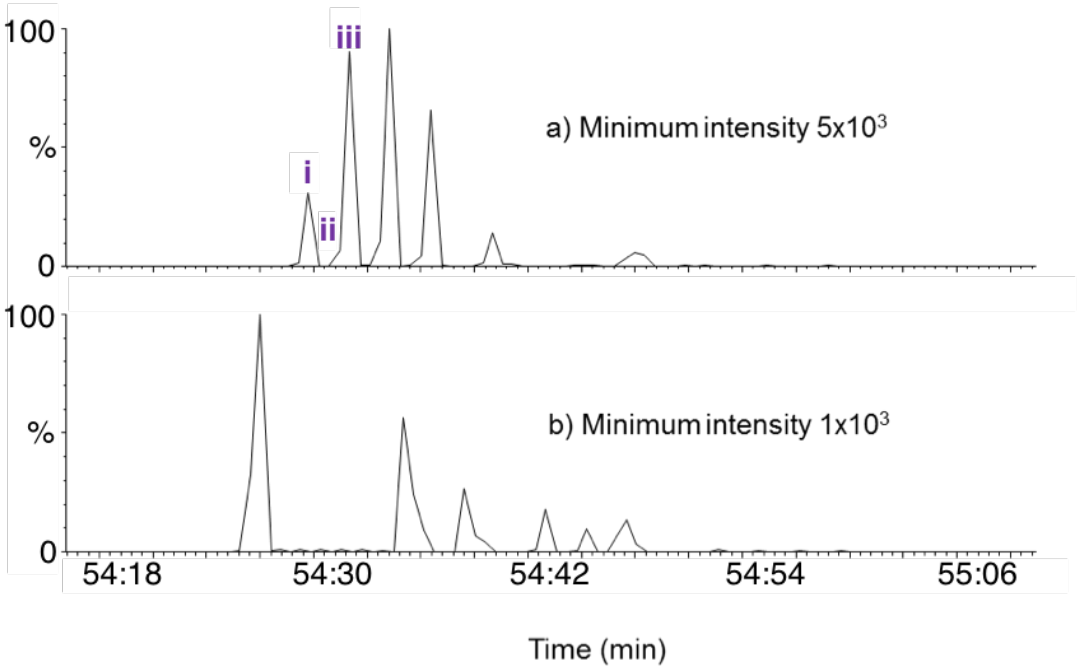

Figure 3.4.18. LC-ETD TIC where DRE setting minimum intensity set to a) 5×10^3 and b) 1×10^3.

The trigger intensity of 5×10^3 which instructs the DRE setting to return to 99.9% was altered to 1×10^3, which resulted in the DRE setting remaining at 1% across the most intense section of the elution, as shown in Figure 3.4.18b. ETD efficiency for the 5 peptides is shown in Figure 3.4.19 when a) no DRE control was used, b) DRE lens control was used with the

minimum trigger intensity set to 5×10^3 and c) DRE lens control was used with the minimum trigger intensity set to 1×10^3.

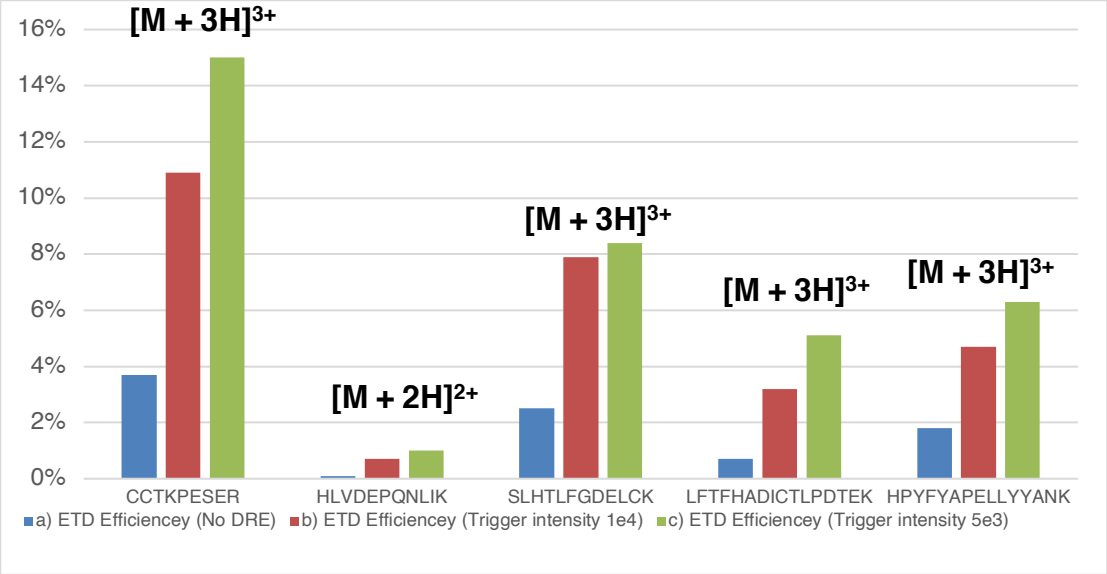

Figure 3.4.19. ETD efficiency for the 5 BSA tryptic peptides when a) no DRE control was used, b) DRE lens control was used with the minimum trigger intensity set to 5×10^3 and c) DRE lens control was used with the minimum trigger intensity set to 1×10^3.

ETD efficiency was lower for LVDEPQNLIK, as the doubly charged precursor ion was selected for MSMS; ETD for $[M + 2H]^{2+}$ has been shown to be less efficient for lower charge states than more highly charged ions. [92] Overall the efficiencies are lower than for substance P, which to some extent is to be expected as the concentration of individual peptides cannot be controlled in a biological process (tryptic digestion) whereas an optimised concentration of substance P was used. Fragmentation efficiency will also strongly depend on the amino acid sequence of the peptide. To put these efficiencies into perspective, Figure 3.4.20 shows the ETD product ion spectra for $[CCTKPESER + 3H]^{3+}$. The most obvious improvements can be seen in both the increased relative intensity of the

charge reduced $[M + 2H]^{2+}$ and $[M + H]^{+}$ species and the higher relative abundance of product ions z_4, z_5 and c_5. Figure 3.4.21 shows the fragmentation schematic for CCTKPESER.

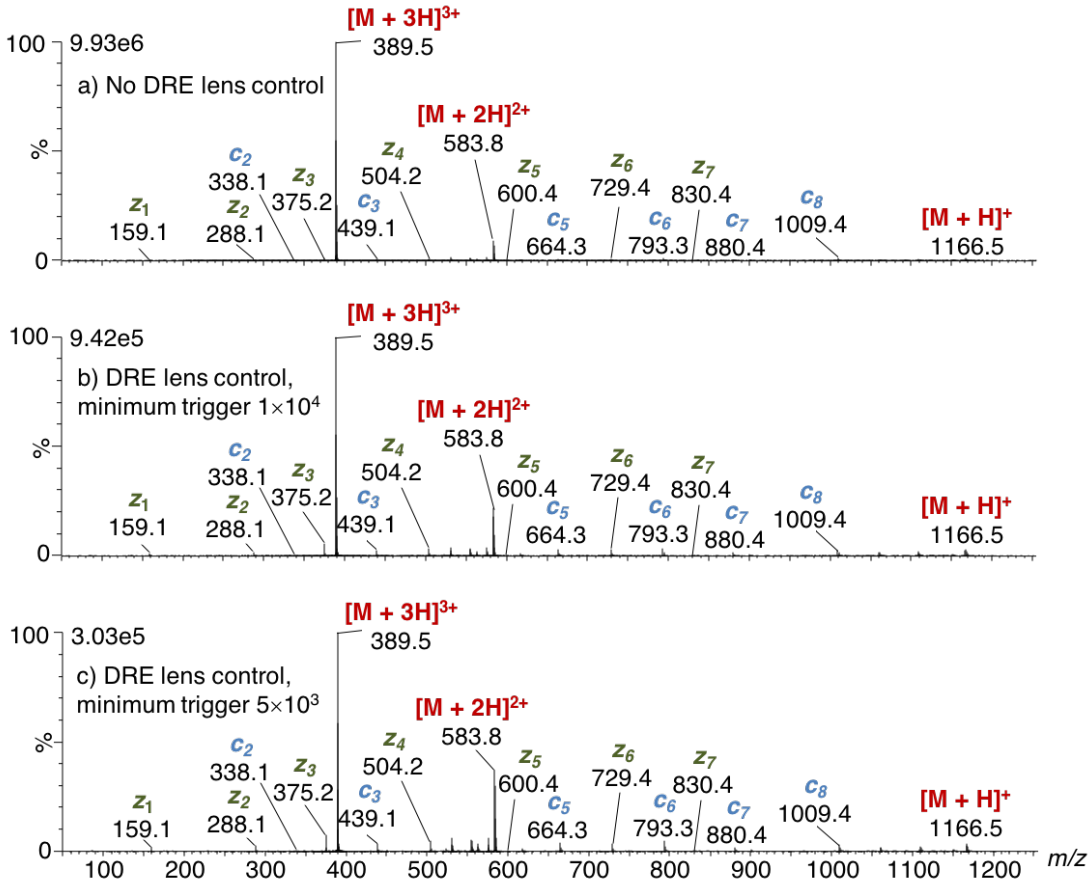

Figure 3.4.20. LC-ETD product ion spectra of CCTKPESER with a) no DRE lens control, b) DRE lens control with the minimum precursor intensity set to 1×10^4 and c) DRE lens control with the minimum precursor intensity set to 5×10^3.

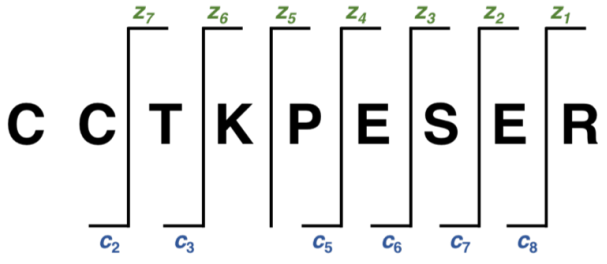

Figure 3.4.21. Fragmentation schematic for BSA peptide 1.

Figure 3.4.22 shows the ETD product ion spectra, averaged over the LC peak for each of the 5 peptides.

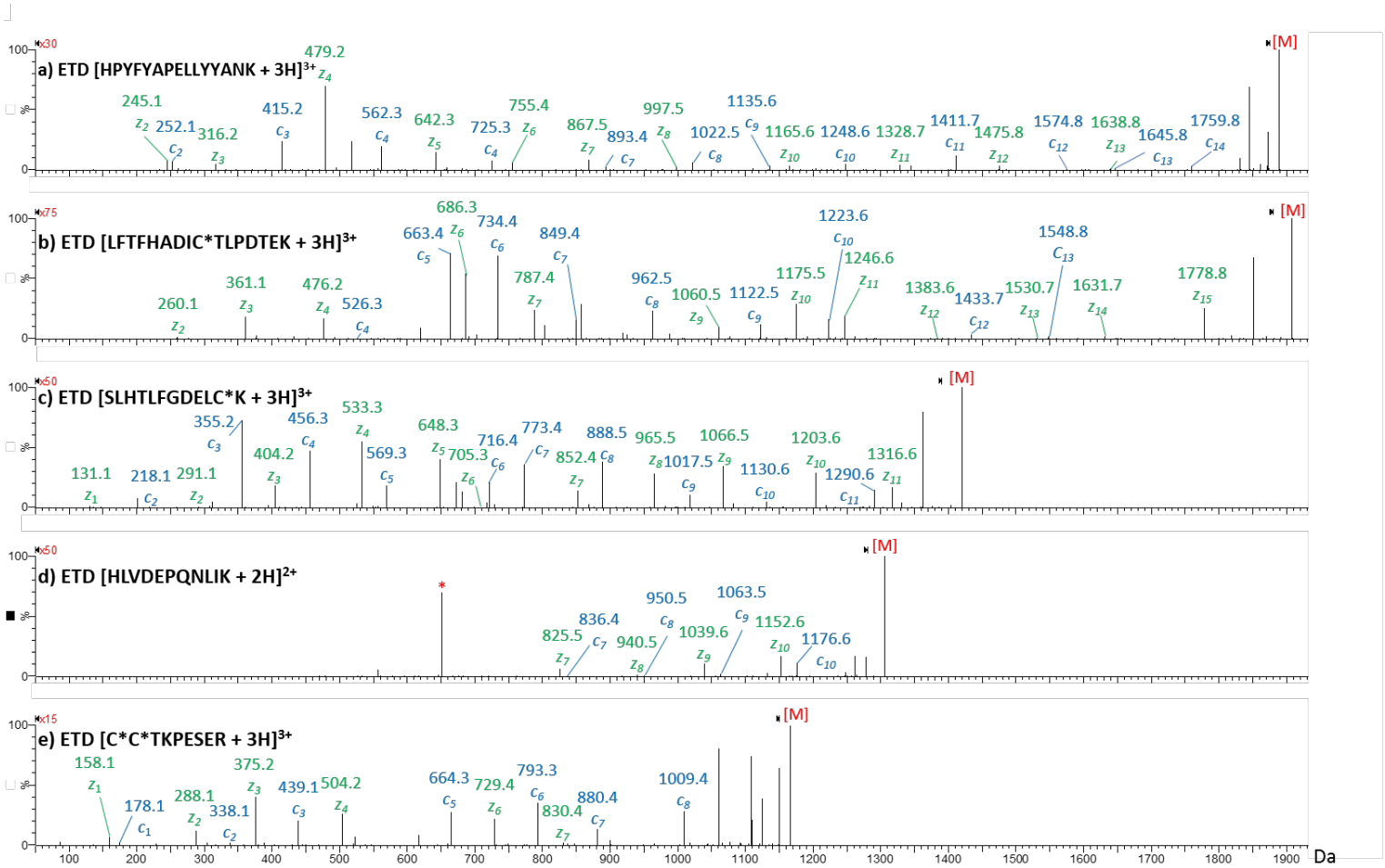

Figure 3.4.22. TOF transformed ETD product ion spectra for each BSA digested peptide. *denotes ions allowed through the isolation window during ETD not related to the precursor ion.

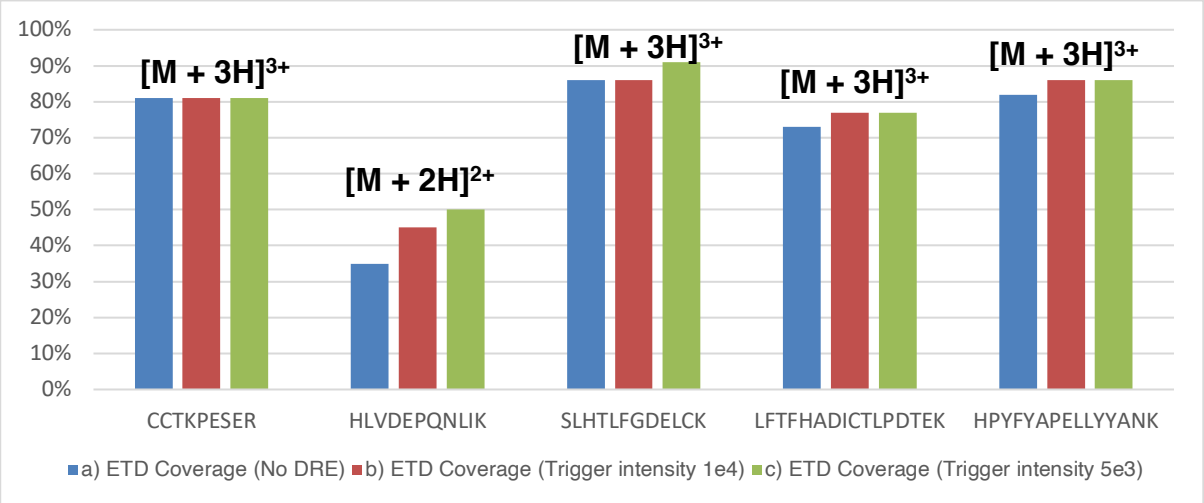

Figure 3.4.23. ETD coverage for the 5 BSA tryptic peptides when a) no DRE control was used, b) DRE lens control was used with the minimum trigger intensity set to 5×10^3 and c) DRE lens control was used with the minimum trigger intensity set to 1×10^3.

As shown in Figure 3.4.23, some increase in sequence coverage was observed for some of the peptides with dynamic control of the DRE lens voltage. The most significant improvement was observed for the doubly protonated peptide. In all cases, the DRE lens script gave the greatest efficiency and sequence coverage.

3.4.1.9. LC-ETD with SC-ESI of small organic molecules

To apply this method to the study of small organic ions, supercharging reagent *m*NBA was introduced into the ESI spray solution post LC using a T-piece and syringe pump at a flow rate of 10 μL/min. A mix of four small molecules (cediranib; AZD9291; chloroquine and dansylcadaverine) were analysed with and without the dynamic DRE lens voltage control. Peptides have known and regular cleavage sites, whereas small molecules do not

so it is hard to make a direct comparison. ETD efficiency was calculated by using product ions formed only by ETD, as identified in Chapter 2, and by using the same method as in Section 3.4.1.1. Figure 3.4.24 shows the ETD efficiency of $[M + 2H]^{2+}$ small molecules for a) standard LC-ETD and b) LC-ETD with dynamic DRE lens control.

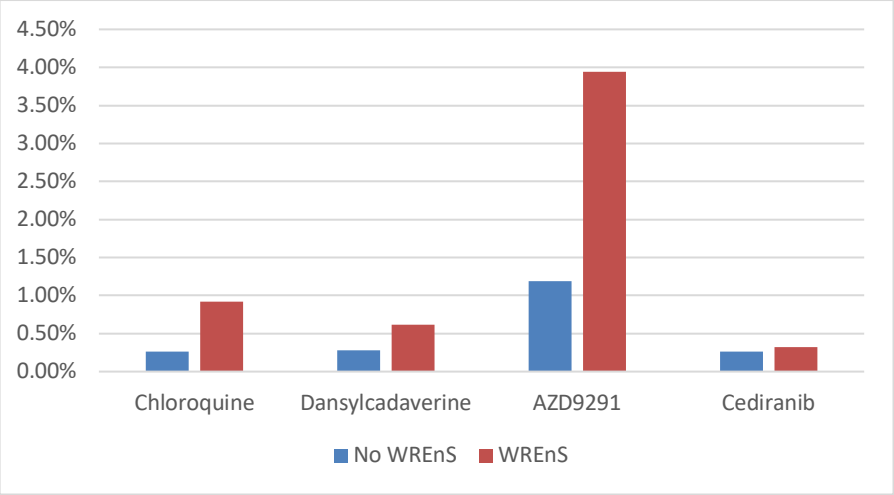

Figure 3.4.24. ETD efficiency of $[M + 2H]^{2+}$ small molecules for a) standard LC-ETD and b) LC-ETD with dynamic DRE lens control.

This is the first time ETD has been successfully performed on small molecules on an LC timescale. The efficiencies are less than 5%, much lower than those shown for the triply protonated peptides. $[M + 2H]^{2+}$ HLVDEPQNLIK has a comparable efficiency of 1%. This is likely due to the precursor ions all being doubly charged, which has been shown to result in inefficient ETD due to the lower charge surface density. [92] The product ion spectra, and discussion related ETD of these small molecules is covered in Chapter 2.

3.4.2. Conclusion

Dynamic control of the DRE lens greatly improved the efficiency for LC-ETD and is shown to be beneficial for routine LC-ETD analysis of peptides and small molecules. In order to use the WREnS script for more than one analyte, the retention times must be determined. In practice, this could be used in harmony with CID: The first LC-MS run could be used to get the retention times and gain CID spectra for the analytes, with the second run being a WREnS LC-ETD run, using the retention times obtained from the first run for the WREnS script. By reducing the overall number of analyte cations able to enter the trap region of the TriWave, but allowing all ETD reagent anions into the trap, a more constant ratio of analyte ion intensity : ETD reagent ion intensity was achieved compared with standard LC-ETD. This enabled ETD to be performed on a range of samples. One factor to take into account is chromatographic peak width; if the chromatographic peaks do not consist of sufficient mass spectra, then the time taken to change the DRE lens settings may not occur fast enough to trigger before peak elution is complete. This could be easily overcome by either reducing scan time or slowing down the chromatography to increase peak width, although this must be balanced with obtaining sufficient ion statistics for accurate mass measurements. In Section 3.4.1.7 it was shown that a greater abundance of ETD reagent anions were available later in the reverse phase gradient due to solvent effects. Interestingly, increased ETD

efficiency for later eluting peptides was not observed in Section 3.4.1.8, although this is likely to differences in the amino acid sequence as previously noted. From an applications point of view, the product ions have an improved signal-to-noise. This increase in signal-to-noise not only allowed for easier manual data processing, but also allows automated peak picking possible for processing software packages. For the small molecules, ETD LC-ETD with the DRE lens control WREnS script was comparable with that achieved by infusion ETD, with the usefulness of ETD for small molecules being discussed at length in Chapter 2. In this work the DRE lens WREnS script has been used as a pure research tool. This work demonstrates the clear advantages using the DRE lens WREnS script in gaining greater ETD efficiency for LC-ETD experiments. Although currently cumbersome to use, a more user-friendly software solution could be developed which could be built into a regular software interface. This would be taken on by a MS manufacture, and is beyond the scope of this work.

4. Conclusion

Electron-based tandem mass spectrometric techniques have been shown to be useful for the structural elucidation of small organic molecules, providing complementary product ion spectra, allowing for more in-depth characterisation. For phosphorylated molecules, the use of EID allows for targeted fragmentation by selection of precursor ions with varying numbers of sodium atoms associated with the ion. The electron from the EID process is likely attracted to the proton or sodium cation, which drives the shift in fragmentation observed. This targeted approach to structural elucidation is useful during the development stages of pharmaceutical drugs, where changes to functional groups are commonly made and may need to be examined in detail. However, in general, the most MSMS information was gained through EID of monosodium species, with unique product ions being formed. This observation indicates that for the structural characterisation of small phosphorylated molecules, EID of a monosodium species should be prioritised.

ETD was successfully performed on doubly protonated small molecules. A competitive reaction between electron-transfer and proton-transfer was observed following interaction of doubly protonated analyte molecules and ETD reagent radical anions. The competition between electron and proton transfer is most likely driven by physicochemical differences between analyte molecules such as electron and proton affinities and Franck-Condon factors. When electron-transfer was observed, complementary product ions to CID were generated, allowing for improved structural

elucidation of the small organic molecules. The use of SCRs to aid in formation of $[M + 2H]^{2+}$ increases the scope of this technique, allowing a greater number of small molecules to be analysed by ETD. *m*NBA was shown to give the most benefit to the formation of doubly protonated species. The main mechanism for the supercharging phenomenon is likely due to the high boiling point of mNBA, which results in less evaporative cooling of ESI droplets and leads to *m*NBA rich, charge dense droplets prior to Columbic explosion and analyte ionisation. In addition, optimisation of source parameters on an analyte-to-analyte basis has proven key in the formation of $[M + 2H]^{2+}$ which, if performed prior to ETD, could also increase the scope of the analysis.

The use of ETD combined with liquid chromatography, whether for small molecules or peptides, has been enhanced by way of a WREnS script that controls the DRE lens in Waters' Synapt G2-S instruments. Typically, LC-ETD is inherently inefficient due to the variance in ratio of multiply charge precursor ion and ETD reagent radical anion as an analyte elutes from a column. A WREnS script that attenuates the ion beam as analyte ions are transmitted to the trap region of the mass spectrometer has been shown to be affective in keeping the ratio of analyte precursor ion to ETD reagent anion relatively constant, which has produced an increase in ETD efficiency across an LC peak. This is a problem limited to Waters instrumentation, with other manufacturers such as Thermo and Bruker implementing an automatic gain control function, which controls precursor ion abundance prior to ETD. This improvement further increases the

potential of ETD performed on Waters' Synapt instruments for the analysis of small pharmaceutical molecules, as limited purification is generally undertaken prior to analysis during the development stages of drug projects, meaning LC is typically utilised.

Overall, ETD is a useful technique for the structural characterisation of small organic molecules, especially when traditional CID yields a low amount of structural information, or characterisation of labile moieties is required. Although the use of ETD for the analysis of small molecules is somewhat limited due the need for multiply charged ions, the unique product ions formed for some of the small molecules tested allowed for a more complete picture of the parent ions structure. This was especially useful for cediranib, where CID of $[M + H]^+$ only forms three product ions, compared with ETD resulting in over four times as many product ions. For the small molecules studied, the efficiency of ETD is comparable with that of ECD. Both ECD and ETD are electronic dissociation techniques, although ECD results from the capture of an electron generated by an indirectly heated dispenser cathode with typical electron energies of 1-5 eV, whereas ETD relies on a chemical reaction between a multiply protonated precursor molecule and ETD reagent radical anion. EID however, which also utilises an indirectly heated dispenser cathode, but with electron energies up to 100 eV, is the most efficient electronic dissociation technique for MSMS of small molecules. Compared with EID and ECD, ETD is a more accessible technique due to it being commercially

available on qToF mass spectrometers, which are cheaper than most instrumentation required to perform ECD and EID.

5. Future Work

The beneficial effect of performing EID on sodium containing phosphorylated ions naturally leads to investigating the use of different salts such as potassium and lithium on phosphorylated ions. The effect of such salts on EID product ion spectra has been previously studied, with some improvements to the number of product ions generated. However, their effect on phosphorylated molecules, and if targeted fragmentation could be achieved, remains to be seen. [104]

The competitive reaction between electron-transfer and proton-transfer when multiply protonated small molecules react with ETD reagent radical anions proved to give mixed results for a number of small molecules. One anecdotal difference between those molecules that underwent proton-transfer rather than electron-transfer was the inclusion of a heteroatom on the precursor ion. This could be studied if the molecules that underwent proton-transfer, such as cediranib, were synthesised with the chlorine atom substituted with a hydrogen, as well as with bromine, fluorine *etc*. The lack or change of an electronegative group, which potentially interacts with the electron from the ETD reagent radical anion during the ETD process could give insights into the role analyte physiochemical properties play in the competitive nature of the electron-transfer or proton-transfer reaction. The driving factors between proton-transfer and electron-transfer is a key feature when assessing the usefulness of ETD for the study of small molecules, and if it could be controlled, would increase the scope of this work.

To increase the efficiency of ETD, further work could be performed by the use of electron-transfer collision activated dissociation (ETcaD). In ETcaD, supplemental collisional activation of charge reduced radical cations is performed. ETD could be performed followed by IMS to select the intact $[M + 2H]^{+\cdot}$ in the IMS cell and perform CID in the transfer. This has been shown to be effective for $[M + 2H]^{2+\cdot}$ in quadrupole ion trap mass spectrometers. [103] The inherent difficulty in this would be balancing pressures in the trap and IMS cell regions of the TriWave. The advent of the cyclic ion mobility cell could be beneficial here, as the pressures in the trap and IMS cell are more closely aligned. An investigation into the use of different ETD reagents could also be performed: The ETD reagent used for this work was *p*-nitrotoluene, which has been shown in both computational and experimental studies, to result in the highest efficiency ETD for peptides and proteins out of a range of ETD reagents. Around twenty reagents, commonly found in superglue, have huge potential for use as ETD reagents, with more favourable Franck-Condon factors and electron affinities compared with *p*-nitrotoluene. These have previously been ruled out for use as ETD reagents by instrument manufactures due to health and safety concerns, as all of these reagents are highly toxic. If an alternative delivery method of ETD reagent to glow-discharge source could be made, mitigating many of the health and safety concerns, the potential increase in ETD efficiency, as well as the wider range of molecules which could be successfully studied (as proton-transfer would

be less likely to occur), would further increase the usefulness of ETD for the study of small molecules.

In order to better understand the mechanism of supercharging small molecules, a systematic study, using regular diaminoalkanes could be performed. This would be a critical study for two reasons; firstly, the chain size and configuration of the molecules tested would help further elucidate the minimum distances between protonation sites for $[M + 2H]^{2+}$ formation, with the effect of SCRs being clear. Secondly, synthesis of the same molecules with the addition of features such as heteroatoms and aromaticity could be investigated in order to pin down the effect of SCRs on a wider range of molecules.

The enhancements to LC-ETD by dynamically controlling the ion abundance of precursor ion by DRE lens attenuation could be further improved. An increase in ETD reagent radical anion abundance was noted at higher organic gradient conditions. The goal of the experiment is to maintain the ratio of ETD reagent to analyte ion abundance as much as possible. The WREnS script could be further modified to account for the change in anion abundance by using information from the gradient (*i.e.* the percentage of organic solvent at that point in the gradient) and calculating the required analyte ion intensity for a final ratio of $1.73 \times 10^4 : 1 \times 10^6$, which has been shown to result in the most efficient ETD for substance P. Additionally, a more user friendly interface would need to be developed

before this technique could be used outside of a research environment due to the complexity of editing computer scripts.

6. References

1. Sleno, L. & Volmer, D.A.: Ion activation methods for tandem mass spectrometry. *Journal of The American Society for Mass Spectrometry*. **39**, 1091-1112 (2004)
2. McLafferty, F.W., Horn, D.M., Breuker, K., Ge, Y., Lewis, M.A., Cerda, B., Zubarev, R.A. & Carpenter, B.K.: Electron capture dissociation of gaseous multiply charged ions by Fourier-transform ion cyclotron resonance. *Journal of The American Society for Mass Spectrometry*. **12**, 245-249 (2001)
3. Zubarev, R.A., Kelleher, N.L. & McLafferty, F.W.: Electron capture dissociation of multiply charged protein cations. A nonergodic process. *Journal of the American Chemical Society*. **120**, 3265-3266 (1998)
4. Nguyen, V.H., Afonso, C. & Tabet, J.C.: Comparison of collision-induced dissociation and electron-induced dissociation of singly charged mononucleotides. *International Journal of Mass Spectrometry*. **316**, 140-146 (2012)
5. Hunt, D.F., Coon, J.J., Syka, J.E.P. & Marto, J.A.: Electron transfer dissociation for biopolymer sequence mass spectrometric analysis. *US Patent 7543622* (2009)
6. Huang, J., Gautam, N., Bathenaa, S.P.R., Roy, U., McMillan, J., Gendelmanb, H.E. & Alnoutia, Y.: UHPLC-MS/MS quantification of nanoformulated ritonavir, indinavir, atazanavir, and efavirenz in mouse serum and tissues. *Journal of Chromatography B.* **879**, 2332-2338 (2011)
7. Reddy, G.V., Kumar, A.P., Reddy, B.V. & Sreeramulu, J.: Application of ion-trap mass spectrometry for identification and structural determination of an unknown impurity in simvastatin. *Die Pharmazie.* **64**, (2009)
8. Malet-Martino, M.C. & Martino, R.: Uses and limitations of nuclear magnetic resonance (NMR) spectroscopy in clinical pharmacokinetics. *Clinical Pharmacokinetics.* **20**, 337-349 (1991)
9. Bonate, P.L. & Howard, D.R.: Pharmacokinetics in drug development: advances and applications. *Springer* (2011)
10. Trajmar, S.: Electron impact spectroscopy. *Accounts of Chemical Research.* **13**, 14-20 (1980)
11. Cody, R.B. & Freiser, B.S.: Electron-impact excitation of ions from organics - alternative to collision-induced dissociation. *Analytical Chemistry.* **51**, 547-551 (1979)
12. Ho, C. S., Lam, C.W.K. Chan, M.H.M., Cheung R.C.K., Law, L.K., Lit, L.C.W. Ng, K.F. Suen, M.W.M., & Tai, H.L.: Electrospray Ionisation Mass Spectrometry: Principles and Clinical Applications. *The Chemical Biochemist Reviews*. **24**, 3-12 (2003)
13. Winger, B.E., Light-Wahl, K.J., Ogorzalek Loo, R.R., Udseth, H.R. & Smith, R.D.: Observation and implications of high mass-to-charge ratio ions from Eeectrospray ionization mass spectrometry. *Journal of The American Society for Mass Spectrometry*. **4**, 536-545 (1993)
14. Yamashita, M. & Fenn, J.B.: Electrospray ion source - another Vvriation on the free-jet theme. *Journal of Physical Chemistry.* **88**, 4451-4459 (1984)
15. Lord Rayleigh, F.R.S.: On the equilibrium of liquid conducting masses charged with electricity. *The London, Edinburgh, and Dublin Philosophical Magazine and Journal of Science*. **14**, 184-186 (1882)

16. Fernandez de la Mora, J.: Electrospray ionization of large multiply charged species proceeds via Dole's charged residue mechanism. *Analytica Chimica Acta.* **406**, 93-104 (2000)
17. Wang, G. & Cole, R.B.: Charged residue versus ion evaporation for formation of alkali metal halide cluster ions in ESI. *Analytica Chimica Acta.* **206**, 53-65 (2000)
18. Iavarone, A.T. & Williams, E.R.: Mechanism of charging and supercharging molecules in electrospray Ionization. *Journal of the American Chemical Society*. **125**, 2319-2327 (2003)
19. Kebarle, P. & Verkerk, U.H.: Electrospray: From ions in solution to ions in the gas phase, what we know now. *Mass Spectrometry Reviews.* **28**, 898-917 (2009)
20. Dole, M., Mack, L.L., Hines, R.L., Mobley, R.C., Ferguson, L.D. & Alice, M.B.: Molecular beams of macroions. *The Journal of Chemical Physics.* **49**, 2240-2249 (1968)
21. Heck, A.J. & Van Den Heuvel, R.H.: Investigation of intact protein complexes by mass spectrometry. *Mass Spectrometry Reviews.* **23**, 368-389 (2004)
22. Kaltashov, I.A. & Mohimen, A.: Estimates of protein surface areas in solution by Electrospray Ionization Mass Spectrometry. *Analytical Chemistry.* **77**, 5370-5379 (2005)
23. Patriksson, A., Marklund, E. & van der Spoel, D.: Protein Structures under electrospray conditions. *Biochemistry.* **46**, 933-945 (2007)
24. Steinberg, M.Z., Breuker, K., Elber, R. &Gerber, R.B.: The dynamics of water evaporation from partially solvated cytochrome c in the gas phase. *Physical Chemistry Chemical Physics.* **9**, 4690-4697 (2007)
25. Ahadi, E. & Konermann, L.: Modeling the behavior of coarse-grained polymer chains in charged water droplets: implications for the mechanism of electrospray ionization. *Journal of Physical Chemistry B*. **116**, 104-112 (2012)
26. Iribarne, J.V. & Thomson, B.A.: On the evaporation of small ions from charged droplets. *Journal of Chemical Physics.* **64**, 2287 (1976)
27. Labowsky, M., Fenn, J.B. & Fernandez de la Mora, J.: A continuum model for ion evaporation from a drop: effect of curvature and charge on ion solvation energy. *Analytica Chimica Acta*. **406**, 105-118 (2000)
28. Ahadi, E. & Konermann, L.: Ejection of solvated ions from electrosprayed methanol/water nanodroplets studied by molecular dynamics simulations. *Journal of the American Chemical Society*. **133**, 9354-9363 (2011)
29. Kebarle, P. & Tang, L.: From ions in solution to ions in the gas phase. *Analytical Chemistry.* **65**, 972A-986A (1993)
30. Cech, N.B. & Enke, C.G.: Practical implications of some recent studies in electrospray ionization fundamentals. *Mass Spectrometry Reviews.* **20**, 362-387 (2001)
31. Null, A.P., Nepomuceno, A.I. & Muddiman, D.C.: Implications of hydrophobicity and free energy of solvation for characterization of Nncleic acids by electrospray ionization mass spectrometry. *Analytical Chemistry.* **75**, 1331-1339 (2003)
32. Kuprowski, M.C. & Konermann, L.: Signal response of coexisting protein conformers in electrospray mass spectrometry. *Analytical Chemistry.* **79**, 2499-2506 (2007)

33. Konermann, L., Ahadi, E., Rodriguez, A.D. & Vahidi, S.: Unraveling the mechanism of electrospray ionization. *Analytical Chemistry.* **85**, 2-9 (2012)
34. Fenn, J.B. & Rosell, J.: In electrospray ionization, how much pull does an ion need to escape its droplet prison? *Journal of The American Society for Mass Spectrometry*. **97**, 1147-1157 (1997)
35. Nguyen, S. & Fenn, J.B.: Gas-phase ions of solute species from charged droplets of solutions. *Proceedings of the National Academy of Sciences of the United States of America.* **104**, 1111-1117 (2007)
36. Hogan, C.J., Jr., Carroll, J.A., Rohrs, H.W., Biswas, P. & Gross, M.L.: Combined charged residue-field emission model of macromolecular electrospray ionization. *Analytical Chemistry.* **81**, 369-377 (2009)
37. Konermann, L., Rodriguez, A.D. & Liu, J.: On the formation of highly charged gaseous ions from unfolded proteins by electrospray ionization. *Analytical Chemistry.* **84**, 6798-6804 (2012)
38. Creighton, T.E.: Proteins: Structures and molecular properties. *W. H. Freeman & Co, New York* (1993)
39. Fersht, A.R.: Structure and mechanism in protein science: a guide to enzyme catalysis and protein folding. *W. H. Freeman & Co, New York* (1999)
40. Mathieson, E. & Harris, T.J.: Quadrupole mass spectrometer. *American Journal of Physics.* **37**, 1054-1059 (1969)
41. Voo, A.C.C., Ng, R., Tunstall, J.J. & Taylor, S.: Transmission through the quadrupole mass spectrometer mass filter the effect of aperture and harmonics. *Journal of Vacuum Science & Technology A.* **15**, (1997)
42. Douglas, D.J.: Linear quadrupoles in mass spectrometry. *Mass Spectrometry Reviews.* **28**, 937-960 (2009)
43. March, R.E.: Quadrupole ion traps. *Mass Spectrometry Reviews.* **28**, 961-989 (2009)
44. March, R.E.: An introduction to quadrupole ion trap mass spectrometry. *Journal of Mass Spectrometry.* **32**, 351-369 (1997)
45. Zhang, M.Y., Pace, N., Kerns, E.H., Kleintop, T., Kagan, N. & Sakuma, T.: Hybrid triple quadrupole-linear ion trap mass spectrometry in fragmentation mechanism studies: Application to structure elucidation of buspirone and one of its metabolites. *Journal of Mass Spectrometry.* **40**, 1017-1029 (2005)
46. Guan, S. & Marshall, A.G.: Ion traps for Fourier Transform ion cyclotron resonance mass spectrometry: Principles and design of geometric and electric configurations. *International Journal of Mass Spectrometry and Ion Processes.* **146–147**, 261-296 (1995)
47. Cotter, R.J.: Time-of-flight mass spectrometry for the structural analysis of Biological molecules. *Analytical Chemistry.* **64**, A1027-A1039 (1992)
48. Cotter, R.J.: Peer Reviewed: The new time-of-flight mass spectrometry. *Analytical Chemistry.* **71**, 445A-451A (1999)
49. Guilhaus, M., Selby, D. & Mlynski, V.: Orthogonal acceleration time-of-flight mass spectrometry. *Mass Spectrometry Reviews.* **19**, 65-107 (2000)
50. Guilhaus, M.: Principles and instrumentation in time-of-flight mass spectrometry - Physical and instrumental concepts. *Journal of Mass Spectrometry.* **30**, 1519-1532 (1995)
51. Amster, I.J.: Fourier Transform Mass Spectrometry. *Journal of Mass Spectrometry.* **31**, 1325-1337 (1996)

52. Marshall, A.G.: Fourier Transform ion cyclotron resonance mass spectrometry. *Accounts of Chemical Research.* **18**, 316-322 (1985)
53. Marshall, A.G., Hendrickson, C.L.: Fourier Transform Ion Cyclotron Resonance Detection: Principles and Experimental Configurations. *International Journal of Mass Spectrometry*. **215**, 59-75 (2002)
54. Busch, K.L., Glish, G. & McLuckey, S.A.: Techniques and applications of tandem mass spectrometry. *Mcluckey VCH Verlagsgesellschaft, New York*. **64** (Ecom), **84** (Pressure Effects) (1988)
55. Durup J.: Recent developments in mass spectrometry. Ogata, K & Hayakawa, T. (eds). *University Park Press, Baltimore* (1970)
56. McLafferty, F.W., Wachs, T., Lifshitz, C., Innorta, G. & Irving, P.: Substituent effects in unimolecular ion decompositions. XV. Mechanistic interpretations and the Quasi-Equilibrium Theory. *Journal of the American Chemical Society*. **92**, 6867-6880 (1970)
57. Shukla, A.K. & Futrell, J.H.: Tandem Mass Spectrometry: Dissociation of ions by collisional activation. *Journal of Mass Spectrometry.* **35**, 1069-1090 (2000)
58. Marcus, R.A. & Rice, O.K.: The Kinetics of the recombination of methyl radicals and iodine atoms. *Journal of Physical Chemistry.* **55**, 894-908 (1951)
59. Baer, T., Mazyar, O.A., Keister, J.W. & Mayer, P.M.: Isomerization and dissociation in competition — The two-component dissociation dynamics of energy-selected C3H6O2+ isomers. *Berichte der Bunsengesellschaft für physikalische Chemie.* **101**, 478-483 (1997)
60. Gilbert, R.G. & Smith, S.C.: Theory of unimolecular and recombination reactions. *Blackwell Scientific Publications* (1990)
61. Marshall, A.G. & Schweikhard, L.: Fourier Transform ion cyclotron resonance mass spectrometry: Technique developments. *International Journal of Mass Spectrometry and Ion Processes.* **118–119**, 37-70 (1992)
62. Kleinnijenhuis, A.J., Heck, A.J.R., Duursma, M.C. & Heeren, R.M.A.: Does double electron capture lead to the formation of biradicals? An ECD-SORI-CID study on lacticin 481. *Journal of The American Society for Mass Spectrometry*. **16**, 1595-1601 (2005)
63. Mayer, P.M. & Poon, C.: The mechanisms of collisional activation of ions in mass spectrometry. *Mass Spectrometry Reviews.* **28**, 608-639 (2009)
64. de Hoffman, E. & Stroobant, V.: Mass Spectrometry: Principles and Applications, Third Edition. *Wiley, England* (2011)
65. Zubarev, R.A.: Reactions of polypeptide ions with electrons in the gas phase. *Mass Spectrometry Reviews.* **22**, 57-77 (2003)
66. Cooper, H.J., Håkansson, K. & Marshall, A.G.: The role of electron capture dissociation in biomolecular analysis. *Mass Spectrometry Reviews.* **24**, 201-222 (2005)
67. Roepstorff, P. & Fohlman, J. Proposal for a common nomenclature for sequence ions in mass spectra of peptides. *Biomedical Mass Spectrometry*. **11**, 601 (1984)
68. Rauniyar, N., Stevens, Jr, S. & Prokai, L. Fourier transform ion cyclotron resonance mass spectrometry of covalent adducts of proteins and 4-hydroxy-2-nonenal, a reactive end-product of lipid peroxidation. *Analytical and Bioanalytical Chemsitry*. **389**, 1421-8 (2007)
69. McLafferty, F.W., Horn, D.M., Breuker, K., Ge, Y., Lewis, M.A., Cerda, B., Zubarev, R.A. & Carpenter, B.K.: Electron capture dissociation of gaseous multiply charged ions by Fourier-Transform ion cyclotron

resonance. *Journal of The American Society for Mass Spectrometry*. **12**, 245-249 (2001)
70. Zubarev, R.A., Haselmann, K.F., Budnik, B., Kjeldsen, F. & Jensen, F.: Towards an understanding of the mechanism of electron-capture dissociation: A historical perspective and modern ideas. *European Journal of Mass Spectrometry.* **8**, 337-349 (2002)
71. Syrstad, E.A. & Turecek, F.: Toward a general mechanism of electron capture dissociation. *Journal of The American Society for Mass Spectrometry*. **16**, 208-224 (2005)
72. Wodrich, M.D., Zhurov, K.O., Vorobyev, A., Hamidane, H.B., Corminboeuf, C. & Tsybin, Y.O.: Heterolytic N–Cα bond cleavage in electron capture and transfer dissociation of peptide cations. *The Journal of Physical Chemistry B.* **116**, 10807-10815 (2012)
73. Cooper, H.J., Hudgins, R.R., Håkansson, K. & Marshall, A.G.: Characterization of amino acid side chain losses in electron capture dissociation. *Journal of The American Society for Mass Spectrometry*. **13**, 241-249 (2002)
74. Cooper, H.J., Hudgins, R.R., Håkansson, K. & Marshall, A.G.: Secondary fragmentation of linear peptides in electron capture dissociation. *International Journal of Mass Spectrometry*. **228**, 723-728 (2003)
75. Leymarie, N., Costello, C.E. & O'Connor, P.B.: Electron capture dissociation initiates a free radical reaction cascade. *Journal of the American Chemical Society*. **125**, 8949-8958 (2003)
76. Kjeldsen, F., Haselmann, K.F., Budnik, B.A., Jensen, F. & Zubarev, R.A.: Dissociative capture of hot (3-13 ev) electrons by polypeptide polycations: An efficient process accompanied by secondary fragmentation. *Chemical Physics Letters.* **356**, 201-206 (2002)
77. Kjeldsen, F., Haselmann, K.F., Sorensen, E.S. & Zubarev, R.A.: Distinguishing of Ile/leu amino acid residues in the pp3 protein by (hot) electron capture dissociation in Fourier Transform ion cyclotron resonance mass spectrometry. *Analytical Chemistry.* **75**, 1267-1274 (2003)
78. Prakash, A.S.: Development of electron based dissociation techniques in mass spectrometry for the structural characterisation of small organic ions and modified proteins. *Department of Chemistry, Durham University* (2012)
79. Wang, B.H. & McLafferty, F.W.: Electron impact excitation of ions from larger organic molecules. *Organic Mass Spectrometry.* **25**, 554-556 (1990)
80. Baba, T., Hashimoto, Y., Hasegawa, H., Hirabayashi, A. & Waki, I.: Electron capture dissociation in a radio frequency ion trap. *Analytical Chemistry.* **76**, 4263-4266 (2004)
81. Budnik, B.A., Haselmann, K.F. & Zubarev, R.A.: Electron detachment dissociation of peptide di-anions: An electron-hole recombination phenomenon. *Chemical Physics Letters.* **342**, 299-302 (2001)
82. Budnik, B.A., Haselmann, K.F., Elkin, Y.N., Gorbach, V.I. & Zubarev, R.A.: Applications of electron-ion dissociation reactions for analysis of polycationic chitooligosaccharides in Fourier Transform mass spectrometry. *Analytical Chemistry.* **75**, 5994-6001 (2003)
83. Huang, Y., Pu, Y., Yu, X., Costello, C.E. & Lin, C.: Mechanistic study on electronic excitation dissociation of the cellobiose-Na+ complex. *Journal of The American Society for Mass Spectrometry*. **27**, 319-328 (2015)

84. Ly, T., Yin, S., Loo, J.A. & Julian, R.R.: Electron-induced dissociation of protonated peptides yields backbone fragmentation consistent with a hydrogen-deficient radical. *Rapid Communications in Mass Spectrometry.* **23**, 2099-2101 (2009)
85. Yoo, H.J. &Håkansson, K.: Determination of double bond location in fatty acids by manganese adduction and electron induced dissociation. *Analytical Chemistry.* **82**, 6940-6946 (2010)
86. Prakash, A.S., Smith, M.J., Kaabia, Z., Hurst, G., Yan, C., Sims, M., Bristow, A.W., Stokes, P., Parker, D. & Mosely, J.A.: Using electron induced dissociation (EID) on an LC time-scale to characterize a mixture of analogous small organic molecules. *Journal of The American Society for Mass Spectrometry*. **23**, 850-857 (2012)
87. Mosely, J. A., Smith, M. J. P., Prakash, A. S., Sims, M. & Bristow, A. W. T.: Electron-Induced Dissociation of Singly Charged Organic Cations as a Tool for Structural Characterization of Pharmaceutical Type Molecules. *Analytical Chemistry*. **83**, 4068-4075 (2011)
88. Syka, J.E.P., Coon, J.J., Schroeder, M.J., Shabanowitz, J. & Hunt, D.F.: Peptide and protein sequence analysis by electron transfer dissociation mass spectrometry. *Proceedings of the National Academy of Sciences of the United States of America.* **101**, 9528-9533 (2004)
89. McLuckey, S.A. & Stephenson, J.L.: Ion/ion chemistry of high-mass multiply charged ions. *Mass Spectrometry Reviews.* **17**, 369-407 (1998)
90. Huang, T. Y., Emory, J.F., O'Hair, R.A.J. & McLuckey, S.A.: Electron-transfer reagent anion formation via electrospray ionization and collision-induced dissociation. *Analytical Chemistry.* **78**, 7387-7391 (2006)
91. McAlister, G.C., Phanstiel, D., Good, D.M., Berggren, W.T. & Coon, J.J.: Implementation of electron-transfer dissociation on a hybrid linear ion trap-orbitrap mass spectrometer. *Analytical Chemistry.* **79**, 3525-3534 (2007)
92. Mikesh, L.M., Ueberheide, B., Chi, A., Coon, J.J., Syka, J.E.P., Shabanowitz, J. & Hunt, D.F.: The utility of ETD mass spectrometry in proteomic analysis. *Biochimica et Biophysica Acta (BBA) - Proteins & Proteomics.* **1764**, 1811-1822 (2006)
93. Compton, P.D., Strukl, J.V., Bai, D.L., Shabanowitz, J. & Hunt, D.F.: Optimization of electron transfer dissociation via informed selection of reagents and operating parameters. *Analytical Chemistry.* **84**, 1781-1785 (2012)
94. Coon, J.J., Syka, J.E.P., Schwartz, J.C., Shabanowitz, J. & Hunt, D.F.: Anion dependence in the partitioning between proton and electron transfer in ion/ion reactions. *International Journal of Mass Spectrometry*. **236**, 33-42 (2004)
95. Li, X.J., Lin, C., Han, L., Costello, C.E. & O'Connor, P.B.: Charge remote fragmentation in electron capture and electron transfer dissociation. *Journal of The American Society for Mass Spectrometry*. **21**, 646-656 (2010)
96. Riley, N.M. & Coon, J.J.: The role of electron transfer dissociation in modern proteomics. *Analytical Chemistry.* **90**, 40-64 (2018)
97. Gunawardena, H.P., He, M., Chrisman, P.A., Pitteri, S.J., Hogan, J.M., Hodges, B.D.M. & McLuckey, S.A.: Electron transfer versus proton transfer in gas-phase ion/ion reactions of polyprotonated peptides. *Journal of the American Chemical Society*. **127**, 12627-12639 (2005)
98. Chalkley, R.J., Medzihradszky, K.F., Lynn, A.J., Baker, P.R. & Burlingame, A.L.: Statistical analysis of peptide electron transfer

dissociation fragmentation mass spectrometry. *Analytical Chemistry.* **82**, 579-584 (2010)
99. Williams, J.P., Brown, J.M., Richardson, K., Campuzano, I., Pringle, S., Denny, R., Dyson, B., Langridge, J. & Morris, M.: in-silico design of electron transfer dissociation reagents evaluated by a Q-ToF with glow discharge anion source. *American Society for Mass Spectrometry Conference, Denver, Colorado* (2011)
100. Kim, M.S. & Pandey, A.: Electron transfer dissociation mass spectrometry in proteomics. *Proteomics.* **12**, 530-542 (2012)
101. Sohn, C.H., Chung, C.K., Yin, S., Ramachandran, P., Loo, J.A. & Beauchamp, J.L.: Probing the mechanism of electron capture and electron transfer dissociation using tags with variable electron affinity. *Journal of the American Chemical Society*. **131**, 5444-5459 (2009)
102. Mikesh, L.M., Ueberheide, B., Chi, A., Coon, J.J., Syka, J.E., Shabanowitz, J. & Hunt, D.F.: The utility of ETD mass spectrometry in proteomic analysis. *Biochimica et Biophysica Acta.* **1764**, 1811-1822 (2006)
103. Swaney, D.L., McAlister, G.C., Wirtala, M., Schwartz, J.C., Syka, J.E. & Coon, J.J.: Supplemental activation method for high-efficiency electron-transfer dissociation of doubly protonated peptide precursors. *Analytical Chemistry.* **79**, 477-485 (2007)
104. Mosely, J.A., Smith, M.J., Prakash, A.S., Sims, M. & Bristow, A.W.: Electron-induced dissociation of singly charged organic cations as a tool for structural characterization of pharmaceutical type molecules. *Analytical Chemistry.* **83**, 4068-4075 (2011)
105. Wills, R.H., Tosin, M. & O'Connor, P.B.: Structural characterization of polyketides using high mass accuracy tandem mass spectrometry. *Analytical Chemistry.* **84**, 8863-8870 (2012)
106. Wei, J., Li, H., Barrow, M.P. & O'Connor., P.B.: Structural characterization of chlorophyll-a by high resolution tandem mass spectrometry. *Journal of The American Society for Mass Spectrometry*. **24**, 753-760 (2013)
107. Anusiewicz, I., Jasionowski, M., Skurski, P. & Simons, J.: Backbone and side-chain cleavages in electron detachment dissociation (EDD). *Journal of Physical Chemistry A.* **109**, 11332-11337 (2005)
108. Taucher, M. & Breuker, K.: Top-down mass spectrometry for sequencing of larger (up to 61 nt) RNA by CAD and EDD. *Journal of The American Society for Mass Spectrometry*. **21**, 918-929 (2010)
109. Nguyen, V.H., Afonso, C. & Tabet, J.C.: Concomitant EDD and EID of DNA evidenced by MSn and double resonance experiments. *International Journal of Mass Spectrometry*. **301**, 224-233 (2011)
110. Song, H.T. & Hakansson, K.: Electron detachment dissociation and negative on infrared multiphoton dissociation of electrosprayed intact proteins. *Analytical Chemistry.* **84**, 871-876 (2012)
111. Wootton, C.A., Sanchez-Cano, C., Liu, H-K., Barrow, M.P., Sadler, P.J. & O'Connor, P.B.: Binding of an organo-osmium(II) anticancer complex to guanine and cytosine on DNA revealed by electron-based dissociations in high resolution Top-Down FT-ICR mass spectrometry. *Dalton Transactions.* **44**, 3624-3632 (2015)
112. Flosadóttir, H., Stano, M. & Ingólfsson, O.: Sodium controlled selective reactivity of protonated deoxy-oligonucleotides in the gas phase. *Journal of The American Society for Mass Spectrometry*. **20**, 689-696 (2009)

113. Bond, A.E., Ding, S., Williams, C.M., Newton, R.P. & Dudley, E.: Mass spectrometric fragmentation behaviour of cAMP analogues. *International Journal of Mass Spectrometry*. **304**, 130-139 (2011)
114. Stensballe, A., Jensen, O.N., Olsen, J.V., Haselmann, K.F. & Zubarev, R.A.: Electron capture dissociation of singly and multiply phosphorylated peptides. *Rapid Communications in Mass Spectrometry.* **14**, 1793-1800 (2000)
115. Chi, A., Huttenhower, C., Geer, L.Y., Coon, J.J., Syka, J.E.P., Bai, D.L., Shabanowitz, J., Burke, D.J., Troyanskaya, O.G. & Hunt, D.F.: Analysis of phosphorylation sites on proteins from saccharomyces cerevisiae by electron transfer dissociation (ETD) mass spectrometry. *Proceedings of the National Academy of Sciences.* **104**, 2193-2198 (2007)
116. Holcapek, M., Jirasko, R. & Lisa, M.: Basic rules for the interpretation of atmospheric pressure ionization mass spectra of small molecules. *Journal of Chromatography A.* **1217**, 3908-3921 (2010)
117. Andreazza, H.J., Fitzgerald, M., Bilusich, D., Hoffmann, R., Hoffmann, P., Elchinger, P.C.H. & Bowie, J.H.: Characteristic negative ion fragmentations of deprotonated peptides containing post-translational modifications: Mono-phosphorylated ser, thr and tyr. A joint experimental and theoretical study. *Rapid Communications in Mass Spectrometry*. **22**, 3305-3312 (2008)
118. Liu, H., Yoo, H.J. & Håkansson, K.: Characterization of phosphate-containing metabolites by calcium adduction and electron capture dissociation. *Journal of The American Society for Mass Spectrometry*. **19**, 799-808 (2008)
119. Creese, A.J. & Cooper, H.J.: The effect of phosphorylation on the electron capture dissociation of peptide ions. *Journal of The American Society for Mass Spectrometry*. **19**, 1263-1274 (2008)
120. Iavarone, A.T., Jurchen, C.J. & Williams, E.R.: Effects of solvent on the maximum charge state and charge state distribution of protein ions produced by electrospray ionization. *Journal of The American Society for Mass Spectrometry*. **11**, 796-985 (2000)
121. Miladinovic, S.M., Fornelli, L., Lu, Y., Piech, K.M., Girault, H.H. & Tsybin, Y.O.: In-spray supercharging of peptides and proteins in electrospray ionization mass spectrometry. *Analytical Chemistry.* **84**, 4647-4651 (2012)
122. Chowdhurry, S.K., Katta, V. & Chait, B.T.: Probing conformational changes in proteins by mass spectrometry. *Journal of the American Chemical Society*. **112**, (1990)
123. Smith, R.D., Loo, J.A., Ogorzalek Loo, R.R., Busman, M. & Udseth, H.R.: Principles and practice of electrospray ionization—mass spectrometry for large polypeptides and proteins. *Mass Spectrometry Reviews.* **10**, 359-452 (1991)
124. Fenn, J.B., Mann, M., Meng, C.K., Wong, S.F. & Whitehouse, C.M.: Electrospray ionization–principles and practice. *Mass Spectrometry Reviews.* **9**, 37-70 (1990)
125. Grandori, R.: Origin of the conformation dependence of protein charge-state distributions in electrospray ionization mass spectrometry. *Journal of Mass Spectrometry*. **38**, 11-15 (2003)
126. Thomson, B.A.: Declustering and fragmentation of protein ions from an electrospray ion source. *Journal of The American Society for Mass Spectrometry*. **8**, 1053-1058 (1997)

127. Iavarone, A.T., Jurchen, C.J. & Williams, E.R.: Supercharged protein and peptide ions formed by electrospray ionization. *Analytical Chemistry.* **73**, 1455-1460 (2001)
128. Iavarone, A.T. & Williams, E.R.: Supercharging in electrospray ionization: effects on signal and charge. *International Journal of Mass Spectrometry*. **219**, 63-72 (2002)
129. Valeja, S.G., Jeremiah, D.T., Emmett, M.R. & Marshall, A.G.: New reagents for enhanced liquid chromatographic separation and charging of intact protein ions for electrospray ionization mass spectrometry. *Analytical Chemistry.* **82**, 7515-7519 (2010)
130. Šamalikova, M. & Grandori, R.: Protein charge-state distributions in electrospray-ionization mass spectrometry do not appear to be limited by the surface tension of the solvent. *Journal of the American Chemical Society*. **125**, 13352-13353 (2003)
131. Samalikova, M., Matecko, I., Muller, N. & Grandori, R.: Interpreting conformational effects in protein nano-ESI-MS spectra. *Analytical and Bioanalytical Chemistry.* **378**, 1112-1123 (2004)
132. Samalikova, M. & Grandori, R.: Testing the role of solvent surface tension in protein ionization by electrospray. *Journal of Mass Spectrometry.* **40**, 503-510 (2005)
133. Zenaidee, M.A. & Donald, W.A.: Extremely supercharged proteins in mass spectrometry: profiling the pH of electrospray generated droplets, narrowing charge state distributions, and increasing ion fragmentation. *Analyst.* **140**, 1894-1905 (2015)
134. Mendes, M.A., de Souza, B.M., dos Santos, L.D., Santos, K.S. & Palma, M.S.: Analyzing glycerol-mediated protein oligomerization by electrospray ionization mass spectrometry. *Rapid Communications in Mass Spectrometery.* **19**, 2636-2642 (2005)
135. Douglass, K.A. & Venter, A.R.: Investigating the role of adducts in protein supercharging with sulfolane. *Journal of The American Society for Mass Spectrometry*. **23**, 489-497 (2012)
136. Testa, L., Brocca, S. & Grandori, R.: Charge-surface correlation in electrospray ionization of folded and unfolded proteins. *Analytical Chemistry.* **83**, 6459-6463 (2011)
137. Lide, D.R.: CRC Handbook of Chemistry and Physics. *CRC Press, London* (2008)
138. Sterling, H.J. & Williams, E.R.: Origin of supercharging in electrospray ionization of noncovalent complexes from aqueous solution. *Journal of The American Society for Mass Spectrometry*. **20**, 1933-1943 (2009)
139. Lomeli, S.H., Peng, I.X., Yin, S., Loo, R.R. & Loo, J.A.: New reagents for increasing ESI multiple charging of proteins and protein complexes. *Journal of The American Society for Mass Spectrometry*. **21**, 127-131 (2010)
140. Going, C.C. & Williams, E.R.: Supercharging with m-nitrobenzyl alcohol and propylene carbonate: forming highly charged ions with extended, near-linear conformations. *Analytical Chemistry.* **87**, 3973-3980 (2015)
141. Sterling, H.J., Daly, M.P., Feld, G.K., Thoren, K.L., Kintzer, A.F., Krantz, B.A. & Williams, E.R.: Effects of supercharging reagents on noncovalent complex structure in electrospray ionization from aqueous solutions. *Journal of The American Society for Mass Spectrometry*. **21**, 1762-1774 (2010)
142. Sterling, H.J., Kintzer, A.F., Feld, G.K., Cassou, C.A., Krantz, B.A. & Williams, E.R.: Supercharging protein complexes from aqueous solution

disrupts their native conformations. *Journal of The American Society for Mass Spectrometry*. **23**, 191-200 (2012)
143. Going, C.C., Xia, Z. & Williams, E.R.: New supercharging reagents produce highly charged protein ions in native mass spectrometry. *Analyst.* **140**, 7184-7194 (2015)
144. Lomeli, S.H., Yin, S., Ogorzalek Loo, R.R. & Loo, J.A.: Increasing charge while preserving noncovalent protein complexes for ESI-MS. *Journal of The American Society for Mass Spectrometry*. **20**, 593-596 (2009)
145. Susa, A.C., Xia, Z., Tang, H.Y., Tainer, J.A. & Williams, E.R.: Charging of proteins in native mass spectrometry. *Journal of The American Society for Mass Spectrometry*. **28**, 332-340 (2017)
146. Sterling, H.J., Cassou, C.A., Trnka, M.J., Burlingame, A.L., Krantz, B.A. & Williams, E.R.: The role of conformational flexibility on protein supercharging in native electrospray ionization. *Physical Chemistry Chemical Physics.* **13**, 18288-18296 (2011)
147. Chingin, K., Xu, N. & Chen, H.: Soft supercharging of biomolecular ions in electrospray ionization mass spectrometry. *Journal of The American Society for Mass Spectrometry*. **25**, 928-934 (2014)
148. Sterling, H.J., Prell, J.S., Cassou, C.A. & Williams, E.R.: Protein conformation and supercharging with DMSO from aqueous solution. *Journal of The American Society for Mass Spectrometry*. **22**, 1178-1186 (2011)
149. Susa, A.C., Mortensen, D.N. & Williams, E.R.: Effects of cations on protein and peptide charging in electrospray ionization from aqueous solutions. *Journal of The American Society for Mass Spectrometry*. **25**, 918-927 (2014)
150. Cassou, C.A. & Williams, E.R.: Desalting protein ions in native mass spectrometry using supercharging reagents. *Analyst.* **139**, 4810-4819 (2014)
151. Metwally, H., McAllister, R.G., Popa, V. & Konermann, L.: Mechanism of protein supercharging by sulfolane and m-nitrobenzyl alcohol: Molecular dynamics simulations of the electrospray process. *Analytical Chemistry.* **88**, 5345-5354 (2016)
152. Kjeldsen, F., Giessing, A.M.B., Ingrell, C.R. & Jensen, O.N.: Peptide sequencing and characterization of post-translational modifications by enhanced ion-charging and liquid chromatography electron-transfer dissociation tandem mass spectrometry. *Analytical Chemistry.* **79**, 9243-9252 (2007)
153. Wiesner, J., Premsler, T. & Sickmann, A.: Application of electron transfer dissociation (ETD) for the analysis of posttranslational modifications. *Proteomics.* **8**, 4466-4483 (2008)
154. Madsen, J.A. & Brodbelt, J.S.: Comparison of infrared multiphoton dissociation and collision-induced dissociation of supercharged peptides in ion traps. *Journal of The American Society for Mass Spectrometry*. **20**, 349-358 (2009)
155. Sterling, H.J. & Williams, E.R.: Real-time hydrogen/deuterium exchange kinetics via supercharged electrospray ionization tandem mass spectrometry. *Analytical Chemistry.* **82**, 9050-9057 (2010)
156. Mess, D.V., Montalibet, J. & Garofolo, F.: Impact of mobile phase modifiers and supercharging reagents on charge state distribution and sensitivity of therapeutic peptides by LC-HRMS. *Algorithme Pharma Inc* (2015)

157. Garcia, B.A.: What does the future hold for Top Down mass spectrometry? *Journal of The American Society for Mass Spectrometry*. **21**, 193-202 (2010)
158. Yin, S. & Loo, J.A.: Top-Down mass spectrometry of supercharged native protein-ligand complexes. *International Journal of Mass Spectrometry*. **300**, 118-122 (2011)
159. Loo, J.A., Benchaar, S.A. & Zhang, J.: Integrating native mass spectrometry and Top-Down MS for defining protein interactions important in biology and medicine. *Mass Spectrometry (Tokyo).* **2**, S0013 (2013)
160. Zhang, J., Ogorzalek Loo, R.R. & Loo, J.A.: Increasing Fragmentation of disulfide-bonded proteins for Top-Down mass spectrometry by supercharging. *International Journal of Mass Spectrometry*. **377**, 546-556 (2015)
161. Krusemark, C.J., Frey, B.L., Belshaw, P.J. & Smith, L.M.: Modifying the charge state distribution of proteins in electrospray ionization mass spectrometry by chemical derivatization. *Journal of The American Society for Mass Spectrometry*. **20**, 1617-1625 (2009)
162. Sterling, H.J., Cassou, C.A., Susa, A.C. & Williams, E.R.: Electrothermal supercharging of proteins in native electrospray ionization. *Analytical Chemistry.* **84**, 3795-3801 (2012)
163. Cassou, C.A., Sterling, H.J., Susa, A.C. & Williams, E.R.: Electrothermal supercharging in mass spectrometry and tandem mass spectrometry of native proteins. *Analytical Chemistry.* **85**, 138-146 (2013)
164. Going, C.C., Xia, Z. & Williams, E.R.: Real-time HD exchange kinetics of proteins from buffered aqueous solution with electrothermal supercharging and Top-Down tandem mass spectrometry. *Journal of The American Society for Mass Spectrometry*. **27**, 1019-1027 (2016)
165. Mortensen, D.N. & Williams, E.R.: Electrothermal supercharging of proteins in native MS: effects of protein isoelectric point, buffer, and nanoESI-emitter tip size. *Analyst*. **141**, 5598-5606 (2016)
166. Flick, T.G. & Williams, E.R.: Supercharging with trivalent metal ions in native mass spectrometry. *Journal of The American Society for Mass Spectrometry*. **23**, 1885-1895 (2012)
167. O'Connor, P., Wootton, C.A., Hussein, H.E.M., Chiu, C.K.C., Baker, L.A., Habershon, S., Stace, A.J. & Barrow, M.P.: In-Licensing Opportunity – improvements to electrospray ionisation. *Warwick Ventures Ltd* (2016)
168. Nielsen, B. & Abaye, D.: Influence of electrolytes and a supercharging reagent on charge state distribution and response of neuropeptide ions generated during positive electrospray ionisation mass spectrometry. *European Journal of Mass Spectrometry.* **19**, 335 (2013)
169. Banerjee, S. & Mazumdar, S.: Electrospray ionization mass spectrometry: a technique to access the information beyond the molecular weight of the analyte. *International Journal of Analytical Chemistry.* **2012**, 282574 (2012)
170. Konermann, L.: A simple model for the disintegration of highly charged solvent droplets during electrospray ionization. *Journal of The American Society for Mass Spectrometry*. **20**, 496-506 (2009)
171. Kalapothakis, J.M.D. & Barran, P.E.I: Ion Mobility Mass Spectrometry – Principles. Roberts, G.C.K. (ed.). *Springer, Berlin* (2013)
172. Barnes, W.S., Martin, D.W. & McDaniel, E.W.: Mass spectrographic identification of the ion observed in hydrogen mobility experiments. *Physical Review Letters.* **6**, 110-111 (1961)

173. Revercomb, H.E. & Mason, E.A.: Theory of plasma chromatography/gaseous electrophoresis. Review. *Analytical Chemistry.* **47**, 970-983 (1975)
174. Wyttenbach, T., Bleiholder, C. & Bowers, M.T.: Factors contributing to the collision cross section of polyatomic ions in the kilodalton to gigadalton range: Application to ion mobility measurements. *Analytical Chemistry.* **85**, 2191-2199 (2013)
175. Giles, K., Pringle, S.D., Worthington, K.R., Little, D., Wildgoose, J.L., & Bateman, R.H.: Applications of a travelling wave-based radio-frequency-only stacked ring ion guide. *Rapid Communications in Mass Spectrometry.* **18**, 2401-2414 (2004)
176. Waters: Waters Synapt G2-S operators manual and maintenance guide. (2012)
177. ThermoFinnagan: LTQ FT Ultra User Hardware Manual. (2004)
178. Szegezdi, J. & Csizmadia, F.: Prediction of dissociation constant using microconstants. *American Chemical Society National Meeting California, ChemAxon* (2004)
179. Turecek, F. & Chen, X.: Protonated adenine: tautomers, solvated clusters, and dissociation mechanisms. *Journal of The American Society for Mass Spectrometry*. **16**, 1713-1726 (2005)
180. Blackburn, G.M., Gait, M.J., Loakes, D. & Williams, D.M.: Nucleic Acids in Chemistry and Biology. *Royal Society of Chemistry Publishing, London* (2015)
181. Dougherty, D.A.: Cation-pi interactions in chemistry and biology: A new view of benzene, Phe, Tyr, and Trp. *Science.* **271**, 163-168 (1996)
182. Feketeová, L., Wong, M.W. & O'Hair, R.A.J.: The Role of metal cation in electron-induced dissociation of tryptophan. *European Physical Journal D - Atomic, Molecular, Optical and Plasma Physics.* **60**, 11-20 (2010)
183. Chang, T.M., Prell, J.S., Warrick, E.R. & Williams, E.R.: Where's the charge? Protonation sites in gaseous ions change with hydration. *Journal of the American Chemical Society*. **134**, 15805-15813 (2012)
184. Fort, K.L., Cramer, C.N., Voinov, V.G., Vasil'ev, Y.V., Lopez, N.I., Beckman, J.S. & Heck, A.J.R.: Exploring ECD on a benchtop Q exactive orbitrap mass spectrometer. *Journal of Proteome Research.* **17**, 926-933 (2018)
185. Kebarle, P. & Tang, L.: From ions in solution to ions in the gas phase - The mechanism of electrospray mass spectrometry. *Analytical Chemistry.* **65**, A972-A986 (1993)
186. Giese, R.W.: Electron-Capture mass spectrometry: Recent advances. *Journal of Chromatography A.* **892**, 329-346 (2000)
187. Sobott, F., Watt, S.J., Smith, J., Edelmann, M.J., Kramer, H.B. & Kessler, B.M.: Comparison of CID versus ETD based MS/MS fragmentation for the analysis of protein ubiquitination. *Journal of The American Society for Mass Spectrometry*. **20**, 1652-1659 (2009)
188. Laskin, J., Yang, Z. & Chu, I.K.: Energetics and dynamics of electron transfer and proton transfer in dissociation of metal(III)(salen)-peptide complexes in the gas phase. *Journal of the American Chemical Society*. **130**, 3218-3230 (2008)
189. Tsybin, Y.O., Witt, M., Baykut, G. & Håkansson, P.: Electron capture dissociation Fourier Transform ion cyclotron resonance mass spectrometry in the electron energy range 0-50 eV. *Rapid Communications in Mass Spectrometry.* **18**, 1607-1613 (2004)

190. Iavarone, A.T., Jurchen, J.C.& Williams, E.R.: Supercharged protein and peptide ions formed by electrospray ionization. *Analytical Chemistry.* **73**, 1455-1460 (2001)
191. ChemSpider: ChemSpider Database. *[online]* Last updated 2020. Accessed June 15th 2017. http://www.chemspider.com/
192. ChemAxon: MarvinSketch 6.2.2. *[online]* Last updated 2019. Accessed June 26th 2017. http://www.chemaxon.com/products/marvin/marvinsketch/
193. Tindal, M. & Sevigny, J.: Canadian Environmental Quality Guidelines for Sulfolane: Water and Soil. *Canadian Council of Ministers of the Environment*. ISBN-10 1-896997-59-7 PDF (2006)
194. Rockwood, A.L., Busman, M. Harold R. Udseth & Smith, R.D.: Thermally induced dissociation of ions from electrospray mass spectrometry. *Rapid Communications in Mass Spectrometry.* **5**, 582-585 (1991)
195. Dudev, T., Grauffel, C., & Lim, C.: How Native and Alien Metal Cations Bind ATP: Implications for Lithium as a Therapeutic Agent. *Scientific Reports*. **7**, 42377 (2017)

7. Appendix

7.1. Chapter 1

Proposed formula	Exact Mass (*m/z*)	EID Ion (*m/z*)	CID Ion (*m/z*)	EID Error (ppm)	CID Error (ppm)
$C_{10}H_{15}N_5O_7P$	348.07036	348.07043	348.07036	0.2	0.0
$C_7H_8N_5O$	178.07234	178.07253	-	1.1	-
$C_6H_6N_5O$	164.05669	164.05681	-	0.7	-
$C_6H_6N_5$	148.06177	148.06184	-	0.5	-
$C_5H_6N_5$	136.06177	136.06177	136.06174	0.0	-0.2
$C_5H_5N_5$	135.05395	135.05397	-	0.1	-
$C_5H_3N_4$	119.03522	119.03521	-	-0.1	-
$C_4H_5N_4$	109.05087	109.05084	-	-0.3	-
$C_4H_4N_4$	108.04305	108.04302	-	-0.3	-
PO_4H_4	98.98417	98.98413	-	-0.4	-
$C_5H_5O_2$	97.02841	97.02837	-	-0.4	-
$C_4H_4N_3$	94.03997	94.03993	-	-0.4	-
$C_4H_2N_3$	92.02432	92.02429	-	-0.3	-
$C_3H_4N_3$	82.03997	82.03994	-	-0.4	-
$C_3H_3N_3$	81.03215	81.03212	-	-0.4	-
$C_3H_3N_2$	67.02907	67.02908	-	0.1	-
$C_3H_2N_2$	66.02125	66.02126	-	0.2	-
C_3HN_2	65.01342	65.01344	-	0.3	-
C_4H_8	56.06205	56.06212	-	1.2	-

$C_2H_3N_2$	55.02907	55.02914	-	1.3	-
C_2HN_2	53.01342	53.01350	-	1.5	-

7.1.1. Protonated AMP CID and EID assignments.

Proposed formula	**Exact Mass (*m/z*)**	**EID Ion (*m/z*)**	**CID Ion (*m/z*)**	**EID Error (ppm)**	**CID Error (ppm)**
$C_{10}H_{14}N_5O_7PNa$	370.05231	370.05228	370.05202	-0.1	-0.8
$C_{10}H_{11}O_3N_5Na$	272.07541	272.07567	272.07532	1.0	-0.3
$C_{10}H_{12}O_3N_5$	250.09347	250.09374	250.09338	1.1	-0.4
$C_5H_9O_7PNa$	234.99781	234.99807	234.9978	1.1	0.0
$C_5H_8O_7PNa$	233.98999	233.99027	-	1.2	-
$C_5H_7O_6PNa$	216.98725	216.98745	-	0.9	-
$C_4H_8O_6PNa$	205.99507	205.99528	-	1.0	-
$C_3H_7O_6PNa$	192.98725	192.98738	-	0.7	-
$C_8H_7O_2N_2Na$	186.03997	186.03875	-	-6.6	-
$C_3H_7O_5PNa$	176.99233	176.99244	-	0.6	-
$C_3H_6O_5PNa$	175.98451	175.9846	-	0.5	-
$C_3H_5O_5PNa$	174.97668	174.97678	-	0.6	-
$C_6H_6ON_5$	164.05669	164.05676	-	0.4	-
$C_2H_5O_5PNa$	162.97668	162.97675	-	0.4	-
$C_5H_5N_5Na$	158.04372	158.04378	158.04364	0.4	-0.5
$C_5H_6N_5$	136.06177	136.06179	-	0.1	-
$C_5H_5N_5$	135.05395	135.05396	-	0.1	-

CH_4O_4PNa	133.97394	133.97396	-	0.1	-
PH_3O_4Na	120.96612	120.96613	-	0.1	-
$C_5H_4O_2Na$	119.01035	119.01036	-	0.1	-
$C_4H_4N_4$	108.04305	108.04305	-	0.0	-
PO_3HNa	102.95555	102.95555	-	0.0	-
$C_5H_5O_2$	97.02841	97.0284	-	-0.1	-
C_5H_5O	81.03349	81.03351	-	0.2	-
C_6H_6	78.0464	78.04643	-	0.4	-
C_4H_9	57.06988	57.07	-	2.1	-
C_4H_8	56.06205	56.06218	-	2.3	-
C_4H_7	55.05423	55.05436	-	2.4	-

7.1.2. Monosodium AMP CID and EID assignments.

Proposed formula	**Exact Mass (*m/z*)**	**EID Ion (*m/z*)**	**CID Ion (*m/z*)**	**EID Error (ppm)**	**CID Error (ppm)**
$C_{10}H_{13}N_5O_7PNa_2$	392.03425	392.03424	392.03439	0.0	0.4
$C_{10}H_{11}O_6N_5PNa_2$	374.02369	374.02373	374.02358	0.1	-0.3
$C_5H_6O_6PNa_2$	238.96919	238.96926	-	0.3	-
$C_3H_4O_5PNa_2$	196.95863	196.95878	-	0.8	-
$C_2H_4O_5PNa_2$	184.95863	184.95866	-	0.2	-
$C_5H_4N_5Na_2$	180.02566	180.02571	-	0.3	-
$C_6H_6ON_5$	164.05669	164.05672	-	0.2	-
$CH_3O_4PNa_2$	155.95589	155.9559	-	0.1	-

$PO_4H_2Na_2$	142.94806	142.94806	-	0.0	-
PO_4HNa_2	141.94024	141.94024	-	0.0	-
$C_5H_6N_5$	136.06177	136.06178	-	0.1	-
PO_3HNa_2	125.94532	125.94531	-	-0.1	-
PO_3Na_2	124.9375	124.93749	-	-0.1	-
PH_3O_4Na	120.96612	120.96611	-	-0.1	-
C_6H_6	78.0464	78.04644	-	0.5	-
C_5H_{10}	70.0777	70.07775	-	0.7	-
C_4H_9	57.06988	57.06999	-	1.9	-
C_4H_8	56.06205	56.06218	-	2.3	-
C_4H_7	55.05423	55.05436	-	2.4	-

7.1.3. Disodium AMP CID and EID assignments.

Proposed formula	**Exact Mass (*m/z*)**	**EID Ion (*m/z*)**	**CID Ion (*m/z*)**	**EID Error (ppm)**	**CID Error (ppm)**
$C_{10}H1_6N_5O_{10}P_2$	428.03669	428.03602	428.03652	-1.6	-0.4
$C_{10}H_{15}O_7N_5P$	348.07036	348.07079	348.07029	1.2	-0.2
$C_{10}H_{13}O_6N_5P$	330.0598	-	330.05966	-	-0.4
$C_{10}H_{11}O_3N_5$	249.08564	249.08586	-	0.9	-
$C_{10}H_{10}O_2N_5$	232.0829	232.08307	232.08289	0.7	0.0
$C_7H_8O_2N_5$	194.06725	194.06731	-	0.3	-
$P_2O_7H_5$	178.9505	178.95057	-	0.4	-
$C_7H_8ON_5$	178.07234	178.0724	-	0.3	-

$C_7H_7ON_5$	177.06451	177.06456	-	0.3	-
$C_6H_6ON_5$	164.05669	164.05672	-	0.2	-
$P_2O_6H_3$	160.93994	160.93998	-	0.2	-
$C_6H_6N_5$	148.06177	148.06179	-	0.1	-
$C_5H_6N_5$	136.06177	136.06178	-	0.1	-
$C_5H_5N_5$	135.05395	135.05395	-	0.0	-
$C_5H_5N_4$	121.05087	121.0509	-	-0.1	-
$C_5H_3N_4$	119.03522	119.03521	-	-0.1	-
$C_4H_5N_4$	109.05087	109.05086	-	-0.1	-
$C_4H_4N_4$	108.04305	108.04303	-	-0.2	-
PO_4H_4	98.98417	98.98416	-	-0.1	-
$C_5H_5O_2$	97.02841	97.02839	-	-0.2	-
$C_4H_4N_3$	94.03997	94.0400	-	-0.1	-
$C_4H_2N_3$	92.02432	92.02431	-	-0.1	-
$C_3H_4N_3$	82.03997	82.03997	-	0.0	-
$C_3H_3N_3$	81.03215	81.03214	-	-0.1	-
$C_3H_3N_2$	67.02907	67.0291	-	0.4	-
$C_3H_2N_2$	66.02125	66.02128	-	0.5	-
C_3HN_2	65.01342	65.01346	-	0.6	-
$C_2H_4N_2$	56.0369	56.03697	-	1.2	-
$C_2H_3N_2$	55.02907	55.02914	-	1.3	-

7.1.4. Protonated ADP CID and EID assignments.

Proposed formula	Exact Mass (*m/z*)	EID Ion (*m/z*)	CID Ion (*m/z*)	EID Error (ppm)	CID Error (ppm)
$C_{10}H_{15}N_5O_{10}P_2Na$	450.01864	450.01864	450.01872	0.0	0.2
$C_{10}H_{12}O_6N_5PNa$	352.04174	-	352.04139	-	-1.0
$C_5H_{10}O_{10}P_2Na$	314.96414	-	314.96415	-	0.0
$C_5H_9O_{10}P_2Na$	313.95632	313.95659	-	0.9	-
$C_5H_8O_9P_2Na$	296.95358	296.95384	296.95358	0.9	0.0
$C_4H_9O_9P_2Na$	285.9614	285.96165	-	0.9	-
$C_3H_8O_9P_2Na$	272.95358	272.95381	-	0.8	-
$C_4H_7O_8P_2Na$	267.95084	267.95101	-	0.6	-
$C_3H_7O_8P_2Na$	255.95084	255.95101	-	0.7	-
$C_3H_6O_8P_2Na$	254.94301	254.9432	-	0.7	-
$C_{10}H_{12}O_3N_5$	250.09347	250.09363	250.09344	0.6	-0.1
$C_2H_6O_8P_2Na$	242.94301	242.94314	-	0.5	-
$C_5H_9O_7PNa$	234.99781	234.99796	-	0.6	-
$C_2H_6O_7P_2Na$	226.9481	226.94824	-	0.6	-
$C_5H_7O_6PNa$	216.98725	216.98736	216.98726	0.5	0.0
$CH_5O_7P_2Na$	213.94027	213.94039	-	0.6	-
$P_2O_7H_4Na$	200.93245	200.93247	200.9324	0.1	-0.2
$P_2O_7H_3Na$	199.92462	199.92468	-	0.3	-
$C_5H_5O_5PNa$	198.97668	198.97677	-	0.5	-
$P_2O_6H_2Na$	182.92188	182.92195	-	0.4	-
$C_7H_8ON_5$	178.07234	178.07238	-	0.2	-
$C_6H_6ON_5$	164.05669	164.05672	-	0.2	-

$C_2H_5O_5PNa$	162.97668	162.97672	-	0.2	-
$C_5H_5N_5Na$	158.04372	158.04374	-	0.1	-
$C_6H_6N_5$	148.06177	148.0618	-	0.2	-
$C_2H_3PO_4Na$	144.96612	144.96613	-	0.1	-
$C_5H_6N_5$	136.06177	136.06178	-	0.1	-
$C_5H_5N_5$	135.05395	135.05395	-	0.0	-
PO_4H_3Na	120.96612	120.96611	-	-0.1	-
$C_5H_4O_2Na$	119.01035	119.01034	-	-0.1	-
$C_4H_4N_4$	108.04305	108.04303	-	-0.2	-
PO_3HNa	102.9555	102.95554	-	0.4	-
$C_5H_5O_2$	97.02841	97.02839	-	-0.2	-
C_5H_5O	81.03349	81.03348	-	-0.1	-
C_6H6	78.0464	78.0464	-	0.0	-
C_4H_4O	68.02567	68.02569	-	0.3	-
C_4H_8	56.06205	56.06211	-	1.1	-

7.1.5. Monosodium ADP CID and EID assignments.

Proposed formula	**Exact Mass (*m/z*)**	**EID Ion (*m/z*)**	**CID Ion (*m/z*)**	**EID Error (ppm)**	**CID Error (ppm)**
$C_{10}H_{14}N_5O_{10}P_2Na_2$	472.00058	472.00049	472.00084	-0.2	0.6
$C_{10}H_{11}O_6N_5PNa_2$	374.02369	374.02399	374.02352	0.8	-0.5
$C_5H_9O_{10}P_2Na_2$	336.94609	336.94617	336.94612	0.2	0.1
$C_5H_7O_9P_2Na_2$	318.93552	318.93556	318.93552	0.1	0.0
$C_3H_6O_8P_2Na_2$	277.93278	277.93287	-	0.3	-

$C_2H_5O_8P_2Na_2$	264.92496	264.92501	-	0.2	-
$C_5H_6O_6PNa_2$	238.96919	238.96923	238.96912	0.2	-0.3
$CH_4O_7P_2Na_2$	235.92222	235.92223	-	0.0	-
$P_2O_7H_3Na_2$	222.91439	222.91442	222.91428	0.1	-0.5
$P_2O_7H_2Na_2$	221.90657	221.90657	-	0.0	-
$C_5H_4O_5PNa_2$	220.95863	220.95863	-	0.0	-
$P_2O_6HNa_2$	204.90383	204.90385	-	0.1	-
$C_3H_4O_5PNa_2$	196.95863	196.95863	-	0.0	-
$C_2H_2O_4PNa_2$	166.94806	166.94808	-	0.1	-
$C_5H_5N_5Na$	158.04372	158.04375	-	0.2	-
$PO_4H_2Na_2$	142.94806	142.94806	-	0.0	-
PO_4HNa_2	141.94024	141.94022	-	-0.1	-
$C_5H_6N_5$	136.06177	136.06174	-	-0.2	-
PO_3Na_2	124.9375	124.93748	-	-0.2	-
PO_4H_3Na	120.96612	120.9661	-	-0.2	-
C_6H_6	78.0464	78.0464	-	0.0	-
C_5H_{10}	70.0777	70.07772	-	0.3	-
C_4H_8	56.06205	56.06211	-	1.1	-

7.1.6. Disodium ADP CID and EID assignments.

Proposed formula	**Exact Mass (*m/z*))**	**EID Ion (*m/z*)**	**CID Ion (*m/z*)**	**EID Error (ppm)**	**CID Error (ppm)**
$C_{10}H_{13}N_5O_{10}P_2Na_3$	493.98253	493.98265	493.98293	0.2	0.8
$C_{10}H_{11}N_5O_9P_2Na_3$	475.97196	-	475.97237	-	0.9

$C_{10}H_{11}O_6N_5PNa_2$	374.02396	374.02395	374.02406	0.0	0.3
$P_2O_7H_2Na_3$	244.89634	244.89644	-	0.4	-
$P_2O_6Na_3$	226.88577	226.88585	-	0.4	-
$C_5H_4N_5Na_2$	180.02566	180.02569	-	0.2	-
PO_4HNa_3	164.93001	164.93004	-	0.2	-
$PO_4H_2Na_2$	142.94806	142.94808	-	0.1	-
PO_3Na_2	124.9375	124.9375	-	0.0	-
C_6H_6	78.0464	78.04642	-	0.3	-
C_5H_{10}	70.0777	70.07773	-	0.4	-
C_4H_9	57.06988	57.06994	-	1.1	-
C_4H_8	56.06205	56.06212	-	1.2	-
C_4H_7	55.05423	55.0543	-	1.3	-

7.1.7. Trisodium ADP CID and EID assignments.

Proposed formula	**Exact Mass (*m/z*)**	**EID Ion (*m/z*)**	**CID Ion (*m/z*)**	**EID Error (ppm)**	**CID Error (ppm)**
$C_{10}H_{17}N_5O_{13}P_3$	508.00302	508.0017	508.0031	-2.6	0.1
$C_{10}H_{16}O_{10}N_5P_2$	428.03669	428.0376	428.0366	2.1	-0.2
$C_{10}H_{14}O_9N_5P_2$	410.02613	410.027	410.0262	2.1	0.0
$C_{10}H_{15}O_7N_5P$	348.07036	348.0709	348.0704	1.4	0.0
$C_{10}H_{13}O_6N_5P$	330.0598	-	330.0599	-	0.2
$P_3O_{10}H_6$	258.91683	258.9171	-	1.1	-
$C_{10}H_{11}O_3N_5$	249.08564	249.0859	-	1.2	-
$C_{10}H_{10}O_2N_5$	232.0829	232.0831	232.0831	0.9	0.7

$C_9H_4O_3N_4$	216.02779	216.0283	-	2.5	-
$C_5H_5O_2N_5P$	198.01754	198.0177	-	0.6	-
$C_7H_8O_2N_5$	194.06725	194.0674	-	0.7	-
$C_8H_8ON_5$	190.07234	190.0725	-	0.8	-
$P_2O_7H_5$	178.9505	178.9506	-	0.6	-
$C_7H_8ON_5$	178.07234	178.0725	-	0.6	-
$C_7H_7ON_5$	177.06451	177.0646	-	0.6	-
$C_6H_7ON_5$	165.06451	165.0646	-	0.5	-
$C_6H_6ON_5$	164.05669	164.0568	-	0.4	-
$C_7H_8N_5$	162.07742	162.0775	-	0.6	-
$P_2O_6H_3$	160.93994	160.94	-	0.4	-
$C_6H_8N_5$	150.07742	150.0775	-	0.4	-
$C_6H_7N_5$	149.0696	149.0697	-	0.4	-
$C_6H_6N_5$	148.06177	148.0618	-	0.4	-
$C_5H_6N_5$	136.06177	136.0618	-	0.1	-
$C_5H_5N_5$	135.05395	135.054	-	0.2	-
$C_6H_5N_4$	133.05087	133.0509	-	0.2	-
$C_5H_3N_4$	119.03522	119.0352	-	0.2	-
$C_5H_6O_3$	114.03115	114.0312	-	0.0	-
$C_4H_4N_4$	108.04305	108.0431	-	0.1	-
$C_4H_3N_4$	107.03522	107.0352	-	0.2	-
PO_4H_4	98.98417	98.98418	-	0.1	-
PO_4H_3	97.97635	97.97636	-	0.1	-
$C_5H_5O_2$	97.02841	97.02842	-	0.1	-

$C_4H_4N_3$	94.03997	94.03999	-	0.2	-
C_4H_2N3	92.02432	92.02434	-	0.2	-
$C_3H_4N_3$	82.03997	82.04	-	0.4	-
$C_3H_3N_3$	81.03215	81.03218	-	0.4	-
C_3H_2N	80.02432	80.02436	-	0.5	-
C_6H_6	78.0464	78.04644	-	0.5	-
C_5H_{10}	70.0777	70.07777	-	1.0	-
C_4H_5O	69.03349	69.03356	-	1.0	-
$C_3H_3N_2$	67.02907	67.02915	-	1.2	-
$C_3H_2N_2$	66.02125	66.02133	-	1.2	-
C_3HN_2	65.01342	65.01351	-	1.4	-
C_4H_9	57.06988	57.07	-	2.1	-
C_4H_8	56.06205	56.06218	-	2.3	-
$C_2H_3N_2$	55.02907	55.02921	-	2.5	-
C_2HN_2	53.01342	53.01358	-	3.0	-

7.1.8. Protonated ATP CID and EID assignments.

Proposed formula	**Exact Mass (*m/z*)**	**EID Ion (*m/z*)**	**CID Ion (*m/z*)**	**EID Error (ppm)**	**CID Error (ppm)**
$C_{10}H_{16}N_5O_{13}P_3Na$	529.98497	529.98384	529.9848	-2.1	-0.3
$C_5H_{11}O_{13}P_3Na$	394.93047	-	394.9304	-	-0.2
$C_5H_{10}O_{13}P_3Na$	393.92265	393.92309	-	1.1	-
$C_5H_9O_{12}P_3Na$	376.91991	376.92033	376.9199	1.1	-0.1
$C_4H_{10}O_{12}P_3Na$	365.92773	365.92808	-	1.0	-

$C_3H_8O_{11}P_3Na$	335.91717	335.91751	-	1.0	-
$C_2H_7O_{11}P_3Na$	322.90934	322.90966	-	1.0	-
$C_5H_{10}O_{10}P_2Na$	314.96414	314.96443	-	0.9	-
$C_2H_7O_{10}P_3Na$	306.91443	306.91471	-	0.9	-
$C_5H_8O_9P_2Na$	296.95358	296.95383	296.9533	0.8	-1.1
$CH_6O_{10}P_3Na$	293.9066	293.90686	-	0.9	-
$P_3H_5O_{10}Na$	280.89878	280.89886	280.8988	0.3	-0.1
$P_3O_9H_3Na$	262.88821	262.88841	-	0.8	-
$C_{10}H_{12}O_3N_5$	250.09347	250.09361	250.0934	0.6	-0.3
$C_2H_6O_8P_2Na$	242.94301	242.94315	-	0.6	-
$C_5H_9O_7PNa$	234.99781	234.99797	-	0.7	-
$C_{10}H_{10}O_2N_5$	232.0829	232.08296	-	0.3	-
$C_2H_6O_7P_2Na$	226.9481	226.94821	-	0.5	-
$C_5H_7O_6PNa$	216.98725	216.98735	-	0.5	-
$CH_5O_7P_2Na$	213.94027	213.94038	-	0.5	-
$P_2O_7H_4Na$	200.93245	200.93251	-	0.3	-
$P_2O_7H_3Na$	199.92462	199.92469	-	0.4	-
$C_5H_5O_5PNa$	198.97668	198.97675	-	0.4	-
$P_2O_6H_2Na$	182.92188	182.92195	-	0.4	-
$P_2O_7H_5$	178.9505	178.95053	-	0.2	-
$C_7H_8ON_5$	178.07234	178.07238	-	0.2	-
$C_3H_5O_5PNa$	174.97668	174.97671	-	0.2	-
$C_6H_6ON_5$	164.05669	164.05671	-	0.1	-
$C_6H_8O_4N$	158.04478	158.04373	-	-6.6	-

$C_6H_6N_5$	148.06177	148.06178	-	0.1	-
$C_5H_6N_5$	136.06177	136.06177	-	0.0	-
$C_5H_5N_5$	135.05395	135.05394	-	-0.1	-
PO_4H_3Na	120.96612	120.96611	-	-0.1	-
PO_4H_2Na	119.95829	119.95828	-	-0.1	-
$C_5H_3N_4$	119.03522	119.03522	-	0.0	-
$C_5H_4O_2Na$	119.01035	119.01034	-	-0.1	-
$C_4H_4N_4$	108.04305	108.04304	-	-0.1	-
PO_3HNa	102.95555	102.95554	-	-0.1	-
PO_4H_3	97.97635	97.97635	-	0.0	-
$C_5H_5O_2$	97.02841	97.0284	-	-0.1	-
$C_4H_4N_3$	94.03997	94.03996	-	-0.1	-
$C_3H_4N_3$	82.03997	82.03998	-	0.1	-
C_5H_5O	81.03349	81.0335	-	0.1	-
C_6H_6	78.0464	78.04643	-	0.4	-
C_5H_{10}	70.0777	70.07775	-	0.7	-
C_4H_4O	68.02567	68.02572	-	0.7	-
$C_3H_3N_2$	67.02907	67.02913	-	0.9	-
$C_3H_2N_2$	66.02125	66.0213	-	0.8	-
C_4H_9	57.06988	57.06998	-	1.8	-
C_4H_8	56.06205	56.06216	-	2.0	-
C_4H_7	55.05423	55.05434	-	2.0	-

7.1.9. Monosodium ATP CID and EID assignments.

Proposed formula	Exact Mass (*m/z*)	EID Ion (*m/z*)	CID Ion (*m/z*)	EID Error (ppm)	CID Error (ppm)
$C_{10}H_{15}N_5O_{13}P_3Na_2$	551.9669	551.964	551.97	-4.8	0.1
$C_{10}H_{11}O_{11}N_5P_3Na$	492.956	492.955	-	-2.2	-
$C_{10}H_{12}O_9N_5P_2Na_2$	453.99	453.991	453.99	2.7	0.1
$C_5H_{10}O_{13}P_3Na_2$	416.9124	416.913	416.91	2.2	0.0
$C_5H_9O_{13}P_3Na_2$	415.9046	415.905	-	2.0	-
$C_5H_8O_{12}P_3Na_2$	398.9019	398.903	398.9	1.9	0.1
$C_4H_9O_{12}P_3Na_2$	387.9097	387.91	-	1.8	-
$C_3H_8O_{12}P_3Na_2$	374.9019	374.903	-	1.9	-
$C_{10}H_{11}O_6N_5PNa_2$	374.0237	374.024	-	1.8	-
$C_3H_7O_{11}P_3Na_2$	357.8991	357.9	-	1.7	-
$C_2H_6O_{11}P_3Na_2$	344.8913	344.892	-	1.6	-
$C_5H_9O_{10}P_2Na_2$	336.9461	336.947	-	2.0	-
$C_2H_6O_{10}P_3Na_2$	328.8964	328.897	-	1.7	-
$C_5H_7O_9P_2Na_2$	318.9355	318.936	-	1.6	-
$CH_5O_{10}P_3Na_2$	315.8886	315.889	-	1.5	-
$P_3O_{10}H_4Na_2$	302.8807	302.881	302.88	0.2	-0.1
$P_3O_{10}H_3Na_2$	301.8729	301.873	-	1.3	-
$C_5H_5O_8P_2Na_2$	300.925	300.925	-	1.4	-
$P_3O_9H_3Na_2$	285.878	285.878	-	1.1	-
$P_3O_9H_2Na_2$	284.8702	284.87	-	1.1	-
$P_3O_{10}H_5Na$	280.8988	280.899	-	1.3	-
$C_3H_5O_8P_2Na_2$	276.925	276.925	-	1.2	-

$C_2H_5O_8P_2Na_2$	264.925	264.925	-	1.2	-
$P_3O_9H_3Na$	262.8882	262.889	-	1.2	-
$C_5H_8O_7PNa_2$	256.9798	256.98	-	0.7	-
$C_{10}H_{12}O_3N_5$	250.0935	250.094	-	1.0	-
$C_2H_3O_7P_2Na_2$	246.9144	246.915	-	0.9	-
$C_5H_6O_6PNa_2$	238.9692	238.969	-	1.0	-
$CH_4O_7P_2Na_2$	235.9222	235.922	-	0.7	-
$P_2O_7H_3Na_2$	222.9144	222.915	-	0.7	-
$P_2O_7H_2Na_2$	221.9066	221.907	-	0.8	-
$P_2O_6H_2Na_2$	205.9117	205.912	-	0.9	-
$P_2O_6HNa_2$	204.9038	204.904	-	0.5	-
$P_2O_7H_4Na$	200.9325	200.933	-	0.7	-
$C_3H_4PO_5Na_2$	196.9586	196.959	-	0.6	-
$C_7H_8ON_5$	178.0723	178.072	-	0.4	-
$C_2H_2PO_4Na_2$	166.9481	166.948	-	0.3	-
$C_6H_6ON_5$	164.0567	164.057	-	0.2	-
$C_5H_5N_5Na$	158.0437	158.044	-	0.3	-
$C_6H_6N_5$	148.0618	148.062	-	0.5	-
$PO_4H_2Na_2$	142.9481	142.948	-	0.1	-
PO_4HNa_2	141.9402	141.94	-	0.1	-
$C_5H_6N_5$	136.0618	136.062	-	0.1	-
$C_5H_5N_5$	135.054	135.054	-	0.1	-
PO_3Na_2	124.9375	124.938	-	0.0	-
PO_4H_3Na	120.9661	120.966	-	0.0	-

$C_5H_3N_4$	119.0352	119.035	-	0.0	-
PO_2Na_2	108.9426	108.943	-	0.0	-
$C_4H_4N_4$	108.0431	108.043	-	-0.1	-
$C_5H_5O_2$	97.02841	97.0284	-	-0.1	-
$C_3H_4N_3$	82.03997	82.04	-	0.1	-
C_5H_5O	81.03349	81.0335	-	0.1	-
C_6H_6	78.0464	78.0464	-	0.4	-
C_5H_{10}	70.0777	70.0778	-	0.7	-
$C_3H_3N_2$	67.02907	67.0291	-	0.9	-
C_3H_8N	58.06513	58.0652	-	1.4	-
C_4H_9	57.06988	57.07	-	1.8	-
C_4H_8	56.06205	56.0622	-	2.0	-
C_4H_7	55.05423	55.0543	-	2.0	-
C_4H_6	54.0464	54.0465	-	2.4	-

7.1.10. Disodium ATP CID and EID assignments.

Proposed formula	**Exact Mass (*m/z*)**	**EID Ion (*m/z*)**	**CID Ion (*m/z*)**	**EID Error (ppm)**	**CID Error (ppm)**
$C_{10}H_{14}N_5O_{13}P_3Na_3$	573.94886	573.9433	-	-9.7	-
$C_{10}H_{11}O_9N_5P_2Na_3$	475.97196	475.9732	475.97155	2.5	-0.9
$C_5H_9O_{13}P_3Na_3$	438.89436	438.8953	438.89423	2.1	-0.3
$C_5H_8O_{13}P_3Na_3$	437.88654	437.8875	-	2.2	-
$C_5H_7O_{12}P_3Na_3$	420.8838	420.8847	420.88379	2.1	0.0
$C_4H_8O_{12}P_3Na_3$	409.89162	409.8925	-	2.2	-

$C_5H_7O_{11}P_3Na_3$	404.88888	404.8897	-	1.9	-
$C_5H_5O_{11}P_3Na_3$	402.87323	402.8742	-	2.3	-
$C_3H_7O_{12}P_3Na_3$	396.8838	396.8845	-	1.8	-
$C_4H_6O_{11}P_3Na_3$	391.88106	391.8819	-	2.2	-
$C_3H_7O_{11}P_3Na_3$	380.88888	380.8897	-	2.0	-
$C_3H_6O_{11}P_3Na_3$	379.88106	379.8819	-	2.1	-
$C_3H_5O_{11}P_3Na_3$	378.87323	378.8741	-	2.3	-
$C_{10}H_{12}O_6N_5PNa_2$	375.03151	375.0277	-	-10.3	-
$C_{10}H_{11}O_6N_5PNa_2$	374.02369	374.0244	-	1.8	-
$C_2H_5O_{11}P_3Na_3$	366.87323	366.874	-	2.0	-
$C_2H_5O_{10}P_3Na_3$	350.87832	350.879	-	1.9	-
$C_2H_4O_{11}P_3Na_2$	342.87564	342.8739	-	-5.1	-
$C_5H_6O_9P_2Na_3$	340.91747	340.9181	340.91759	1.8	0.4
$C_5H_5O_9P_2Na_3$	339.90964	339.9102	-	1.6	-
$CH_4P_3O_{10}Na_3$	337.87049	337.8711	-	1.7	-
$P_3O_{10}H_3Na_3$	324.86267	324.8626	-	-0.3	-
$P_3O_{10}H_2Na_3$	323.85484	323.8554	-	1.7	-
$C_5H_4O_8P_2Na_3$	322.9069	322.9074	-	1.6	-
$C_5H_7O_9P_2Na_2$	318.93552	318.9362	-	2.0	-
$CH_5O_{10}P_3Na_2$	315.88855	315.8891	-	1.6	-
$C_4H_5O_8P_2Na_3$	311.91473	311.9152	-	1.5	-
$C_4H_4O_8P_2Na_3$	310.9069	310.9074	-	1.6	-
$P_3O_9H_2Na_3$	307.85993	307.8604	-	1.6	-
$P_3O_9HNa_3$	306.8521	306.8523	-	0.8	-

$P_3O_9Na_3$	305.84428	305.8448	-	1.5	-
$P_3O_{10}H_4Na_2$	302.88072	302.8811	-	1.4	-
$C_3H_4O_8P_2Na_3$	298.9069	298.9074	-	1.5	-
$P_3O_9H_2Na_2$	284.87016	284.8705	-	1.3	-
$P_3O_9HNa_2$	283.86233	283.8628	-	1.5	-
$C_2H_2O_7P_2Na_3$	268.89634	268.8966	-	1.0	-
$C_5H_8O_7PNa_2$	256.97975	256.98	-	1.0	-
$C_{10}H_{12}O_3N_5$	250.09347	250.0938	-	1.2	-
$P_2O_7H_2Na_3$	244.89634	244.8965	-	0.7	-
$P_2O_7HNa_3$	243.88851	243.8888	-	1.1	-
$C_5H_6O_6PNa_2$	238.96919	238.9694	-	1.0	-
$P_2O_6Na_3$	226.88577	226.8856	-	-0.6	-
$P_2O_7H_3Na_2$	222.91439	222.9146	-	0.9	-
$P_2O_7H_2Na_2$	221.90657	221.9068	-	0.8	-
$C_5H_4O_5PNa_2$	220.95863	220.9588	-	0.9	-
$P_2O_6HNa_2$	204.90383	204.904	-	0.7	-
$P_2O_6Na_2$	203.896	203.8962	-	0.8	-
$C_3H_4O_5PNa_2$	196.95863	196.9588	-	0.7	-
$C_5H_4N_5Na_2$	180.02566	180.0258	-	0.5	-
$C_7H_8ON_5$	178.07234	178.0724	-	0.3	-
$C_2H_2O_4PNa_2$	166.94806	166.9481	-	0.5	-
PO_4HNa_3	164.93001	164.9301	-	0.4	-
$C_6H_6ON_5$	164.05669	164.0567	-	0.3	-
PO_4Na_3	163.92218	163.9222	-	0.4	-

$C_5H_5N_5Na$	158.04372	158.0438	-	0.3	-
PO_4HNa_2	141.94024	141.9403	-	0.1	-
$C_5H_6N_5$	136.06177	136.0618	-	0.1	-
$C_5H_5N_5$	135.05395	135.054	-	0.1	-
PO_3Na_2	124.9375	124.9375	-	0.0	-
PO_4H_3Na	120.96612	120.9661	-	0.1	-
$C_5H_3N_4$	119.03522	119.0352	-	0.1	-
PO_2Na_2	108.94258	108.9426	-	0.1	-
$C_4H_4N_4$	108.04305	108.0431	-	0.1	-
$C_5H_5O_2$	97.02841	97.02841	-	0.0	-
$C_3H_4N_3$	82.03997	82.04001	-	0.5	-
C_5H_5O	81.03349	81.03352	-	0.4	-
C_6H_6	78.0464	78.04644	-	0.5	-
C_5H_{10}	70.0777	70.07777	-	1.0	-
$C_3H_3N_2$	67.02907	67.02916	-	1.3	-
Na_2OH	62.98173	62.98182	-	1.4	-
Na_2O	61.97391	61.974	-	1.5	-
C_4H_9	57.06988	57.07	-	2.1	-
C_4H_8	56.06205	56.06219	-	2.5	-
C_4H_7	55.05423	55.05436	-	2.4	-

7.1.11. Trisodium ATP CID and EID assignments.

Proposed formula	Exact Mass (*m/z*)	Observed ion (m/z)	Error (ppm)
$C_{23}H_{27}O_9N_6PF$	581.15557	581.15481	-1.3
$C_{22}H_{23}O_9N_6PF$	565.12427	565.12522	1.7
$C_{23}H_{24}O_8N_6PF$	562.13718	562.13807	1.6
$C_{23}H_{24}O_5N_6F$	483.17867	483.1792	1.1
$C_{23}H_{23}O_5N_6$	463.17244	463.17302	1.3
$C_{21}H_{18}O_5N_6F$	453.13172	453.13242	1.5
$C_{21}H_{20}O_4N_6F$	439.15246	439.15289	1.0
$C_{21}H_{17}O_5N_6$	433.12549	433.1261	1.4
$C_{18}H_{19}O_4N_6F$	402.14463	402.14375	-2.2
$C_{19}H_{17}O_3N_6$	377.13566	377.13587	0.6
$C_6H_{12}O_5N_4$	220.08022	220.07987	-1.6

7.1.12. Protonated Fostamatanib CID and EID assignments.

Proposed formula	Exact Mass (*m/z*)	EID ion (m/z)	Error (ppm)
$C_{23}H_{26}O_9N_6PFNa$	603.13751	603.13722	-0.5
$C_{23}H_{26}O_9N_6PF$	580.14774	580.14986	3.7
$C_{22}H_{24}O_8N_6PFNa$	573.12695	573.12884	3.3
$C_{22}H_{23}O_9N_6PF$	565.12427	565.12522	1.7
$C_{23}H_{23}O_5N_6FNa$	505.16062	505.16205	2.8
$C_{22}H_{23}O_5N_6FNa$	493.16062	493.162	2.8
$C_{23}H_{24}O_5N_6F$	483.17867	483.17994	2.6

$C_{22}H_{20}O_5N_6F$	467.14737	467.14867	2.8
$C_{23}H_{23}O_5N_6$	463.17244	463.1736	2.5
$C_{21}H_{20}O_4N_6F$	439.15246	439.15345	2.3
$C_{21}H_{17}O_5N_6$	433.12549	433.12645	2.2
$C_{19}H_{17}O_3N_6$	377.13566	377.13662	2.5

7.1.13. Monosodium Fostamatanib CID and EID assignments.

Proposed formula	**Exact Mass (*m/z*)**	**EID ion (m/z)**	**Error (ppm)**
$C_{23}H_{25}O_9N_6PFNa_2$	625.11946	625.11872	-1.2
$C_{22}H_{23}O_8N_6PFNa_2$	595.10889	595.11049	2.7
$C_{23}H_{23}O_5N_6FNa$	505.16062	505.16172	2.2
$C_{22}H_{23}O_5N_6FNa$	493.16062	493.16164	2.1
$C_{23}H_{22}O_6N_3FNa$	478.13833	478.13848	0.3
$C_{23}H_{21}O_6N_3FNa$	477.13067	477.13073	0.1
$C_{22}H_{23}O_5N_6F$	470.17165	470.17165	0.0
$C_{20}H_{17}O_5PFNa$	463.11367	463.11443	1.6
$PO_4H_2Na_2$	142.94806	142.94807	0.1
PO_3Na_2	124.9375	124.93749	-0.1

7.1.14. Disodium Fostamatanib CID and EID assignments.

7.2. Chapter 2

Proposed formula	Exact Mass (*m/z*)	ETD Ion (*m/z*)	ETD Error (ppm)
$C_{25}H_{28}N_4O_3F$	451.2145	451.2139	-0.1
$C_{24}H_{26}N_4O_3F$	437.1989	437.1968	-0.5
$C_{25}H_{28}N_4O_3$	432.2161	432.2186	0.6
$C_{24}H_{26}N_4O_2F$	421.2040	421.2010	-0.7
$C_{22}H_{22}N_4O_3F$	409.1676	409.1678	0.0
$C_{24}H_{19}N_3O_2$	381.1477	381.1464	-0.3
$C_{20}H_{17}N_3O_3F$	366.1254	366.1190	-1.7
$C_{20}H_{18}N_3O_2F$	351.1383	351.1370	-0.4
$C_{18}H_{15}N_3O_3F$	340.1097	340.1091	-0.2
$C_{18}H_{15}N_3O_2F$	324.1137	324.1148	0.3
$C_{18}H_{14}N_3O_2F$	323.1070	323.1062	-0.2
$C_{16}H_{22}N_3O_3$	304.1661	304.1654	-0.2
$C_{25}H_{28}N_4O_3F$	226.1109	226.1112	0.2
C_5H1_0N	84.0813	84.0803	-1.2

7.2.1. [Cediranib + 2H]$^{2+}$ ETD product ion assignments

Proposed formula	Exact Mass (*m/z*)	CID 2+ Ion (*m/z*)	CID 2+ Error (ppm)
$C_{22}H_{22}N_4O_3F$	409.1676	409.1681	0.1
$C_{20}H_{17}N_3O_3F$	366.1254	366.1251	-0.1

$C_{18}H_{15}N_3O_3F$	340.1097	340.1085	-0.4
$C_{18}H_{13}N_3O_3F$	338.0941	338.0938	-0.1
$C_{17}H_{13}N_3O_2F$	310.0992	310.0988	-0.1
$C_{16}H_{22}N_3O_3$	304.1661	304.1639	-0.7
$C_{25}H_{28}N_4O_3F$	226.1109	226.1110	0.0
$C_{11}H_{11}N_2O_3$	219.0770	219.0766	-0.2
$C_9H_7N_2O_3$	191.0457	191.0465	0.4
C_9H_9NOF	166.0668	166.0676	0.5
C_9H_7NF	148.0563	148.0571	0.5
C_9H_5NF	146.0406	146.0393	-0.9
$C_7H_{14}N$	112.1126	112.1134	0.7
$C_5H_{10}N$	84.0813	84.0819	0.7
$C_{21}H_{20}N_3O_3F$	70.0657	70.0664	1.0

7.2.2. $[Cediranib + 2H]^{2+}$ CID product ion assignments

Proposed formula	**Exact Mass (*m/z*)**	**CID 1+ Ion (*m/z*)**	**CID 1+ Error (ppm)**
$C_{25}H_{28}N_4O_3F$	451.2145	451.2132	-0.3
$C_{18}H_{15}N_3O_3F$	340.1097	340.1061	-1.1
$C_7H_{14}N$	112.1126	112.1133	0.6
C_5H1_0N	84.0813	84.0815	0.2

7.2.3. $[Cediranib + H]^{+}$ CID product ion assignments

Proposed formula	Exact Mass (*m/z*)	ETD Ion (*m/z*)	ETD Error (ppm)
$C_{28}H_{35}N_7O_2$	501.2848	501.2844	-0.1
$C_{28}H_{34}N_7O_2$	500.2774	500.2776	0.0
$C_{27}H_{32}N_7O_2$	486.2612	486.2612	0.0
$C_{26}H_{28}N_6O_2$	456.2274	456.2270	-0.1
$C_{25}H_{27}N_6O_2$	443.2195	443.2188	-0.2
$C_{24}H_{26}N_6O_2$	430.2117	430.2122	0.1
$C_{24}H_{25}N_5O_2$	415.2008	415.2000	-0.2
$C_{23}H_{21}N_5O_2$	399.1695	399.1699	0.1
$C_{22}H_{20}N_6O$	384.1699	384.1717	0.5
$C_{15}H_{23}N_3O_2$	277.1790	277.1798	0.3
$C_{12}H_4N_5O_2$	250.0365	250.0284	-3.2

7.2.4. $[AZD9291 + 2H]^{2+}$ ETD product ion assignments

Proposed formula	Exact Mass (*m/z*)	CID 2+ Ion (*m/z*)	CID 2+ Error (ppm)
$C_{24}H_{25}N_6O_2$	429.2039	429.2023	-0.4
$C_{23}H_{25}N_6O$	401.2090	401.2076	-0.3
$C_{21}H_{22}N_6O$	374.1855	374.1845	-0.3
$C_{20}H_{19}N_6$	343.1671	343.1658	-0.4
$C_{28}H_{35}N_7O_2$	250.6424	250.6421	-0.1
$C_{26}H_{28}N_6O_2$	228.1137	228.1131	-0.3
$C_{13}H_{13}N_4$	225.1140	225.1140	0.0

$C_{22}H_{22}N_6O$	193.0928	193.0932	0.2
$C_{24}H_{24}N_6O_2$	72.0813	72.0816	0.4

7.2.5. $[AZD9291 + 2H]^{2+}$ CID product ion assignments

Proposed formula	**Exact Mass (*m/z*)**	**CID 1+ Ion (*m/z*)**	**CID 1+ Error (ppm)**
$C_{28}H_{34}N_7O_2$	500.2774	500.2767	-0.1
$C_{26}H_{27}N_6O_2$	455.2195	455.2187	-0.2
$C_{24}H_{23}N_6O_2$	427.1882	427.1877	-0.1
$C_{22}H_{21}N_6O$	385.1777	385.1818	1.1
$C_{13}H_{15}N_2O_2$	231.1134	231.1136	0.1
$C_{13}H_{13}N_4$	225.114	225.1131	-0.4
$C_{10}H_{13}N_2O$	177.1028	177.103	0.1
$C_4H_{10}N$	72.0813	72.0818	0.7

7.2.6. $[AZD9291 + H]^{+}$ CID product ion assignments

Proposed formula	**Exact Mass (*m/z*)**	**ETD Ion (*m/z*)**	**ETD Error (ppm)**
$C_{31}H_{44}N_3O_5F_2S_2$	640.269	640.2678	-0.2
$C_{30}H_{42}N_3O_5F_2S_2$	626.2534	626.2531	0.0
$C_{31}H_{43}N_3O_4F_2S_2$	623.2663	623.27	0.6
$C_{30}H_{42}N_3O_3F_2S$	562.2915	562.2905	-0.2
$C_{29}H_{38}N_3OF$	482.2983	482.2974	-0.2
$C_{23}H_{36}N_3O_3F_2S$	472.2445	472.2444	0.0

$C_{24}H_{38}N_3O_3S$	448.2634	448.2619	-0.3
$C_{22}H_{36}N_3O_2F_2S$	444.2496	444.2466	-0.7
$C_{24}H_{30}N_2OF_2$	400.2326	400.2320	-0.1
$C_{31}H_{45}N_3O_5F_2S_2$	320.6384	320.6383	0.0

7.2.7. $[AZD5672 + 2H]^{2+}$ ETD product ion assignments

Proposed formula	**Exact Mass (*m/z*)**	**CID 2+ Ion (*m/z*)**	**CID 2+ Error (ppm)**
$C_{30}H_{42}N_3O_3F_2S$	562.2915	562.2908	-0.1
$C_{30}H_{40}NO_5SF$	545.2611	545.2626	0.3
$C_{28}H_{35}N_2O_3F_2S$	517.2336	517.2326	-0.2
$C_{27}H_{34}N_2O_3F_2S$	504.2258	504.2256	0.0
$C_{25}H_{32}N_2O_3F_2S$	478.2102	478.2092	-0.2
$C_{22}H_{36}N_3O_2F_2S$	444.2496	444.2481	-0.3
$C_{20}H_{34}N_3O_2FS$	399.2356	399.2447	2.3
$C_{21}H_{34}N_3F_2$	366.2721	366.2714	-0.2
$C_{18}H_{27}N_2O_3S$	351.1742	351.1723	-0.5
$C_{16}H_{23}N_2O_2F_2S$	345.1448	345.1435	-0.4
$C_{17}H_{25}N_2O_3S$	337.1586	337.1577	-0.3
$C_{19}H_{27}N_2F_2$	321.2142	321.2136	-0.2
$C_{31}H_{44}N_3O_5F_2S_2$	320.6384	320.6383	0.0
$C_{30}H_{43}N_3O_3F_2S$	281.6497	281.6492	-0.2
$C_{11}H_{16}NO_3S$	242.0851	242.084	-0.5
$C_{14}H_{16}NF_2$	236.1251	236.1241	-0.4

$C_{13}H_{16}NF_2$	224.1251	224.1246	-0.2
$C_{20}H_{35}N_3O_2FS$	200.1178	200.0993	-9.2
$C_4H_{10}NO_2S$	136.0432	136.0398	-2.5
$C_6H_{12}N$	98.097	98.0968	-0.2
$C_5H_{10}N$	84.0813	84.0811	-0.2
CH_3O_2S	78.9854	78.985	-0.5

7.2.8. $[AZD5672 + 2H]^{2+}$ CID product ion assignments

Proposed formula	**Exact Mass (*m/z*)**	**CID 1+ Ion (*m/z*)**	**CID 1+ Error (ppm)**
$C_{31}H_{44}N_3O_5F_2S_2$	640.2690	640.2685	-0.1
$C_{22}H_{36}N_3O_2F_2S$	444.2496	444.2498	0.0
$C_{20}H_{29}N_2O_2F_2S$	399.1918	399.1914	-0.1
$C_{18}H_{25}N_2O_2F_2S$	371.1605	371.1604	0.0
$C_{17}H_{23}N_2O_2F_2S$	357.1448	357.1443	-0.1
$C_{16}H_{23}N_2O_2F_2S$	345.1448	345.1443	-0.1
$C_{15}H_{18}NO_2F_2S$	314.1026	314.1022	-0.1
$C_{16}H_{22}NO_3S$	308.1315	308.132	0.2
$C_{13}H_{16}NO_2F_2S$	288.087	288.0861	-0.3
$C_{16}H_{20}N_2F_2$	278.1595	278.156	-1.3
$C_{11}H_{16}NO_3S$	242.0851	242.0844	-0.3
$C_{14}H_{16}NF_2$	236.1251	236.1241	-0.4
$C_{14}H_{13}F_2$	219.0985	219.0981	-0.2
$C_{13}H_{13}F_2$	207.0985	207.098	-0.2

$C_{11}H_{14}NF_2$	198.1094	198.1092	-0.1
$C_{10}H_7F_2$	165.0516	165.0517	0.1
$C_3H_8NO_2S$	122.0276	122.0278	0.2
$C_2H_6NO_2S$	108.0119	108.0121	0.2
$C_6H_{12}N$	98.097	98.0969	-0.1

7.2.9. $[AZD5672 + H]^+$ CID product ion assignments

Proposed formula	**Exact Mass (*m/z*)**	**ETD Ion (*m/z*)**	**ETD Error (ppm)**
$C_{12}H_{15}N_4$	215.1297	215.1284	-0.6
$C_{12}H_{13}N_3$	199.1109	199.1097	-0.6
$C_{12}H_9N_2$	181.0766	181.0744	-1.2
$C_{11}H_{11}N_2$	171.0922	171.0917	-0.3
$C_{12}H_{13}$	157.1017	157.1004	-0.8
$C_{12}H_{12}$	156.0939	156.0932	-0.4
$C_6H_8N_2$	108.0687	108.0685	-0.2
$C_6H_7N_4$	79.0548	79.0538	-1.3

7.2.10. $[DAB + 2H]^{2+}$ ETD product ion assignments

Proposed formula	**Exact Mass (*m/z*)**	**CID 2+ Ion (*m/z*)**	**CID 2+ Error (ppm)**
$C_{12}H_{15}N_4$	215.1297	215.1297	0.0
$C_{12}H_{12}N_3$	198.1031	198.1032	0.1

$C_{12}H_9N_2$	181.0766	181.0768	0.1
$C_{11}H_{11}N_2$	171.0922	171.0923	0.1
$C_{11}H_8N$	154.0657	154.0656	-0.1
$C_{10}H_7$	127.0548	127.0548	0.0
$C_6H_8N_2$	108.0687	108.0684	-0.3
C_7H_9N	107.0735	107.0737	0.2
$C_{12}H_{13}N_3$	99.55545	99.5553	-0.2
C_6H_5N	91.0422	91.0421	-0.1
$C_{11}H_{12}N_2$	86.0500	86.0499	-0.1
$C_{11}H_8N$	77.0329	77.0378	6.4

7.2.11. $[DAB + 2H]^{2+}$ CID product ion assignments

Proposed formula	**Exact Mass (*m/z*)**	**CID 1+ Ion (*m/z*)**	**CID 1+ Error (ppm)**
$C_{12}H_{15}N_4$	215.1297	215.1297	0.0
$C_{12}H_{12}N_3$	198.1031	198.1113	4.1
$C_{12}H_{14}N_2$	186.1157	186.1164	0.4
$C_{12}H_9N_2$	181.0766	181.0768	0.1
$C_{11}H_{11}N_2$	171.0922	171.0923	0.1
$C_{11}H_8N$	154.0657	154.0656	-0.1
$C_6H_8N_2$	108.0687	108.0684	-0.3

7.2.12. $[DAB + H]^{+}$ CID product ion assignments

Proposed formula	Exact Mass (*m/z*)	ETD Ion (*m/z*)	ETD Error (ppm)
$C_{18}H_{27}N_3Cl$	320.1894	320.1879	-0.5
$C_{16}H_{23}N_3Cl$	292.1581	292.1566	-0.5
$C_{18}H_{27}N_3Cl$	285.2205	285.2238	1.2
$C_{16}H_{22}N_3$	256.1814	256.1756	-2.3
$C_{14}H_{17}N_2Cl$	248.1080	248.1069	-0.4
$C_{12}H_{12}N_2Cl$	219.0689	219.0725	1.6
$C_{11}H_{11}N_2Cl$	206.0611	206.0597	-0.7
$C_{10}H_9N_2Cl$	192.0454	192.0452	-0.1
$C_9H_8N_2Cl$	179.0376	179.037	-0.3
$C_{18}H_{28}N_3Cl$	160.5986	160.5988	0.1
$C_9H_{21}N$	143.1674	143.1673	-0.1
$C_5H_{12}N$	86.097	86.0965	-0.6

7.2.13. [Chloroquine + 2H]$^{2+}$ ETD product ion assignments

Proposed formula	Exact Mass (*m/z*)	CID 2+ Ion (*m/z*)	CID 2+ Error (ppm)
$C_{18}H_{27}N_2Cl$	320.1894	320.189	-0.1
$C_{16}H_{23}N_3Cl$	292.1581	292.1565	-0.5
$C_{14}H_{19}N_3Cl$	264.1267	264.1254	-0.5
$C_{14}H_{16}N_2Cl$	247.1002	247.099	-0.5
$C_{12}H_{12}N_2Cl$	219.0689	219.0679	-0.5
$C_{11}H_{10}N_2Cl$	205.0533	205.0525	-0.4

$C_{10}H_8N_2Cl$	191.0376	191.0371	-0.3
$C_9H_8N_2Cl$	179.0376	179.037	-0.3
$C_{18}H_{28}N_3Cl$	160.5986	160.5986	0.0
$C_{16}H_{23}N_3Cl$	146.58295	146.5823	-0.4
$C_9H_7N_2Cl$	142.1596	142.1575	-1.5
$C_{14}H_{20}N_3Cl$	132.56725	132.5673	0.0
$C_7H_{16}N$	114.1283	114.1282	-0.1
$C_6H_3N_2$	103.0296	103.0306	1.0
$C_5H_{12}N$	86.097	86.0971	0.1
$C_{13}H_{18}N_3Cl$	69.0704	69.0705	0.1
C_3H_8N	58.0657	58.0657	0.0

7.2.14. $[Chloroquine + 2H]^{2+}$ CID product ion assignments

Proposed formula	**Exact Mass (*m/z*)**	**CID 1+ Ion (*m/z*)**	**CID 1+ Error (ppm)**
$C_{18}H_{27}N_3Cl$	320.1894	320.188	-0.4
$C_{14}H_{16}N_2Cl$	247.1002	247.0992	-0.4
$C_{10}H_8N_2Cl$	191.0376	191.0369	-0.4
$C_9H_8N_2Cl$	179.0376	179.037	-0.3
C_9H_7NCl	164.0267	164.0264	-0.2
$C_9H_{20}N$	142.1596	142.1594	-0.1
$C_5H_{12}N$	86.0978	86.0971	-0.8
$C_5H_{10}N$	84.0813	84.0813	0.0
C_5H_9	69.0704	69.0705	0.1

7.2.15. $[Chloroquine + H]^{+}$ CID product ion assignments

7.3. Chapter 3

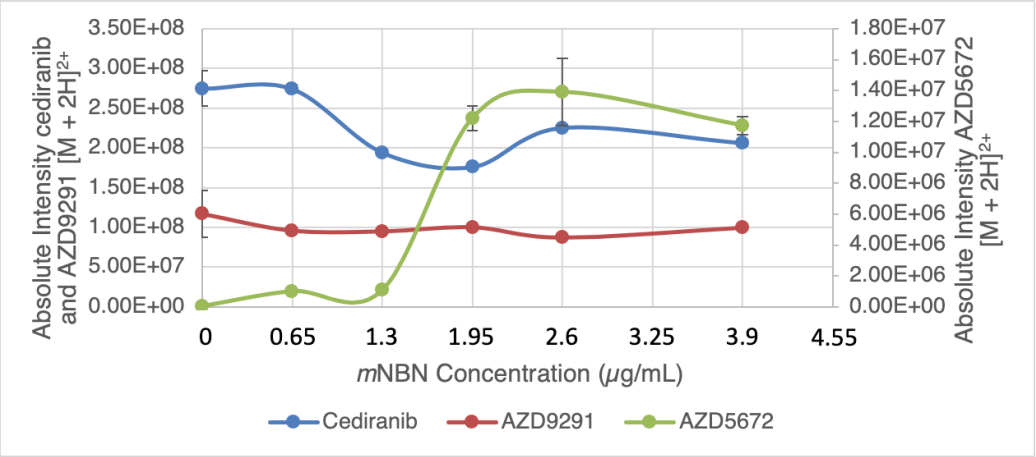

Figure 7.3.1. Absolute intensity of $[M + 2H]^{2+}$ cediranib, AZD9291 and AZD5671 for a range of *m*NBN concentrations.

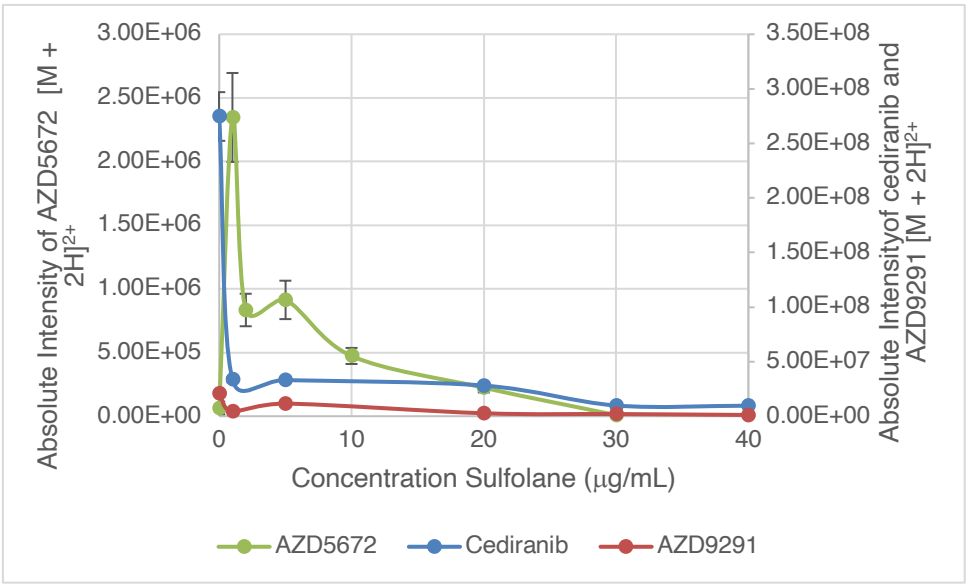

Figure 7.3.2. Absolute intensity of $[M + 2H]^{2+}$ cediranib, AZD9291 and AZD5671 for a range of sulfolane concentrations.

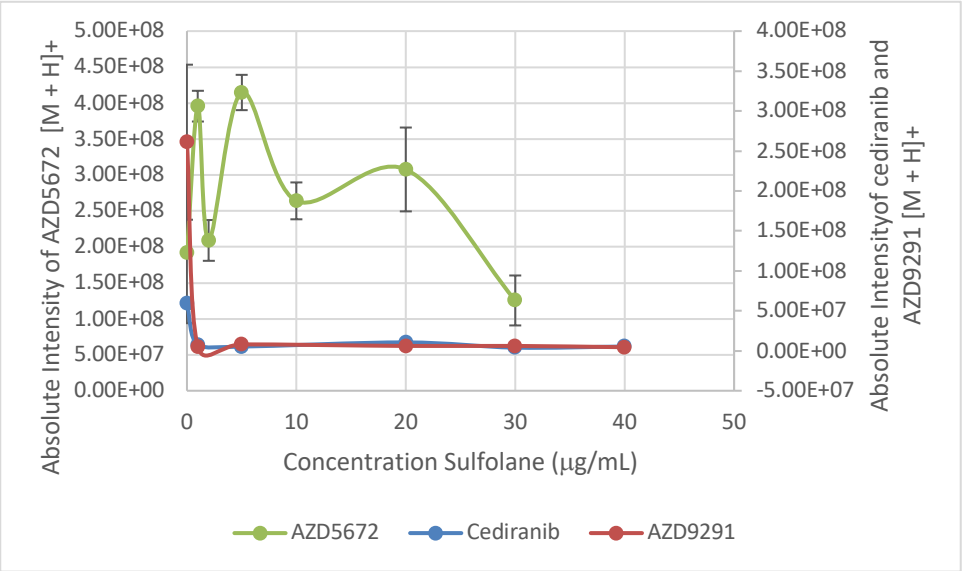

Figure 7.3.3. Absolute intensity of $[M + H]^+$ cediranib, AZD9291 and AZD5671 for a range of sulfolane concentrations.

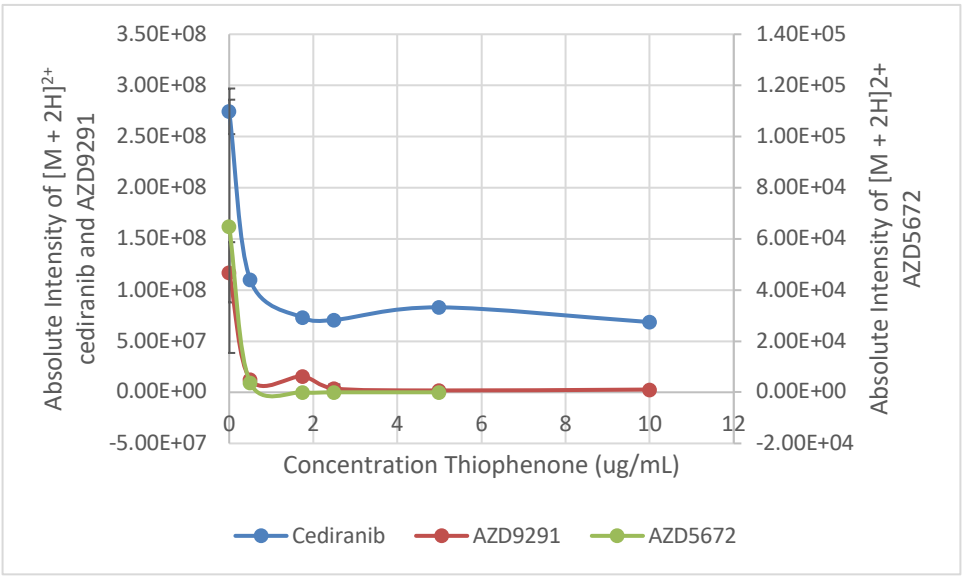

Figure 7.3.4. Absolute intensity of $[M + 2H]^{2+}$ cediranib, AZD9291 and AZD5671 for a range of thiophenone concentrations.

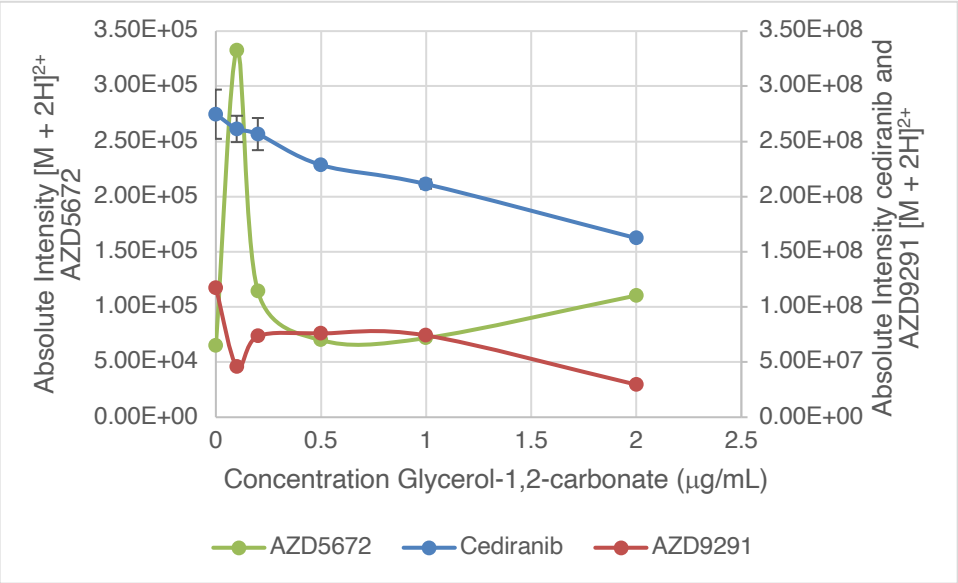

Figure 7.3.5. Absolute intensity of $[M + 2H]^{2+}$ cediranib, AZD9291 and AZD5671 for a range of glycerol-1,2,-carbonate concentrations.

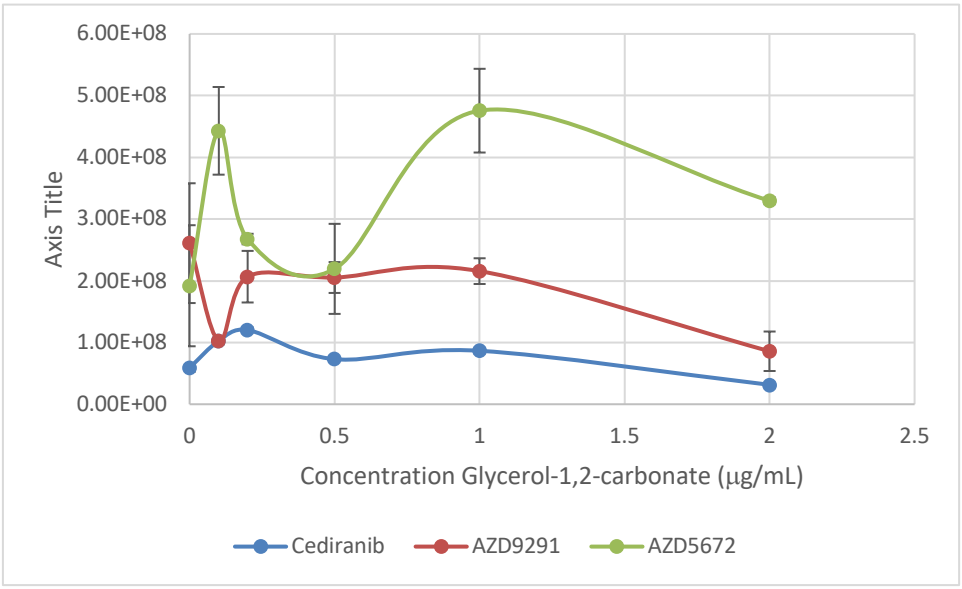

Figure 7.3.6. Absolute intensity of $[M + H]^{+}$ cediranib, AZD9291 and AZD5671 for a range of glycerol-1,2,-carbonate concentrations.

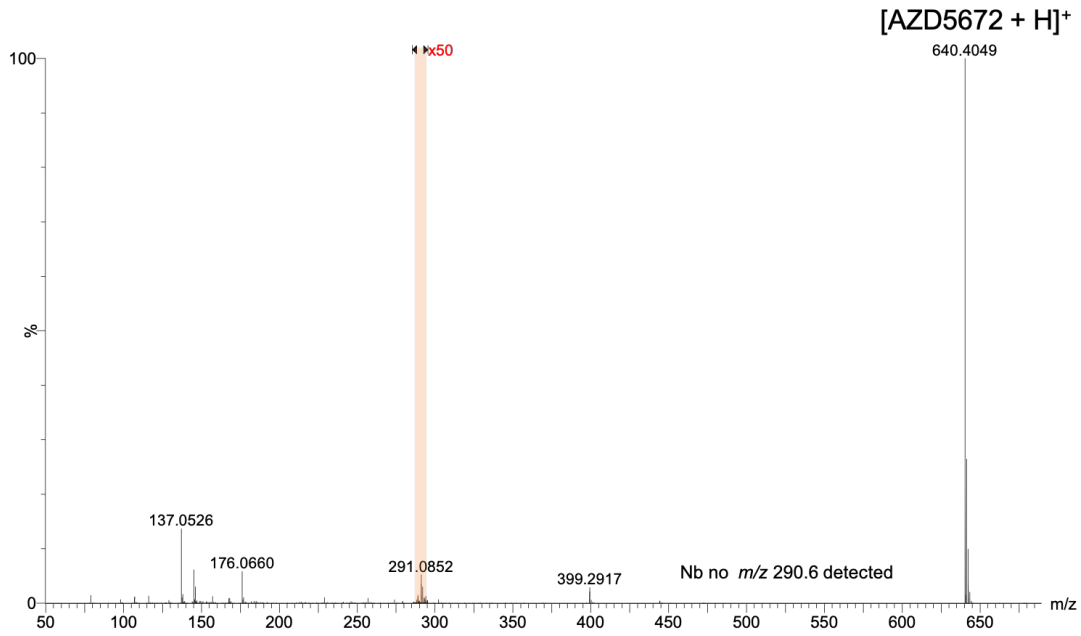

Figure 7.3.7. Spectra resulting from 1 μL/mL AZD5672 with 5 μL/mL DMSO in 50:50 0.1% formic acid ACN:H_2O.

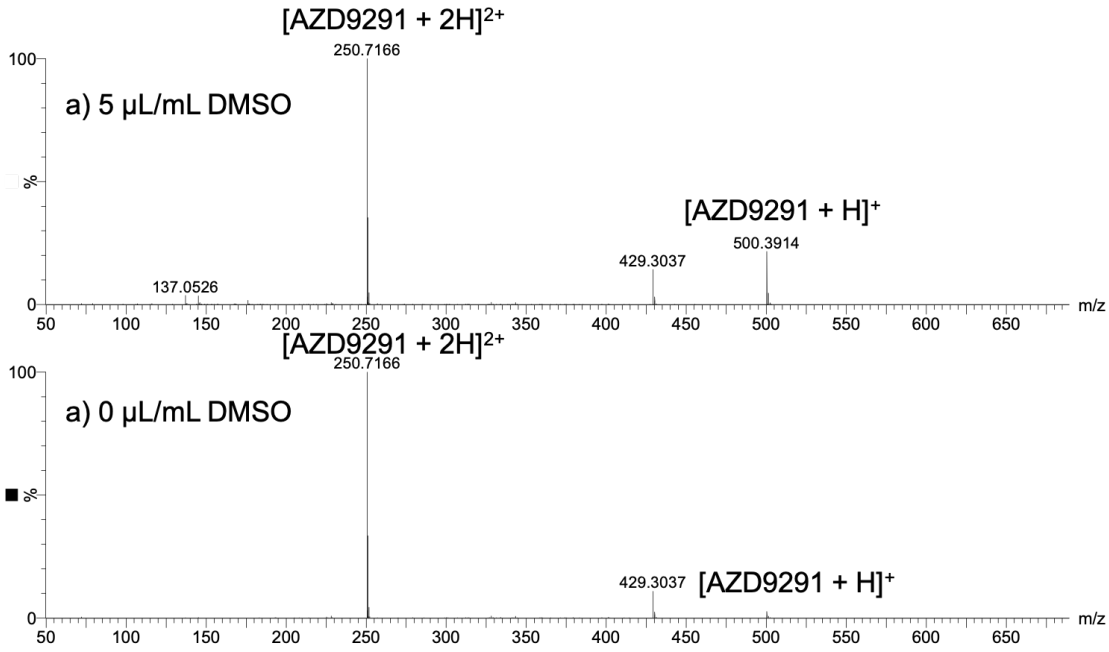

Figure 7.3.8. Spectra resulting from a) 1 μL/mL AZD9291 with 5 μL/mL DMSO in 50:50 0.1% formic acid ACN:H_2O and b) 1 μL/mL AZD9291 in 50:50 0.1% formic acid showing the decrease in detection of $[M + 2H]^{2+}$.

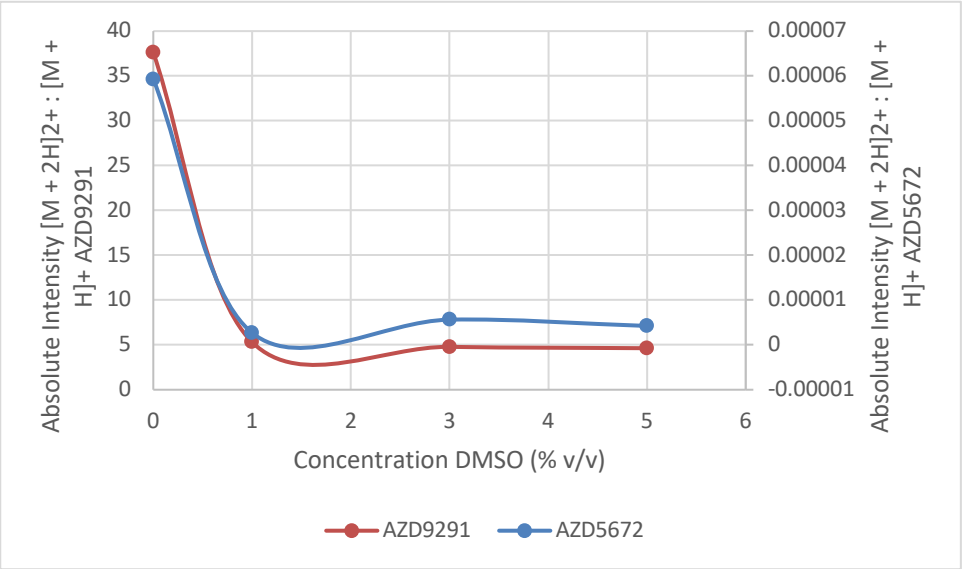

Figure 7.3.9. Ratio of the absolute intensity of $[M + 2H]^{2+}$: $[M + H]^{+}$ AZD9291 and AZD5672 for a range of DMSO concentrations.

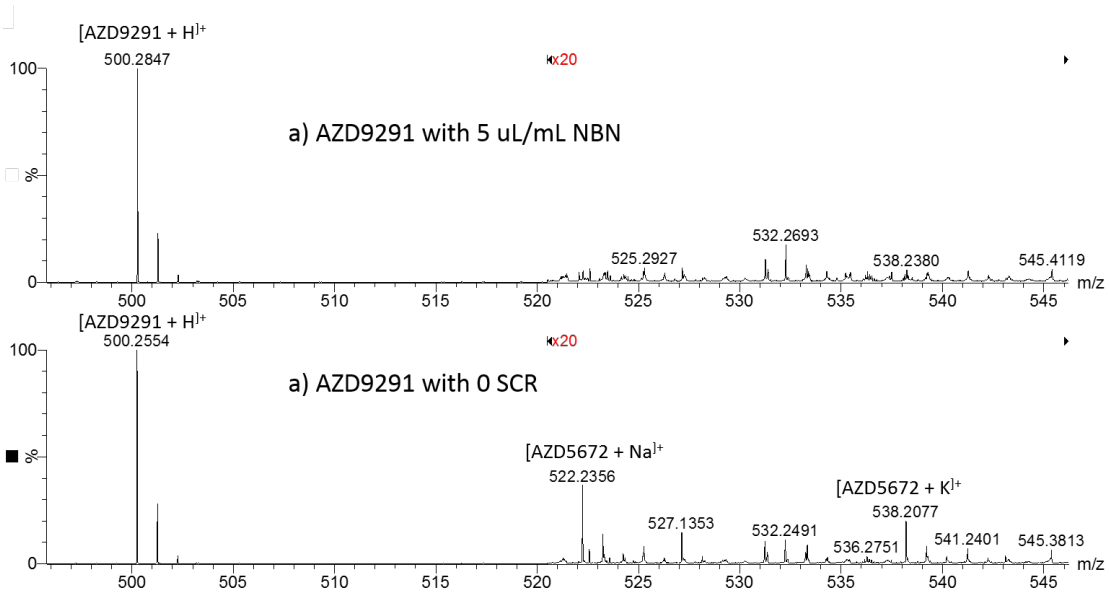

Figure 7.3.10. AZD9291 with 0 ad 5 μL/mL *m*NBN showing less salt adduction when *m*NBN was in the ESI solution.

7.4. Chapter 4

Time (Min)	Flow Rate (mL/min)	% H_2O	% ACN	Curve
0.0	0.4	95	5	6
0.3	0.4	95	5	6
4.3	0.4	5	95	6
4.7	0.4	5	95	6
4.71	0.4	95	5	6
5	0.4	95	5	6

Table 7.4.1. LC gradient for substance P LC-ETD.

Time (Min)	Flow Rate (mL/min)	% H_2O	% ACN	Curve
0.0	0.2	99	1	6
2.0	0.2	99	1	6
72.0	0.2	64	36	6
78.0	0.2	50	50	6
78.5	0.2	10	90	6
83.0	0.2	10	90	6
83.5	0.2	99	1	6
90	0.2	99	1	6

Table 7.4.2. LC gradient for BSA digest LC-ETD.

```
//====================================
//  ETD with Capillary Voltage Control
//====================================
public override void main()
{
      string property="CAPILLARY_VOLTAGE_SETTING";
      double analyteMass=450;
      double maxVoltage=3;
      double minVoltage=0.2;
      double downstepSize=0.5;
      double upstepSize=0.5;
      double maxIntensity=5000;
      double intensity=0;
      double voltage=2;
      double minIntensity=0.2;

      connect("epc");
    send_cmd("initPropertyArraysV");//clears old property banks


send_cmd("addPropV,0,Voltage_MARK_SPACE_SETTING,"+voltage.ToStrin
g()+ ",false");
    send_cmd("enableSyncWriteV");
    send_cmd("setSwitchCountV,0,3");
    start_function("WrensStartScan","writePropertyBankV");//start
the banks running

      enable_data_capture();
      reset_data();
      set_data_capture_range(analyteMass-1,analyteMass+1,50);
       set_property(property,(voltage).ToString());

    while(true)
    {
     if(intensity>maxIntensity)
      {
        //if(voltage>minVoltage+downstepSize)
        //{
       //     voltage=voltage-downstepSize;
                voltage=0.5;
            SetDRE(voltage);
            //set_property(property,(voltage).ToString());
           // print("New voltage: "+voltage.ToString());
        //}
        //reset_data();
        wait(650);
        string data=get_data();
        intensity=get_max(data);
        print("Intensity more than Max: "+intensity.ToString());
        print("New voltage: "+voltage.ToString());

      }

     else if (intensity<minIntensity)
      {
        //if(voltage<maxVoltage-upstepSize)
       // {
       //     voltage=voltage+upstepSize;
       voltage=99;
            //set_property(property,(voltage).ToString());
            SetVoltage(voltage);
           // print("New voltage: "+voltage.ToString());
     //   }
        reset_data();
```

```
        wait(650);
        string data=get_data();
        intensity=get_max(data);
        print("Intensity less than Min: "+intensity.ToString());
        print("New voltage: "+voltage.ToString());
      }

      else
      {
         //reset_data();
        wait(650);
        string data=get_data();
        intensity=get_max(data);
       print("Intensity inbetween: "+intensity.ToString());
        print(voltage.ToString());
      }

    }
}

public void SetVoltage(double Voltage)
{
        send_cmd("initPropertyArraysV");//clears   old   property
banks

send_cmd("addPropV,0,VOLTAGE_MARK_SPACE_SETTING,"+Voltage.ToStrin
g()+ ",false");
        send_cmd("enableSyncWriteV");
            send_cmd("setSwitchCountV,0,1");

      start_function("WrensStartScan","writePropertyBankV");

}
```

Script 7.4.1. WREnS LC-ETD script using capillary voltage to control analyte ion abundance.

```
//====================================
//  Dynamic Control of DRE lens setting
//====================================
public override void main()
{
      string property="DRE_MARK_SPACE_SETTING";
      double analyteMass=450;
      double maxDRESetting=99.9;
      double minDRESetting=1;
      //double downstepSize=95; //This has been hard coded in an
'on off' fasion...could be improved
      //double upstepSize=95;
      double  maxIntensity=2000;  //These  are  what  needs  to  be
optimised
    double minIntensity=500;
      double intensity=0;
      double DRESetting=99.9;
      int waitTime=645;


      connect("epc");
    send_cmd("initPropertyArraysV");//clears old property banks
```

```
send_cmd("addPropV,0,DRE_MARK_SPACE_SETTING,"+DRESetting.ToString
()+ ",false");
    send_cmd("enableSyncWriteV");
    send_cmd("setSwitchCountV,0,3");
    start_function("WrensStartScan","writePropertyBankV");//start
the banks running

      enable_data_capture();
      reset_data();
      set_data_capture_range(analyteMass-1,analyteMass+1,50);
       set_property(property,(DRESetting).ToString());

    while(true)
    {
     if(intensity>maxIntensity)
      {
        //if(DRESetting>minDRESetting+downstepSize)
        //{
       //     DRESetting=DRESetting-downstepSize;
                DRESetting=12;  //this  is  the  hard  coded  min
DREsetting
            SetDRE(DRESetting);
            //set_property(property,(DRESetting).ToString());
           // print("New DRESetting: "+DRESetting.ToString());
        //}
        wait(waitTime);
        string data=get_data();
        intensity=get_max(data);
        print("Intensity more than Max: "+intensity.ToString());
        print("New DRESetting: "+DRESetting.ToString());

      }

     else if (intensity<minIntensity)
      {
        //if(DRESetting<maxDRESetting-upstepSize)
       // {
       //     DRESetting=DRESetting+upstepSize;
                    DRESetting=99;  //this  is  the  hard  coded
max DREsetting
            //set_property(property,(DRESetting).ToString());
                  SetDRE(DRESetting);
           // print("New DRESetting: "+DRESetting.ToString());
     //   }
                reset_data();
                wait(waitTime);
                string data=get_data();
                intensity=get_max(data);
                print("Intensity      less      than      Min:
"+intensity.ToString());
                print("DRESetting: "+DRESetting.ToString());
      }

      else
      {
         //reset_data();
        wait(waitTime);
        string data=get_data();
        intensity=get_max(data);
            print("Intensity inbetween: "+intensity.ToString());
        print(DRESetting.ToString());
      }
```

```
    }
}

public void SetDRE(double DREvoltage)
{
        send_cmd("initPropertyArraysV");//clears   old   property
banks

send_cmd("addPropV,0,DRE_MARK_SPACE_SETTING,"+DREvoltage.ToString
()+ ",false");
        send_cmd("enableSyncWriteV");
            send_cmd("setSwitchCountV,0,1");

      start_function("WrensStartScan","writePropertyBankV");

}
```

Script 7.4.2. WREnS LC-ETD script using DRE lens attenuation to control analyte ion abundance.

```
//====================================
//  LC-ETD Optimisation using DRE lense settings
//====================================

double maxDRESetting=99.9;
double minDRESetting=1;
double maxIntensity=5000; //These are what needs to be optimised
double minIntensity=1000;
double intensity=0;
double DRESetting=99.9;

public override void main()
{
      string property="DRE_MARK_SPACE_SETTING";
      double analyteMass1=528.97;
      double analyteMass2=522.96;
      double analyteMass3=482.27;
      double analyteMass4=549.29;
      double analyteMass5=555.04;

      int elutionDelay1=520000;
      int elutionDelay2=20000;
      int elutionDelay3=260000;
      int elutionDelay4=140000;
      int elutionDelay5=200000;

      double maxDRESetting=99.9;
      double minDRESetting=1;
      //double downstepSize=95; //This has been hard coded in an
'on off' fasion...could be improved
      //double upstepSize=95;
      double  maxIntensity=5000;  //These  are  what  needs  to  be
optimised
    double minIntensity=1000;
      double intensity=0;
      double DRESetting=99.9;


      connect("epc");
    send_cmd("initPropertyArraysV");//clears old property banks
```

```
send_cmd("addPropV,0,DRE_MARK_SPACE_SETTING,"+DRESetting.ToString
()+ ",false");
    send_cmd("enableSyncWriteV");
    send_cmd("setSwitchCountV,0,3");
    start_function("WrensStartScan","writePropertyBankV");//start
the banks running

    FindPeak(analyteMass1,elutionDelay1);
    FindPeak(analyteMass2,elutionDelay2);
    FindPeak(analyteMass3,elutionDelay3);
    FindPeak(analyteMass4,elutionDelay4);
    FindPeak(analyteMass5,elutionDelay5);

}

public void FindPeak(double mass, int elutionDelay)
{
    disable_data_capture();
      enable_data_capture();
      reset_data();
      set_data_capture_range(mass-1,mass+1,50);
      StartProcessing(elutionDelay);
}

public void StartProcessing(int delay)
{
  int time=0;
    while(time<delay)
    {
     if(intensity>maxIntensity)
      {
        //if(DRESetting>minDRESetting+downstepSize)
        //{
       //     DRESetting=DRESetting-downstepSize;
                DRESetting=12; //this is the hard coded min
DREsetting
            SetDRE(DRESetting);
            //set_property(property,(DRESetting).ToString());
           // print("New DRESetting: "+DRESetting.ToString());
        //}
        wait(650);
        string data=get_data();
        intensity=get_max(data);
        print("Intensity more than Max: "+intensity.ToString());
       print("Mass: "+get_mass(data).ToString());
        print("New DRESetting: "+DRESetting.ToString());

      }

     else if (intensity<minIntensity)
      {
        //if(DRESetting<maxDRESetting-upstepSize)
       // {
       //     DRESetting=DRESetting+upstepSize;
                      DRESetting=99; //this is the hard coded
max DREsetting
            //set_property(property,(DRESetting).ToString());
                  SetDRE(DRESetting);
           // print("New DRESetting: "+DRESetting.ToString());
     //   }
                reset_data();
                wait(650);
                string data=get_data();
```

```
                intensity=get_max(data);
                print("Intensity      less      than      Min:
"+intensity.ToString());
        print("Mass: "+get_mass(data).ToString());
                print("DRESetting: "+DRESetting.ToString());
      }

      else
      {
         //reset_data();
        wait(650);
        string data=get_data();
        intensity=get_max(data);
        print("Intensity inbetween: "+intensity.ToString());
         print("Mass: "+get_mass(data).ToString());
        print(DRESetting.ToString());
      }

      time=time+650;

    }
}

public void SetDRE(double DREvoltage)
{
        send_cmd("initPropertyArraysV");//clears   old   property
banks

send_cmd("addPropV,0,DRE_MARK_SPACE_SETTING,"+DREvoltage.ToString
()+ ",false");
        send_cmd("enableSyncWriteV");
            send_cmd("setSwitchCountV,0,1");

      start_function("WrensStartScan","writePropertyBankV");

}
```

Script 7.4.3. WREnS LC-ETD script using DRE lens attenuation to control analyte ion abundance for multiple analytes at different RTs.

Research Article

Rapid Communications in Mass Spectrometry

Received: 21 April 2016 Revised: 16 July 2016 Accepted: 21 July 2016 Published online in Wiley Online Library

Rapid Commun. Mass Spectrom. **2016**, *30*, 2155–2163
(wileyonlinelibrary.com) DOI: 10.1002/rcm.7701

Characterisation of phosphorylated nucleotides by collisional and electron-based tandem mass spectrometry

Andrew T. Ball[1], Aruna S. Prakash[1], Anthony W.T. Bristow[2], Martin Sims[3] and Jackie A. Mosely[1]*

[1]Department of Chemistry, Durham University, South Road, Durham DH1 3LE, UK
[2]Global Medicines Development, AstraZeneca, Macclesfield SK10 2NA, UK
[3]Pharmaceutical Sciences, Innovative Medicines and Early Development, AstraZeneca, Macclesfield SK10 2NA, UK

RATIONALE: Tandem mass spectrometry of phosphorylated ions can often yield a limited number of product ions owing to the labile nature of phosphate groups. Developing techniques to improve dissociation for this type of ion has implications for the structural characterisation of many different phosphorylated ions, such as those from nucleotides, pharmaceutical compounds, peptides and polymers.
METHODS: Solutions of adenosine monophosphate, diphosphate and triphosphate (AMP, ADP and ATP) were studied in a hybrid linear ion trap–Fourier transform ion cyclotron resonance (FTICR) mass spectrometer. Precursor ions with an overall single positive charge, including protonated nucleotides or nucleotide cations containing one, two or three sodium atoms, were isolated for tandem mass spectrometry. Collision-induced dissociation (CID) was performed in the linear ion trap, with electron-induced dissociation (EID) being conducted in the FTICR cell.
RESULTS: EID resulted in many product ions not seen in CID. EID product ion spectra were seen to vary for AMP, ADP and ATP when the nucleotide cation contained zero, one, two or three sodiums. Precursor cations that contain two or three sodiums mainly formed product ions derived from the phosphate group. Conversely, when a precursor ion containing no sodium underwent EID, product ions mainly relating to the non-phosphate end of the ion were observed. The number of phosphate groups was not seen to greatly affect either CID or EID product ion spectra.
CONCLUSIONS: The presence of sodium in a precursor ion directs electron-induced bond dissociation, thus enabling targeted, and therefore tuneable, fragmentation of groups within that precursor ion. For all precursor ions, the most useful product ion spectra were obtained by EID for a precursor ion containing one sodium, with bond dissociation occurring across the entire nucleotide cation. The findings of this study can be used to improve the structural elucidation of many phosphorylated molecules by broadening the range of product ions achievable. © 2016 The Authors. *Rapid Communications in Mass Spectrometry* Published by John Wiley & Sons Ltd.

Electron-capture dissociation (ECD) is an electron-based dissociation technique that has been widely adopted for the structural characterisation of biological macromolecules. It uses low-energy electrons (typically 1–5 eV), which interact with multiply charged analyte ions in Fourier transform ion cyclotron resonance mass spectrometers.[1–4] In essence, an electron is captured by the analyte ion, forming an excited charge-reduced radical cation that then dissociates.[2,5,6] Unimolecular dissociation by this method is able to provide complementary fragmentation information to collision-induced dissociation (CID) and infrared multiphoton dissociation (IRMPD), retaining post-translational biological modifications that are otherwise lost and providing protein sequence information from intact proteins.[1,2,7–9] The analysis of synthetic polymers also benefits from ECD as fewer complex rearrangements allow for easier characterisation.[10,11] Hot electron-capture dissociation (hECD) was developed by Kjeldsen *et al.* where higher energy electrons (10 eV) were used for the analysis of multiply charged polypeptides, resulting in increased fragmentation compared with ECD.[12,13] More recently, electron-induced dissociation (EID) was developed, which allows for the study of singly charged positive and negative ions. Here, electrons with a high kinetic energy (10–30 eV) interact with precursor ions causing concurrent ionisation and excitation.[14–16] EID has been shown to yield product ions as the result of vibrational and electronic dissociation for a wide range of singly charged ions, including peptides, where cleavage is induced along the backbone and at side-chain groups, forming product ions that are observed in CID and ECD.[15–18] EID has proved useful for the structural elucidation of protonated pharmaceutical compounds, as well as sodium, potassium and ammonium adducts, with EID providing complementary information to CID, thus allowing

* *Correspondence to*: J. A. Mosely, Department of Chemistry, Durham University, South Road, Durham DH1 3LE, UK.
E-mail: jackie.mosely@durham.ac.uk

for better characterisation of these ions.[19] Similarities can be drawn between the product ions formed by EID of the protonated and ammonium-adducted precursors, although a small amount of extra structural information could be observed for the ammonium adduct. The alkali-metal-adducted precursors formed more product ions than the protonated and ammonium-adducted precursors, with sodium-containing precursor ions providing the most structural information.[20] Metal-adducted polyketide precursor ions have also been studied by EID and CID, with lithium-adducted precursor ions resulting in the most structural information. Although product ions were similar for all techniques, the most abundant were formed by EID.[21] EID, CID and IRMPD have also been compared for the study of chlorophyll-*a* where EID was shown to provide complementary product ions to CID. It was noted that loss of $H^{\bullet}$ was common from EID along with fragmentation resulting in odd-election species.[22] DNA and RNA have been studied by electron-detachment dissociation (EDD), an electron-based fragmentation technique used for multiply charged anions. When compared with CID and IRMPD, EDD resulted in minimal base loss and no secondary fragmentation. Determination of the binding position for Os complexes to DNA was also possible due to Os-bound product ions being formed by EDD.[23–28] Flosadóttir *et al.*[29] observed the effect of exchanging up to seven protons with sodium ions on bond cleavages by matrix-assisted laser desorption/ionisation (MALDI) for deoxy-oligonucleotides. Here, backbone cleavages were greatly reduced with increasing sodium content. Conversely, the neutral loss of certain bases increased with a greater number of sodium atoms on the precursor, thought to be owing to protonation of an adjacent base with higher proton affinity. Unique product ions were formed with the inclusion of sodium atoms, such as a complex fragmentation pathway involving the loss of several central bases and recombination to form a product ion.[29]

Phosphorylated ions have predictable vibrational tandem mass spectrometric behaviour, with loss of phosphate groups predominantly observed owing to the labile nature of the bond.[30–34] Cyclic adenosine monophosphate (cAMP) analogues have been studied by CID, with limited product ions formed. The majority of product ions related to cleavage between the ribose-phosphate and aminopurine sub-structures.[30] The limited nature of the product ions formed from CID for this type of ion has led to studies aimed at gaining increased information from tandem mass spectrometry, including the use of electron-based techniques. ECD of adenosine triphosphate (ATP) and analogous ions was shown to yield complementary product ions to CID for doubly charged precursor ions. Unique to ECD, ribose cross-ring cleavage was observed as well as several hydrated product ions formed by cross-ring cleavages at other groups. As CID also yields unique product ions, Liu *et al.* concluded that a combination of ECD and CID can be implemented to gain maximum product ion information for acidic metabolites.[35] ECD also results in high sequence coverage for phosphopeptides containing up to four phosphorylation sites.[31] The effect of increasing the number phosphate groups has on sequence coverage by ECD was that for $[M + 2H]^{2+}$, increased levels of phosphorylation results in lower sequence coverage of the peptides. This is thought to be caused by the phosphate groups forming salt bridges with amino acid side chains.[7] Losses usually observed by CID, such as H_2O, phosphate groups and phosphoric acid, were not observed by ECD.[21]

In this study, adenosine monophosphate diphosphate and triphosphate (AMP, ADP and ATP) have been analysed using CID and EID with varying numbers of sodium atoms contained within the precursor ion. The aim was to observe the effect of increasing numbers of phosphate groups and increasing number of sodium cations upon the two types of dissociation, and then use that information to gain maximum structural information and to determine the extent to which desired or directed fragmentation could be achieved through design.

EXPERIMENTAL

Sample preparation

AMP, ADP and ATP were purchased from Sigma-Aldrich Company Ltd (Gillingham, UK). All samples were made up to 1 μg mL^{-1} in 50:50 HPLC-grade acetonitrile from Fisher Scientific (Loughborough, UK) and deionised water (18.2 MΩ cm) with 0.1% formic acid from Sigma-Aldrich.

Mass spectrometry

All mass spectrometric measurements were performed on a hybrid linear ion trap–Fourier transform-ion cyclotron mass spectrometer equipped with a 7.0 T superconducting magnet (LTQFT from ThermoFinnigan, Bremen, Germany). Sample solutions were infused directly into an electrospray ionisation (ESI) source at 5 μL min^{-1}, from which positive ions were chosen for analysis. A heated capillary was set to 350°C and a sheath gas (nitrogen) optimised to a flow rate that delivered a stable spray. The spray voltage was 4 kV and the tube lens voltage was optimised to give the most intense precursor ion signal. For tandem mass spectrometry the isolation window was set 4 u. CID was performed in the ion trap region of this hybrid instrument using helium as the collision gas with 20–30 eV normalised collision energy, with the product ions measured in the FTICR instrument. For EID, the indirectly heated dispenser cathode inside the FTICR cell generated electrons at 26.5 eV for 70 ms. All data were recorded and processed using Xcalibur software (version 2.0; ThermoFinnigan, San Jose, CA, USA). Data were internally calibrated from the precursor ion and the common product ion $[H_4PO_4]^+$.

RESULTS AND DISCUSSION

Terminology

The overall charge state for each nucleotide cation studied was 1+, yet such ions with a net single positive charge could be thought of in a number of ways. This paper has employed the terminology of protonated nucleotide to refer to the cation of a nucleotide that only contains the atoms C, H N O and P and must be protonated (e.g. $[C_{10}H_{14}N_5O_7P + H^+]$ for AMP). The terminology 'monosodium nucleotide' refers to the cation, which could be either a sodiated nucleotide with OH groups,

Rapid Communications in Mass Spectrometry

or a protonated nucleotide that has an ONa group, e.g. $[C_{10}H_{14}N_5O_7P + Na^+]$ or $[C_{10}H_{13}N_5O_7PNa + H^+]$, respectively, for AMP. The terminology 'disodium nucleotide' is used to encompass both the possibility of a sodiated nucleotide with one ONa group and OH groups, and a protonated nucleotide that has two ONa groups; the terminology 'trisodium nucleotide' encompasses both sodiated nucleotide with two ONa groups and a protonated nucleotide that has three ONa groups.

EID and CID of protonated AMP, monosodium AMP and disodium AMP

CID of protonated AMP (Fig. 1(a)) yielded only one product ion at *m/z* 136.0617, relating to cleavage **A**, $[C_5H_6N_5]^+$, with an error of −0.2 ppm (Fig. 2). When monosodium AMP underwent CID (Fig. 1(b)), cleavage at **A** occurred again, with a sodium-containing ion being produced: $[C_5H_5N_5Na]^+$ at *m/z* 158.0436 (−0.5 ppm). Cleavage **B** resulted in an ion at *m/z* 234.9978, again with the inclusion of sodium, $[C_5H_9O_7PNa]^+$, with an error of 0.0 ppm. This indicates that the sodium cation can be retained by either fragment of the monosodium AMP precursor ion although the relative peak intensities would suggest that the phospho-ribose region has the stronger affinity for the sodium cation. Two other product ions, formed by cleavage **C**, were also observed (*m/z* 250.0934 and 272.0753) one with and one without the sodium atom, $[C_{10}H_{12}N_5O_3]^+$ and $[C_{10}H_{11}N_5O_3Na]^+$, with errors of −0.4 and −0.3 ppm, respectively. The relative abundance of $[C_{10}H_{12}N_5O_3]^+$ to $[C_{10}H_{11}N_5O_3Na]^+$ would suggest that the more favourable location for the sodium is on the phosphate. Conversely, disodium AMP is a very stable cation, only able to lose water by CID, as shown in Fig. 1(c) (*m/z* 374.0235, $[C_{10}H_{11}N_5O_6PNa_2]^+$, −0.3 ppm).

In contrast to CID, EID of protonated AMP resulted in the formation of significantly more product ions, as shown in Fig. 3. When protonated AMP (Fig. 3(a)) undergoes EID, over 80% of the product ions relate to cleavage at the aminopurine group. Cross-ring cleavages are only observed by EID for this precursor ion, such as cleavages across the aminopurine (**Pur**) and ribose (**Rib**) groups. There is precedence for this as Liu *et al.* noted that cross-ring cleavage for the ribose group of metabolites including ATP was only observed by ECD.[35] For protonated AMP, either the phosphate group or the aminopurine group can retain the proton, as demonstrated by cleavages **A** (*m/z* 136.0618, $[C_5H_6N_5]^+$, 0.0 ppm) and **D** (*m/z* 98.9841, $[H_4PO_4]^+$, −0.4 ppm).

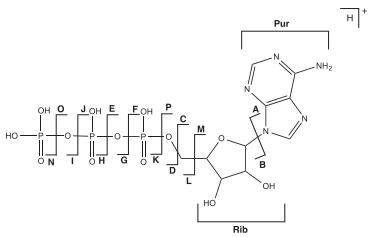

Figure 2. Diagram of protonated ATP describing the nomenclature used to identify a particular bond cleavage and corresponding product ion, plus the terminology used to discuss cleavages involving the purine (**Pur**) and ribose (**Rib**) regions. By extension, this diagram also applies to AMP and ADP and the mono-, di- and trisodium species.

EID of monosodium AMP (Fig. 3(b)) resulted in significantly more product ions than seen by CID, with over 75% pertaining to cleavage at the ribose group. The cross-ring cleavages at the aminopurine group seen for EID of protonated AMP are less numerous for EID of monosodium AMP, with an increased number across the ribose group (**Rib**) being observed. Some cleavages are common to EID of protonated AMP, such as **A** and **D**. **A** is seen with and without sodium (*m/z* 136.0618 and 158.0438, $[C_5H_6N_5]^+$ and $[C_5H_5NNa_5]^+$, 0.1 and 0.4 ppm) whereas **D** is seen exclusively containing sodium (*m/z* 120.9661, $[H_3PO_4Na]^+$, 0.1 ppm), suggesting that the phosphate group has a higher affinity for sodium cations. Cleavage **BC** relating to the central methyl-

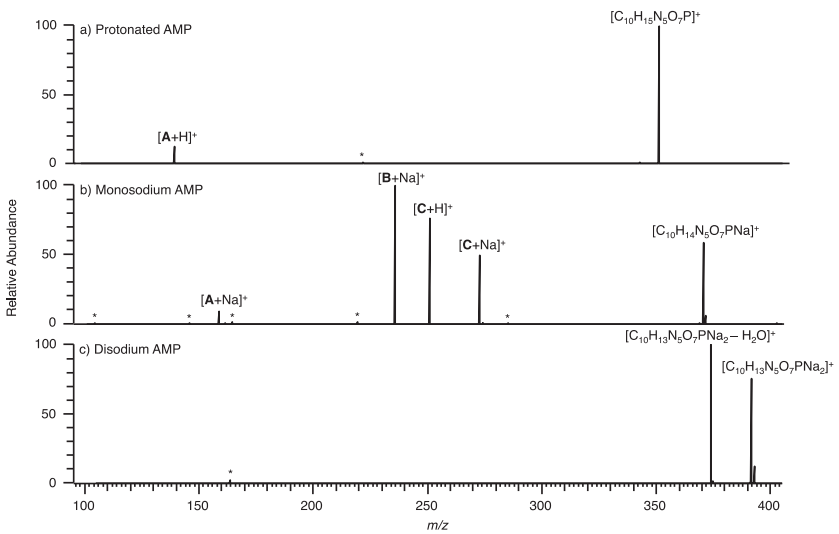

Figure 1. CID of precursor ions with an overall single charge for (a) protonated AMP, (b) monosodium AMP, and (c) disodium AMP. A full list of *m/z* values and corresponding molecular formulae are given in the Supporting Information. * indicates instrument noise.

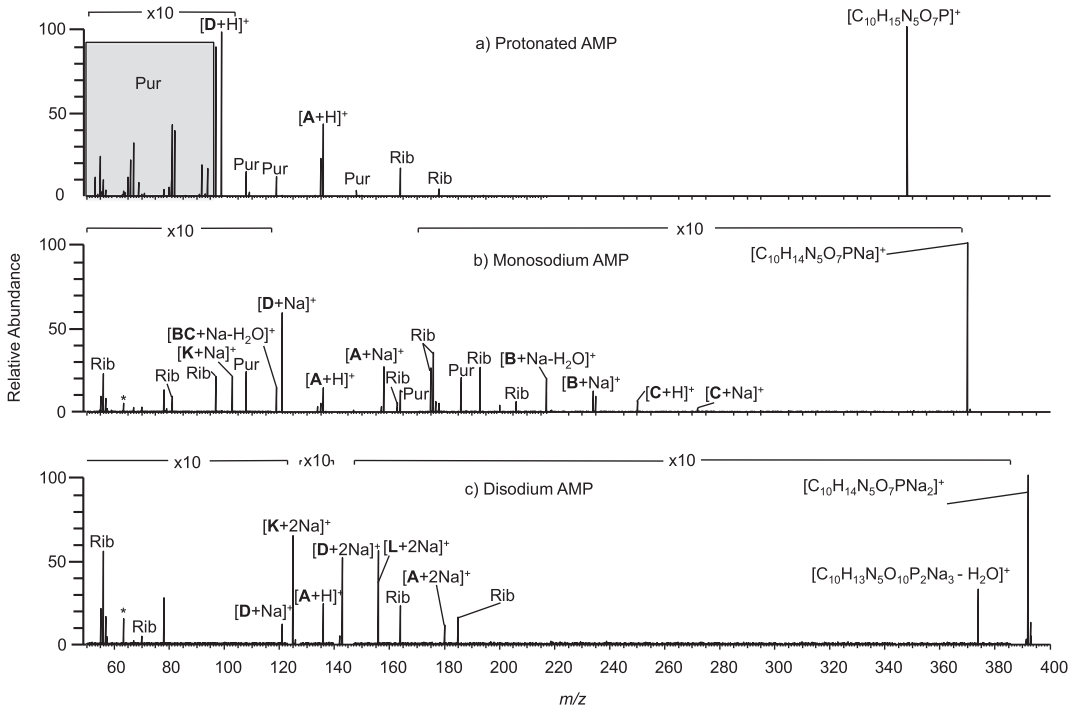

Figure 3. EID of precursor ions with an overall single charge for (a) protonated AMP, (b) monosodium AMP, and (c) disodium AMP. A full list of *m/z* values and corresponding molecular formulae is given in the Supporting Information. * indicates instrument noise.

ribose group was observed with and without sodium (*m/z* 119.0104, $[C_5H_4O_2Na]^+$, 0.1 ppm and *m/z* 97.0284, $[C_5H_5O_2]^+$, −0.1 ppm), showing that the ribose group is also capable of retaining a sodium cation. **BC** was not formed by EID of protonated AMP, which demonstrates that the location of the sodium causes this bond cleavage.

For disodium AMP (Fig. 3(c)), EID yielded fewer product ions than seen for protonated AMP and monosodium AMP. Increased cleavage at the phosphate group was observed, with over 50% of all the product ions relating to this region of the precursor ion. Cross-ring cleavages were only seen to occur at the ribose group (**Rib**). Two sodium cations are seen to reside on the phosphate group as well as independently on the aminopurine group following cleavages **D** and **A**, respectively. **A** is seen with zero and two sodiums (*m/z* 136.0618, $[C_5H_6N_5]^+$, 0.1 ppm and *m/z* 180.0257, $[C_5H_4N_5Na_2]^+$, 0.3 ppm) whereas **D** is seen with one and two sodiums (*m/z* 120.9661, $[H_3PO_4Na]^+$, −0.1 ppm and *m/z* 142.9481, $[H_2PO_4Na_2]^+$, 0.0 ppm) and **L** only with two sodiums (*m/z* 155.9559, $[CH_3PO_4Na_2]^+$, 0.1 ppm), lending further evidence that the aminopurine group has a stronger proton affinity than the phosphate group. Non-covalent cation-π interactions have been reported for tryptophan and other aromatic molecules and indicate that cations such as sodium can be tightly bound to the aromatic regions of a molecule in the gas phase, supporting this assignment.[36,37] The precursor ion was observed to lose water (*m/z* 374.0236, $[C_{10}H_{11}N_5O_6PNa_2]^+$, 0.1 ppm) as previously seen by CID, but not by ECD, supporting the conclusion that vibrational dissociation is a factor in EID.[18] In each case EID was able to generate a greater degree of information than CID, but as with CID the richest spectra were obtained from the monosodium species. Table 1 summarises the bonds cleaved in AMP, AMP monosodium and AMP disodium. As more sodium is included with the precursor ion, dissociation is clearly biased towards the phosphate group.

EID and CID of protonated ADP, monosodium ADP, disodium ADP and trisodium ADP

Figure 4 shows the CID product ion spectra for protonated, monosodium, disodium and trisodium ADP with the monosodium species providing the most information, analogous to AMP. CID of protonated ADP (Fig. 4(a)) yielded only product ions related to dissociation at one or both phosphate groups. As with protonated AMP, EID of protonated ADP (Fig. 5(a)) yielded many more product ions than CID, with most relating to extensive cleavage at the aminopurine group. Cross-ring cleavages at the aminopurine (**Pur**) and ribose (**Rib**) groups are common, as well as some cleavage along the phosphate backbone. As the majority of product ions are seen to contain at least part of the aminopurine group, this is the most likely location of the proton.

Monosodium ADP produces six product ions by CID (Fig. 4(b)). Cleavage **F** occurred by loss of one phosphate group (*m/z* 352.0414, $[C_{10}H_{12}N_5O_6PNa]^+$, −1.0 ppm) and cleavage at the **A**/**B** relates to the loss of aminopurine (*m/z* 314.9642, $[C_5H_{10}O_{10}P_2Na]^+$, 0.0 ppm), and loss of aminopurine with water (*m/z* 296.9536, $[C_5H_8O_9P_2Na]^+$, 0.1 ppm). **BF** corresponds to an internal product ion formed from the neutral loss of one phosphate and the aminopurine group with the addition of sodium (*m/z* 216.9874, $[C_5H_7O_6PNa]^+$, 0.0 ppm) while cleavage at **D** forms a product

Table 1. Summary of product ions formed by CID and EID for all precursor ions

Compound	Adduct	Cleavages from EID	Cleavages from CID
AMP	H	Purine(15), Ribose(2), **A**, **D**	**A**
	Na	Purine(4), Ribose(8), **M**, **A**, **A***, **B***, [**B***-H_2O], [**BC***-H_2O], **D***, **K***, **M***	**A**, **C**, **B***, **C***
	2Na	Ribose(4), **A***, **D***, **A****, **D****, **K****, **L****	-H_2O
ADP	H	Purine(8), Ribose(4), **A**, **C**, **D**, **E**	[**C**-H_2O], [**E**-H_2O], **E**
	Na	Purine(2), Ribose(14), **A**, [**BC**-H_2O], **M**, **A***, **B***, [**B***-H_2O], **BE***, **BF***, **D***, **K***, **L***	**C**, **F**, **B***, **BF***, [**B***-H_2O], **D***
	2Na	Ribose(7), **A**, **M**, **A***, **B***, [**B***-H_2O], **BE***, **BF***, **D***, **G***, **H***, **K***, **L***, **G****	**B****, [**B****-H_2O], **BF****, **D****, **F****
	3Na	Ribose(3), **A**, **G**, **F****, **G****, **H****, **D*****, **K*****	-H_2O, **F****
ATP	H	Purine(5), Ribose(4), **A**, **BC**, [**BC**-H_2O], **G**, **H**, **I**	**E**, **K**, [**K**-H_2O]
	Na	Purine(3), Ribose(7), **A**, **BC**, **C**, **G**, **I**, **B***, [**B***-H_2O], **BF***, BK*, **D***, **G***, **I***, **JB***, **K***, **L***, **N***	**B***, [**B***-H_2O], **C***, **J***
	2Na	Purine(1), Ribose(11), **A**, **C**, **A***, **I***, **G***, **B****, [**B****-H_2O], **D****, **F****, **G****, **H****, **I****, **J****, **JB****, **K****, **L****, **N****	**B****, [**B****-H_2O], **D****, **J****
	3Na	Purine(2), Ribose(8), **A**, **A***, **A****, **F****, **G****, **H****, **I****, **N****, **B*****, [**B*****-H_2O], **D*****, **G*****, **H*****, **I*****, **J*****, **JB*****, **K*****, **L*****	**B*****, [**B*****-H_2O], **J*****, **JB*****

Denotes the sodium content for each product ion (= 1; ** = 2 and *** = 3).

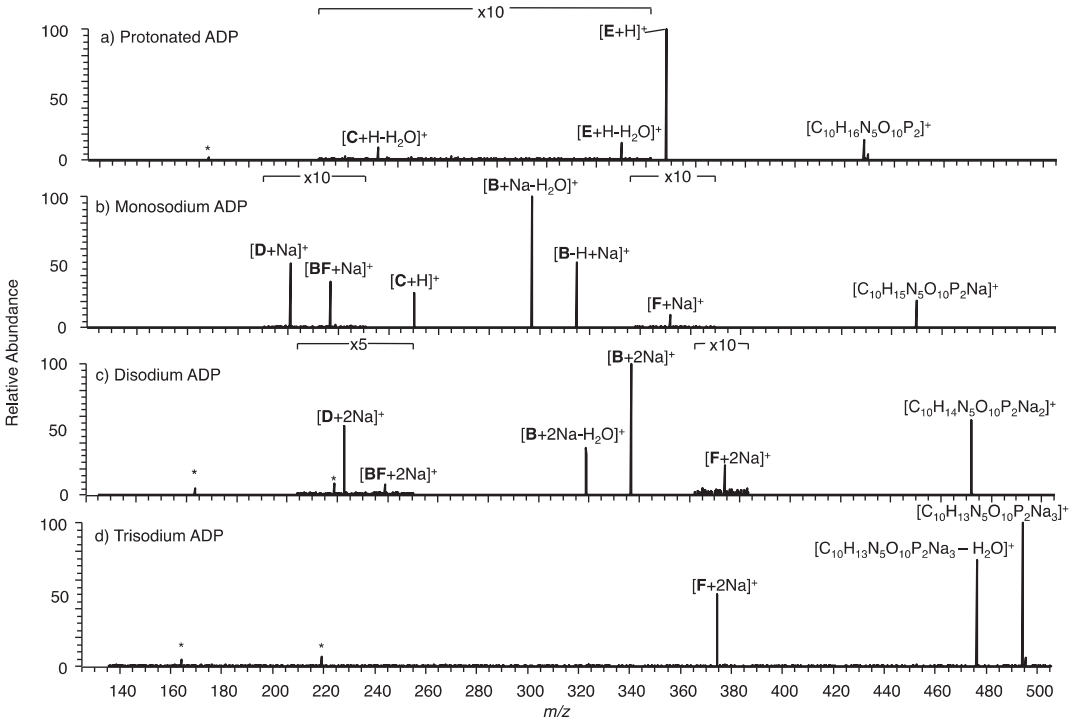

Figure 4. CID of precursor ions with an overall single charge for (a) protonated ADP, (b) monosodium ADP, (c) disodium ADP, and (d) trisodium ADP. A full list of *m/z* values and corresponding molecular formulae is given in the Supporting Information. * indicates instrument noise.

ion that relates to both phosphate groups (*m/z* 200.9324, $[H_4P_2O_7Na]^+$, −0.2 ppm). This shows that the sodium, probably located on the phosphate group, stabilises this group, allowing the aminopurine group to be lost and the diphosphate group to retain a charge. EID of monosodium ADP (Fig. 5(b)) induces bond cleavages mainly concentrated in the ribose region of the ion as with monosodium AMP; the majority being cross-ring cleavages at the ribose group (**Rib**). The sodium was always retained if the phosphate group was a part of the product ion and was also retained by the lone ribose product ion, **BC**-H_2O (*m/z* 119.0103, $[C_5H_4O_2Na]^+$, −0.1 ppm) and the lone aminopurine product ion **A** (*m/z* 158.0437, $[C_5H_5N_5Na]^+$, 0.1 ppm). These data show that although the sodium is always retained by

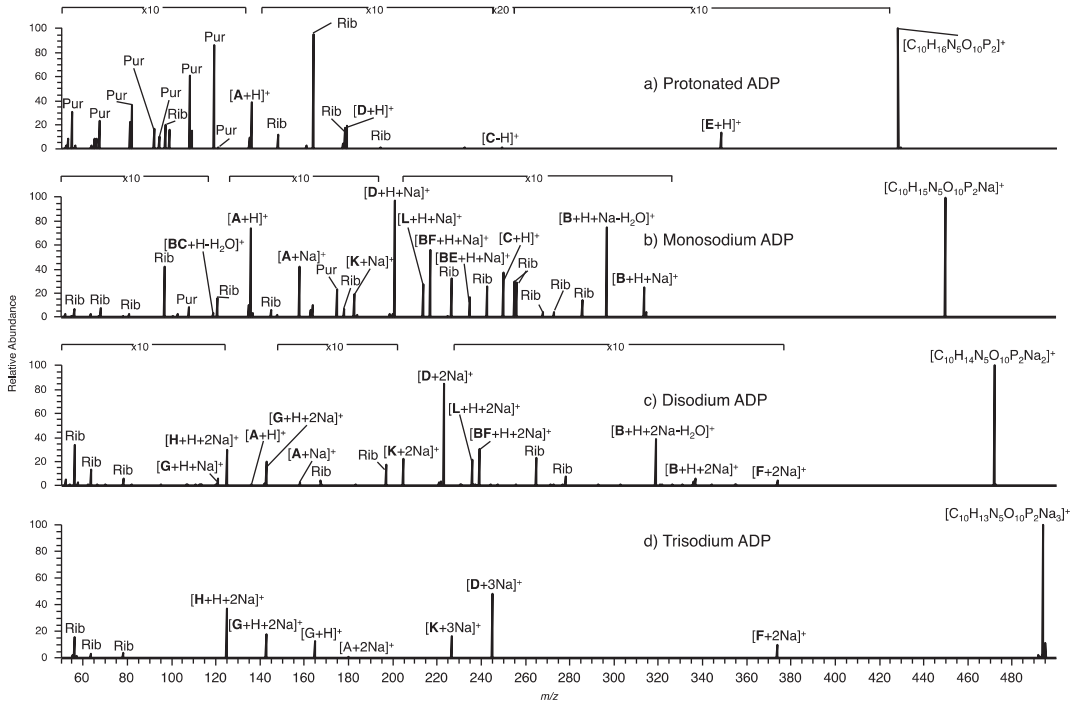

Figure 5. EID of precursor ions with an overall single charge for (a) protonated ADP, (b) monosodium ADP, (c) disodium ADP, and (d) trisodium ADP. A full list of *m/z* values and corresponding molecular formulae is given in the Supporting Information. * indicates instrument noise.

phosphate-containing product ions, it can also be retained, although not exclusively, by lone ribose and aminopurine product ions.

CID for disodium ADP (Fig. 4(c)) results in cleavage at nearly all the same bonds as for monosodium ADP, with the product ions retaining both sodiums. Cleavage at **C** was not observed however, as all the product ions from the disodium ADP contain the phosphate. The majority of the EID product ions for disodium ADP (Fig. 5(c)) pertain to cleavages along the phosphate backbone and at the ribose group. In contrast to EID of protonated ADP, all but two product ions contain part of the phosphate group, always with at least one sodium retained. Fewer cross-ring cleavages at the ribose group were observed (**Rib**), which is analogous to disodium AMP; cleavages are mainly concentrated at the diphosphate group. As this region of the precursor ions is the most likely location of sodium cations, the data suggests that EID is strongly affected by the presence and position of sodium.

CID of trisodium ADP (Fig. 4(d)) resulted in very limited fragmentation, with fewer product ions than monosodium and disodium ADP being formed. The product ions unique to CID of monosodium ADP and disodium ADP are only seen with the inclusion of sodium, showing that the presence of sodium on the diphosphate can weaken the bonds in this region. The loss of H_2O was observed for the first time (*m/z* 475.9724, $[C_{10}H_{11}N_5O_9P_2Na_3]^+$, 0.9 ppm) and **F**, as was the loss of one sodium and one phosphate group (*m/z* 374.0241, $[C_{10}H_{11}N_5O_6PNa_2]^+$, 0.3 ppm). EID of trisodium ADP (Fig. 5(d)) yielded fewer product ions than EID of protonated, monosodium and disodium ADP, and induced no cross-ring cleavage, leading to the proposition that the sodium is associated with the longer phosphate chains, concentrating dissociation in this region of the ion. This is supported by three observations: first that all but one of the sodium-containing product ions formed are related to the phosphate group; secondly, the formation of **G** (*m/z* 164.9300, $[HPO_4Na_3]^+$, 0.2 ppm) demonstrates that a single phosphate group can retain three sodiums; and, thirdly, that all the product ions relating to the phosphate groups contain sodium. In general product ions are formed by cleavage at the phosphate groups, always retaining two or three sodiums. The only product ion seen to contain the ribose group was **F** (*m/z* 374.0259, $[C_{10}H_{11}N_5O_6PNa_2]^+$, 5.2 ppm), formed by the loss of one phosphate group and one sodium. Cleavage at **A** forms the lone aminopurine product ion (*m/z* 180.0260, $[C_5H_4N_5Na_2]^+$, 1.9 ppm), showing that the aminopurine group can exist in the disodium form.

EID and CID of protonated ATP, monosodium ATP, disodium ATP and trisodium ATP

CID and EID of all the ATP precursor ions (Fig. 6) generated similar information to the AMP and ADP precursor ions. EID provided much more information than CID, with the monosodium species again being the most informative. CID of monosodium ATP (Fig. 6(b)) resulted in cleavage at **B**, relating to loss of the aminopurine group, not observed in CID of protonated ATP (Fig. 6(a)), with one sodium, and with one sodium and loss of H_2O (*m/z* 394.9304, $[C_5H_{11}O_{13}P_3Na]^+$, −0.2 ppm and *m/z* 376.9199 $[C_5H_9O_{12}P_3Na]^+$, −0.1 ppm, respectively) showing that the sodium cation affects the stability in this region of the ion. CID of trisodium ATP (Fig. 6(d)) induced cleavage **JB** (*m/z* 340.9176, $[C_5H_6O_9P_2Na_3]^+$, 0.4 ppm), which relates to the simultaneous loss of one phosphate group and the aminopurine group. This is the only precursor ion that

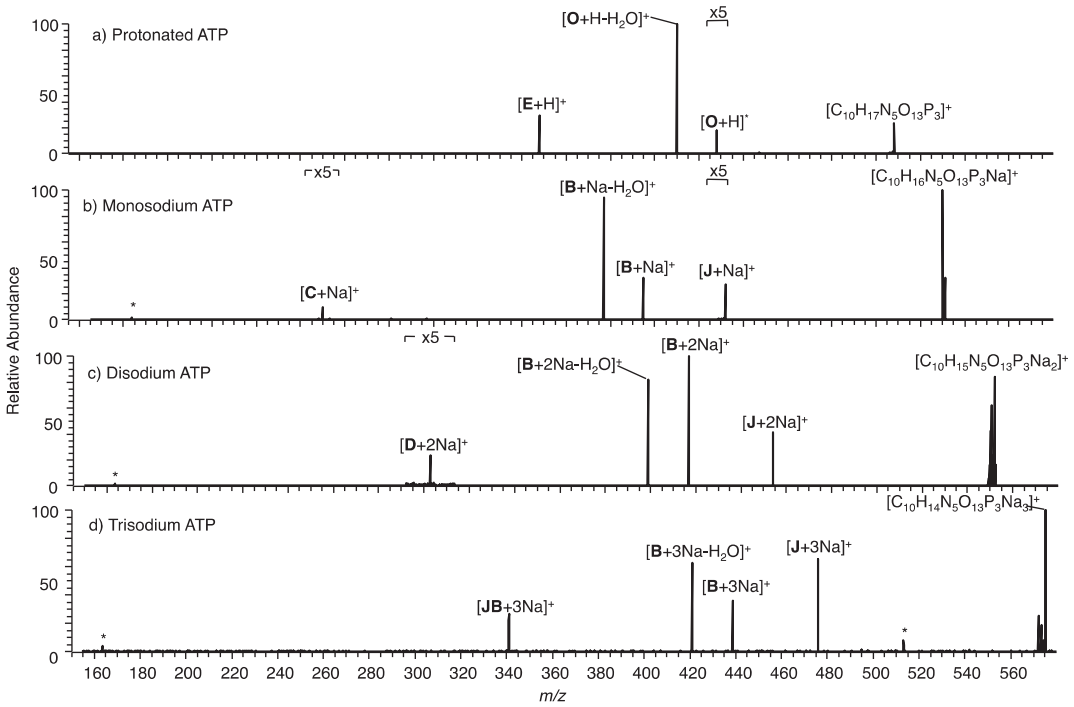

Figure 6. CID of precursor ions with an overall single charge for (a) protonated ATP, (b) monosodium ATP, (c) disodium ATP, and (d) trisodium ATP. A full list of *m/z* values and corresponding molecular formulae is given in the Supporting Information. * indicates instrument noise.

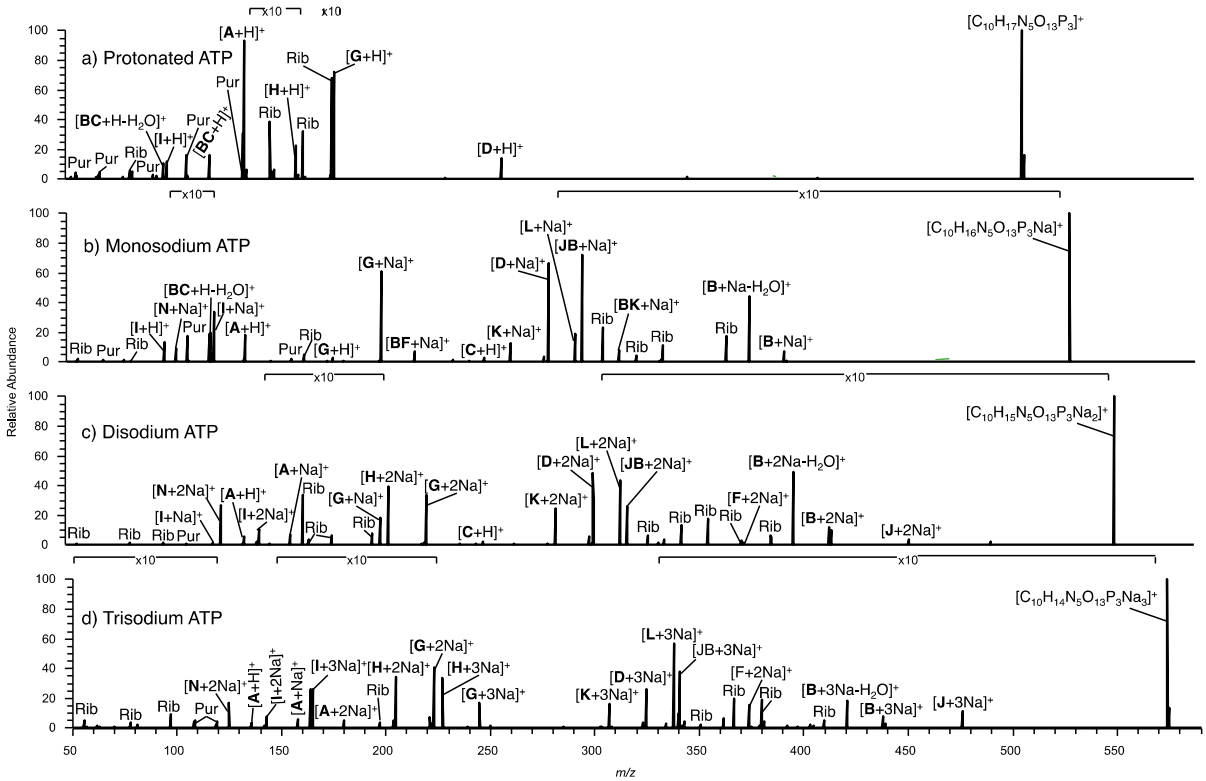

Figure 7. EID of precursor ions with an overall single charge for (a) protonated ATP, (b) monosodium ATP, (c) disodium ATP, and (d) trisodium ATP. A full list of *m/z* values and corresponding molecular formulae is given in the Supporting Information. * indicates instrument noise.

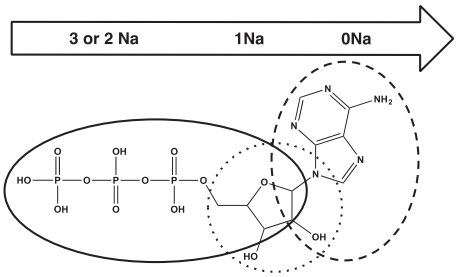

Figure 8. An ATP molecule has been used here to demonstrate the main regions of fragmentation that the ATP ions undergo with EID. For protonated ATP the main regions of fragmentation are shown by the dashed line, for monosodium ATP the dotted line and for di- and trisodium ATP the solid line. By extension, this diagram also applies to AMP and ADP.

formed this product ion by CID, probably caused by the location of the three sodium cations affecting the stability of the ribose diphosphate region of the ion.

EID of monosodium ATP (Fig. 7(a)) did not result in a product ion relating to the aminopurine ring retaining sodium, as previously seen for monosodium AMP and monosodium ADP. This is probably because the addition of a third phosphate group in the precursor ion biases the location of the sodium cation. EID of trisodium ATP (Fig. 7(d)) resulted in a greater number of small product ions relating to cross-ring cleavages at the aminopurine group (**Pur**) than for monosodium ATP and disodium ATP (Figs. 7(b) and 7(c)). This is proposed to be because, when three sodiums are included with the precursor ion, there is more chance of one of the sodium cations being located on the aminopurine group, directing some fragmentation towards this group.

CONCLUSIONS

EID gave significantly more diagnostic information for all the AMP, ADP and ATP precursor ions than CID, where cleavage was mainly limited to the phosphate group. The number of phosphate groups present was not seen to affect the EID product ion spectra, as has been noted for phosphorylated peptides, with common bond cleavages seen for one, two and three phosphate groups.[30] The number of sodium cations included in the precursor ion had limited effect on the CID product ion spectra. Sodium content did, however, have a dramatic effect on the EID product ion spectra, with the likely locations of the sodium cations directing fragmentation. Regardless of the number of phosphates, when no sodium was included with the precursor ion, EID focused at the aminopurine group suggesting this as the site for protonation. For EID of monosodium precursor ions, dissociation was predominantly seen at the ribose group whereas for EID for disodium and trisodium precursor ions, bond cleavage was generally induced at the phosphate group (demonstrated by Fig. 8 for AMP). The greatest number of product ions for AMP and ADP were observed using EID for the monosodium species, with product ions relating to all regions of the precursor ion. For ATP, however, EID for the trisodium precursor ion formed the most product ions, although the product ion spectra provided limited information as cleavage was mainly limited to the phosphate group. When studying phosphorylated ions, this study indicates that the most diagnostic and prolific tandem mass spectrometric information can be gained by performing EID on a monosodium species. For ions analogous to AMP, ADP and ATP, it is possible to direct EID by fragmenting ions that contain zero to three sodium atoms, enabling targeted study of different groups in the ion.

Acknowledgements

We would like to thank AstraZeneca, Waters Corporation and the Engineering and Physical Sciences Research Council for funding this project, and the British Mass Spectrometry Society for travel grant funding in order to present this research. Particular thanks must go also to Professor Mike Morris for support and advice in producing this paper.

REFERENCES

[1] R. A. Zubarev, N. L. Kelleher, F. W. McLafferty. Electron capture dissociation of multiply charged protein cations. A nonergodic process. *J. Am. Chem. Soc.* **1998**, *120*, 3265.
[2] R. A. Zubarev, D. M. Horn, E. K. Fridriksson, N. L. Kelleher, N. A. Kruger, M. A. Lewis, B. K. Carpenter, F. W. McLafferty. Electron capture dissociation for structural characterization of multiply charged protein cations. *Anal. Chem.* **2000**, *72*, 563.
[3] N. A. Kruger, R. A. Zubarev, D. M. Horn, F. W. McLafferty. Electron capture versus energetic dissociation of protein ions. *Int. J. Mass Spectrom.* **1999**, *187*, 787.
[4] R. A. Zubarev. Reactions of polypeptide ions with electrons in the gas phase. *Mass Spectrom. Rev.* **2003**, *22*, 57.
[5] K. Håkansson, H. J. Cooper, M. R. Emmett, C. E. Costello, A. G. Marshall, C. L. Nilsson. Electron capture dissociation and infrared multiphoton dissociation MS/MS of an N-glycosylated tryptic peptide to yield complementary sequence information. *Anal. Chem.* **2001**, *73*, 4530.
[6] H. J. Cooper, K. Håkansson, A. G. Marshall. The role of electron capture dissociation in biomolecular analysis. *Mass Spectrom. Rev.* **2005**, *24*, 201.
[7] A. J. Creese, H. J. Cooper. The effect of phosphorylation on the electron capture dissociation of peptide ions. *J. Am. Soc. Mass. Spectrom.* **2008**, *19*, 1263.
[8] S. D. Shi, M. E. Hemling, S. A. Carr, D. M. Horn, I. Lindh, F. W. McLafferty. Phosphopeptide/phosphoprotein mapping by electron capture dissociation mass spectrometry. *Anal. Chem.* **2001**, *73*, 19.
[9] D. M. Horn, Y. Ge, F. W. McLafferty. Activated ion electron capture dissociation for mass spectral sequencing for larger (42 kDa) proteins. *Anal. Chem.* **2000**, *72*, 4778.
[10] B. A. Cerda, D. M. Horn, K. Breuker, F. W. McLafferty. Sequencing of specific copolymer oligomers by electron-capture-dissociation mass spectrometry. *J. Am. Chem. Soc.* **2002**, *124*, 9287.
[11] B. A. Cerda, D. M. Horn, K. Breuker, F. W. McLafferty. Electron capture dissociation of multiply-charged oxygenated cations. *Eur. J. Mass Spectrom.* **1999**, *5*, 335.
[12] F. Kjeldsen, K. F. Haselmann, B. A. Budnik, F. Jensen, R. A. Zubarev. Dissociative capture of hot (3–13 eV) electrons by polypeptide polycations: an efficient process accompanied by secondary fragmentation. *Chem. Phys. Lett.* **2002**, *356*, 201.

[13] F. Kjeldsen, K. F. Haselmann, E. S. Sorensen, R. A. Zubarev. Distinguishing of Ile/Leu amino acid residues in the PP3 protein by (hot) electron capture dissociation in Fourier transform ion cyclotron resonance mass spectrometry. *Anal. Chem.* **2003**, *75*, 1267.
[14] B. A. Budnik, K. F. Haselmann, Y. N. Elkin, V. I. Gorbach, R. A. Zubarev. Applications of electron-ion dissociation reactions for analysis of polycationic chitooligosaccharides in Fourier transform mass spectrometry. *Anal. Chem.* **2003**, *75*, 5994.
[15] H. Lioe, R. A. J. O'Hair. Comparison of collision-induced dissociation and electron-induced dissociation of singly protonated aromatic amino acids, cystine and related simple peptides using a hybrid linear ion trap–FT-ICR mass spectrometer. *Anal. Bioanal. Chem.* **2007**, *389*, 1429.
[16] Y. M. E. Fung, C. M. Adams, R. A. Zubarev. Electron ionization dissociation of singly and multiply charged peptides. *J. Am. Chem. Soc.* **2009**, *131*, 9977.
[17] A. S. Prakash, E. J. Humphrey, J. A. Mosely. Electron-induced dissociation of anions. *Int. Labmate* August/September, **2012**.
[18] V. H. Nguyen, C. Afonso, J.-C. Tabet. Comparison of collision-induced dissociation and electron-induced dissociation of singly charged mononucleotides. *Int. J. Mass Spectrom.* **2012**, *316-318*, 140.
[19] A. S. Prakash, M. P. J. Smith, Z. Kaabia, J. A. Mosely. Using electron induced dissociation (EID) on an LC time-scale to characterize a mixture of analogous small organic molecules. *J. Am. Soc. Mass. Spectrom.* **2012**, *23*, 850.
[20] J. A. Mosely, M. J. Smith, A. S. Prakash, M. Sims, A. W. Bristow. Electron-induced dissociation of singly charged organic cations as a tool for structural characterization of pharmaceutical type molecules. *Anal. Chem.* **2011**, *83*, 4068.
[21] R. H. Wills, M. Tosin, P. B. O'Connor. Structural characterization of polyketides using high mass accuracy tandem mass spectrometry. *Anal. Chem.* **2012**, *84*, 8863.
[22] J. Wei, H. Li, M. P. Barrow, P. B. O'Connor. Structural characterization of chlorophyll-***a*** by high resolution tandem mass spectrometry. *J. Am. Soc. Mass. Spectrom.* **2013**, *5*, 753.
[23] B. A. Budnik, K. F. Haselmann, R. A. Zubarev. Electron detachment dissociation of peptide di-anions: an electron ± hole recombination phenomenon. *Chem. Phys. Lett.* **2001**, *342*, 299.
[24] I. Anusiewicz, M. Jasionowski, P. Skurski, J. Simons. Backbone and side-chain cleavages in electron detachment dissociation (EDD). *J. Phys. Chem. A* **2005**, *109*, 11332.
[25] H. T. Song, K. Hakansson. Electron detachment dissociation and negative ion infrared multiphoton dissociation of electrosprayed intact proteins. *Anal. Chem.* **2012**, *84*, 871.
[26] V. H. Nguyen, C. Afonso, J.-C. Tabet. Concomitant EDD and EID of DNA evidenced by MS^n and double resonance experiments. *Int. J. Mass Spectrom.* **2011**, *301*, 224.
[27] M. Taucher, K. Breuker. Top-down mass spectrometry for sequencing of larger (up to 61 nt) RNA by CAD and EDD. *J. Am. Soc. Mass Spectrom.* **2010**, *6*, 918.
[28] C. A. Wootton, C. Sanchez-Cano, H. K. Liu, M. P. Barrow, P. J. Sadler, P. B. O'Connor. Binding of an organo–osmium(II) anticancer complex to guanine and cytosine on DNA revealed by electron-based dissociations in high resolution top–down FT-ICR mass spectrometry. *Dalton Trans.* **2015**, *44*, 3624.
[29] H. Flosadóttir, M. Stano, O. Ingólfsson. Sodium controlled selective reactivity of protonated deoxy-oligonucleotides in the gas phase. *J. Am. Soc. Mass Spectrom.* **2009**, *20*, 689.
[30] A. E. Bond, S. Ding, C. M. Williams, R. P. Newton, E. Dudley. Mass spectrometric fragmentation behaviour of cAMP analogues. *Int. J. Mass Spectrom.* **2011**, *304*, 130.
[31] A. Stensballe, O. N. Jensen, J. V. Olsen, K. F. Haselmann, R. A. Zubarev. Electron capture dissociation of singly and multiply phosphorylated peptides. *Rapid Commun. Mass Spectrom.* **2000**, *14*, 1793.
[32] A. Chi, C. Huttenhower, L. Y. Geer, J. J. Coon, J. E. P. Syka, D. L. Bai, J. Shabanowitz, D. J. Burke, O. G. Troyanskaya, D. F. Hunt. Analysis of phosphorylation sites on proteins from Saccharomyces cerevisiae by electron transfer dissociation (ETD) mass spectrometry. *Proc. Natl. Acad. Sci. USA* **2007**, *104*, 2193.
[33] M. Holcapek, R. Jirasko, M. Lisa. Basic rules for the interpretation of atmospheric pressure ionization mass spectra of small molecules. *J. Chromatogr. A* **2010**, *1217*, 3908.
[34] H. J. Andreazza, M. Fitzgerald, D. Bilusich, R. Hoffmann, P. Hoffmann, P. C. H. Elchinger, J. H. Bowie. Characteristic negative ion fragmentations of deprotonated peptides containing post-translational modifications: mono-phosphorylated Ser, Thr and Tyr. A joint experimental and theoretical study. *Rapid Commun. Mass Spectrom.* **2008**, *22*, 3305.
[35] H. Liu, H. J. Yoo, K. Håkansson. Characterization of phosphate-containing metabolites by calcium adduction and electron capture dissociation. *J. Am. Soc. Mass. Spectrom.* **2008**, *19*, 799.
[36] D. A. Dougherty. Cation-pi interactions in chemistry and biology: a new view of benzene, Phe, Tyr, and Trp. *Science* **1996**, *271*, 163.
[37] L. Feketeová, M. W. Wong, R. A. J. O'Hair. The role of metal cation in electron-induced dissociation of tryptophan. *Eur. Phys. J. D* **2010**, *60*, 11.

SUPPORTING INFORMATION

Additional supporting information may be found in the online version of this article at the publisher's website.